

Research and development of the High-Granularity Timing Detector (HGTD) for the ATLAS Detector as the preparation of the High-Luminosity LHC operation phase

Valentina Raskina

▶ **To cite this version:**

Valentina Raskina. Research and development of the High-Granularity Timing Detector (HGTD) for the ATLAS Detector as the preparation of the High-Luminosity LHC operation phase. High Energy Physics - Experiment [hep-ex]. Sorbonne Université, 2023. English. ⟨NNT : 2023SORUS235⟩. ⟨tel-04228097⟩

HAL Id: tel-04228097

https://theses.hal.science/tel-04228097v1

Submitted on 4 Oct 2023

HAL is a multi-disciplinary open access archive for the deposit and dissemination of scientific research documents, whether they are published or not. The documents may come from teaching and research institutions in France or abroad, or from public or private research centers.

L'archive ouverte pluridisciplinaire **HAL**, est destinée au dépôt et à la diffusion de documents scientifiques de niveau recherche, publiés ou non, émanant des établissements d'enseignement et de recherche français ou étrangers, des laboratoires publics ou privés.



HAL Authorization






SORBONNE UNIVERSITÉ

École doctorale des Sciences de la Terre et de l'Environnement et Physique de l'Univers, Paris (ED 560)

Laboratoire de Physique Nucléaire et de Hautes Énergies - UMR 7585

Recherche et développement pour le détecteur de temps hautement granulaire (HGTD) pour le détecteur ATLAS en préparation de la phase de haute luminosité du LHC

Valentina Raskina

Thèse de doctorat

pour obtenir le grade de

DOCTEUR EN SCIENCES

Dirigée par Prof. Sophie Trincaz-Duvoid

Co-dirigée par Dr. Tristan Beau

Soutenue publiquement le 8 septembre 2023 devant le jury composé de:

Tristan	Beau	Co-encadrant
Stefan	Guindon	Examinateur
Anne-Catherine	Le Bihan	Rapporteure
Christophe	Ochando	Examinateur
Roman	Poeschl	Rapporteur
Boris	Popov	Président du jury
Sophie	Trincaz-Duvoid	Directrice de thèse

Ce travail de thèse a été réalisé avec le soutien de l'Initiative Physique des Infinis de Sorbonne Université






SORBONNE UNIVERSITÉ

École doctorale des Sciences de la Terre et de l'Environnement et Physique de l'Univers, Paris (ED 560)

Laboratoire de Physique Nucléaire et de Hautes Énergies - UMR 7585

Research and development of the High-Granularity Timing Detector (HGTD) for the ATLAS Detector as the preparation of the High-Luminosity LHC operation phase

Valentina Raskina

PhD Thesis

Submitted in fulfilment of the requirements for the degree of

DOCTEUR EN SCIENCES

Supervised by Prof. Sophie Trincaz-Duvoid

Co-supervised by Dr. Tristan Beau

Defended on September 8th 2023 in front of the jury:

Tristan	Beau	Co-supervisor
Stefan	Guindon	Examiner
Anne-Catherine	Le Bihan	Referee
Christophe	Ochando	Examiner
Roman	Poeschl	Referee
Boris	Popov	President of the jury
Sophie	Trincaz-Duvoid	Supervisor

This thesis work has been realised with the support of the Initiative Physique des Infinis de Sorbonne Université

Contents

1 Introduction **13**

2 The ATLAS experiment **17**
2.1 The Standard Model . . . 17
2.2 The Large Hadron Collider . . . 19
2.2.1 CERN accelerator complex . . . 21
2.2.2 The LHC acceleration principle . . . 22
2.2.3 Luminosity and Pile-up . . . 23
2.3 The ATLAS physics highlights . . . 24
2.3.1 The physics goals of the High-Luminosity LHC . . . 28
2.4 The ATLAS Detector . . . 30
2.4.1 Inner Detector . . . 31
2.4.2 Calorimeters . . . 34
2.4.3 Muon Spectrometer . . . 37
2.4.4 Magnets . . . 38
2.4.5 Trigger System . . . 39
2.4.6 Computing . . . 40
2.5 The High-Luminosity Large Hadron Collider . . . 43
2.5.1 Baseline hardware improvements . . . 45
2.6 ATLAS upgrades for the HL-LHC . . . 46
2.6.1 The Inner Tracker . . . 46
2.6.2 The High-Granularity Timing Detector . . . 49

3 High-Granularity Timing Detector **53**
3.1 Physics motivation . . . 53
3.1.1 Physics object performance . . . 53
3.1.2 Impact on the VBF Higgs production analysis . . . 58
3.2 HGTD and luminosity measurement . . . 59
3.3 The HGTD technical aspects . . . 62
3.3.1 Detector overview and key requirements . . . 62
3.3.2 Radiation environment . . . 68

3.4 LGAD sensors . . . 70
3.4.1 LGAD Technology . . . 72
3.4.2 Single Event Burnout . . . 74
3.5 Front-End electronics . . . 77
3.5.1 Single channel readout . . . 77
3.5.2 General ASIC requirements . . . 78
3.5.3 Contribution to the time resolution . . . 79
3.6 Conclusion . . . 81

4 Mechanical R&D for the HGTD **83**
4.1 Detector layout design . . . 83
4.1.1 Modules placement . . . 83
4.1.2 Support units design . . . 84
4.2 Gluing procedure . . . 87
4.2.1 Gluing parameters . . . 89
4.2.2 Tests . . . 92
4.3 Heater demonstrator . . . 96
4.3.1 Introduction . . . 98
4.3.2 Heaters calibration . . . 100
4.3.3 Heaters metrology . . . 101
4.3.4 SUs for the heaters . . . 104
4.3.5 Gluing . . . 104
4.3.6 Demonstrator assembly and tests . . . 106
4.4 Conclusion and outlook . . . 109

5 Performance studies of Low Gain Avalanche Detectors **111**
5.1 Test Beam Setup . . . 112
5.1.1 DESY . . . 112
5.1.2 CERN . . . 114
5.2 Data processing . . . 115
5.2.1 Waveform processing . . . 115
5.2.2 Track reconstruction . . . 117
5.3 LGAD studied characteristics . . . 117
5.3.1 Efficiency . . . 119
5.3.2 Charge . . . 119
5.3.3 Time resolution . . . 120
5.4 Tested Sensors . . . 123
5.4.1 DESY 2020 campaign . . . 124
5.4.2 DESY 2022 campaign . . . 124
5.5 Results of the DESY 2020 campaign . . . 125
5.5.1 Sensors irradiated at fluence of $1.5\times10^{15}\mathrm{n_{eq}cm^{-2}}$ . . . 125

5.5.2 Sensors irradiated at fluence of $2.5\times10^{15}n_{eq}cm^{-2}$ 125
5.5.3 Summary 127
5.6 Performance of the carbon enriched sensors 127
5.6.1 FBK-UFSD3.2-W19 sensors with different irradiations 128
5.6.2 IHEP-IMEv2-W7Q2 sensors with different irradiations 132
5.6.3 USTC-IMEv2.1-W17 sensors with different irradiations 134
5.6.4 Sensor USTC-IMEv2.1-W19 irradiated at $2.5\times10^{15}n_{eq}cm^{-2}$ . . 137
5.6.5 Efficiency uniformity 139
5.6.6 Summary 140
5.7 Comparison of the results from DESY 2022 and CERN SPS 2021 . . . 142
5.8 Conclusion 143

6 HGTD simulation and performance studies 147
6.1 Reconstruction of the charged particles trajectories 148
6.1.1 Track parametrization 148
6.1.2 Particle propagation 150
6.1.3 Track reconstruction in ITk 151
6.1.4 Track-time association in HGTD 153
6.2 Low-level performance of HGTD 154
6.2.1 Particles showering in ITk 154
6.2.2 Extrapolation uncertainties 155
6.2.3 Track-time association efficiency 156
6.2.4 Track-time association resolution 161
6.3 Enhancement of the track-time association performance 163
6.3.1 TDR cleaning procedure 163
6.3.2 Holes on track cleaning concept 165
6.3.3 Holes on track cleaning for the 2-ring HGTD geometry 173
6.3.4 Track reconstruction performance of the 3-ring HGTD 180
6.4 Conclusion and outlook 182

7 HGTD integration in A Common Tracking Software 185
7.1 The ACTS project for HL-LHC 186
7.1.1 Overview 186
7.1.2 The ACTS core components 187
7.2 Integration of ACTS into the ATLAS software framework 193
7.2.1 Athena environement 193
7.2.2 ACTS specific packages 194
7.2.3 ACTS-HGTD reconstruction roadmap 195
7.3 Construction of ACTS tracking geometry for HGTD 196
7.3.1 GeoModel geometry 196
7.3.2 Readout geometry 197

7.3.3 Tracking geometry . . . 197
7.3.4 Propagation test . . . 200
7.4 Conclusion and outlook . . . 203

8 Conclusion **205**

A **209**
A.1 Silicon detectors overview . . . 209
A.1.1 The Band theory . . . 209
A.1.2 P-type semiconductors . . . 211
A.1.3 N-type semiconductors . . . 212
A.1.4 The p-n junction . . . 212
A.1.5 Signal generation in silicon sensors . . . 214
A.1.6 Radiation damage in the silicon detectors . . . 216
A.1.7 The NIEL scaling . . . 216

B **219**
B.1 The heaters measurements . . . 219

C **229**
C.1 Holes on track cleaning performance for the 2-ring HGTD geometry . . . 229

Bibliography **229**

Résumé de la thèse en français

Le Large Hadron Collider (LHC) est un collisionneur protons situé au CERN à Genève. Il a déjà permis de nombreuses avancées scientifiques dont la découverte du boson de Higgs en 2012. En 2013, le programme de mise à niveau du LHC a été annoncé, dans le but d'atteindre une luminosité très élevée, supérieure d'un facteur 5 au schéma initial. C'est ce qu'on appelle la phase HL-LHC (pour High Luminosity - LHC). Le but est d'obtenir une luminosité de 5×10^{34} cm^{-2}s$^{-}1$ mais celle-ci pourrait atteindre 7×10^{34}cm^{-2}s^{-1}. Dans ce scénario, le nombre moyen de collisions par croisement de faisceaux serait de 200 (à comparer par exemple à 25 en 2012). Le collisionneur fournirait alors une luminosité intégrée de 4000 fb^{-1} en 12 ans.

Le but de telles performances techniques est bien sûr d'accroître le potentiel de mesure des expériences, notamment en ce qui concerne les mécanismes de production du boson de Higgs ou la brisure de symétrie électrofaible, mais aussi l'exploration des processus de physique au-delà du modèle standard avec, par exemple, la recherche de particules supersymétriques légères.

Pour faire face à cet afflux de signaux et à un taux de radiations plus important, les détecteurs du LHC vont, eux aussi, être modifiés. Parmi eux, le détecteur ATLAS (A Toroidal LHC ApparatuS) est en cours d'amélioration à plusieurs niveaux : électronique plus rapide sur certains sous-systèmes, remplacement complet de certains sous-détecteurs (dont le nouveau détecteur de traces et de vertex ITk) ou encore ajout de nouvelles parties. Parmi celles-ci figure un nouveau sous-détecteur hautement granulaire permettant une mesure précise en temps du passage de traces dans le détecteur. Ce sous-détecteur appelé HGTD (High-Granularity Timing Detector) sera installé à l'avant du détecteur ATLAS de chaque côté du point de collision pour la phase à haute luminosité du LHC (HL-LHC) en 2029.

Ce détecteur viendra compléter le nouveau détecteur ITk, pour permettre de combiner les informations spatiales que celui-ci permettra d'obtenir, avec des informations temporelles, et ainsi de bien associer les traces au point de collision d'où elles auront été émises.

Ceci permettra de diminuer les effets d'empilement. En effet, à haute luminosité, il va y avoir beaucoup d'interactions entre protons lors des collisions et il importe de faire

la différence entre des événements intéressants à étudier et ceux qui «s'empilent» lors du même croisement ou au croisement suivant.

Ce sous-détecteur devra être très résistant aux radiations qui pourront atteindre une fluence d'environ $5.6 \times 10^{15}\,\mathrm{n_{eq}}\ \mathrm{cm}^{-2}$. Le dispositif de détection est composé de capteurs semi-conducteurs LGAD qui présentent une bonne résistance aux radiations et assurent une résolution en temps comprise entre 30 et 50 ps.

La thèse, comprenant de nombreux aspects, s'inscrit dans la préparation de ce futur sous-détecteur.

Les Chapitres 2 et 3 décrivent le détecteur ATLAS, le LHC, la phase à haute luminosité et le futur HGTD.

Le Chapitre 4 est consacré à la recherche et développement en mécanique pour l'assemblage des modules sur des supports qui seront fixés sur les disques composant HGTD. Il importe que ces modules soient optimisés pour être simples à disposer et à remplacer tout en maximisant la surface active de détection. Le travail a également porté sur la préparation d'un démonstrateur.

Le Chapitre 5 est dédié aux analyses des données prises lors de tests en faisceaux par les capteurs LGAD. Il s'agit de choisir les spécifications des LGAD et les sociétés qui vont les produire en fonction de leur bonne tenue aux radiations, de leur efficacité de détection et de leur résolution en temps.

Le Chapitre 6 est dédié aux performances des algorithmes de reconstruction des traces passant par HGTD et ITk. Une nouvelle méthode de réduction du taux de jets d'empilement est présentée. Le Chapitre 7 décrit l'implémentation de HGTD dans le cadre des algorithmes de reconstruction de traces dans le détecteur ATLAS.

Résumé de la thèse en anglais

The Large Hadron Collider (LHC) is a proton-proton collider located at CERN in Geneva. It served in numerous scientific breakthroughs, including the discovery of the Higgs boson in 2012. In 2013, the LHC upgrade program was announced, aiming to deliver very high luminosity, a factor of five higher than the original design. This is known as the High-Luminosity LHC phase (HL-LHC). The aim is to achieve a luminosity of at least 5.10^{34} $cm^{-2}s^{-}1$ and potentially $7.10^{34}cm^{-2}s^{-1}$. In this scenario, the average number of collisions per beam crossing would be 200 (compared with 25 in 2012, for example). The collider would then deliver an integrated luminosity of 4000 fb^{-1} in 12 years.

The aim of such technical upgrades is of course to increase the measurement potential of the experiments, such as the increase of Higgs boson production or study the electroweak symmetry breaking, but also to explore physics beyond the Standard Model with, for example, supersymmetry.

To cope with the increased data rate and higher radiation levels, the LHC detectors will also be upgraded. Among them, the ATLAS detector (A Toroidal LHC ApparatuS) which is undergoing a major upgrade: faster electronics on certain sub-systems, complete replacement of certain sub-detectors (for example, the new tracking detector ITk) or the addition of new ones such as High-Granularity Timing Detector (HGTD). HGTD will be installed in both endcaps of the ATLAS detector for HL-LHC in 2029. It will provide a precise measurement of the tracks' times complementing the spatial information provided by ITk.

This will greatly reduce the tracking ambiguities. Indeed, the high luminosity will bring a lot of simultaneous interactions between partons during proton bunch crossing, and it's important to distinguish between events that are interesting to study and the pile-up ones.

HGTD must be highly resistant to radiation since the estimated fluence will reach around $5.6 \times 10^{15}\,n_{eq}$ cm^{-2}. The detector is based on LGAD semiconductor sensors, which are highly resistant to radiation and provide a time resolution of between 30 and 50 ps.

The thesis work covers many aspects of HGTD design and operation and is organised as follows.

Chapters 2 and 3 describe the ATLAS detector, the LHC, the HL-LHC phase and the future HGTD.

Chapter 4 is dedicated to the mechanical R&D for the detector assembly procedure and the design of the support structures for modules. It is important that these supports are optimized for easy installation and replacement while maximizing the active sensitive area. It also covers the work on the HGTD heater demonstrator.

Chapter 5 is dedicated to the analysis of data taken during test beams for the LGAD sensors performance studies. The aim is to select the LGAD specifications and the vendors that will produce them, based on their radiation hardness, detection efficiency and time resolution.

Chapter 6 focuses on the performance of HGTD track reconstruction capabilities. A new method for improving the purity of efficiency is presented. Chapter 7 describes the integration of HGTD in a novel tracking software ACTS that will be used by the ATLAS experiment during the HL-LHC phase.

Acknowledgements

I had an amazing time exploring, learning, gaining experience, and working at LPNHE for the ATLAS experiment. This PhD opened a lot of opportunities for me and brought wonderful people in my life for which I am very grateful. Many great people are responsible for this enriching time.

I want to thank the Step'up doctoral school and the Initiative Physique des Infinis de Sorbonne Université for the opportunity and financial support. My gratitude also goes to Marco Zito for welcoming me in LPNHE.

The acknowledgements are dedicated to the jury members, who kindely accepted to participate in my defense. Thank you very much, Anne-Catherine, Roman, Christophe, Boris, and Stefan, I really appreciate this.

Of course, this PhD would not be such a joyful experience without my incredible supervisor Sophie, who became a great example to me. Thank you so much for believing in me and helping me to overcome the complicated times every PhD student may get. I truly appreciate your support throughout these years and priceless advices, both in my professional and personal life. I could not get luckier to get you as a mentor.

Thanks also go to my co-supervisor Tristan for guidance, management and for valuable advices. It was a pleasure to work with you.

The very special person, to whom I am very thankful and whom I consider a brilliant scientist and mentor, is Alexander Leopold. Thank you so much for introducing me to the world of ATLAS software, for your guidance, for your help, and for the most exciting work experience. It is invaluable to have a chance to work with you!

Thank you to Noemi and Paul for the guidance and help in ACTS-connected tasks, for answering millions of my questions and for always finding time for consultations.

Thank you to all the people from the HGTD collaboration I had the luck to work with. Many thanks to Didier Lacour, Stefan, Chiara, Louie, Lucia, Afonso, Djamel, Didier Laporte, Alexander, Ocean, and many-many others.

I am infinitely grateful for my boyfriend Matteo, who was always there for me and gave me nothing but support, help, care and love. It is a pleasure to have such a brilliant and inspiring person by my side.

Thank you so much, Louis, for our friendship and the great time we had during these three years. I will truly miss you as an officemate.

All this would not be possible without my dear family. Father, mother, Andrey, Vasilisa, and babushka, thank you for your love, for support, and for believing in me. Mother and father, this PhD is the product of your continuous care, education, and dedication to your kids. Thank you for the happy childhood and for giving an example.

Thank you from the bottom of my heart to Paolo, Patrizia, and Caterina for your kindness, support and the joyful time we spent together. Many thank to my friends Vika, Zlata, Alina, Enrico, Marco, and Diletta for all the fun and amazing moments. Thank you Roland for my new BMW.

Last, but not least I want to thank the whole LPNHE laboratory for building such a good and friendly environment.

Chapter 1

Introduction

The Large Hadron Collider (LHC) [1] is the world's largest and most powerful particle accelerator, located at CERN (European Organization for Nuclear Research) [2] on the Franco-Swiss border and operated since 2008. A primary motivation for the construction of LHC was the discovery and study of the Higgs boson, a particle predicted by the Standard Model of particle physics. The great advantage of the LHC physics programme, however, is its "no-lose theorem", meaning that together with probing the Standard Model with high precision it has the potential to study the theories Beyond the Standard Model (BSM), such as supersymmetry. The LHC is designed to record proton-proton collisions (p-p) with a maximum centre of mass energy of $\sqrt{s} = 14$ TeV and lead-lead and proton-lead collisions for the quark-gluon plasma studies [2]. The collider serves several experiments including ATLAS (A Toroidal LHC Apparatus) [3], which is of interest for this PhD thesis. ATLAS is a general purpose experiment, its physics program includes the study of the Standard Model, measurements of the Higgs boson properties and searches of new physics such as supersymmetry and dark matter. It is designed to provide an accurate reconstruction of muons, photons, electrons, tau-leptons, jets and missing transverse energy measurements under high luminosity conditions.

An important indicator of the performance of an accelerator is its luminosity, which is proportional to the number of collisions that occur in a given amount of time. The higher the luminosity, the more data the experiments can collect and therefore the higher is the probability to observe a rare process [1]. The High-Luminosity LHC (HL-LHC) [4] upgrade project aims to increase the integrated luminosity by a factor of ten beyond the LHC's design value, with an average of 200 collisions per proton bunches crossing instead of 30 in Run 2, for example. The HL-LHC peak luminosity will reach $5 - 7.5 \times 10^{34}\text{cm}^{-2}\text{s}^{-1}$ and achieve an integrated luminosity of 250 fb^{-1} per year or over 3000 fb^{-1} in the whole opreation period. Its operation is planned to start in 2029 and run for at least 12 years. All the LHC detectors, including ATLAS, have

to cope with it and improve their radiation hardness and enhance the capability to process much higher data rates. Therefore, several ATLAS sub-detector systems are undergoing major improvements during the Phase-II upgrade.

The downside of the high luminosity is that with the interesting high-energy (hard-scatter) collisions associated with the primary vertices also soft collisions, pile-up, are happening. Pile-up "pollutes" the hard-scatter events, which leads to a worse reconstruction of the objects and increased experimental measurement uncertainties. Following the pile-up contamination challenges, the High-Granularity Timing Detector (HGTD) is being designed in order to improve the reconstruction abilities of the ATLAS detector forward region. HGTD, located around 3.5 m away from the interaction point in both ATLAS end-caps, will cover the pseudorapidity region of $2.4 < |\eta| < 4.0$ and will consist of two double-sided discs. The purpose of HGTD is to provide precise time measurements for tracks in the most problematic forward region, with an average time resolution of 30 ps (50 ps) per track at the beginning (by the end) of HL-LHC operation. A good time resolution of HGTD will be achieved by using the Low Gain Avalanche Detectors (LGAD), the new semiconductor sensors technology meant for precise timing measurements. By adding time measurements for tracks to spatial information, HGTD will resolve the track-vertex association ambiguities. Although a track may appear to align spatially with a particular vertex, differences in the track's time and the selected vertex's time can be used to identify and discard pile-up tracks.

This thesis is dedicated to the research and development for HGTD on several topics including mechanical aspects, LGAD sensors performance studies, track reconstruction enhancement, and software developments. The document is structured as follows.

Chapter 2 gives an overview of LHC and the ATLAS experiment. It briefly describes the Standard Model framework and LHC. The chapter also provides a non-exhaustive overview of the ATLAS physics highlights and a description of the ATLAS detector. Last, but not least, the HL-LHC motivation is provided and the corresponding ATLAS upgrade overview including the HGTD.

Chapter 3 is dedicated to HGTD, including the physics motivation supporting the need of timing measurements, the key detector requirements, and the technical design.

In the next chapters, my contributions to the detector development are presented. An extensive R&D is ongoing in order to define the most optimal geometry of the support units holding the HGTD modules, assembly procedure, and cooling. In Chapter 4, the mechanical R&D, in which LPNHE is deeply involved, is described. In this scope, I have conducted several assembly tests of the modules and support units to define an effective gluing procedure. A large part of the mechanical R&D work was dedicated to the heater demonstrator meant to study the mechanical and cooling aspects of HGTD using the silicon-based heater substrate mimicking the real modules. I contributed

to all the activities related to the demonstrator: the calibration of the heaters, the metrology tests of the heaters, the gluing of the heaters onto support units, the demonstrator assembly and data taking. The demonstrator work uncovered some bottlenecks in the module assembly and the cooling. It triggered several detector design changes.

Chapter 5 is dedicated to the performance studies of several LGAD sensors from various vendors. I participated in several test beam campaigns meant to study different aspects of the sensors: the performance characteristics, such as efficiency, time resolution etc., and the sensors mortality described in Section 3.4.2. I also performed the analysis of the data taken in the test beam campaigns described in the chapter. The results of these tests served as an important milestone in defining the baseline LGAD design for HGTD. Last, but not least, two publications are associated to this work.

A comprehensive study was done for the HGTD track reconstruction improvement described in Chapter 6. A dense pile-up environment together with a significant material budget upstream of HGTD and the consequent particle showering causes a low purity of the track-time association in HGTD. I developed and implemented a new algorithm, *holes on track cleaning*, that addresses the problem of the wrong track-time assignment. The algorithm significantly improves the purity of the tracking efficiency.

Last, but not least, ATLAS is planning to make extensive use of A Common Tracking Software (ACTS) during the HL-LHC data-taking. ACTS provides a possibility to make use of the HGTD time measurements in the 4D-tracking, which will largely improve the physics object reconstruction capability in the harsh pile-up environment during the HL-LHC era. Chapter 7 gives an overview of ACTS software and its integration into the ATLAS analysis software. Even though, this work is considered as long-term project, I made the first steps towards the ACTS integration of HGTD.

Chapter 2

The ATLAS experiment

This chapter is dedicated to the ATLAS experiment, including the physics motivation for its operation and the technical design of the detector. Section 2.1 provides an overview of the Standard Model (SM) [5] of particle physics. Section 2.2 describes the background for building the Large Hadron Collider and gives a brief overview of its operation and purposes. In Section 2.3, the ATLAS physics discoveries highlights are presented. The current ATLAS detector systems are described in Section 2.4, while the future High-Luminosity LHC and the dedicated ATLAS upgrade are presented in Sections 2.5 and 2.6 respectively.

2.1 The Standard Model

In the second half of the 20th century, the theoretical framework describing elementary particles and their interactions was developed. This framework, based on the Quantum Field Theory (QFT), is called the Standard Model [5] and has been developed and tested in stages through the work of many scientists worldwide. The SM describes three out of four known fundamental forces in the universe, namely the electromagnetic, weak, and strong interactions, and classifies all known elementary particles (see Figure 2.1). Currently, gravity is the sole remaining force that is explained in the domain of classical physics General Relativity [6]. Its inclusion into the QFT framework has been a persistent theoretical challenge [6].

According to the SM, the universe is composed of 12 fundamental particles called "fermions" (shown in purple and green in Figure 2.1), that have no substructure. These fermions have half-integer spin [1] (1/2) and are divided into two categories: quarks and leptons. The SM also includes the antiparticle version of each fermion, particles with the same mass, but inverse quantum numbers. The interactions between fermions are mediated by gauge bosons of integer spin, which are the photon (γ) for

[1] Spin is an intrinsic form of angular momentum carried by elementary particles

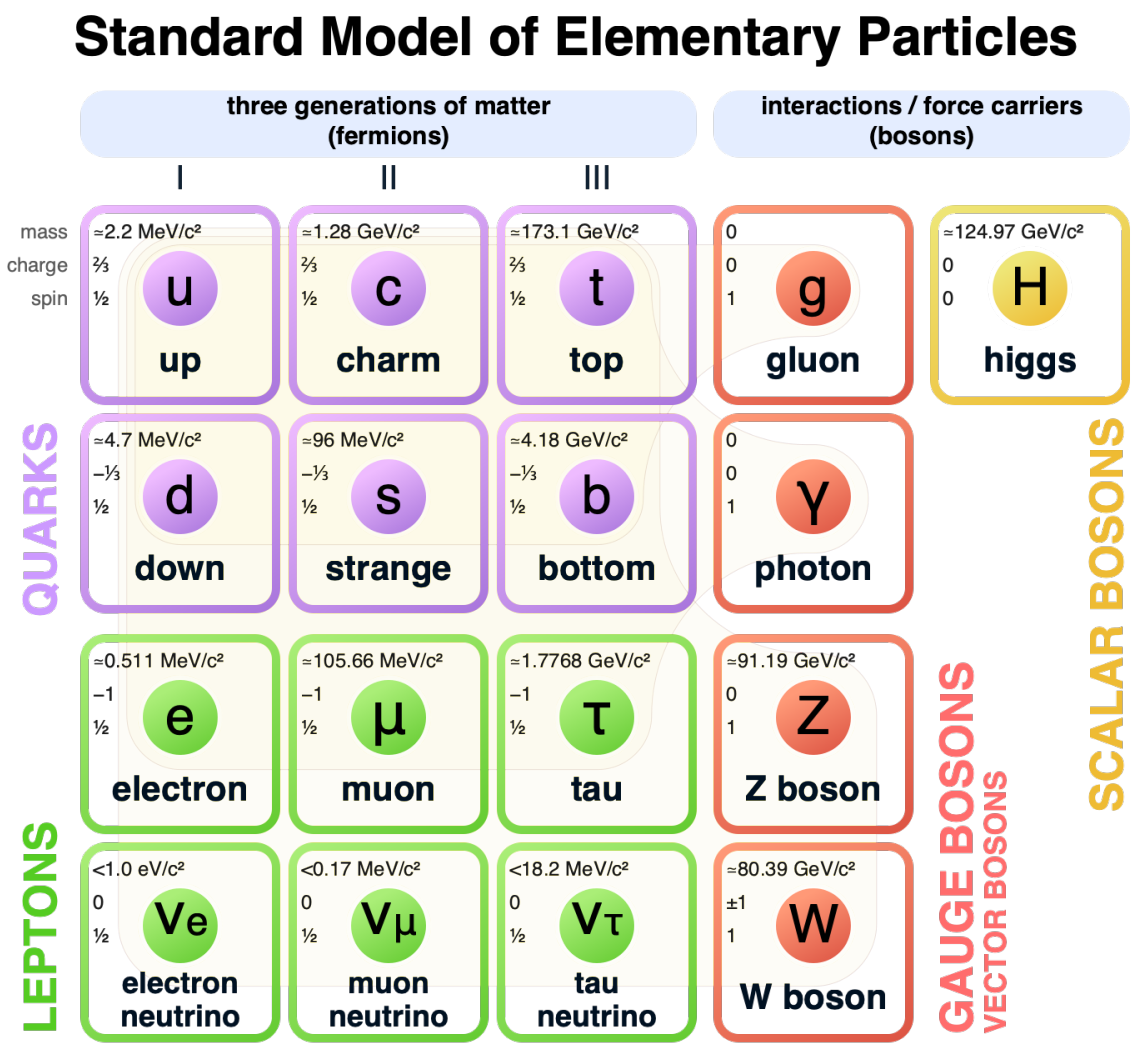


Figure 2.1: *The particles predicted by the Standard Model and observed experimentally. Taken from [7].*

electromagnetism, the $W^{\pm}$ and Z bosons for the weak force, and the gluons (g) for the strong force (shown in red in Figure 2.1). Additionally, Figure 2.1 includes the Higgs boson, associated with the Higgs field, responsible for generating the masses of particles that interact with the Higgs field.

Fermions are arranged into three generations of matter. Each generation consists of two types of quarks (with an electrical charge of 2/3 and -1/3) and two types of leptons (with an electrical charge of -1 and 0), which differ in their masses between the generations but behave similarly with respect to their interactions. Quarks are massive particles that interact through electromagnetic, weak, and strong forces and carry a colour charge. They form colourless bound states called hadrons, which can be either mesons (combinations of quark and anti-quark, where the anti-quark carries an anti-colour charge) or baryons (combinations of three quarks).

Leptons, on the other hand, do not carry a colour charge and are not affected by the strong force. Each generation of leptons includes one electrically charged lepton and one electrically neutral neutrino. The charged leptons have a mass and interact electromagnetically as well as weakly. Neutrinos are considered massless in the classical formulation of the SM and interact only through the weak interaction, having thus a low probability to interact with matter.

Fermions exist in two distinct helicity states [2]. A fermion has a right-handed helicity if the direction of its spin is the same as the direction of its motion and a left-handed helicity if the spin and motion have opposite directions. Only left-handed particles (and right-handed antiparticles) interact through weak interaction. According to the SM, the quarks and charged leptons exist in left- and right-handed states, while neutrinos appear only in left-handed state.

While being a very self-consistent theory, the SM in its current form fails to explain several phenomena. For instance, why are there strictly three generations of fundamental particles? The SM is based on the assumption of massless neutrinos, however, the neutrino oscillations shows unambiguous evidence of mass. Therefore, the theory doesn't explain how neutrinos acquire mass. Also, various astrophysical measurements show that visible matter is not enough to explain the gravitational features observed in space. These observations propose the existence of the additional dark matter that is responsible for these effects. The SM also does not address the observed asymmetry between the amount of baryons (matter) and anti-baryons (antimatter). It is not clear what is the origin of the huge gap between the electroweak unification scale (around 100 GeV) [8] and the Planck scale (around 10^{19} GeV) [8]. Even though the discovery of the Higgs particle completed the SM, without new physics the observed mass of the Higgs boson would require an extremely finetuned SM to keep its mass near the electroweak scale in the presence of other, much larger energy scales (a problem known as the "hierarchy problem") [3]. Last, but not least, the SM does not provide the unification of gravity with other fundamental forces.

2.2 The Large Hadron Collider

In the early 1980s, the discovery of the W and Z intermediate vector bosons at the CERN proton-antiproton collider (SPS) by the UA1 and UA2 experiments [9] greatly enhanced the confidence in the SM of particle physics. The SM predictive power has since been experimentally demonstrated with great accuracy in many generations of low- and high-energy experiments. However, during the 1980s, two missing elements prevented the SM from being fully established as a complete theory of particle physics: the top quark, the heaviest of the six quarks, and the Higgs boson, a scalar boson

[2] Helicity is the projection of the particle's spin onto the direction of its momentum

of unknown mass. The Higgs boson, which would confirm the proposed spontaneous electroweak symmetry breaking mechanism [8], is a manifestation of the scalar field that permeates the entire universe. This mechanism gives the W and Z bosons their heavy masses while leaving the photon massless. The scalar field's interactions with quarks and leptons gives masses to them proportionally to the strength of their couplings to the Higgs boson.

The top quark was expected to be discovered in existing or soon-to-be-operational colliders. Its mass was constrained by measurements from electron-positron colliders (LEP [10] and SLC [11]) and predicted by the electroweak theory to be approximately 172.5 GeV [8], which is now a well-established value. The top quark was eventually discovered by the CDF and D0 experiments at the Tevatron in 1995 [11]. On the other hand, in the 1980s, the scalar Higgs boson had no significant mass prediction, and its mass range was between a few GeV up to around one TeV. At such a high mass, it would be too broad to be visible as a signal peak in experiments, making it potentially beyond the reach of any existing experiment at that time. Therefore, finding the Higgs boson became a central focus in discussions about the future of particle physics, and was a primary motivation for the construction of the Large Hadron Collider (LHC) and its experiments. Additionally, the great advantage of the LHC physics programme was its "no-lose theorem", meaning that together with probing the SM it had a potential to study the theories Beyond the Standard Model (BSM) (such as supersymmetry).

The Large Hadron Collider is the world's largest and most powerful particle accelerator, located at CERN on the Franco-Swiss border. The circular collider is placed in an underground tunnel, at a depth of roughly 100 m and a circumference of 27 km, that was previously used for the Large Electron-Positron (LEP) collider. The initial LHC was designed to record proton-proton collisions (p-p) with a maximum centre of mass energy of $\sqrt{s} = 14$ TeV and lead-lead and proton-lead collisions for the quark-gluon plasma studies [2].

The collider serves four large experiments - ATLAS (A Toroidal LHC Apparatus), ALICE (A Large Ion Collider Experiment), CMS (Compact Muon Solenoid), and LHCb (a precision measurement experiment dedicated to the study of B-physics) and smaller ones - LHCf (LHC forward), TOTEM (TOTal Elastic and diffractive cross section Measurement), FASER (ForwArd Search ExpeRiment), SND@LHC (Scattering and Neutrino Detector at the LHC), and MoEDAL-MAPP (Monopole and Exotics Detector at the LHC) experiments.

The LHC operation started on the 10th of September 2008. The data-taking of LHC is divided into Runs differing in the operational modes (luminosity described in Section 2.2.3 and energy) and detectors configurations. In Run 1 (years 2009-2013) the proton-proton collisions energy reached 8 TeV, in Run 2 (years 2015-2018) the

energy was 13 TeV and in Run 3, started in 2022, is currently running with an energy of 13.6 TeV. In between the Runs, the upgrades of the LHC and detectors are ongoing.

2.2.1 CERN accelerator complex

The accelerator complex at CERN includes several machines that successively accelerate particles to higher energies before injecting them into the next machine in the sequence (see Figure 2.2). The last element of the boosting chain is LHC, where particles are accelerated up to the energy of 6.8 TeV per beam.

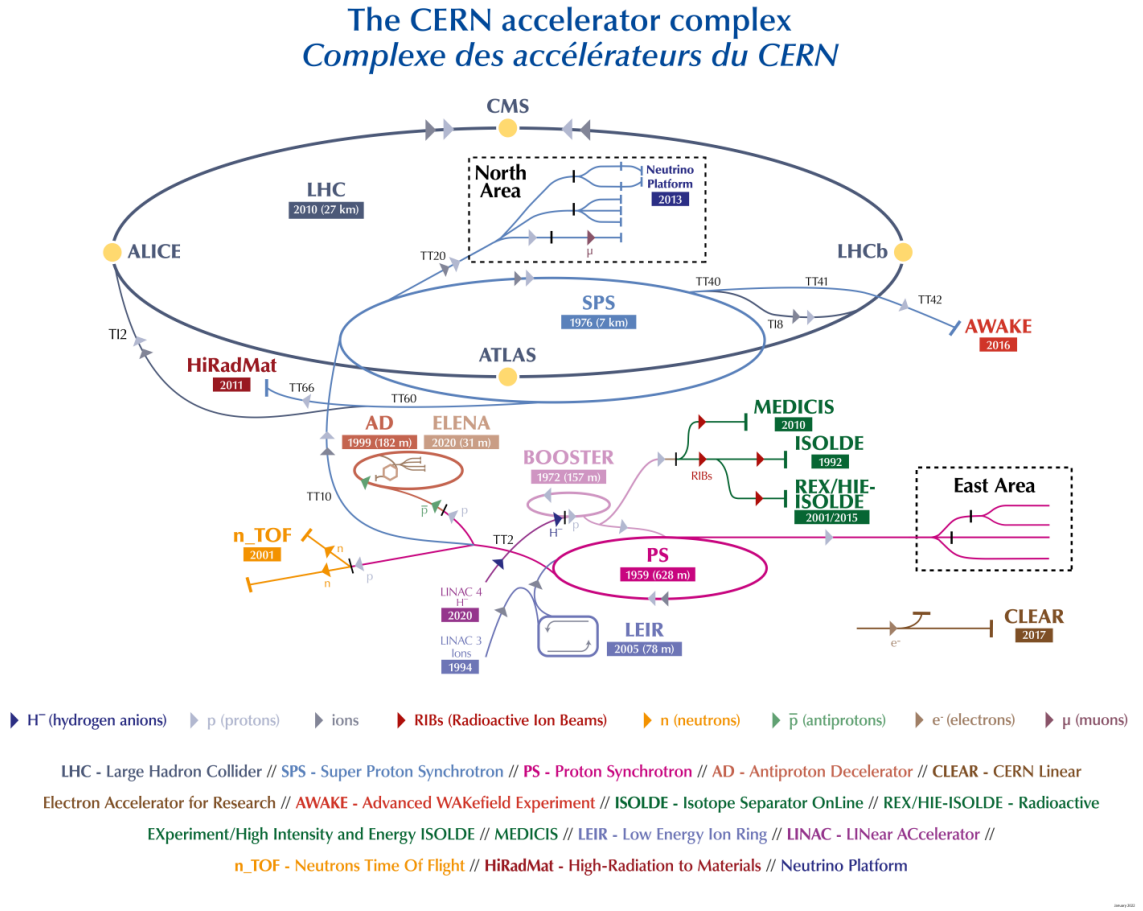


Figure 2.2: *CERN accelerator complex, taken from [2].*

Since 2020, the proton beams for the CERN accelerator chain are delivered by the Linear accelerator 4 (Linac4), which accelerates negative hydrogen ions (H-) to the energy of 160 MeV. The next acceleration step is the Proton Synchrotron Booster (PSB). During injection from Linac4 into PSB, the H- ions are deprived of their two electrons leaving only protons. These protons are then accelerated in PSB to 2 GeV and transferred to the 638 m long Proton Synchrotron (PS) that in addition serves the test beam areas used for R&D of the LHC detectors upgrades. After PS, the 26 GeV beam enters the Super Proton Synchrotron (SPS) with a 6 km circumference,

where it is accelerated further to 450 GeV. SPS also provides proton beams to the test beam areas and to the following experiments: NA61/SHINE, NA62, COMPASS and AWAKE [2].

In the last acceleration step, the protons are injected into the two LHC beam pipes. The two beams in LHC circulate in opposite directions (clockwise and anticlockwise). It takes 4 minutes and 20 seconds to fill each LHC ring and 20 minutes for the protons to reach their maximum speed (close to the speed of light) in LHC. Beams circulate for many hours inside the LHC beam pipes under normal operating conditions. After several hours of circulation in the LHC, the two beams collide inside ATLAS, CMS ALICE and LHCb detectors with a total energy of ≈14 TeV.

The lead ions are obtained from vaporised lead. For the ions, the acceleration starts in the Linear accelerator 3 (Linac3) and is followed by Low Energy Ion Ring (LEIR). From LEIR, the lead ions are injected into the PS and then follow the same trajectory as protons up to the LHC.

2.2.2 The LHC acceleration principle

Circular accelerators such as LHC use electromagnetic fields to accelerate and bend the trajectory of particles. The LHC consists of a chain of superconducting electromagnets with a number of accelerating components to steer, focus, and boost the energy of particles.

Electric fields along the accelerator switch from positive to negative at a given frequency to ensure the separation of particles in closely spaced "bunches". There are 2808 bunches per proton beam with $\approx 10^{11}$ protons per bunch [2]. The electric field is provided by 16 Radio Frequency (RF) cavities, that are designed to resonate at specific frequencies. When a beam passes through an RF cavity, energy from the electro-magnetic waves is transferred to the particles, pushing them forward [12].

The electromagnets' coils are operated in a superconducting state. They use a current of 11080 A to produce the field, allowing the high currents to flow without losing energy to electrical resistance [13]. This requires cooling of the magnets to -271.3 °C provided by liquid helium.

The LHC includes 1232 dipole magnets and 392 quadrupole magnets. The 15 m long dipole magnets are used to bend the paths of the particles. The 5–7 m long quadrupole magnets help to keep the particles in a tight beam squeezing it vertically or horizontally by four magnetic poles arranged symmetrically around the beam pipe.

In the ATLAS, ALICE, CMS, and LHCb detectors, the insertion magnets take over to squeeze the beam (from 0.2 mm down to 16 μm) to increase the collision rate.

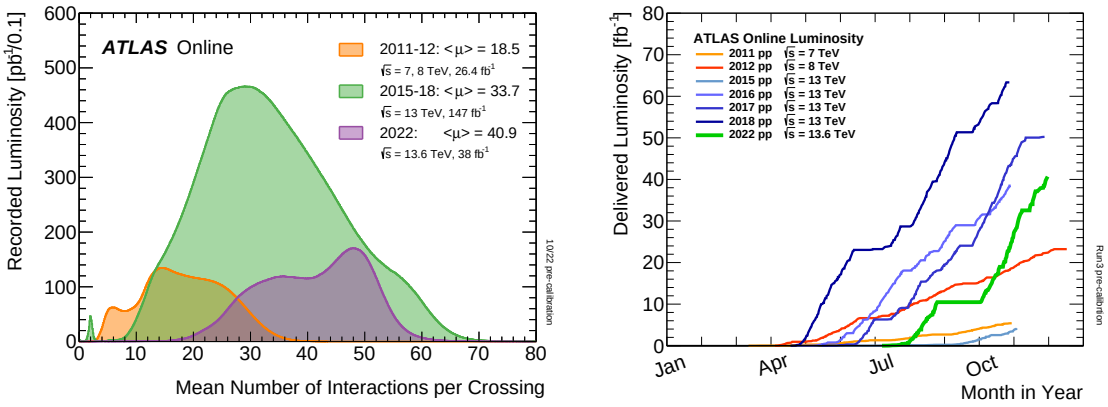
Insertion magnets also clean the beams from the stray particles to prevent them from contact with the LHC most sensitive components [13].

2.2.3 Luminosity and Pile-up

One of the most important performance characteristics of the LHC is the instantaneous luminosity $\mathcal{L}$:

$$\mathcal{L} = \frac{1}{\sigma}\frac{dN}{dt}\ [\mathrm{cm}^{-2}\mathrm{s}^{-1}], \tag{2.1}$$

where σ corresponds to the cross section, N is the number of potential collisions, and t is time. The higher the luminosity is, the more data the experiments can collect, and therefore the higher is the probability to observe a rare process [1]. The integral of luminosity over time provides a measure of the collected data size estimated in fb^{-1} which corresponds to $\approx 10^{12}$ proton-proton collisions. In Run 2 (data-taking years 2015-2018), the integrated luminosity reached almost 160 fb^{-1} (see Figure 2.3).



a) b)

Figure 2.3: *Recorded integrated luminosity by ATLAS vs mean number of interactions per batch crossing (a) and delivered integrated luminosities in the years 2011-2022 (b). Taken from [14].*

Knowledge of the integrated luminosity helps to calculate a cross section, or probability, of a specific physics process. This can be calculated by the ratio between the number of times the process was observed and the integrated luminosity. Therefore, the precision of luminosity measurement plays a big role in many analyses.

The primary luminosity measurements in ATLAS are provided by LUCID2 (Luminosity Cherenkov Integrating Detector 2) in the far forward region ($\pm$17 m from the interaction point) and BCM (Beam Conditions Monitor) located $\pm$1.84 m away from the interaction point, both arranged around the beam pipe in each arm of ATLAS [15]. The LUCID detector contains 16 photomultiplier tubes (PMTs) with thin quartz windows as Cherenkov medium. BCM consists of four 8×8 mm^2 diamond sensors and provides

beam conditions information and beam abort functionality to protect the ATLAS inner detector together with bunch-by-bunch luminosity measurements.

With the increasing luminosity, or the number of interactions per bunch crossing, the probability to record the interesting interactions increases. The downside of the high luminosity is that with the interesting high-energy (hard-scatter) collisions, also the soft, zero-bias, collisions are happening. This effect, called pile-up, pollutes the hard-scatter events, which leads to a worse reconstruction of the objects and increased experimental measurement uncertainties.

2.3 The ATLAS physics highlights

The seeds for building the ATLAS detector were planted in the late 1980s in parallel with the development of the LHC. The experiment, whose Letter of Intent was approved in 1993, was designed to investigate the existence of the Higgs boson (supposedly responsible for the mechanism of the electroweak symmetry breaking), top quark (discovered in 1995, before the start of ATLAS operation), and supersymmetry (theory meant to unify all the fundamental forces including gravity). This section provides a non-exhaustive overview of the ATLAS experiment physics program and results.

2.3.0.1 The Higgs boson discovery

The discovery of the Higgs boson was announced on 4 July 2012 at a CERN seminar by ATLAS and CMS collaborations. Many different decay channels of the Higgs boson were studied in order to cover the full predicted by the SM mass range. The analysis of three decay modes overlapping in the energy range between 120 GeV and 130 GeV led to the Higgs boson discovery: $H \to ZZ^* \to 4l$, $H \to WW^* \to l\nu l\nu$ and $H \to \gamma\gamma$.

Figure 2.4 shows the evolution of combined significance using the di-photon, four lepton and WW^* channels as a function of the Higgs boson mass. With the full 2011 data set of 5fb^{-1} integrated luminosity (see Section 2.2.3), that corresponds to approximately 5×10^{12} proton-proton collisions, the significant three standard deviations σ excess in the region of 125 GeV was present in the ATLAS experiment (see Figure 2.4 (b)). By convention, the discoveries in particle physics are claimed at a significance of 5σ. In the summer of 2012, when the integrated luminosity reached 10fb^{-1}, the significance raised to 6σ at a mass of approximately 125 GeV in the ATLAS experiment, see Figure 2.4 (c). The discovery was undoubtable: it was done by two experiments independently reaching significance of 5σ (ATLAS, CMS), the three decay channels were studied independently and the analysis of all the channels was compatible between the experiments in resolution with the expected signal. The discovery has been fully confirmed with the data taken ever since. According to Particle Data Group 2022 [16], the Higgs boson mass is measured to be m_H=125.25±0.17 GeV.

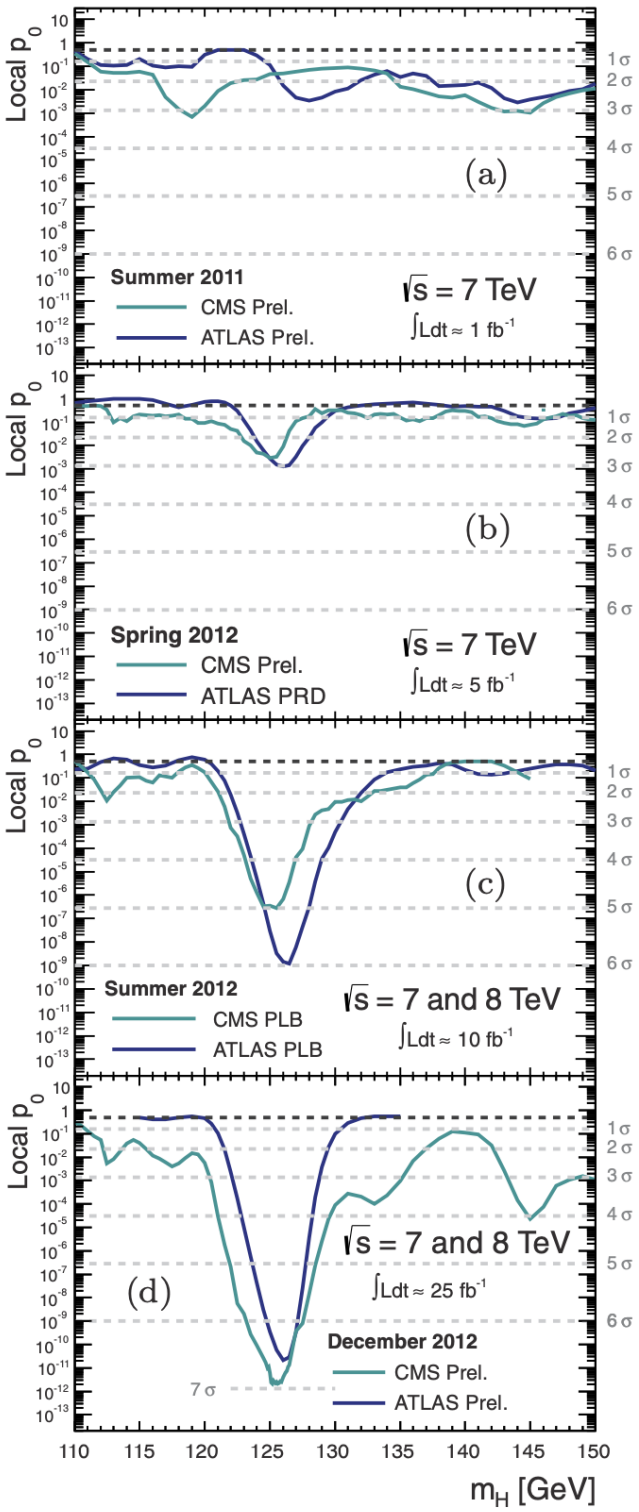


Figure 2.4: *Evolution of the combined significance of the signal from 2011 to December 2012 in ATLAS and CMS, taken from [3].*

The ATLAS Higgs program includes further probes of the Higgs couplings and different production and decay modes not only to enhance the SM precision measurements but also to search for scenarios where the Higgs acts as a mediator to new physics (for example, dark matter). For instance, the production of a pair of Higgs bosons (HH) is a rare process in the SM, while a number of Beyond the Standard Model (BSM) models predict much larger cross sections for HH production than that of the SM [17].

2.3.0.2 The SM processes measurements

Concerning the SM probes, the physics program of ATLAS covers the diboson and triboson processes (γ, W, Z) in order to test the couplings of the bosons to each other. The deviations of these couplings from the SM predictions could lead to the new physics (BSM).

In addition, LHC provides a large production cross section of the bottom quarks, allowing ATLAS to measure charge-parity violation, search for anomalous rates of rare decays of B hadrons and make the QCD tests.

The LHC is often called a top factory because of the high rate of production of the top quark. The mass of the top quark is the heaviest (direct measurements of the top quark mass result in m_t=172.69±0.30 GeV [16]) and therefore its precise measurement is important for the overall consistency of the SM. Given its high mass, it strongly interacts with the Higgs boson and is assumed to have strong interactions with hypothetical new particles. Thus, one of ATLAS priorities is to do high precision measurements of all the top quark properties, such as the spin correlations, polarisation, charge asymmetry and searches for strongly suppressed decays of the top quark due to possible flavour-changing neutral currents, which are compared with the SM predictions and the BSM theories predictions. So far, no significant deviations from the SM were found.

Figure 2.5 shows an overview of a selection of the ATLAS cross section measurements of the SM processes in Run 1 and Run 2 compared to the theoretical expectations.

2.3.0.3 Beyond the SM searches

The SM was carefully tested in various accelerators including LHC and no significant deviations were detected so far. However, as mentioned in Section 2.1, there are the strong evidences, that the SM does not provide the complete picture of nature.

The goal of the ATLAS physics program is to detect any new phenomena at the energy frontier. These "blind" searches are very challenging both technically and analytically, since new physics may appear anywhere and in any process. Several theories extending the SM are used as an experimental guide, while the analyses are designed to be as general as possible including wide range of signals.

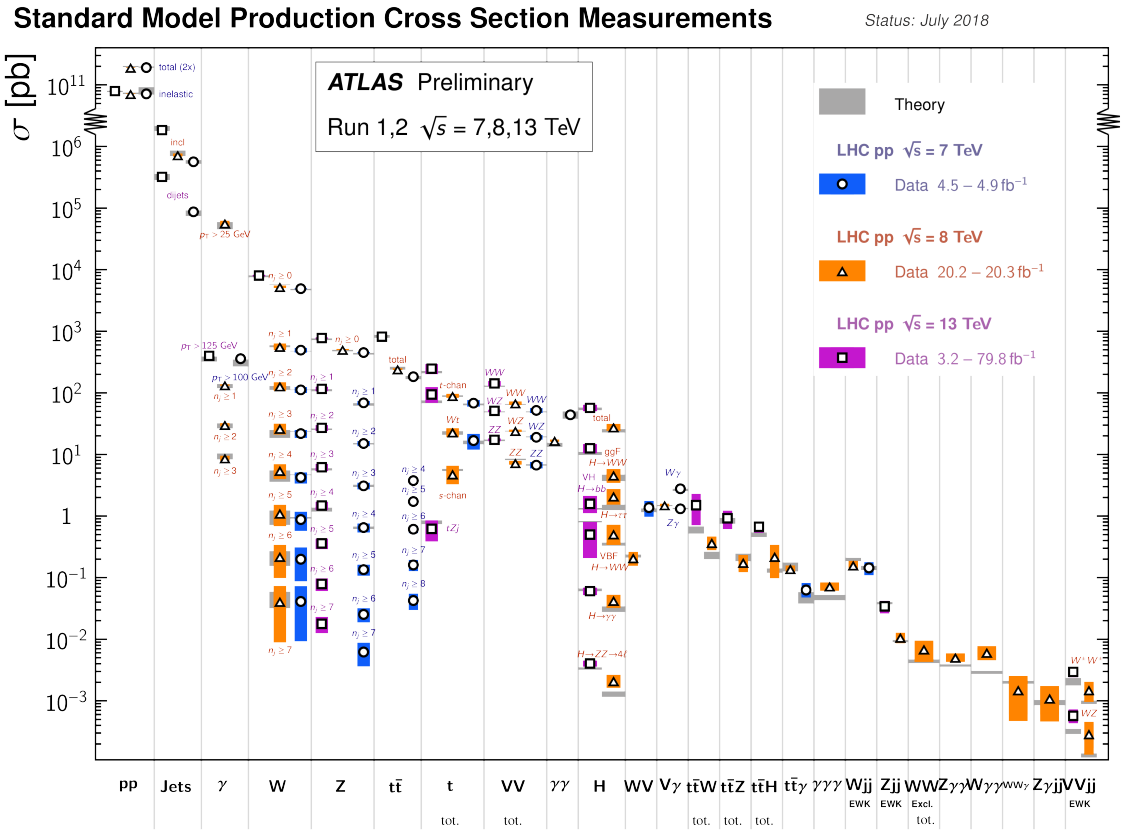


Figure 2.5: *Summary of several Standard Model total and fiducial production cross section measurements, corrected for leptonic branching fractions, compared to the corresponding theoretical expectations. The luminosity used for each measurement is indicated close to the data point. Some measurements have been extrapolated using branching ratios as predicted by the Standard Model for the Higgs boson. Uncertainties for the theoretical predictions are quoted from the original ATLAS papers. They were not always evaluated using the same prescriptions for PDFs and scales. Not all measurements are statistically significant yet. Taken from [18].*

The ATLAS collaboration is doing an intensive search for the dark matter. These searches are especially difficult, since the dark matter does not interact with the detector and its signatures are measured through the missing transverse energy, the energy not detected but expected due to the laws of conservation of energy and conservation of momentum. So far, LHC has not observed any strong indications of the dark matter.

Extensions of the SM involving Supersymmetry (SUSY) theory are also appealing from a theoretical perspective, due to their potential to address the limits of the the SM. SUSY introduces new set of particles that share with the known bosons and fermions the same mass and internal quantum numbers but have spin different by half-unit. A number of searches have been performed for both strong and electroweak SUSY in

ATLAS but, as of today, no significant excess has been observed above the expected background [17].

2.3.0.4 Heavy-Ion collisions

In addition to the proton-proton (p-p) collisions, ATLAS also studies the heavy-ion collisions. These measurements are meant to study the Quark-Gluon Plasma (QGP), a state of hot and dense hadronic matter with unbound quarks and gluons expected to have been present in the very early Universe ($10^{-10} - 10^{-6}$ s after the Big Bang). In the QGP, the products of the hard scattering evolve as parton showers that propagate through the medium and experience in-medium energy loss in a process referred to as jet quenching. The basic observable signature of jet quenching is a strong suppression of jets or charged hadrons measured in heavy ion collisions with respect to those measured in p-p collisions. The amount of suppression for a given final state (charged hadron, jet, electroweak boson, etc.) can be quantified by a nuclear modification factor R_{AA} [19]. The compilation of results for the nuclear modification factor in different channels from the Run 2 Pb+Pb and p-p data is shown in Figure 2.6. The closer the R_{AA} to one, the less the physics object is influenced by the QGP medium (such as Z and W bosons). Because of the strong interaction, all the hadronic observables in Figure 2.6 are suppressed, due to energy loss in the medium [3]. To understand the QGP medium properties, ATLAS also studies the multi-particle collective processes in the medium such as flow.

2.3.1 The physics goals of the High-Luminosity LHC

The most important LHC parameters for the ATLAS physics program are the integrated luminosity and the collision energy. Increasing either or both of these leads to the increase of the rate of rare processes, which ATLAS explores [3]. The High-Luminosity LHC (HL-LHC) described in Section 2.5 will increase the luminosity by a factor of ten comparing to the LHC's design value.

During the HL-LHC operation, ATLAS will measure the main couplings of the Higgs boson with high precision at the percent level, thanks to the large amount of data. This will be particularly useful for studying complicated final states, like those that arise from ttH production [3]. In addition, the yet unobserved Higgs decay channels, such as $H \to \mu^+\mu^-$, should be visible during HL-LHC. Invisible Higgs boson decays ($H \to Z(\nu\nu)Z(\nu\nu)$) will be searched for at HL-LHC in all production channels, with Vector Boson Fusion (VBF) being the most sensitive. The VBF production shown in Figure 2.7 is a pair of vector bosons (ZZ or W^+W^-) radiated from quarks that fuse to produce the Higgs boson. The combination of ATLAS and CMS Higgs boson coupling measurements will set an upper limit on the Higgs invisible branching ratio of 2.5%, at the 95% confidence level [21]. The HL-LHC's Higgs studies will boost the

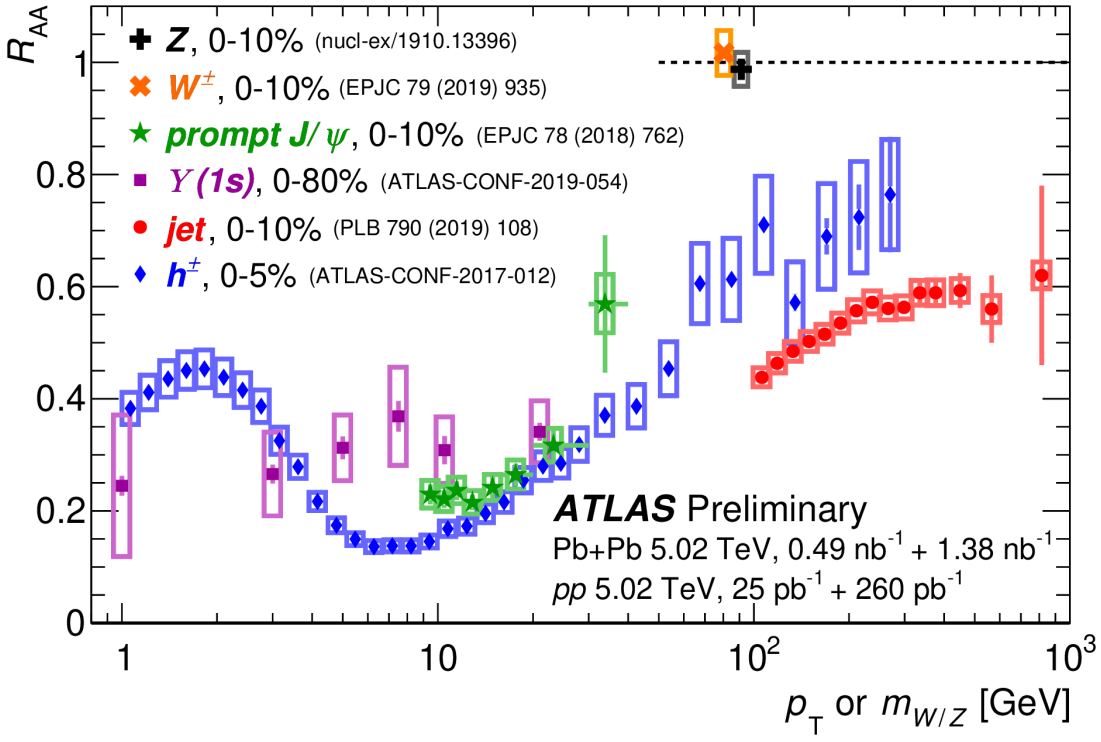


Figure 2.6: *Ratio of the measured yield in lead-lead collisions to the pp cross section in different channels. Taken from [19].*

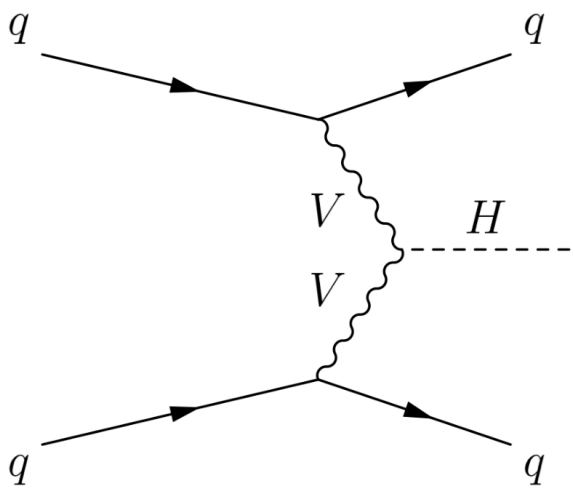


Figure 2.7: *Feynman diagram for the VBF Higgs production from the fusion of either W or Z bosons. Taken from [20].*

sensitivity to BSM physics by utilising indirect probes through precise measurements and direct search targets. These targets range from exotic decays of the 125 GeV Higgs boson, for example decays including light scalars or axion-like particles, to the

production of new Higgs bosons, both neutral and charged, at masses above or below 125 GeV [21].

Precision measurements offer a powerful tool to explore BSM physics associated with mass scales beyond the LHC's direct reach. The Effective Field Theory (EFT) framework supplements the Standard Model Lagrangian with dimension-6 operators, allowing systematically describe BSM effects and their influence on the SM processes [3].

The HL-LHC program also includes the measurement of production of pairs or triplets of Electroweak (EW) gauge boson, meant to test the mechanism of EW symmetry breaking. The observations of EW multiboson interactions have been achieved in vector boson scattering (VBS) and are expected to be more frequent due to higher statistics and larger acceptance in the forward direction [4].

Another important measurements will include the precision of the weak mixing angle $sin^2\theta_{eff}$, W boson mass and top quark mass [4].

Flavour physics has also a great potential in the HL-LHC era. This includes the CKM matrix unitarity tests, studies of top quark properties (its large mass and its large O(1) Yukawa coupling to the Higgs), etc. [3].

Other studies within the physics program of HL-LHC such as the QCD studies (PDFs improvements), searches for new physics (Supersymmetry, Dark matter, Long-lived particles, etc.) and many other topics may be found in the Report on the Physics at the HL-LHC, and Perspectives for the HE-LHC [4].

2.4 The ATLAS Detector

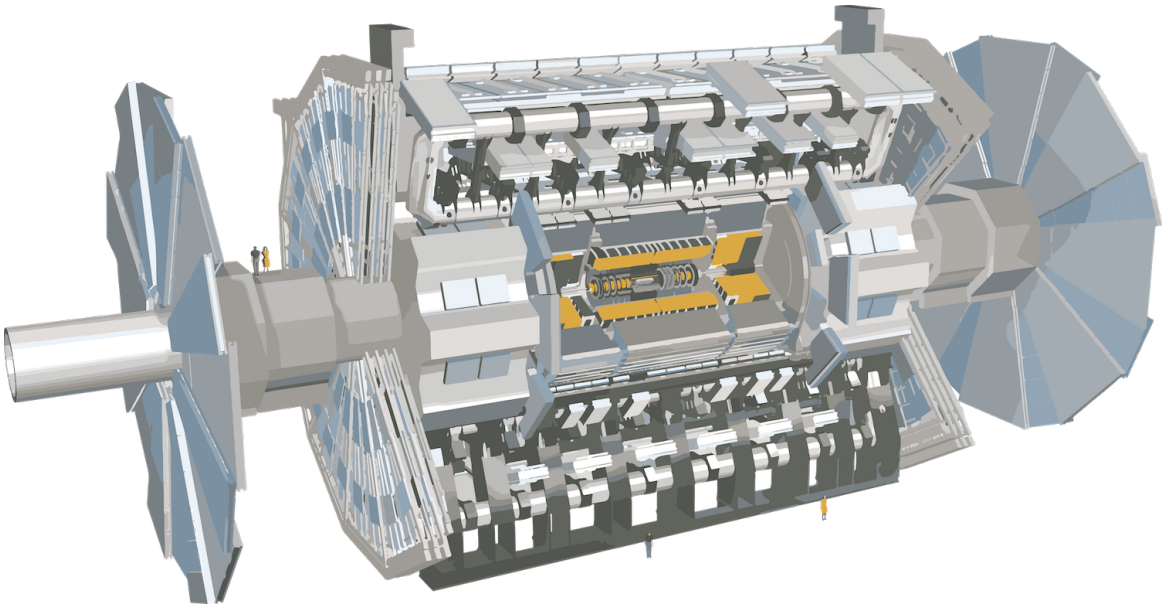


Figure 2.8: *ATLAS detector schematic view, taken from [22].*

ATLAS is a general purpose experiment located at Point 1 of the LHC, see Figures 2.8 and 2.2. The physics program of the detector includes study of the SM, measurements of the Higgs boson properties, and searches for the new physics such as supersymmetry and dark matter. It is designed to provide an accurate reconstruction of muons, photons, electrons, tau-leptons, jets, and missing transverse energy measurements under high luminosity conditions. ATLAS detector weighs 7000 tonnes, is 46 m long, has diameter of 25 m, and is situated in a cavern 100 m under the ground.

The ATLAS detector uses a right-handed coordinate system, with the origin at the Interaction Point (IP), the z-axis defined by the beam direction and the x-y plane transverse to the beam (x pointing towards the center of LHC). ATLAS detector may be sectorized in three parts: barrel (the central region) and two end-caps (A corresponds to positive z and C corresponds to negative z) in the forward regions further from the IP. The whole detector has a cylindrical shape, thus it is convinient to use the cylindrical coordinates (θ, ϕ, z) in measurements. The azimuthal angle ϕ is measured in the transverse plane around the beam axis ($-\pi, \pi$), and the polar angle θ is the angle from the beam axis. The polar angle is usually replaced with the Lorentz invariant under longitudinal boosts pseudorapidity η:

$$\eta = -\ln\tan(\frac{\theta}{2}), \tag{2.2}$$

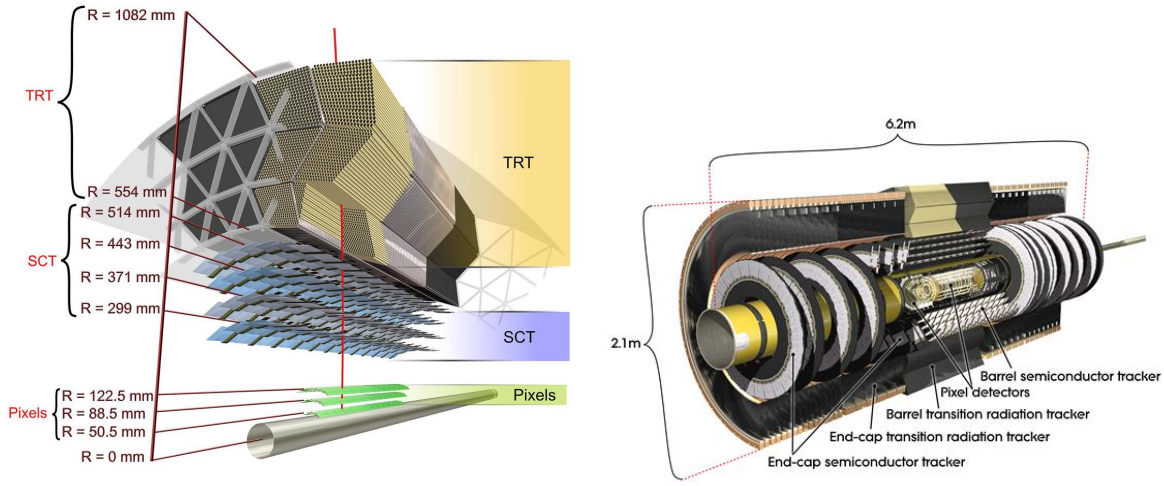
where $\eta = 0$ corresponds to the center of the detector ($\theta = 90°$) and $\eta \to \infty$ approaches the beam axis. The angular distance between two objects is defined by Lorentz invariant $\triangle R = \sqrt{\triangle\eta^2 + \triangle\phi^2}$.

The ATLAS detector consists of several sub-detectors described in the following Sections (2.4.1-2.4.5): the inner tracker responsible for reconstruction of the trajectories of charged particles, the calorimeters measuring their energy, the muon system performing precision measurements of muons, and the magnet system bending the particles tracks.

2.4.1 Inner Detector

The Inner Detector (ID) is the innermost sub-detector of ATLAS that covers a pseudorapidity range of $|\eta| \leq 2.5$ and consists of three different sub-systems shown in Figure 2.9: the Pixel Detector (Section 2.4.1.1), the Semiconductor Tracker (Section 2.4.1.2) and the Transition Radiation Detector (Section 2.4.1.3) [23], [24]. The purpose of the ID is to measure the trajectories (tracks) of the charged particles, their momentum and charge and to reconstruct the interaction vertices where the particles were produced in $p-p$ collission. The detector design is optimized to meet the requirements in terms of measurements precision and to keep the total material budget low. When a charged particle passes through the ID, it generates several hits in the detection layers allowing to reconstruct the track of the particle from these hits (the track reconstruction procedure is described in more detailes in Section 6.1.3). The

whole ID is immersed in a 2 T magnetic field parallel to the beam axis provided by a solenoid coil. This field is meant to bend particle trajectories allowing to infer the momentum from the particles' path as well as their electric charge using the formula of the Lorentz force for magnetic field.



a) b)

Figure 2.9: *Detailed overview of the ATLAS Inner Detector. (a): the central part (barrel) of the system including the dimensions and particle's track passing through it (red line). The sketch is missing the IBL barrel layer installed in 2015. (b): the full Inner detector including barrel and end-cap parts, taken from [22].*

2.4.1.1 The Pixel Detector

The pixel detector is the closest ID sub-system to the IP. Due to the high density of the $p-p$ collission products in the innermost region of the ID, the pixel detector requires a very fine granularity to separate the charged tracks and to fulfil the requirements on track position and vertex[3] resolution. The hybrid n-in-n planar silicon pixel sensors were picked as a baseline technology for this purposes [25].

The pixel detector consists of three parts: the cylindrical barrel layers covering $|\eta| < 1.5$ and the end-caps disc layers covering $1.5 \leq |\eta| \leq 2.5$. Initially, the detector was built with three barrel concentric cylindrical layers around the beam pipe and three rings perpendicular to the beam axis in each end-cap deploying the 250 μm thick sensors with the pixel size of $50 \times 400\ \mu\text{m}^2$. The three barrel layers have a radius of 50.5 mm, 88.8 mm, and 122.5 mm and a length of 80 cm.

In 2015, an additional Insertable B-Layer (IBL) of 33 mm radius was installed for the LHC Run 2. For the IBL, the sensors with a smaller pixel size of $50 \times 250\ \mu\text{m}^2$ were used.

[3] the point at which a proton-proton interaction occurred

Due to the high granularity, the pixel detector has a resolution of 12 μm in R and 50 μm in z. An overlap between the modules provides hermetic detection coverage and an average of four measurements per track. Each module has the dimensions of 19 mm $\times$ 63 mm and contains a sensors with 47232 pixels and 16 readout chips (FE-I3 or FE-I4 for IBL). In total the pixel detector has 2024 sensor modules with over 92 million readout channels.

2.4.1.2 The Semiconductor Tracker

The Semiconductor Tracker (SCT) is the tracking system surrounding the Pixel Detector. The detector is divided into a barrel and two end-cap parts, with the barrel having four concentric layers with radii of 299 mm, 371 mm, 443 mm, and 514 mm. The end-cap has radii from 275 mm to 560 mm. The end-caps are made up of nine disks, providing coverage up to $|\eta| < 2.5$. The SCT uses 285 μm thick p-in-n micro-strip sensors, which are mounted parallel to the solenoid field and beam axis in the barrel region and perpendicularly on the SCT disks. It comprises 4088 double-sided modules and over 6 million readout strips. Two sensors on each side of the module are wire-bonded together to give 768 strips of $\approx$12 cm in length, providing an intrinsic resolution of 17 μm perpendicular to and 580 μm parallel to the strips. To achieve better z resolution, strips are mounted on both sides of a module at a small stereo angle of 40 mrad. The barrel sensors have a pitch of 80 μm, whereas the end-cap sensors have a pitch in the range from 50.9 μm to 90.4 μm.

2.4.1.3 The Transition Radiation Tracker

The Transition Radiation Tracker (TRT) is the outermost component of the Inner Detector (ID). It is located over the Pixel Detector and SCT volumes and provides coverage up to $|\eta| = 2$. The TRT consists of 4 mm diameter straw tubes that are filled with a mixture of Xenon (70%), CO_2 (27%), and O_2 (3%), with a 31 μm diameter gold-plated Tungsten anode wire in the centre. Particles passing through the straw ionize the gas and create the free electrons. The potential difference of 1500 V between the edge of the tube and the wire triggers the ionization electrons drift towards the anode where they are collected.

The TRT is composed of three parts: one barrel and two end-caps. The barrel section contains 52544 straws that are 144 cm in length, and each end-cap contains 122880 straws that are 37 cm in length. The straw tubes offer a high degree of modularity and can easily be integrated into a medium that produces transition radiation without compromising the continuous tracking concept. The TRT extends the tracks that are seeded and built in the pixel detector and SCT by providing the additional measurements (average of 36 measurements per track). The TRT can also be used to discriminate between electron and pion tracks by measuring the transition radiation

photons emitted when particles enter the gas inside the drift tube. The gaps between the straws are filled with transition radiator (polypropylene film or polypropylene fibres). Different particles deposit different transition radiation energy, for example, photons typically deposit the energy between 8-10 keV, while pions deposit about 2 keV. The spatial resolution of TRT is the worst among all the ID detectors and reaches 130 μm in $R-\phi$, however it is essential for enhancing the intrinsic spatial resolution and momentum resolution of tracks.

2.4.2 Calorimeters

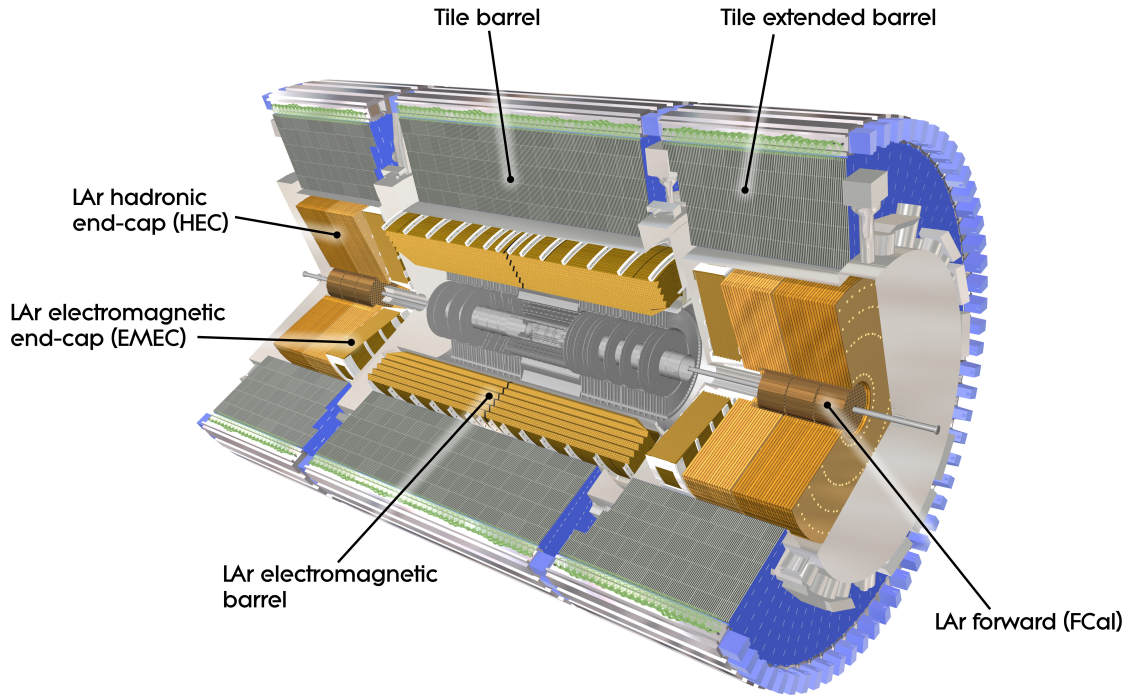


Figure 2.10: *Cutaway view of ATLAS calorimeters, taken from [26].*

Calorimeters are detectors used to measure the energy of particles by forcing them to deposit all of their energy and stop within the calorimeter volume. The absorbing high-density material of calorimeter stops incoming particles, while the active medium measures the particles energy. When particles enter calorimeter and interact with absorber medium, they initiate a shower of daughter particles, which is measured in the active material. The energy of the primary particle can be inferred from the charge deposited by the shower products.

The calorimeters can be homogeneous or sampling, with the former made entirely of sensitive material while the latter consists of alternating layers of sensitive and absorber material. Calorimeters stop most known particles, except muons and neutrinos. Two types of calorimeters exist: electromagnetic and hadronic calorimeters. Electromagnetic

calorimeters measure the energy of electrons and photons as they interact with matter through the electromagnetic interaction. Hadronic calorimeters are used to measure the energy of hadrons as they interact with atomic nuclei through the electromagnetic or strong interaction.

The ATLAS calorimeter system has three sub-detectors (see Figure 2.10): the Electromagnetic calorimeter (Section 2.4.2.1), the Hadronic Calorimeter (Section 2.4.2.2) and the Forward Calorimeter (Section 2.4.2.3). The system is designed to be deep enough to contain the entire particle shower and has a coverage of up to $|\eta| = 4.9$ to ensure that all the event's energy can be measured. The calorimeter system also has excellent directional measurement as well as good particle identification capabilities.

2.4.2.1 The Electromagnetic Calorimeter

The ATLAS Electromagnetic Calorimeter (ECAL) surrounds the ID and measures the energy of photons, electrons and hadrons. The primary energy loss mechanisms for photons and electrons are bremsstrahlung, pair-production, and ionisation, which result in a cascade of particles with progressively lower energies known as an electromagnetic shower. The radiation length X_0 is a characteristic of a material, that describes the energy loss of high energy particles electromagnetically interacting with it. As the X_0 depends on the atomic number (Z) of the material penetrated by particle, high-Z materials are used to stop particles. The ECAL is made of lead absorbers and active medium filled with liquid Argon (LAr), and is composed of a barrel (EMB) and two end-cap (EMEC) parts. The particles showers initiated in absorbers ionise the active medium and deposit the charge, from which the energy of the primary particle is deduced. The EMB covers pseudorapidity range $|\eta| < 1.475$ and has a length of 6.4 m, an inner radius of 1.4 m and an outer radius of 2 m. Each EMEC consists of two 63 cm thick co-axial wheels covering $1.375 < |\eta| < 3.2$ having an inner radius of 33 cm and an outer radius of 210 cm.

The accordion-shaped geometry of the absorbers and electrodes (see Figure 2.11) provides full ϕ coverage of the detector without any gaps. The ECAL operates in an energy range from several GeV to the TeV scale and is kept at -184 °C. The half-barrel is made of 1024 accordion-shaped absorbers interleaved with readout electrodes and is mechanically divided into 16 modules. The thickness of the modules (22-33 X_0 depending on $|\eta|$) ensures full confinement of the electromagnetic showers in the detector.

The barrel of the ECAL is separated into three sampling layers with different granularity, with the more spreading shower the granularity decreases. The first sampling layer has the highest granularity allowing to reconstruct the direction of detected photon candidates as well as particle identification. The energy resolution of the ECAL

depends on the particle energy and can be described by a quadratic sum

$$\frac{\sigma_E}{E} = \frac{a}{\sqrt{E}} \oplus \frac{b}{E} \oplus c, \tag{2.3}$$

where the first term on the right-hand side is the stochastic term that comprises the fluctuations in the amount of secondary particle signals from showers, the second term is the noise term which is caused by electronic noise in the readout and the third term is the constant that stands for non-uniformities or imperfections in the detector system [27]. The coefficients a, b, c vary depending on the region of the detector.

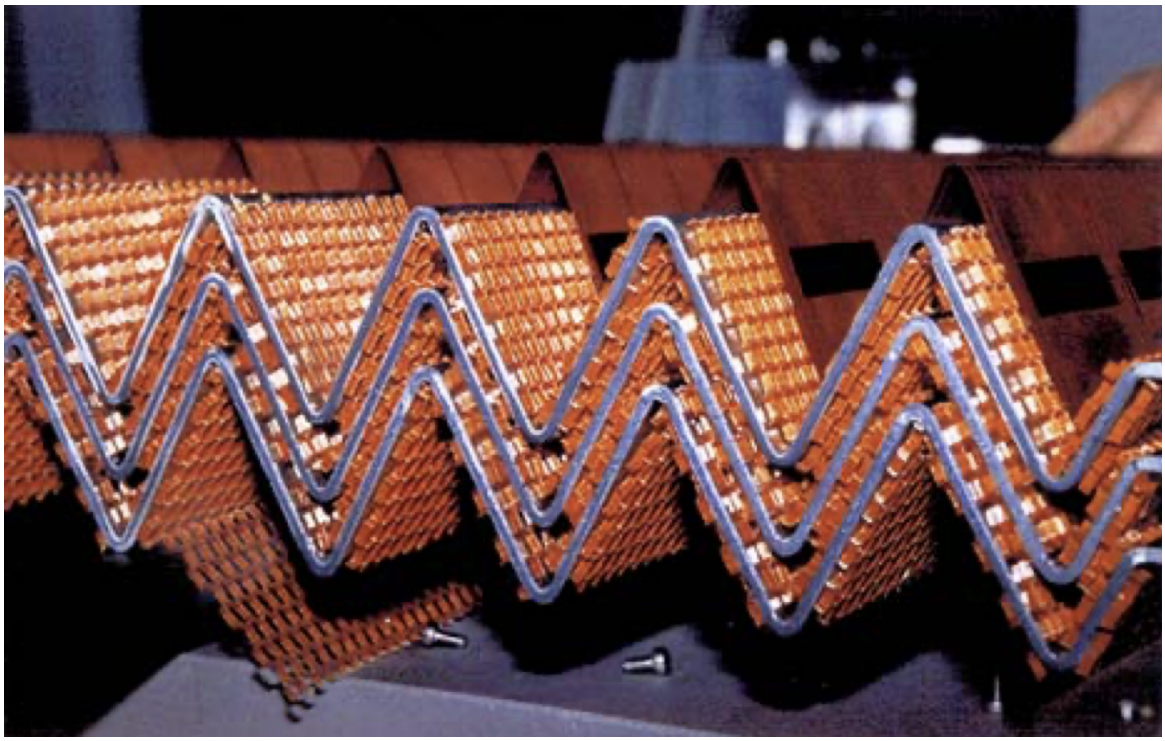


Figure 2.11: *The accordion structure of ECAL including the honeycomb spacers, electrodes and lead absorber plates, taken from [28].*

2.4.2.2 The Hadronic Calorimeter

The hadronic calorimeter (HCAL) system is placed around the ECAL and is designed to evaluate the energy of hadrons, which, unlike electrons and photons, are not completely stopped in the ECAL. Addiationally to the electromagnetic interaction, hadrons undergo strong interactions with matter, resulting in hadronic showers. These interactions are parametrized by the interaction length λ, the hadronic analogy to the electromagnetic X_0. The interaction length is usually significantly larger than the radiation length, therefore hadronic calorimeters require more material. The HCAL, having the overall coverage of $|\eta| < 3.2$ and a thickness of 7.4 λ is able to stop all the known particles (except for muons and neutrinos). The detector consists of three parts:

barrel (Tile Calorimeter) with pseudorapidity $|\eta| < 1.7$ and two hadronic end-cap calorimeters (HEC) placed in $1.5 < |\eta| < 3.2$.

The Tile Calorimeter is a sampling hadronic calorimeter with steel absorbers and plastic scintillator tiles as active media, segmented into three layers of different λ (1.5, 4.1 and 1.8) with overall radius ranging from 2.28 m to 4.25 m. Charged particles traversing the active media produce ultraviolet light, which is converted to visible light by a wavelength-shifting optical fiber connected to theoretical photomultiplier tubes where the signal is measured. The Tile calorimeter is the heaviest part of the hadronic calorimeter system and is composed of approximately 420000 plastic scintillator tiles and 9,500 photomultiplier tubes.

Each hadronic end-cap calorimeter (HEC) is composed of two wheels and shares the same cryostat as EMECs. They are the sampling calorimeters exploiting the same technology as LAr, but using copper absorber instead of lead and the flat-shaped layers instead of accordion.

Overall, the hadronic calorimeter system is crucial for identifcation, energy and direction measurements of jets and the missing transverse energy reconstruction. The energy resolution of the hadronic calorimeter can be calculated from Equation 2.3.

2.4.2.3 The Forward Calorimeter

The Forward Calorimeter (FCal) consists of an electromagnetic calorimeter and two hadronic ones placed in the forward region ($3.1 < |\eta| < 4.9$) in both end-caps. The FCal is segmented into three disc layers, which use liquid argon as active medium: the first disc designed to detect forward EM particles uses copper absorbers, the other two use tungsten absorbers. The detector allows for the reconstruction of the particles jet at small angles and contributes to the overall event energy calculation.

2.4.3 Muon Spectrometer

The Muon Spectrometer (MS) is the outermost subdetector of ATLAS detector and is used to measure muons which usually pass through the ID and Calorimeter undetected. The MS has its own magnetic, tracking and trigger systems (see Figure 2.12), consisting of four different types of detectors with different purposes:

- Monitored Drift Tubes (MDTs) provides precise measurements of muons tracks in pseudorapidity $|\eta| < 2$. The MDT chamber is based on three to eight layers of straw tubes filled with a gas mixture with an average resolution of 80 μm per tube (35 μm per chamber). An incident muon ionizes the gas producing the electrons, that are then collected by a wire in the center of the tube;

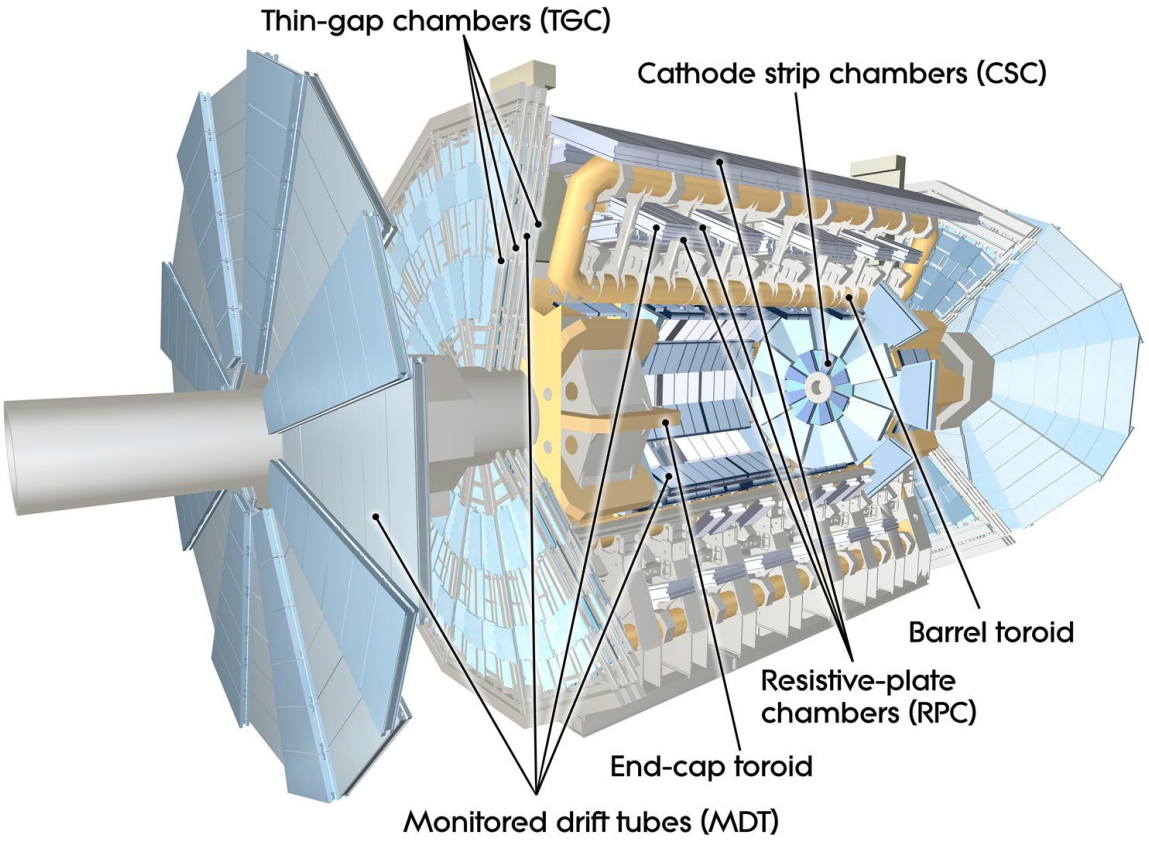


Figure 2.12: *Schematic view of the ATLAS Muon Spectrometer system, taken from [29].*

- Cathode Strip Chambers (CSCs) are the multiwire proportional chambers used to improve the reconstruction of muons in the region of $2 < |\eta| < 2.7$, where the event rate is too high for the single wire MDTs. CSCs provide a resolution of 40 μm per chamber;
- Resistive Plate Chambers (RPCs) used in the trigger system in the barrel ($|\eta| < 1.05$) as well as for the complementary position measurement;
- Thin Gap Chambers (TGCs) provides fast signals usable in the trigger and tracking in the end-caps ($1.05 < |\eta| < 2.4$).

The full system is arranged in a way that a single muon crosses three muon stations. The three toroidal magnets (one in the barrel and one per end-cap) provide the track bending used to precisely measure the momenta of muons.

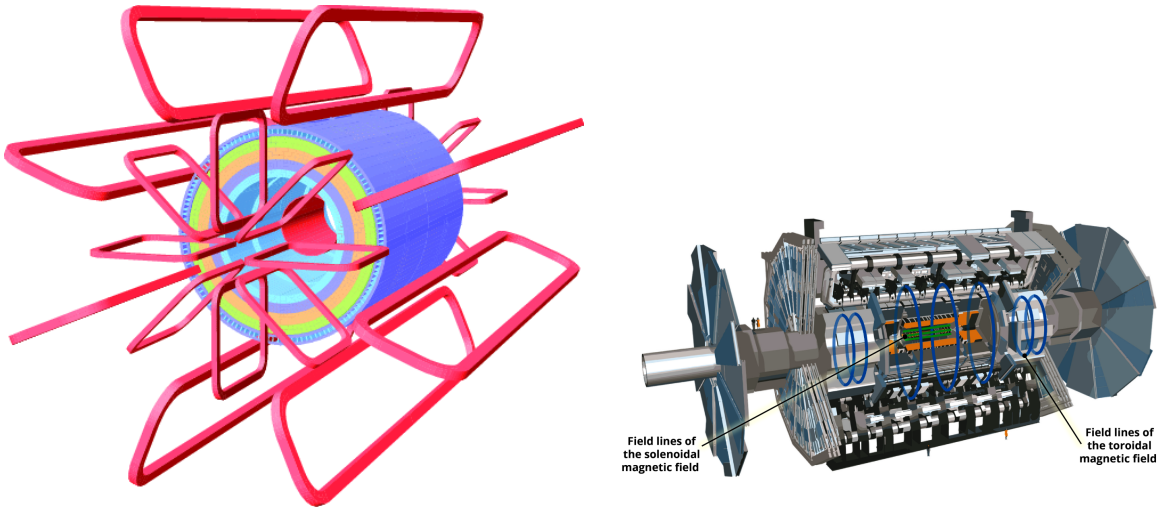
2.4.4 Magnets

The ATLAS detector is equipped with a complex magnet system that enables the determination of momentum and charge of charged particles. The system consists of four magnets: Central Solenoid Magnet and three toroid magnets (one barrel, two

end-caps) that provide magnetic fields to the inner detector and muon detector system, respectively, see Figure 2.13 [30].

The solenoid magnet coils are made of superconducting NbTi, delivering a high axial magnetic field of 2 T while keeping the material budget as low as possible. The 5.6 m long solenoid surrounds the inner detector and has a diameter of 2.5 m.

The barrel and end-cap toroids provide the bending power required for the muon system and make use of Al/NbTi/Cu conductor. The barrel toroid consists of eight coils surrounding the calorimeter volume and generating a maximum magnetic field of 4 T. The end-cap toroids are composed of eight flat coil elements on each side and generate a magnetic field up to 4 T. The barrel toroid magnet has a length of 25.3 m and a diameter of 20.1 m, while the end-cap system is 5 m long and has a diameter of 10.7 m.



a) b)

Figure 2.13: *(a): The layout of the magnet system in ATLAS shown in red, taken from [31]. (b): Field lines of the solenoid magnetic field (green) and the toroidal magnetic field in the barrel and end-caps (blue), taken from [30].*

2.4.5 Trigger System

The collision rate at ATLAS is extremely high (40 MHz) being much larger than the event recording frequency of the ATLAS detector (1 kHz under normal conditions). To filter out uninteresting events (pile-up) and ensure that the most useful ones for physics analysis are recorded, a trigger system is used. This system consists of two levels: the Level 1 trigger (L1) and the High Level Trigger (HLT) [32].

The L1 trigger is implemented in custom hardware and reduces the rate of accepted events from an input rate of up to 40 MHz to a maximum of 100 kHz. The L1 trigger consists of the L1Calo and L1Muon subsystems, which process inputs from the

calorimeter and muon detectors, respectively. The L1 identifies event features such as missing transverse energy, candidate electrons, muons, photons and jets. Additionally, the L1Topo trigger performs topology-based selections such as cuts on the angular distance or on the invariant mass of pairs of particle candidates. The L1 decision is taken within only 2.5 μs.

After the L1 decision, the full detector data are readout and temporarily buffered, and HLT decides whether the event should be saved to tape. HLT is a software-based trigger that reduces the rate of recorded events to an average of 1 kHz. The trigger algorithms are executed within the multi-threaded software framework AthenaMT [33]. The HLT selection is done within 200 ms.

2.4.6 Computing

Computing plays a crucial role in the ATLAS experiment, as it is utilized for various purposes such as operation and monitoring of the ATLAS detector, selection of the events of interest, and storing the collected data. Moreover, it is responsible for the reconstruction of physical quantities, calibration, and analysis. The ATLAS computing is divided into two domains: online and offline.

Processes that take place during the detector's operation are referred to as online computing. In order to collect data with the detector, numerous hardware systems connected to sensitive elements and auxiliary components must be controlled. Proper configuration and monitoring of all these systems are crucial for ensuring the optimal performance of the detector. Online computing is also involved in the HLT software, that determines the events of interest for the physics analysis, and data quality monitoring during data-taking.

Computing that is not directly related to the detector's operation is refered to as offline computing. The physics analysis, detector simulation, and the events reconstruction are done with the ATLAS offline software framework, Athena [34]. Athena is based on the Gaudi [35] event processing framework, which runs various algorithm components for each event (either real data or simulation).

Algorithms can share and exchange information by writing to and reading from a common whiteboard (a design pattern [36]). Additionally, they may utilize various tools that offer specialized functionalities which can be reused across algorithms. The execution of the event processing sequence is currently being migrated to a concurrent paradigm.

Since the experiment deals with a very large amount of data, the local batch resources are insufficient. Therefore, the LHC experiments including ATLAS implemented the Worldwide LHC Computing Grid (WLCG), a system of computing centers, that share

data processing loads and storage resources. WLCG does not only store the data, but also runs the computational processes such as the simulation and reconstruction.

Data processing and reconstruction involves several formats [37] depending on the purpose. The RAW record has digitized and preprocessed signals from the detector, with a size of roughly 1 MB per event, and is permanently stored. The reconstruction is executed on the RAW files, and the results are saved in the 500 kB/event ESD (Event Summary Data) record, which includes detailed reconstruction information useful for calibration parameters calculation. Lastly, (x)AOD (Analysis Object Data) contains only the reconstruction information required for analysis and weights about 100 kB/event. The xAOD are further shrinked to the DAOD (Derived AOD), the analysis specific file. Even though the DAODs are smaller in size than xAODs, their large number contributes significantly to the ATLAS storage consumption. The derivation approach and the analysis model is revised for future Runs.

The ATLAS experiment utilizes a very detailed simulation of its detector system to study its response and evaluate the performance of its reconstruction algorithms [38]. This simulation is integrated into the ATLAS analysis Athena software, and uses the Geant4 simulation toolkit [39] for the detailed detector description. It is divided into three steps: event generation, detector simulation, and digitisation. The data flow of the ATLAS simulation software can be seen in Figure 2.14. The ATLAS detector geometry is built based on the real physical construction and conditions during the data taking.

The event generation step defines the stable particles after the decays of promptly produced particles, e.g. Z or W bosons, originated from the p-p interaction. The stable particles are then propagated through the detector geometry (built by Geant4) during the simulation step. The particles passing the active sensor materials are stored as hits and contain the information on the total energy deposition, position, and time. Additionally, in both event generation and detector simulation, the "truth" information is saved for each event. The truth records include the origin and interactions (or decays) of the particle from the generation step. This information is crucial for reconstruction performance validation, as it allows to test if measurements done by the reconstruction are in agreement with the true particle evolution and behaviour. The last step in the simulation chain is digitisation of the energy deposited in the detector by particles into the detector electronics response (voltages and currents) including noise. The digitisation also performs an addition, called overlay, of pile-up to the events of interest (hard-scatter events). After digitization, the simulation data has a format equivalent to the ATLAS detector output and can be passed to the same reconstruction software to build the final objects used as inputs for physics analyses.

The High-Luminosity LHC (see Section 2.5) puts the new challenges on the computing. The events (both real and simulated) will be more complex than in the LHC era, there

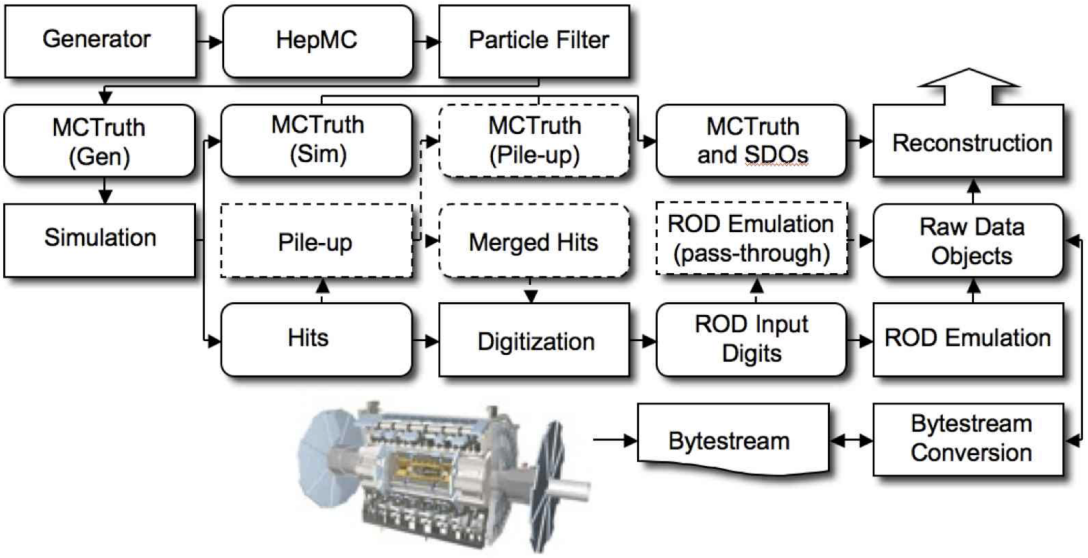


Figure 2.14: *Overview of the ATLAS simulation data flow, taken from [38]. Square-cornered boxes represent the algorithms and applications, the round-cornered boxes represent the data objects. Generators are used to generate data in HepMC format (events). Monte Carlo truth information and energy depositions in the detector are saved in Hits. During the digitization stage, the truth is merged into Simulated Data Objects (SDOs) and the Read Out Driver (ROD) electronics is simulated.*

will be an order of magnitude more of them, and the simulated data must be produced with higher physics fidelity than previously. Moreover, a straightforward and efficient data access for individual physicists must also be addressed.

The HEP computing environment is changing rapidly. Despite the fact that tape storage is significantly cheaper, the cost of disk storage has not decreased in recent years due to limited competition among vendors. Additionally, solid-state technology is still too costly to be utilized for bulk data storage, and this is expected to continue into the HL-LHC era. As a result, it is probable that the experiments will need to find ways to optimize the disk resources primarily for active tasks, while relying more on tape for long-term storage. This will require physicists to use more compact data formats.

Although the number of transistors in a typical processor keeps doubling every two years (Moore's Law) [33], the performance of a single core no longer shows the same trend in terms of computation. This is mainly because of thermal limitations in the hardware. The recent increases in speed have been achieved by adding multiple processing cores instead of increasing the speed of individual cores. Taking into account the fact that the CPU resources needed for event reconstruction are expected to exceed the available computing budget by at least a factor of two, it has become crucial to leverage concurrency in event processing [33].

Multi-processing (AthenaMP) implemented at the start of Run 2 became the first step towards processing parallelization. AthenaMP is designed to perform concurrent execution on multiple CPU cores through its division into multiple processes. These processes are generated from an initial process via forking, with the already allocated memory of the original process being available to all newly generated processes. This allows the sharing of the memory pages allocated for large static structures, such as detector geometry and magnetic field, between processes, taking advantage of the Linux kernel's copy on write feature [40]. Athena employs some strategies to maximize the amount of shared read-only memory usable in this way [41]. Unfortunately, there are limitations to how much memory can be saved with multi-processing. The change of a single bit would result in an entire memory page being copied, and C++ memory model does not allow for fine control over which data objects are assigned to which physical pages.

In order to overcome these limits of memory sharing, it is possible to execute multiple threads within a single process. These threads can share the entire memory of the process, permitting both reading and writing. Although this approach enhances the potential for more efficient memory usage, it's crucial to take sufficient precautions to prevent any memory corruption caused by simultaneous read and write operations to the same memory locations.

For the Run 3 and further, ATLAS has deployed a multithreaded framework AthenaMT [33] making use of multi-threading. In AthenaMT, a scheduler is used to execute most of the components in the event processing chain in a data driven way, distributing the work among multiple threads (potentially out of order). By declaring data-flows explicitly, the scheduler can ensure that components that rely on the output of other components are executed in the appropriate order. Figure 2.15 depicts this execution strategy, where four threads (each row) execute algorithms (shapes) on five events (colours). The scheduler uses available resources to run algorithms as their inputs become available. It's essential for individual components to be either designed or migrated to be thread-safe so that they can be safely executed in this manner. In this execution environment, components can make use of in-process shared memory.

2.5 The High-Luminosity Large Hadron Collider

The High-Luminosity Large Hadron Collider (HL-LHC) project aims to increase the integrated luminosity by a factor of 10 beyond the LHC's design value (300 fb^{-1}). The significantly increased collision rate of protons in the LHC, will help to collect more data and perform more precise measurements of fundamental particles and their interactions. This increased collision rate will provide access to rare and hard-

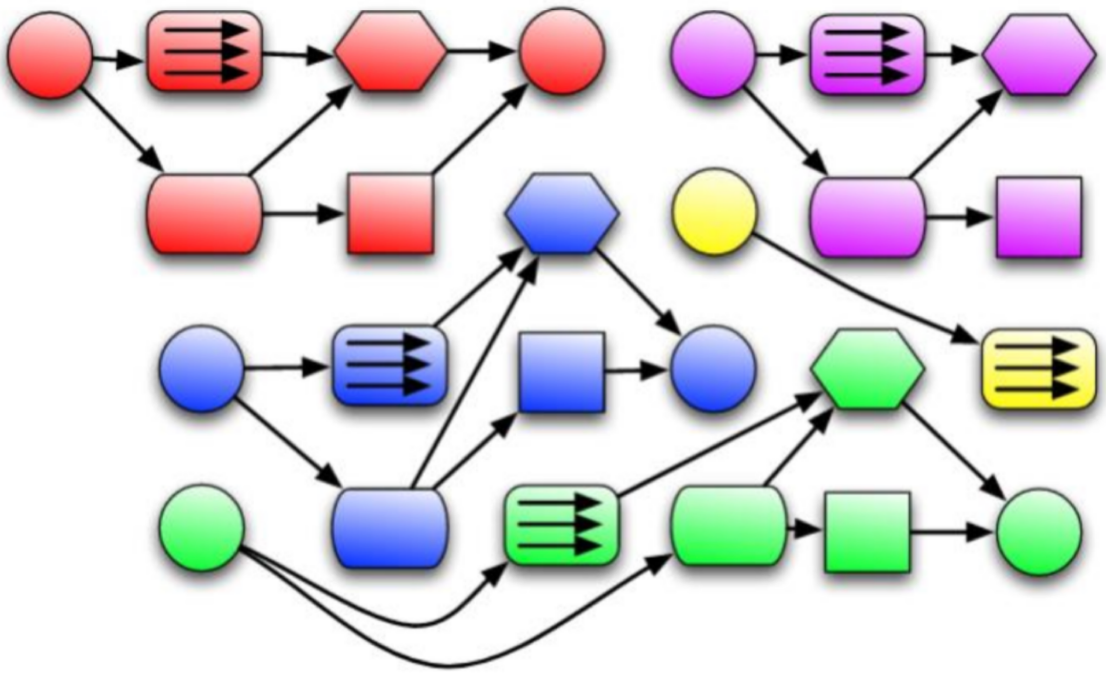


Figure 2.15: *Example of multithreaded execution in AthenaMT. Four threads are shown, each corresponding to one row. Different events are shown with different colours, and different algorithms are shown with different shapes. The algorithms are executed as soon as their input data are available and a thread is free. Taken from [42].*

to-observe physics phenomena, potentially leading to new discoveries and a deeper understanding of the universe.

In Run 1, the LHC operated with 50 ns bunch spacing and integrated luminosity reached up to 30 fb^{-1}, whereas in Run 2, the bunch spacing was reduced to 25 ns, and the luminosity was increased to attain the nominal design luminosity of $1 \times 10^{34}\text{cm}^{-2}\text{s}^{-1}$. A peak luminosity of $2 \times 10^{34}\text{cm}^{-2}\text{s}^{-1}$ was achieved in 2018 and is limited for the further improvement by the heat deposition from luminosity debris and the insufficient cooling of the inner triplet magnets. In Run 3, the goal is to further increase the integrated luminosity to 350 fb^{-1} by the end of the run period (2022-2024).

The high-luminosity LHC (HL-LHC) project was established to increase the LHC's peak luminosity to $5 - 7.5 \times 10^{34}\text{cm}^{-2}\text{s}^{-1}$ and achieve an integrated luminosity of 250 fb^{-1} per year or over 3000 fb^{-1} in Phase-II period. The HL-LHC should be operational from 2029 and run at least until 2040, with a goal of increasing the integrated luminosity by a factor of ten beyond the LHC's design value.

The main equipment upgrades for HL-LHC will be carried out in the insertion regions of LHC: Point 1 (ATLAS) and LHC Point 5 (CMS). Additionally, more than 1.2 km of LHC will be modified and 1 km of technical services and equipment required by the new components will be added. The LHC operation timeline is shown in Figure 2.16.

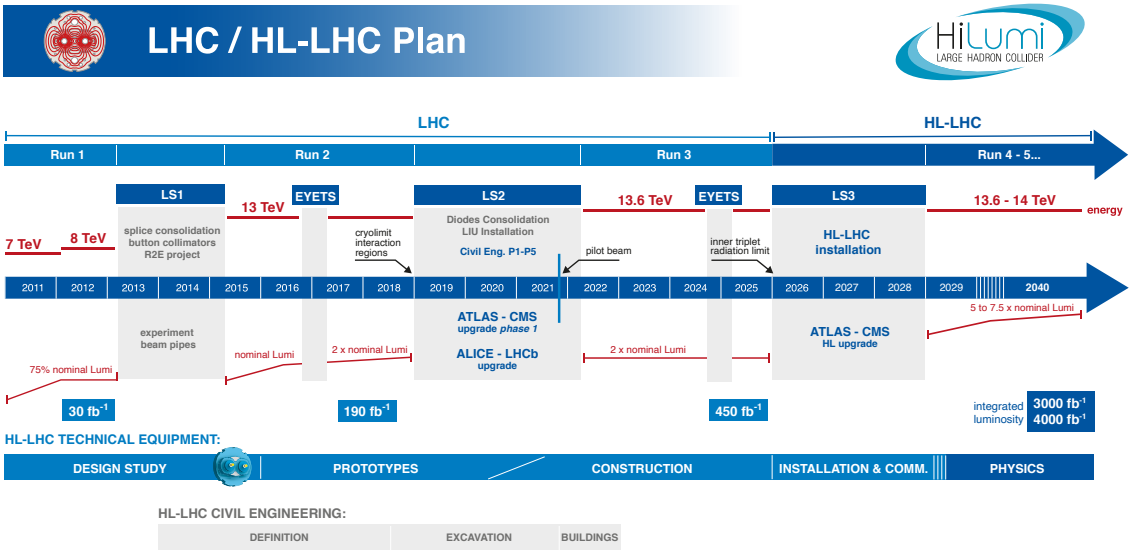


Figure 2.16: *The LHC operation plan for the next decade and beyond with the collision energy (upper line) and luminosity (lower line), taken from [43].*

2.5.1 Baseline hardware improvements

Several key technologies are being developed within the scope of the project [43]:

- more powerful quadrupole magnets based on niobium and tin (Nb3Sn) installation in the insertion region IR1 (ATLAS experiment) and IR5 (CMS) delivering the 12 T magnetic field (instead of 8 T currently installed in the LHC) as a response to the more dense beam,
- the new cryogenics in order to increase intervention flexibility and to provide the required additional cooling power,
- the new beam optics will help to maintain a constant collision rate throughout the time the beams will collide,
- an installation of the new collimators, devices that absorb particles that deviate from the beam trajectory and might damage the machine,
- insertion of the superconducting compact RF crab cavities for a better overlap of the colliding bunches at the interaction point (see Figure 2.17),
- modification of the extraction and injection systems, including the upgrade of absorbers to cope with injection failures,
- the new superconducting power lines (made of magnesium diboride) will connect the power converters to the new magnets, and will be able to work at a higher temperature, carrying currents of up to 10^5 A.



Figure 2.17: *An illustration of the proton bunches crossing without the crab cavities (left) and with the crab cavities (right), taken from [43].*

The increase in the luminosity will bring two main challenges for the LHC experiments: the harsher radiation environment and the much higher data rates. Thus, the experiments need to undergo the major upgrades in order to cope with the HL-LHC operation.

2.6 ATLAS upgrades for the HL-LHC

The data collection for HL-LHC is set to begin in 2029, with an average of 200 collisions per bunch crossing (instead of $\langle\mu\rangle = 30$ in on Run 2), requiring the ATLAS detector to improve its radiation hardness (to a fluence of around 1×10^{16} n_{eq}/cm^2 and an irradiation of 10 MGy [44]) and enhance the capability to process much higher data rates.

Therefore, several sub-detector systems are undergoing major improvements during the Phase-II upgrade: the Inner Tracker (ITk), the LAr and Tile calorimeters, muon, trigger, and data acquisition systems [45]. In general, the trigger and data acquisition systems will improve granularity and achieve an output rate of 10 kHz. The *ID* will be replaced by the new *Inner Tracker (ITk)*, which will have a higher granularity and an extended acceptance [44], [46]. The *calorimeter* system will replace the photomultiplier tubes in the most radiation exposed region and install new front-end and back-end electronics designed for the higher data rates [47]. The *muon system* will increase its coverage in the barrel region with the new MDTs and RPCs and in the end-cap with TGCs, improving also the trigger capabilities [48]. In addition, the brand new *High-Granularity Timing Detector (HGTD)* will be installed in the forward region.

2.6.1 The Inner Tracker

The ITk for the HL-LHC phase is an ATLAS all-silicon tracker detector that features 2 subsystem: Pixel Detector and Strip Detector. The pixel system, consisting of 5 barrel layers and end-cap rings, will cover a pseudorapidity of up to $|\eta| = 4$, while the strip system, consisting of 4 barrel layers and six end-cap disks, will cover up to $|\eta| < 2.7$ (see Figure 2.18).

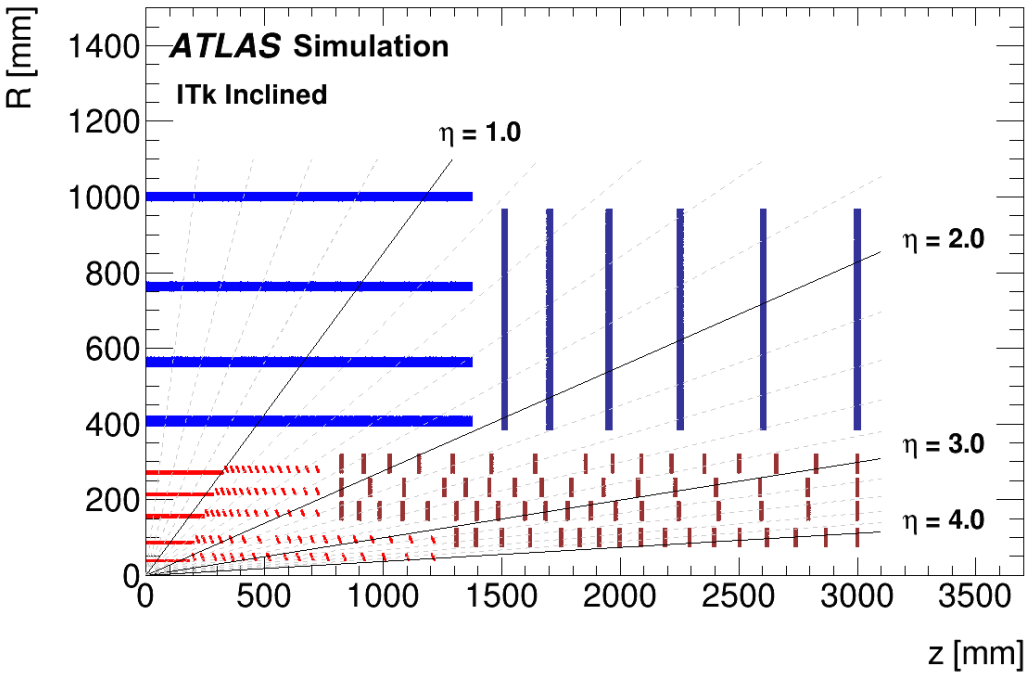
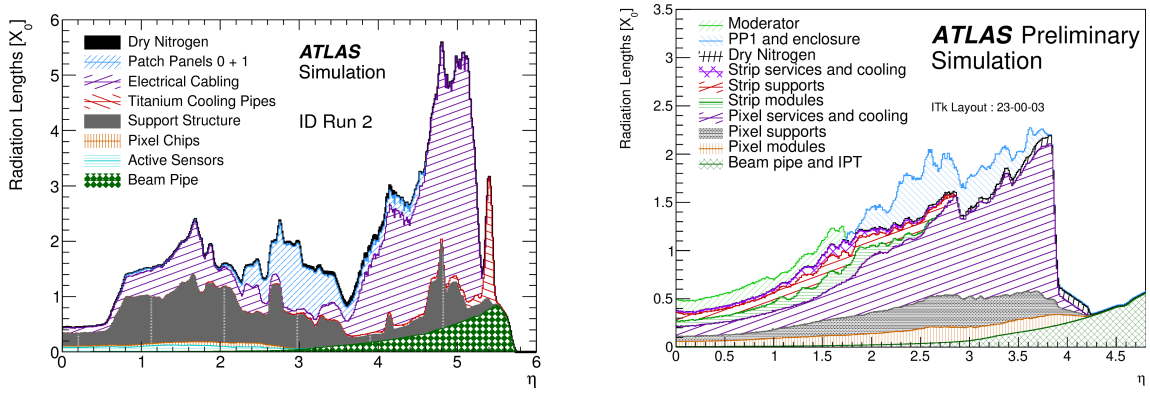


Figure 2.18: *Schematic layout of one quadrant of ITk for the HL-LHC phase of ATLAS. The active elements of the barrel and end-cap Strip Detector are shown in blue, for the Pixel Detector the sensors are shown in red for the barrel layers and in dark red for the end-cap rings. Taken from [44].*

Despite its increased surface and complexity, ITk has a reduced quantity of material compared to the Inner Detector, achieved by using thinner modules, inclined sections, and advanced materials for the support units (see Figure 2.19). The track reconstruction performance of ITk will benefit from the finer granularity, the reduction in the quantity of material budget, better hermeticity and the increased number of expected hits-on-track. The ITk is designed to provide at least 9 hits-on-track in the barrel and 13 hits-on-track in the forward region for particles with $p_T > 1$ GeV/c[4]. The momentum measurement will use the same 2 T solenoidal magnetic field as the current ID.

The pixel system covers a total surface area of approximately $13m^2$ and is composed of around 9000 modules, which are organized into three separate parts that are mechanically independent. The Inner System (IS) comprises the two innermost pixel layers, designed to be removed from ITk at approximately half of the detector's lifetime (after accumulating 2000 fb^{-1}). The second part, called the Outer System (OS), includes the 3 outer barrel layers flat staves and inclined sections. The rest of the layers build the Outer End-caps (EC). The pixel detector deploits 2 different radiation hard sensor technologies implemented in different regions of ITk depending

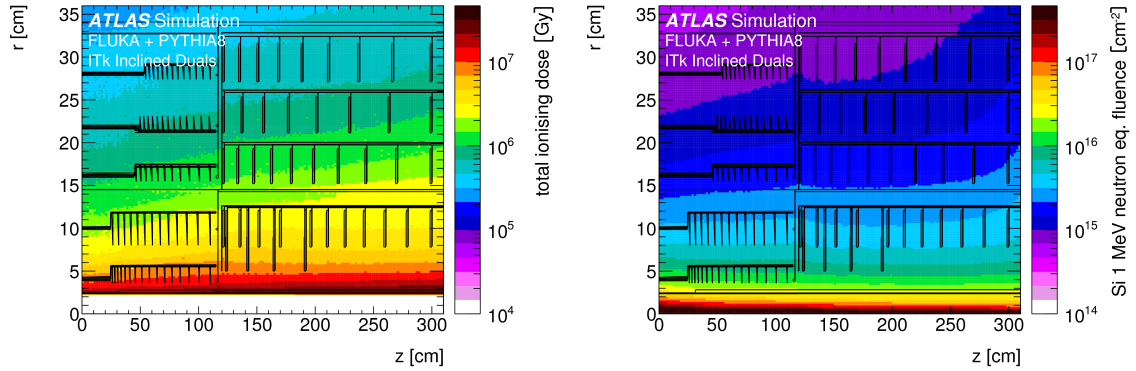
[4] p_T is the transverse momentum, the amount of a particle's momentum which is perpendicular to the beam direction



a) b)

Figure 2.19: *Material distribution within the ITk volume in radiation lengths X_0 versus $|\eta|$ for the Inner Detector (a) and ITk (b), broken down by sub-system and material category. Taken from [49].*

on the radiation load (see Figure 2.20): the innermost barrel layer will use the 3D pixels (150 μm thick), while the rest will use the planar sensor (100-150 μm thick).



a) b)

Figure 2.20: *Total ionising dose (TID) (a) and 1 MeV neutron equivalent fluence (b) in the ITk region from a FLUKA+PYTHIA8 simulation. The TID and fluence are normalised to 3000 fb^{-1} of pp collisions at 14 TeV.. Taken from [44].*

The core of the ITk pixel detector is a hybrid module, consisting of a silicon pixel sensor bump bonded to the readout chip. The pixel size of the planar sensor will be 50×50 μm^2, while for the 3D one 25×100 μm^2.

The 320 strip sensors have a thickness of 75.5 μm, a pitch of 75.5 μm and a length of either 24.1 mm or 48.2 mm in the barrel and 19–60 mm in the end-cap depending on the location. The detector is made of staves in the barrel and of petals in the end-caps. The barrel consists of 392 staves (with 14 strip modules on each side), each petal consists of 9 modules per side. Each module is composed of one or two printer

circuit boards (flex) glued on a sensor and hosting the readout ASICs, a controller and a power board.

For further understanding, it is helpful to show the vertex topologies in pp collisions at the LHC to understand the difference between the primary vertices originating from hard-scatters, secondary vertices usually being the primary particles' decays, and the pile-up vertices originating from the soft interactions (see Figure 2.21). The

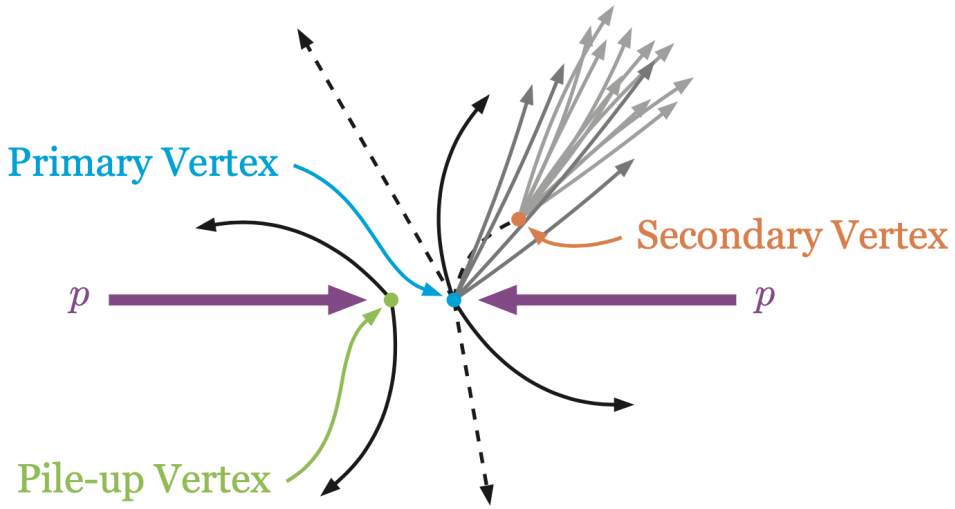
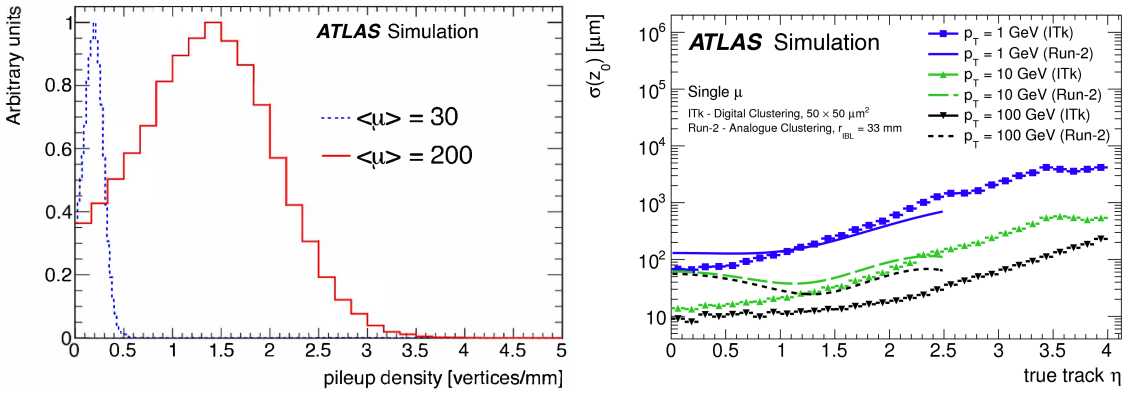


Figure 2.21: *Illustration of a set of three vertices in a proton-proton collision. A primary vertex and a secondary vertex are shown in addition to a pile-up vertex. Taken from [41].*

expected average pile-up vertex density in Run 4 is expected to be 1.8 vertices/mm (see Figure 2.22 (a)). For sufficient spatial separation of the collision vertices, ITk longitudinal impact parameter resolution σ_{z_0} should be significantly better than 600 μm, the inverse of the average pile-up density. Even though, ITk will have an outstanding spatial resolution in the central region, already at $|\eta| \sim 2.2$, σ_{z_0} is in 1 mm range for low p_T tracks and reaches 3 mm at $|\eta| \sim 4$ (see Figure 2.22 (b)). This leads to the ambiguoties in track-vertex associations in the forward region.

2.6.2 The High-Granularity Timing Detector

Following the pile-up contamination challenges in the forward region, the High-Granularity Timing Detector (HGTD) was designed in order to improve the reconstruction abilities of ATLAS detector. The purpose of HGTD is to provide precise time measurements for tracks in the forward region, with an average time resolution of 30 ps (50 ps) per track at the beginning (by the end) of HL-LHC operation. HGTD located around 3.5 m away from the interaction point will cover the pseudorapidity



a) b)

Figure 2.22: *(a): Local pile-up vertex densities at generator level for two values of pile up: 30 (Run2-Run3) and 200 (HL-LHC) collisions per batch crossing. (b): Resolution of the longitudinal track impact parameter, z_0, as a function of η for muons of $p_{\mathrm{T}} > 1$ GeV/c (blue), $p_{\mathrm{T}} > 10$ GeV/c (green) and $p_{\mathrm{T}} > 100$ GeV/c (black) using Inner Detector in Run 2 and ITk with HGTD in Run4. Taken from [20].*

region of $2.4 < |\eta| < 4.0$ and will consist of 2 double sided discs in each ATLAS end-cap (see Figure 2.23).

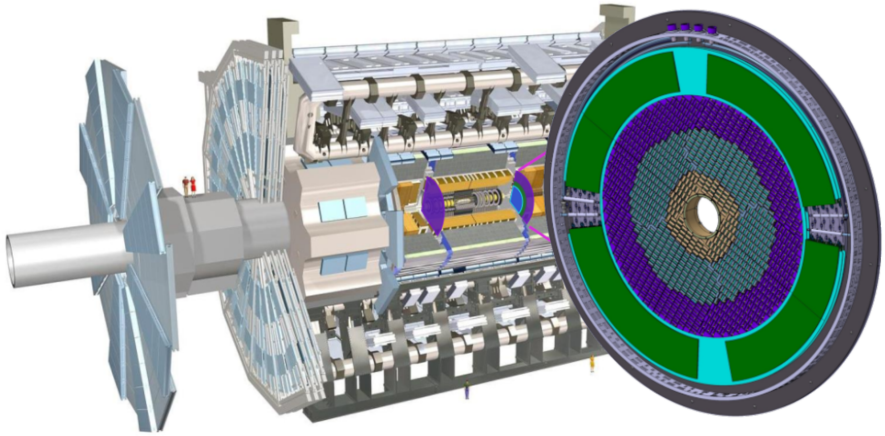


Figure 2.23: *Position of the HGTD within the ATLAS Detector. The HGTD acceptance is defined as the surface covered by the HGTD between a radius of 120 mm and 640 mm at a position of $z = \pm 3.5$ m along the beamline, on both sides of the interaction point. Taken from [20].*

By providing an additional time measurements for a track, HGTD will resolve the vertex association ambiguities. Although a forward track may appear to align spatially with a particular vertex, differences in the track's time and the selected vertex's time can be used to identify and discard pile-up tracks. Indeed, as shown in Figure 2.24, interactions in the dense pile-up environment occur very close to each other in z plane, being very difficult to be distinguished. Looking at the time spread of interactions

with a high precision helps to identify the hard-scatter event of interest, even though the z positions spread of the vertices may be smaller than the resolution of ITk.

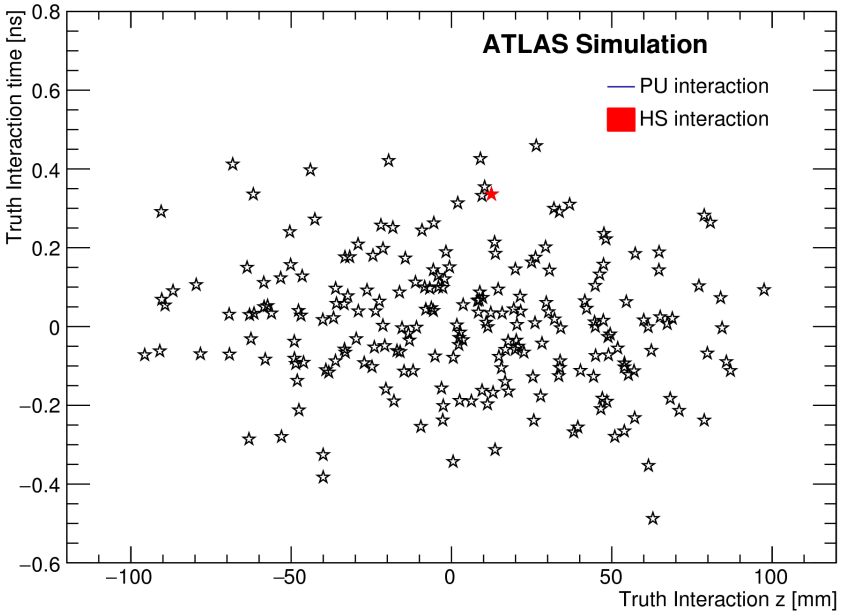


Figure 2.24: *Visualisation of the truth interactions in a single bunch crossing in the $z-t$ plane for $t\bar{t}$ simulated events at $\langle\mu\rangle$ =200. The read star represents a Hard-Scatter (HS) event, while the black stars are the superimposed pile-up interactions. Taken from [20].*

Assuming a beam spread of 175 ps and a track resolution of 30 ps, the pile-up can be decreased by a factor of 6 within the HGTD's acceptance range. The time component will improve the object reconstruction, leading to a better object identification and more effective pile-up rejection. Additionally, HGTD will provide luminosity measurements.

The detector is presented in details in the next chapter.

Chapter 3

High-Granularity Timing Detector

As mentioned in the previous chapter, ATLAS plans to install the new High-Granularity Timing Detector (HGTD) in order to mitigate the pile-up effects. HGTD will be composed of two double sided discs consisting of the Low-Gain Avalanche Detectors (LGAD), located in both end-cap regions (A, C) covering $2.4 < |\eta| < 4.0$. This chapter is dedicated to the key design features of HGTD and its impact on the ATLAS performance, namely: the simulation-based physics studies with HGTD (Section 3.1), the luminosity measurements application (Section 3.2), the technical design of HGTD (Section 3.3) and the introduction to the LGAD technology used in HGTD (Section 3.4).

3.1 Physics motivation

The precise assignment of tracks to primary vertices is crucial for the mitigation of the pile-up effects on the objects reconstructions. Jet reconstruction and calibration, pile-up mitigation for jets, b-tagging, lepton isolation, and jet substructure measurements rely strongly on the correct assignment of tracks to primary vertices and jets [20]. It has to be pointed out, that in this section, all the presented studies were done for the Technical Design Report (TDR) with the 2-ring HGTD geometry, that is now replaced by the 3-ring geometry (see Section 3.3.1). The two differ in the placement of the modules on the discs, more precisely in the overlap between the modules on two sides of one HGTD disc. The 2-ring geometry was discarded due to the optimization for the radiation hardness discussed in Section 3.3.2.2.

3.1.1 Physics object performance

A track is associated to a vertex if its origin is spatialy compatible in z with the vertex position z_{vertex}, such as:

$$|\frac{z_0 - z_{vertex}}{\sigma_{z_0}}| < s, \tag{3.1}$$

where z_0 is the track longitudinal impact parameter, σ_{z_0} is the per-track resolution on the longitudinal impact parameter which depends on the track pseudorapidity and p_{T}, and s is a significance cut (typically 2.5 or 3). With ITk only, the tracks of 1 GeV with $|\eta| = 3$ have a z_0 resolution of approximately 1 mm. Having an average vertex density of 1.8 vertices/mm at z = 0 (at $\langle\mu\rangle = 200$), a forward low p_{T} track can be compatible with up to 9 near-by vertices on average. Thus, the track-to-vertex association will suffer significantly from pile-up contamination, reducing the efficiency of track-based pile-up suppression methods [20].

Timing information will address this challenge by requiring all tracks within a z window around the primary vertex to have a compatible time with the time of the hard-scatter vertex. There are two main approaches on how to use the timing information. In one approach, denoted as *global* t_0, the hard-scatter vertex time t_0 is determined so that it can be used as a global reference to check the time compatibility of tracks associated to jets or other physics objects in the event, for details see [20].

A second approach, denoted as *self-tagging*, checks the consistency of the measured production time for all tracks associated to the same physics object (for instance, a jet) among themselves, in more details explained here [20]. Therefore, it does not require the t_0. Both approaches are complementary to each other, and can be combined for maximum performance across jet p_{T} [20]. In the following subsections, the expected improvements in the physics objects performance using the HGTD measurements are discussed.

3.1.1.1 Suppression of pile-up jets

Pile-up jets can negatively impact both the precision measurements of the SM and the sensitivity to discover new physics. These jets can lead to more background events passing a selection, while also decreasing the effectiveness of kinematic variables or discriminants that are used to differentiate signals from backgrounds. Therefore, it is crucial to efficiently identify and reject pile-up jets to improve the physics potential of the HL-LHC. The pile-up jets can be produced through a hard QCD process (known as QCD jets) from a pile-up vertex or by random combinations of particles from multiple vertices. The latter mechanism is dominant at low p_{T}, whereas QCD jets are the primary source of pile-up jets at high p_{T}.

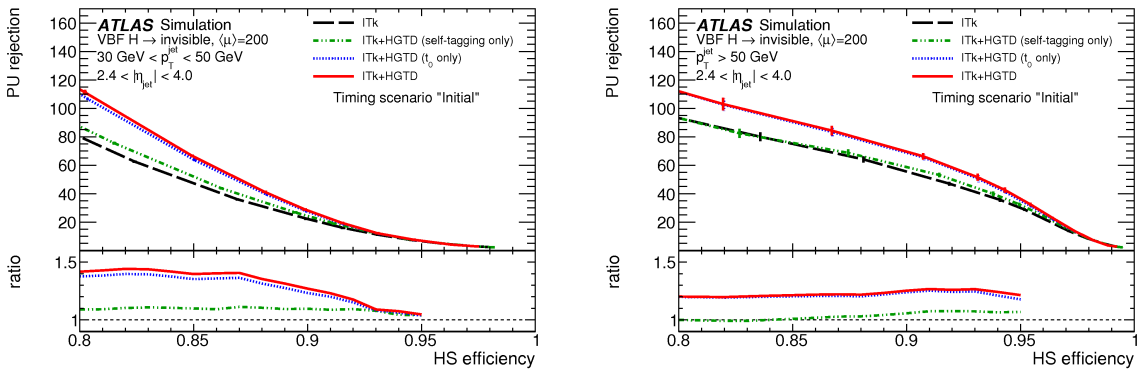
One powerful discriminant used for accurate association of jets with tracks and vertices is the R_{pT} jet variable. It is defined as the scalar sum of the p_{T} of all tracks within the jet cone that originate from the hard-scatter vertex PV_0, divided by the fully calibrated jet p_{T}:

$$R_{p_{\mathrm{T}}} = \frac{\Sigma p_{\mathrm{T}}^{\mathrm{trk}}(\mathrm{PV}_0)}{p_{\mathrm{T}}^{\mathrm{jet}}}. \tag{3.2}$$

For the presented study, the anti-k_t algorithm with a radius parameter of $R = 0.4$ is used to reconstruct jets from clusters of calorimeter energy deposits. The reconstructed hard-scatter jets must be within $\triangle R = \sqrt{(\triangle\eta)^2 + (\triangle\phi)^2} < 0.3$ of a truth jet with a p_{T} greater than 10 GeV. Hard-scatter and pile-up jets for simulated events are distinguished by their matching to truth jets, which are reconstructed from stable and interacting final state particles resulting from the hard interaction. To be considered a pile-up jet, it must be at least $\triangle R > 0.6$ away from any truth hard scattering jet with a p_{T} greater than 4 GeV.

Two approaches mentioned before were used to integrate the time information associated with each track and modify the R_{pT} variable. In the global t_0 approach, if an event contains a global t_0 relative to which tracks can be compared, it can be utilized to eliminate tracks originating from a proton-proton interaction other than the hard scatter interaction. In the self-tagging approach, if a global t_0 cannot be established for an event, the time information can be used to assess the time compatibility between tracks within a given jet to identify instances of pile-up contamination.

Figure 3.1 shows the pile-up jets rejection, i.e. inverse of mis-tag efficiency, as a function of the efficiency for selecting hard-scatter jets using the R_{pT} discriminant for low, Figure 3.1 (a), and high, Figure 3.1 (b), p_{T} jets in VBF H $\rightarrow$ invisible events (see Section 2.3.1) with $\langle\mu\rangle = 200$. The graphs present the performance with and without HGTD using three approaches: self-tagging, global t_0 and combined. The combined approach enhances the rejection of pile-up jets in the forward region with $30 < p_{\mathrm{T}} < 50$ GeV by approximately 1.5 times at a signal efficiency of 85%. For the high p_{T} jets, the performance is approximately 20% better when using HGTD. In Figure 3.2, the relative pile-up-jet rate is shown for $30 < p_{\mathrm{T}} < 50$ GeV jets as a



a) b)

Figure 3.1: *Pile-up jet rejection as a function of hard-scatter jet efficiency in the $2.4 < |\eta| < 4.0$ region at the beginning of the lifetime of the detector for low (a) and high (b) p_T jets. The VBF H $\rightarrow$ invisible events are simulated for the ITk-only and combined ITk + HGTD pile-up jet rejection performance. Taken from [20].*

function of pseudorapidity, utilizing the combined timing reconstruction. A notable improvement is seen at larger values of pseudorapidity where the z impact parameter resolution is lower and timing information plays a more important role in associating tracks with vertices.

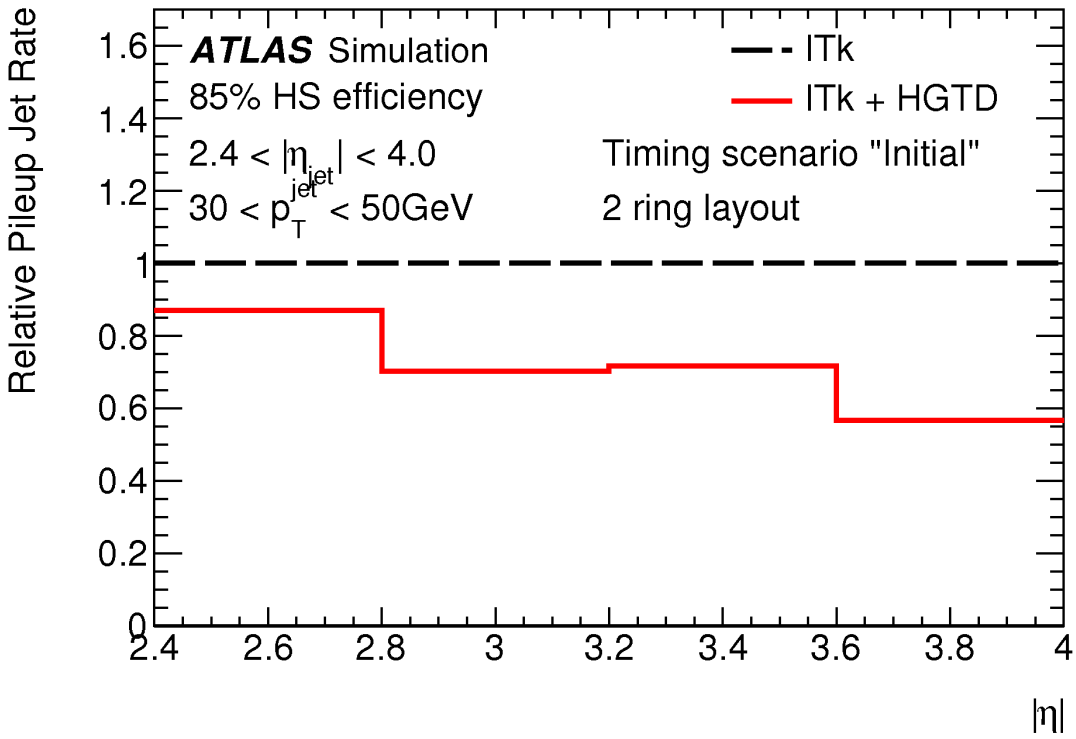


Figure 3.2: *Relative pile-up jet rate as a function of jet pseudorapidity, for jets with 30 GeV $< p_T <$ 50 GeV in the VBF $H \rightarrow$ invisible events reconstructed with ITk only (black dashed line) and with ITk+HGTD (red line). Taken from [20].*

3.1.1.2 Lepton track isolation

The time information associated with leptons can be utilized to mitigate the effects of pile-up when applying track-isolation criteria to forward-region leptons. The efficiency of track-based lepton isolation is defined as the probability of no additional tracks with $p_{\mathrm{T}} > 1$ GeV being reconstructed within an $\triangle R < 0.2$ cone around the lepton track. In the forward region, this efficiency is reduced due to pile-up track contamination coming from the larger z-window required to associate tracks with the primary vertex. To address this issue, the time is associated to lepton tracks, helping to reject tracks originating from pile-up interactions that are spatially close to the hard-scatter vertex.

This approach was studied using electrons from Z boson events, but similar results are expected for τ lepton decays. The forward electrons with $p_{\mathrm{T}} > 20$ GeV that pass the standard ATLAS "medium" identification criteria [50] were selected. The time of all tracks with $p_{\mathrm{T}} > 1$ GeV which are within the $\triangle R < 0.2$ isolation cone are

compared with the time of the electron track. If the time difference $|t_{electron} - t_{track}|$ is larger than twice the quadratic sum of the timing resolution of both tracks, or if the surrounding track fails to obtain a time, the track is discarded.

Figure 3.3 shows the lepton isolation efficiency as a function of the pile-up density with ITk-only and HGTD information. The efficiency denominator includes all the electron tracks, even if the time was not available for them.

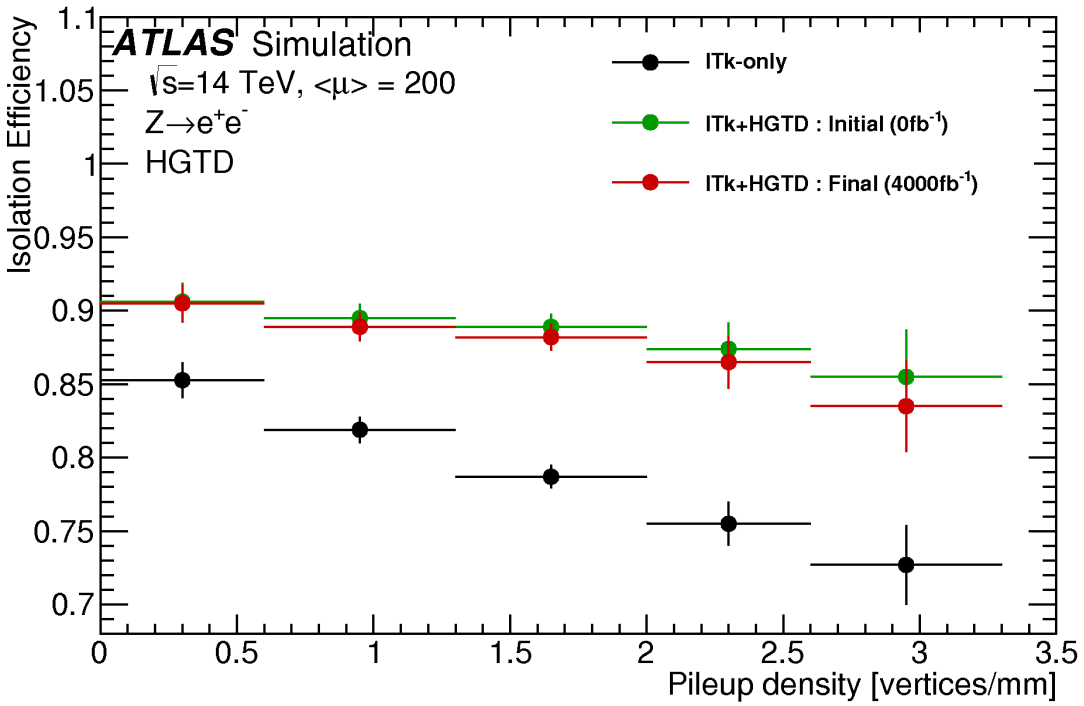


Figure 3.3: *Efficiency for electrons to pass track-isolation criteria as function of the local vertex density, for the ITk-only (black points) and ITk+HGTD (red and green points) scenarios. The isolation efficiency is shown for both the "initial" time resolution of the detector (green) as well as the "final" time resolution at the end of detector's lifetime (red). Taken from [20].*

With pile-up density, the lepton isolation efficiency drops, reaching 73% when only using ITk tracking. The addition of the HGTD timing information not only enhances the efficiency, but also reduces the drop slope over the whole pile-up density range. HGTD helps to keep an efficiency above 85% even at high pile-up density (up to three additional vertices per mm around the hard-scatter vertex). These studies show that the expected HGTD performance is sufficient to achieve a forward lepton track isolation efficiency essentially independent of the pile-up vertex density and at a level similar to that achieved in the central region [20].

3.1.1.3 b-tagging

HGTD is expected to be useful for mitigation of the impact of pile-up track contamination on the b-tagging [20]. The pile-up tracks with relatively large z impact parameter (comparing to the hard-scatter vertex) can create fake secondary vertices, which leads to the insufficient light-quark jet rejection. A combination of self-tagging and global t_0 approaches could potentially enhance the rejection of pile-up tracks to compensate for the lost b-tagging performance at high vertex densities. The full incorporation of timing information within the software framework for heavy-flavour tagging requires major infrastructure changes and is left for a future study [20].

3.1.1.4 Particle-flow jet reconstruction

Particle-flow jet reconstruction relies havily on correct matching of charged particle tracks with calorimeter signals and primary vertices. The jets energy resolution can be improved by removing the contributions originating from pile-up vertices. This can be achieved by using the timing information to distinguish between hard-scatter and pile-up tracks within a jet. These improvements in jet energy resolution can have a significant impact on the sensitivity of important physics channels, including VBF analyses. The full integration of HGTD into the particle-flow reconstruction chain, however, is a long-term goal, involving many steps at the level of calorimeter reconstruction and calibration that are still under development [20].

3.1.1.5 Missing transverse energy

There are three potential ways to utilize the HGTD to enhance the resolution of the missing transverse energy. The first approach is to exploit the improved jet energy resolution obtained through particle-flow reconstruction using HGTD. The second approach involves reducing the contamination from forward pile-up in the track-based soft-term of the missing transverse energy [20]. The soft-term consists of all detector signals that did not get associated to any of the hard objects (electrons, muons, etc.), but still can be matched to the primary vertex. By using the knowledge of the track time, it is possible to select forward tracks more accurately in the soft-term component of the missing transverse energy. Last but not least, the improved suppression of forward pile-up jets will directly lead to an enhancement in the missing transverse energy resolution itself. A full propagation of the pileup jet suppression and the incorporation of timing information to the soft-term reconstruction will be pursued in the future [20].

3.1.2 Impact on the VBF Higgs production analysis

HGTD will enhance the physics capabilities of ATLAS in two main ways [20]:

- by improving the reconstruction of physics objects such as forward jets and leptons by providing the timing information,
- by providing a precise online and offline luminosity measurements, targeting to achieve the luminosity uncertainty of 1% for the Higgs precision physics programme of the HL-LHC.

As an example, the VBF H $\rightarrow$ invisible analysis improvement with HGTD is presented. The VBF Higgs production (see Secction 2.3.1) plays a crucial role in the HL-LHC physics programme due to its high cross section and its distinctive features that help separate the signal from the backgrounds. The VBF events are characterized by the presence of two jets with a large rapidity gap, with one jet being within the HGTD acceptance most of the times. HGTD contribution can enhance the sensitivity of VBF topologies in multiple ways. First of all, HGTD will mitigate the impact of pile-up, which is especially challenging in the forward region due to the limitations of the tracking-based pile-up jet suppression algorithms. In addition, the improved reconstruction of jets and missing transverse energy can also enhance the signal to background ratio (S/B), further increasing the sensitivity of VBF topologies.

The study described in the TDR considers the VBF produced Higgs bosons decaying to neutrinos via $H \rightarrow Z(\nu\nu)Z(\nu\nu)$. These invisible Higgs decays are of interest for dark matter searches for model in which a dark matter particle χ could couple to the SM via the Higgs boson alone and induce a $H \rightarrow \chi\chi$ decay, increasing thus the overall rates of invisibly decaying Higgs bosons. Since this invisible decay leaves only missing transverse momentum in the detector, tagging these types of events with the two jets appearing in the VBF production mechanism are key. The dominant background for this signature are events with Z (decaying to neutrinos) and a jet. Rejection of the pile-up jet can thus improve the rejection of this background and improve the signal sensitivity [51].

Figure 3.4 shows the expected improvement in signal-to-background ratio as a function of the improvement in pile-up jet rejection for events in which both jets are forward (FF), one-forward and one-central (CF) and the mix.

An enhancement of 12% to 25% is observed with an improved pile-up suppression of 20% to 40%. Future improvements are possible by exploring the potential of testing time compatibility between two jets within the HGTD acceptance.

3.2 HGTD and luminosity measurement

A precise measurement of integrated luminosity is crucial for the majority of physics analyses conducted in ATLAS. For instance, during the Run 1 and Run 2, the luminosity uncertainty was one of the leading uncertainties in measurements of some

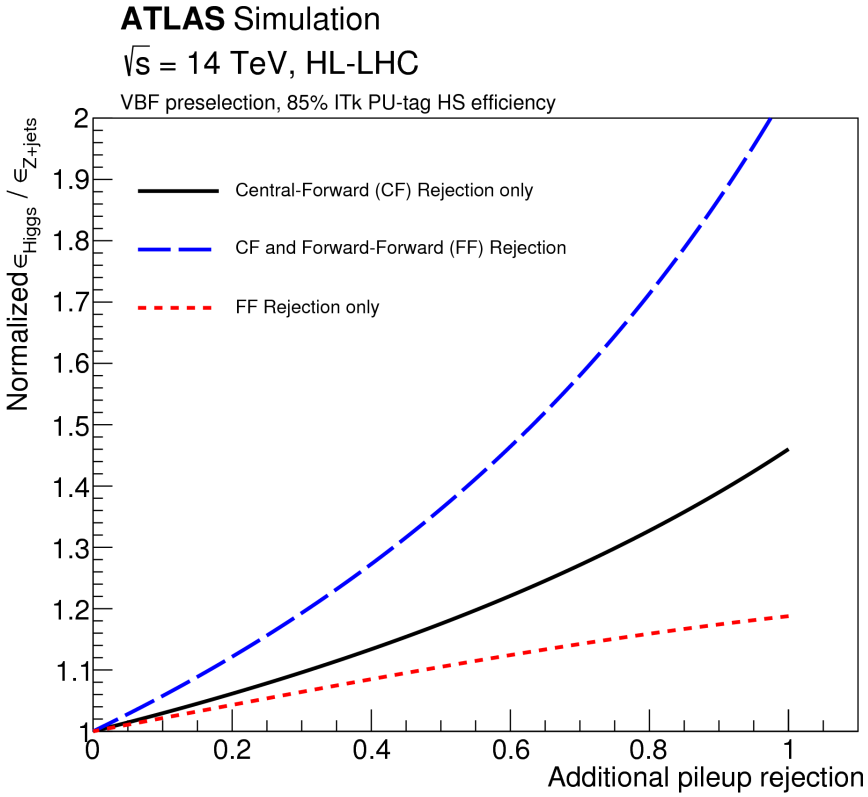


Figure 3.4: *Normalized signal over background gain relative to ITk-only pile-up jet suppression performance, as a function of the additional pile-up jet rejection from HGTD. The black curve corresponds to the case when HGTD is only used in events where one jet is central and one is forward (CF). The red curve corresponds to the case when both jets are forward (FF). The dotted blue line shows the total improvement when the combined HGTD+ITk pile-up suppression algorithm is applied to all jets in the event. Taken from [20].*

Higgs couplings (around 1.7 % [52]) and thus its properties. A luminometer aims to measure an observable that is proportional to the instantaneous luminosity and to the average number of inelastic interactions per bunch crossing $\langle\mu\rangle$, such as the average number of charged-particle reconstructed tracks or the noise-corrected clusters.

Currently, the baseline ATLAS luminometer exploits the hit counting method. It applies a Poisson statistics to extract $\langle\mu\rangle$ from the average number of detector hits recorded per bunch crossing. Therefore, the finer the granularity of the luminometer is, and the smaller the acceptance of its individual channels is, the higher the pile-up value at which the method eventually saturates.

HGTD can provide a great tool to precisely measure luminosity. The high granularity gives a low occupancy, and therefore a linearity between the average number of hits and $\langle\mu\rangle$ over the full range of luminosity expected at HL-LHC.

In the $2.4 < |\eta| < 2.8$ range, the average number of hits per inelastic p-p collision for one HGTD layer is 14.7, and approximately 16.0% of these collisions result in 0 hits. The Figure 3.5 shows the average number of hits per bunch crossing registered in the first double-sided HGTD disc as a function of the number of simultaneous inelastic pp interactions $\langle\mu\rangle$. The black points are determined from fully simulated minimum-bias events with $\mu = 1$ and $\langle\mu\rangle$ in the range 190-210, respectively. The green stars represent

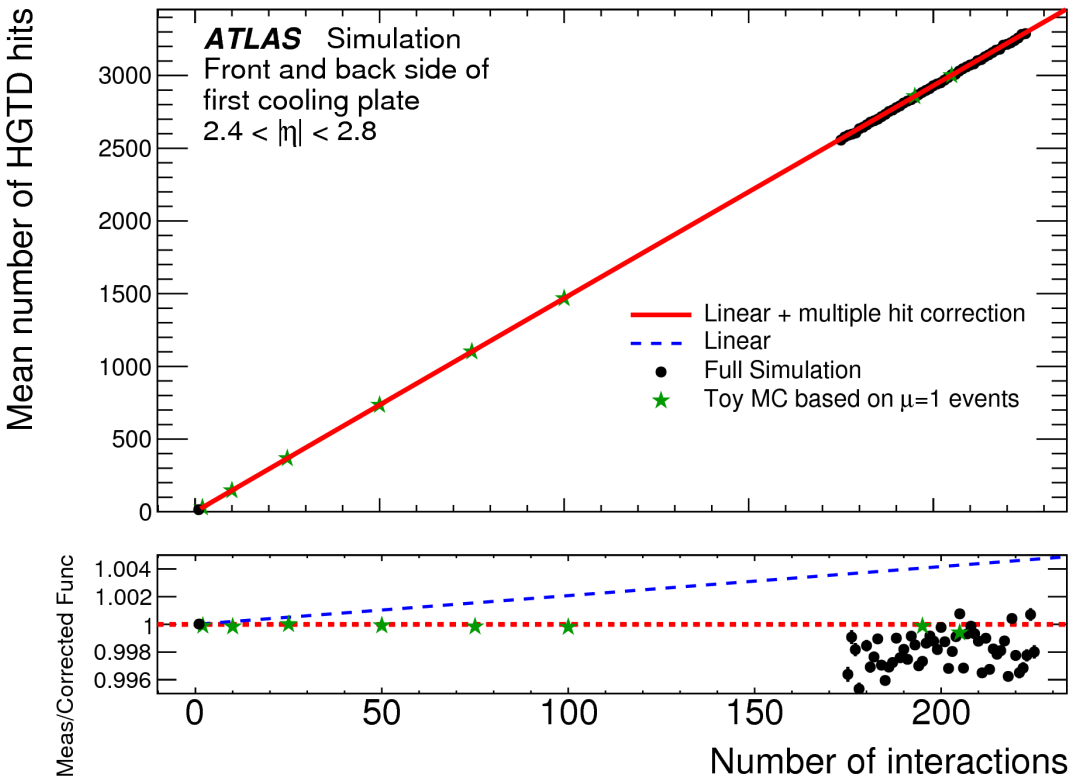


Figure 3.5: *Mean number of HGTD hits per bunch crossing as a function of the number of p-p interactions. The black points are the results from fully simulated samples. The green stars represent results from a toy Monte-Carlo (MC) simulation where several $\mu = 1$ minimum-bias events have been overlaid to produce samples with intermediate numbers of interactions. The blue dashed line is the ideal linear relationship between the mean number of hits and the number of interactions, derived from the $\mu = 1$ sample. The red line is the result of adding a correction from multiple particles hitting the same pad to the linear parameterisation. In the bottom panel, both lines can be compared to the fully simulated samples at $\mu \sim 200$. Taken from [20].*

results from a toy MC where several $\mu = 1$ minimum-bias events have been overlaid to produce samples. A linear, ideal, relationship between the mean number of hits and the number of interactions (blue dashed line), derived from the fully simulated sample at $\mu = 1$, is extrapolated to the $\mu \approx 200$ region where its prediction can be compared to the hit multiplicities extracted from fully simulated high pile-up samples.

The small discrepancy, of approximately 0.6%, between the blue dashed line and the simulated points in the bottom left frame around $\mu \approx 200$ is mostly attributed to multiple particles hitting the same pad. The red line is the result of correcting the linear function with the contribution from multiple particles hitting the same pad [20].

The detector can accurately determine charged-particle multiplicities for each bunch crossing separately, given that the detector signal durations are in the range of a few nanoseconds. Additionally, the occupancy information is sent at a 40 MHz frequency, which allows for per-BCID (bunch crossing identifier) luminosity measurements both online and offline, independent of the ATLAS trigger.

The luminosity determination is made in a reduced pseudorapidity range $2.4 < |\eta| < 2.8$ (430 mm $<$ r $<$ 640 mm). The HGTD design allows to constrain many systematic uncertainties and limit the total uncertainty on integrated luminosity measurements in the HL-LHC to 1%, despite the harsh experimental conditions.

3.3 The HGTD technical aspects

The design of HGTD is being developed to operate with $\langle\mu\rangle = 200$ and sustain a total integrated luminosity of 4000 fb^{-1}. Giving the space constraints in ATLAS, it was decided to locate the HGTD between the barrel and the end-cap calorimeters, approximately 3.5 m away from the interaction point in both endcaps. This spot is currently occupied by the Minimum-Bias Trigger Scintillators [53], which will be removed. The extensive R&D programme is taking place to meet all the performance requirements while taking into account the cost, spatial, and radiation limitations.

3.3.1 Detector overview and key requirements

3.3.1.1 General overview

The envelope of the detector vessel with a radial extent of 110 to 1000 mm has a width of 125 mm (in z). One HGTD end-cap includes a hermetic vessel (front and back covers, inner and outer rings), two instrumented double-sided discs (with sensors on the front and back of each cooling disc) and two moderator discs placed inside and outside the hermetic vessel to reduce the back-scattered neutrons created by the forward calorimeters. The HGTD components in one end-cap are shown in Figure 3.6. The cooling/support discs are mechanicaly separated in two half circles and the two HGTD layers are rotated in opposite directions with respect to one another by 20° in order to maximize the hit efficiency.

LGAD was chosen as a baseline timing detector technology due to the space limitations, radiation hardness requirements and its sufficienct time resolution (∼30 ps), see Section 3.4. An extensive R&D program on different LGAD designs is still ongoing in

close collaboration with RD50 [54] and several manufacturers. The pad size of LGAD for HGTD is 1.3×1.3 mm^2 with an active thickness of 50 μm. This pad size ensures occupancies below 10% at the highest expected instantaneous luminosity, small dead areas between pads, and sufficiently low sensor capacitance, which is important for the time resolution. The thickness provides the best compromise between capacitance and deposited charge, both favouring large thickness, and signal slope and Landau fluctuations, both favouring a small thickness. In order to mitigate the impact of irradiation, the sensors will be operated at low temperatures (-30 °C).

The HGTD cooling system is based on the evaporating liquid CO_2. It will be integrated with the general cooling system developed for the ATLAS ITk [46]. CO_2 cooling is chosen because it evaporates at much higher pressures than common refrigerants, keeping the vapour compressed and therefore the volume low. Taking into account the radiation environment in which the HGTD will operate, CO_2 is one of the most appropriate refrigerants because of its radiation hardness and low activation [20]. The CO_2 will be distributed through the layer in a serpentine manner through 5 mm wide pipes.

To fulfill the requirements on time resolution and radiation hardness of the sensor readout, a custom Application-Specific Integrated Circuit (ASIC) called ALTIROC (ATLAS LGAD Time Read Out Chip) [55], is being developed. ALTIROC will

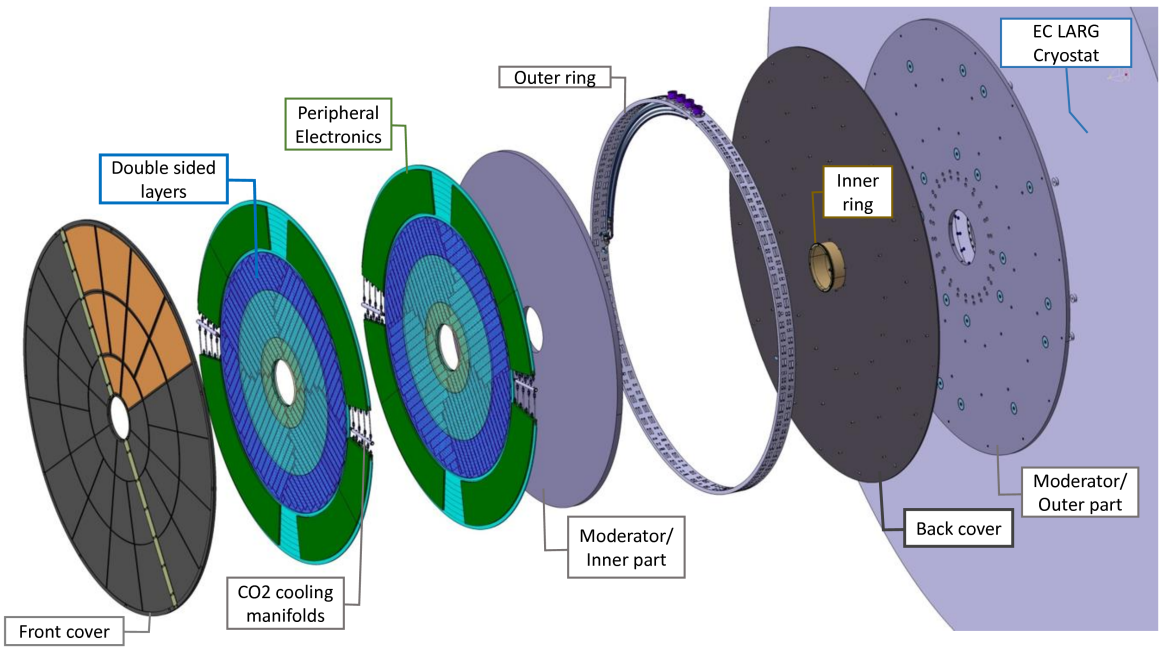


Figure 3.6: *Global view of the HGTD in one endcap, including a hermetic vessel, two instrumented double-sided layers (mounted on two cooling/support discs), and two neutron moderators placed inside and outside the hermetic vessel protecting both the ITk and the HGTD from the back-scattered neutrons created by the forward calorimeters. Taken from [20].*

additionally provide the hits count detected by the sensor bump-bonded to it. The chip will transmit this data at a rate of 40 MHz, which will allow for unbiased, bunch-by-bunch luminosity measurements, as well as the implementation of a minimum-bias trigger.

The optimimization of the layout for timing performance, cost and radiation tolerance, led to the division of HGTD layer in three active regions (rings) depending on the modules placement: 120 mm < r < 230 mm, 230 mm < r < 470 mm, and 470 mm < r < 640 mm with an average of 2.6, 2.4 and 2.0 hits per track respectively. This HGTD configuration is denoted as a 3-ring geometry. The HGTD layout optimization is discussed in Section 3.3.1.4 in more details. The active area of HGTD covers $2.4 < |\eta| < 4.0$, while the peripheral electronics aggregating the data from ALTIROCs are located beyond r > 640 mm. The key design parameters and performance requirements are summarized in Table 3.1

Pseudo-rapidity coverage	$2.4 < \|\eta\| < 4.0$
Thickness in z	75 mm (+50 mm moderator)
Position of active layers in z	±3.5 m
Weight per end-cap	350 kg
Radial extension:	
Total	$110\,\text{mm} < r < 1000\,\text{mm}$
Active area	$120\,\text{mm} < r < 640\,\text{mm}$
Pad size	1.3×1.3 mm^2
Active sensor thickness	50 μm
Number of channels	3.6 M
Active area	6.4 m^2
Module size	30×15 pads (4×2 cm^2)
Modules number	8032
Collected charge per hit	> 4.0 fC
Average number of hits per track	
$2.4 < \|\eta\| < 2.7$ $(640\ mm > r > 470\ mm)$	≈2.0
$2.7 < \|\eta\| < 3.5$ $(470\ mm > r > 230\ mm)$	≈2.4
$3.5 < \|\eta\| < 4.0$ $(230\ mm > r > 120\ mm)$	≈2.6
Average time resolution per hit (start and end of operational lifetime)	≈ 35 ps, ≈ 70 ps
Average time resolution per track (start and end of operational lifetime)	≈ 30 ps, ≈ 50 ps

Table 3.1: *Main parameters and requirements of HGTD.*

A high single hit efficiency is essential throughout the lifetime of the HGTD. The minimum hit efficiency should be at least 95% and the minimum charge collected for a Minimum Ionizing Particle (MIP) of at least 4 fC for an irradiated sensor with the fluence of $2.5 \times 10^{15}\,\text{n}_{\text{eq}}\ \text{cm}^{-2}$. The target time resolution per track is from 30 ps at the start of lifetime to 50 ps after accumulating 4000 fb^{-1}. In order to achieve this

performance, the time resolution per hit should be about 35 ps and not worse than 70 ps at the start of detector operation and at the end of detector lifetime respectively.

3.3.1.2 Time resolution

As mentioned above, the main goal of HGTD is to provide a good time resolution. The time resolution of a detector element can be decomposed in the following factors:

$$\sigma^2_{\text{total}} = \sigma^2_{\text{L}} + \sigma^2_{\text{elec}} + \sigma^2_{\text{clock}} \tag{3.3}$$

where σ^2_{L} are Landau fluctuations in the deposited charge as the charged particle traverses the sensor, σ^2_{elec} represents the contributions from the readout electronics, and σ^2_{clock} is from the non-deterministic jitter contribution from the clock distribution [20]. The first contribution is caused by the non-uniformity in the local density of electrons-holes pairs along the particle's path, which creates irregularities in the signal that follows the Landau distribution. Beam and laboratory tests and sensor simulations show that the thinner the silicon sensors are the smaller the contribution from Landau fluctuations is. With a 50 μm thick LGAD sensor, this contribution is approximately 25 ps, see Section 3.4. The readout electronics contribution can be be kept to approximately 25 ps, giving the fast detector signals and a high signal-to-noise ratio, which is described in Section 3.5. The clock contribution is expected to be approximately 15 ps and coming mainly from the lpGBT[1] [56] clock jitter and the additional jitter contributions from the flex cable and ALTIROC.

3.3.1.3 The HGTD modules

The LGAD pad size of 1.3×1.3 mm^2 is the same for the entire HGTD and was chosen as the best compromise between occupancy, electronic noise, sufficient number of channels, and the cumulative area of inter-pad dead zones. In addition, this choice ensures a low double-hit probability for a single pad within a bunch crossing. One HGTD module with a total area of 4×2 cm^2 consists of two LGAD sensors (each containing 15×15 pads) bump-bonded to two ALTIROCs and of a module flex, which is wire-bonded to the ASICS (see Figure 3.7). The module flex is a six-layer flexible printed circuit design that connects the differential data, clock, control signals and power of the HGTD front-end ASICs as well as the high voltage to bias the sensors. For easier detector assembly, the modules will be glued on support units (SU) forming detector units (DU) (DU is a SU with modules mounted on it).

Each module flex will be connected to the Peripheral Electronic Boards (PEBs, see green ring on Figure 3.6) through a flex tail. The PEBs provide power, clock and

[1] low-power Gigabit Transceivers, an ASIC responsible for the serialization of up-stream data and down-stream transmission of ASIC control parameters

control and transmit the readout data to the Data Acquisition system (DAQ). The detector units will be mounted on the HGTD cooling disc.

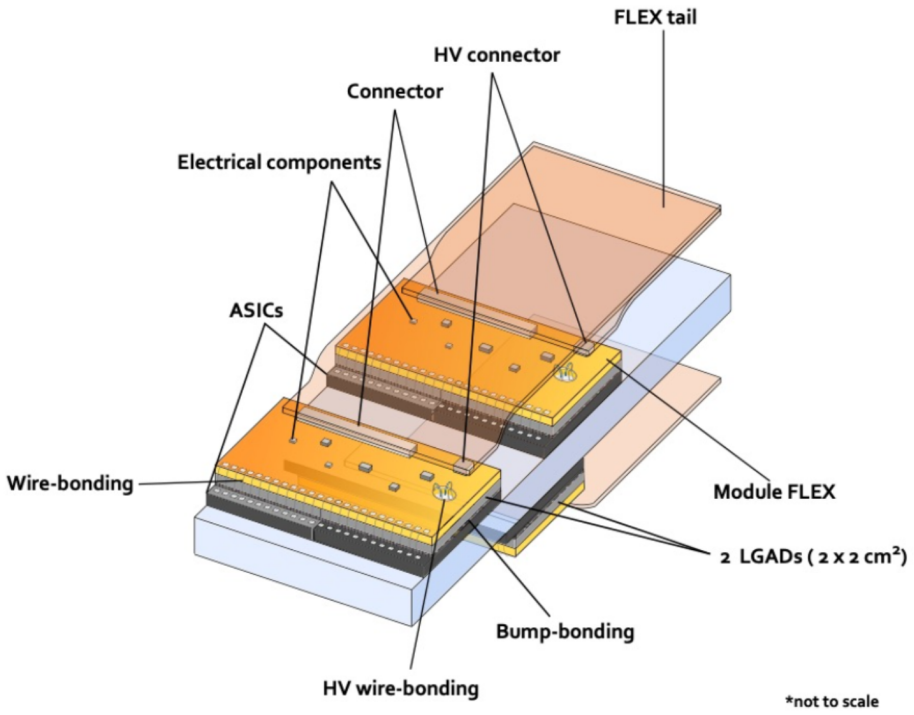


Figure 3.7: *Components, placement and connection of three HGTD modules mounted on a cooling plate (lightblue). The wire-bonds for both ASIC and sensor bias voltage (HV) are indicated. The flex tails are sketched as well. Taken from [57].*

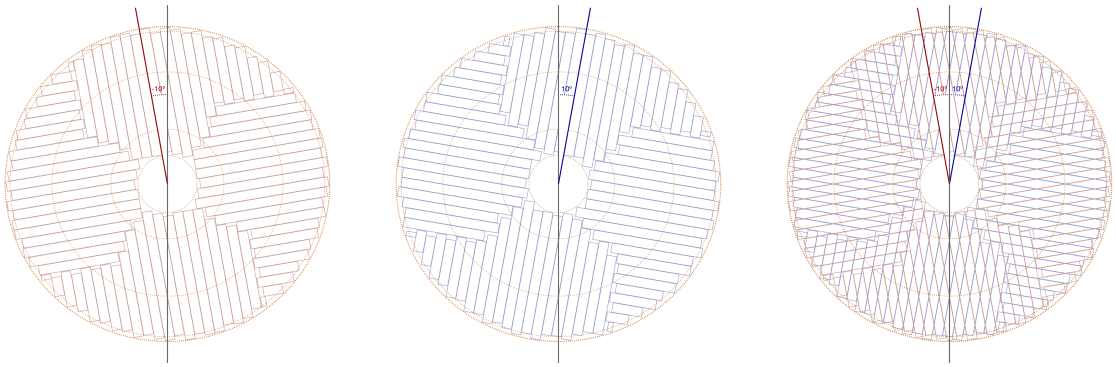
3.3.1.4 Detector layout and optimisation

The HGTD design includes 8032 modules that are placed in a way that maximizes the coverage and minimizes the non-instrumented regions. The overlap between modules on the front and back of the disk was optimised to enhance a uniformity of performance as a function of radius.

The data transmission from the HGTD modules is organized in rows. A row is the set of modules whose flex tails are guided together in line towards the PEBs. Due to the rectangular shape of a module, the coverage at innermost part of HGTD, at radius of 120 mm, is limited and gets complete only for r $>$ 150 mm. Figure 3.8 (a, b) shows the layout of the readout rows in two HGTD layers. The total effective width of one row is 42 mm.

The distance between the neighbouring modules is expected to be around 1.4 mm, leading to the dead areas of the detector. In order to maximize the amount of hits of a transversing particle in the detector, the two layers of HGTD are rotated in opposite directions by 20° creating an overlap (see Figure 3.8, c). While optimizing

the coverage, this rotation angle also takes into account the needed space for the Peripheral Electronic Boards (PEB), connectors and flex stack up as well as cooling manifolds access space [20].



a) b) c)

Figure 3.8: *The orientation of the readout rows for the first (a), second (b) layer and overlay between them (c). Each layer is rotated in alternating directions by 20°. The three circles represent the three regions of overlap between the modules of one layer. Taken from [20].*

As was mentioned before, the modules with sensors and ASICs are mounted on both sides of an HGTD layer with an overlap. There are three overlap rings: for r > 470 mm, 230 mm < r < 470 mm and r < 230 mm an overlap is 20%, 54% and 70% respectively. Figure 3.9 shows an arrangment of modules on both sides of a disc. The maximal

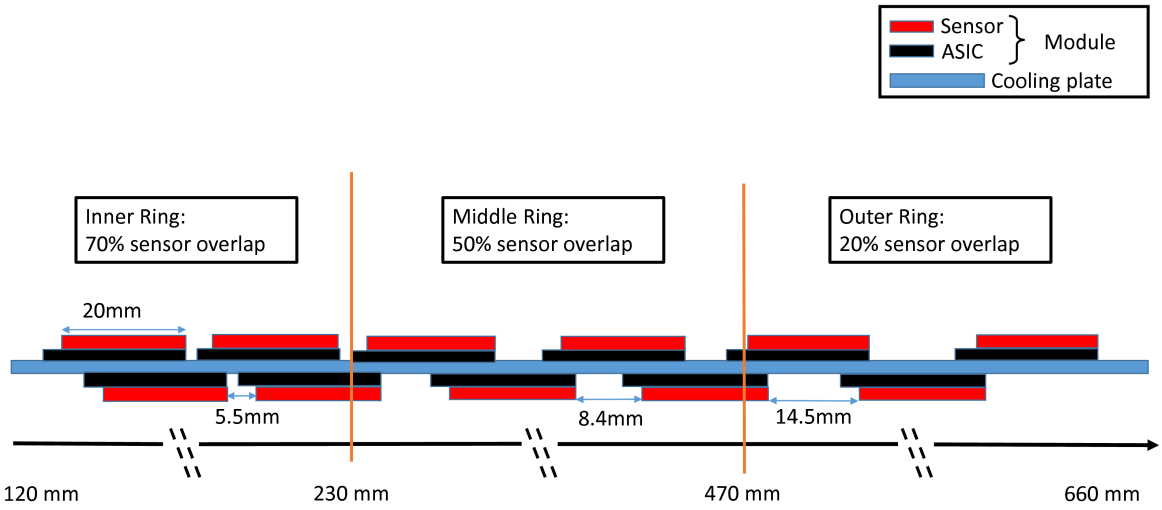
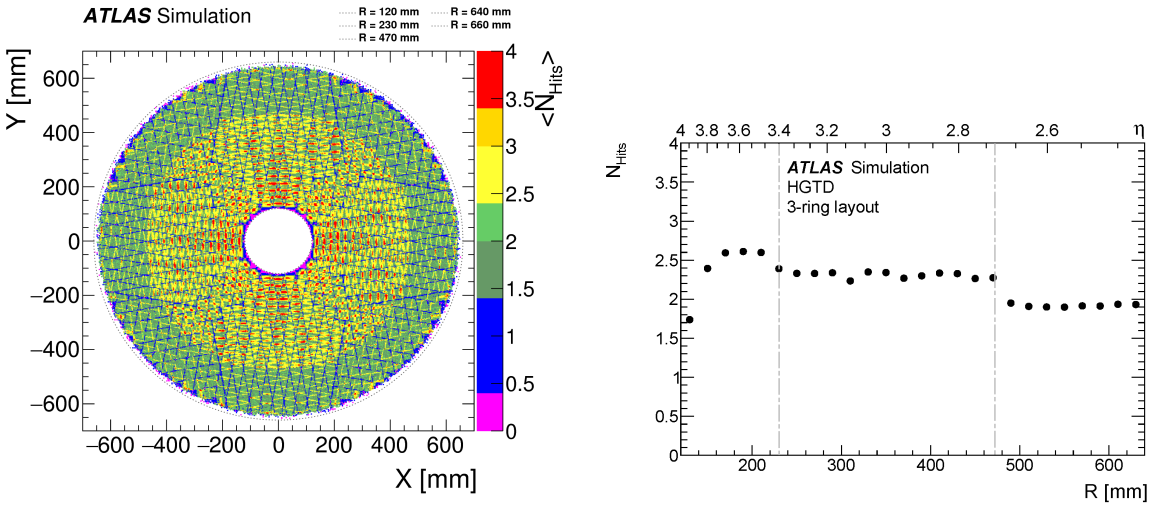


Figure 3.9: *Schematic drawing showing the overlap between the modules on the front and back of the cooling disk. Taken from [20].*

overlap is limited by the space constraints for the readout of the data. The expected number of hits per track as a function of radius and x-y plane position is shown in Figure 3.10. A study using full simulation was performed to determine the optimal

overlap between modules in three rings to achieve the required timing resolution via the average number of simulated hits given the expected time resolution of the sensor [20].



a) b)

Figure 3.10: *Average hit multiplicity as function of transverse plane (a) and radius (b). The figures were made using simplified simulations, resulting in an uncertainty of roughly 10 %. Taken from [20].*

3.3.2 Radiation environment

Due to radiation damage, the time resolution of the detector will be degrading with the increase of integrated luminosity delivered by the LHC. This radiation level is higher for the detector part closer to the beam axis which should be taken into account in the detector layout design. The HGTD geometry optimization addressed to the radiation damage is discussed in this section.

3.3.2.1 Radiation damage effects in the silicon detectors

The radiation damage strongly influences the performance of the silicon detectors. The three main effects affecting the reversely biased silicon sensors are the following.

- **Change of bulk doping concentration**. The irradiation causes the change of the doping concentration of the sensor bulk. The impurity atoms may lose their function as acceptor or donor, becoming electrically inactive. Furthermore, this can lead to the inversion of the material type, when an n-type material may change into a p-type and the other way round after prolonged irradiation. The effective doping of unirradiated p-type sensor is calculated as the difference of acceptor and donor dopants concentration. For the irradiated sensors, the formula is extended with the terms that include the accumulated fluence [58].

- **Trapping** The radiation-induced lattice defects make traps, which capture charge and liberate it very slowly. The trapped charges can function as recombination centers, reducing detector efficiency [59].
- **Leakage current** The bulk damage induced by radiation creates new energy levels in silicon. This increases the likelihood of thermal excitations of electrons to the conductive band, leading to an increase in leakage current. However, it is possible to compensate for this effect by lowering the operating temperature. The leakage current is proportional to the fluence and to the depleted width [59].

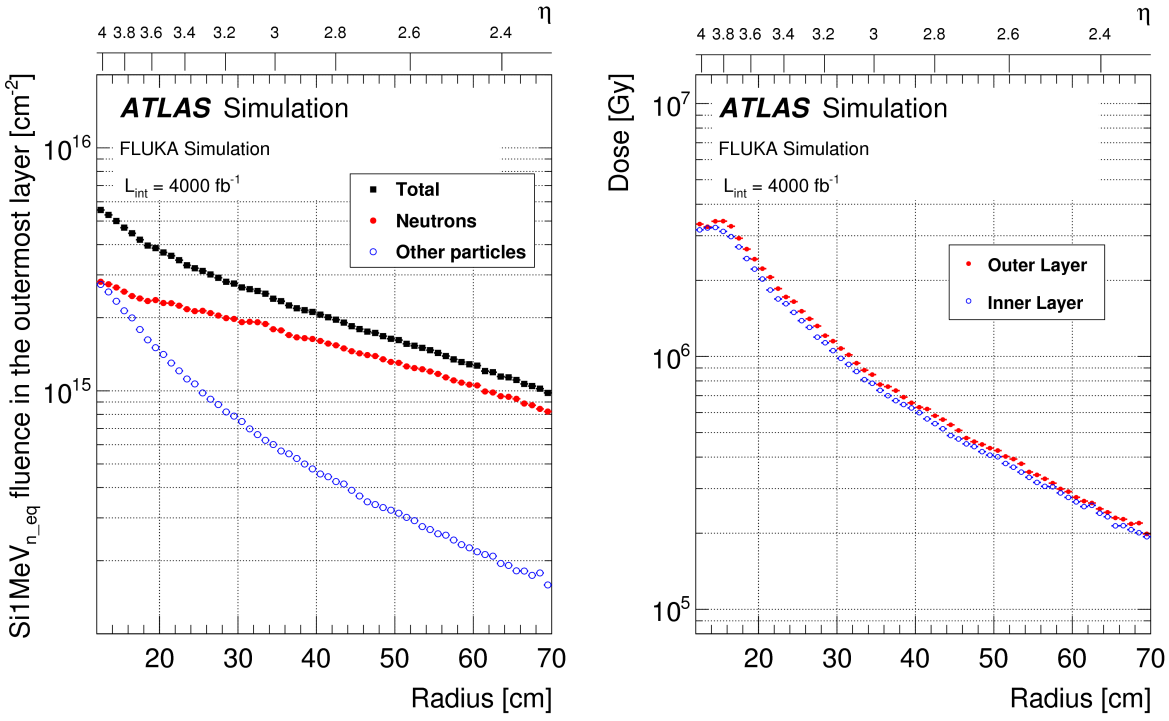
Bulk defects resulting from radiation act as acceptors and attract charges, which can negatively impact device performance. However, over time and with varying temperature, these defects can undergo reconfiguration, break-up, recombination, and diffusion within the bulk. The evolution of defect concentration with temperature and time is called annealing [60].

3.3.2.2 Radiation hardness of HGTD

Due to the location of HGTD and since the detector should withstand radiation levels throughout the whole HL-LHC operation, it is essential to design radiation hard sensors and electronics. At a radius of 120 mm, the neutron-equivalent fluence is expected to reach $5.6 \times 10^{15}\,\mathrm{n_{eq}\ cm^{-2}}$ and the Total Ionising Dose (TID) about 3.3 MGy (see Figure 3.11). Given the fact that the sensors are most sensitive to the particle fluence, a safety factor of 1.5 is aplied to it due to the simulation uncertainties. The electronics, for which also the low-doses-rate radiation effects should be accounted, are more sensitive to the TID. This leads to the total safety factor of 2.25 for TID. After applying these, HGTD would need to cope with $8.3 \times 10^{15}\,\mathrm{n_{eq}\ cm^{-2}}$ and 7.5 MGy.

The HGTD layout design considers a replacement scenario during the HL-LHC to sustain the radiation loads and keep a sufficient performance.

The extensive LGAD and ALTIROC studies showed, that the required minimum charge collection of 4 fC can be achieved up to a radiation damage of $2.5 \times 10^{15}\,\mathrm{n_{eq}\ cm^{-2}}$ and 2 MGy. Therefore, the modules from the inner ring ($r < 230$ mm) and from the middle ring ($230\,\mathrm{mm} < r < 470\,\mathrm{mm}$) will be replaced after each accumulated 1000 $\mathrm{fb^{-1}}$ and 2000 $\mathrm{fb^{-1}}$, i.e. half of the data-taking, respectively. Overall about 52% of the modules will need to be replaced during the HL-LHC operation. In Figure 3.12, one can see the expected maximum fluence (a) and TID (b) as a function of the radius including the replacement of the rings and safety factors. The total fluence in the inner ring has a similar contribution from neutrons and charged particles while in the middle and outer rings the radiation damage comes from neutrons. The FLUKA [61] simulation (from 2019) showed that the fluence and TID limits ($2.5 \times 10^{15}\,\mathrm{n_{eq}\ cm^{-2}}$ and 2 MGy) are not exceeded in all the HGTD rings [20].



a) b)

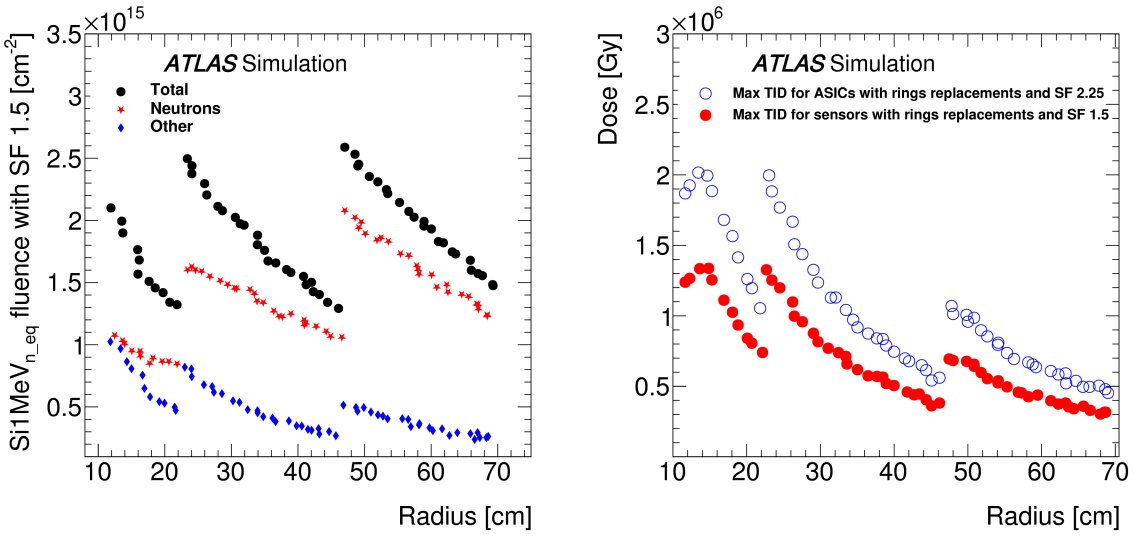
Figure 3.11: *Expected nominal 1MeV n_{eq} fluence (a) and TID (b) as functions of the radius for 4000 fb^{-1} in HGTD, i.e. before including safety factors. The contribution from charged hadrons is included in 'Other particles'. These estimations used Fluka [61] simulations with ATLAS Fluka geometry 3.1Q7 (from December 2019). Taken from [20].*

Figure 3.13 shows the simulation of the time resolution per hit (a) and per track (b) as a function of the radius for several integrated luminosities, taking into account the rings replacements described above. According to the simulation, the time resolution per hit throughout the whole HGTD will not go beyond the project limit of 70 ps even at the highest integrated luminosity of 4000 fb^{-1}. The HGTD layout design will manage to successfully cope with radiation loads and preserve the required performance.

The exact radial transition between the three rings will be tuned for the final detector layout, once the FLUKA [61] simulations will be updated with the final ITk layout, and the radiation hardness of the final sensors and ASICs are re-evaluated [20].

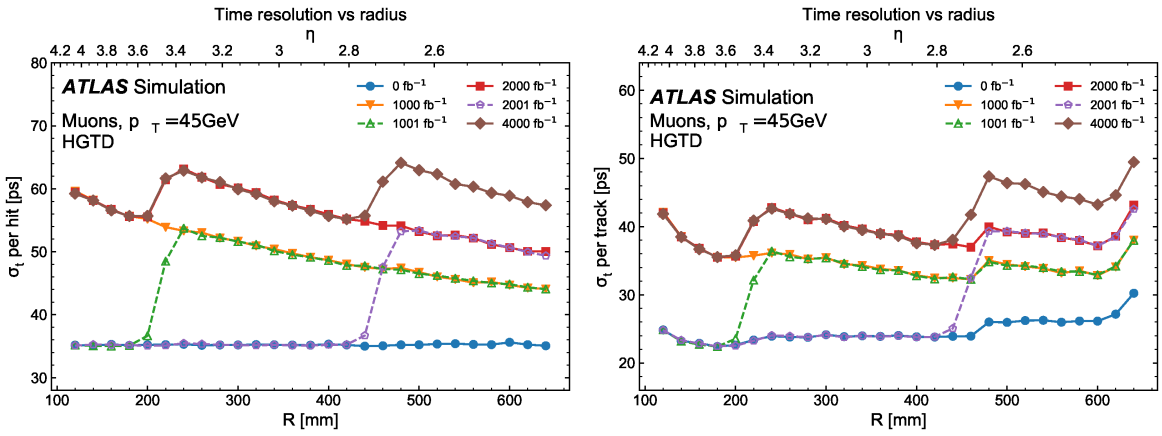
3.4 LGAD sensors

Semiconductor detectors are devices used in experimental physics to detect and measure the energy, position and timing of charged particles. The basic operation principle can be explained as follows: a charged particle passing through the detector deposits



a) b)

Figure 3.12: *Expected 1MeV n_{eq} fluence (a) and TID (b) in HGTD, using Fluka simulations [61], as a function of the radius considering a replacement of the inner ring every 1000 fb^{-1} and the middle ring replaced at 2000 fb^{-1}. For the radiation levels, the particle type is included and the contribution from charged hadrons is included in "Others". These curves included a safety factor (SF) of 1.5 to account for simulation uncertainty. An additional safety factor of 1.5 is applied to the TID to account for low dose-rate effects on the electronics, leading to a safety factor of 2.25. Taken from [20].*



a) b)

Figure 3.13: *Time resolution per hit (a) and per track (b) within HGTD acceptance as a function of the radius. The time resolution is shown for various integrated luminosities (different colors). The time resolution is improved at higher luminosities corresponding to the replacements of inner-most rings during the lifetime of the detector. Taken from [20].*

the energy by ionizing the sensitive material (i.e. creating the free charges: electrons and holes). Under the p-n junction built-in potential the free charge carriers drift to the electrodes, where the induced potential is measured. More information on the semiconductor detectors can be found in Appendix A.1.

3.4.1 LGAD Technology

One of the most promising technologies for the timing applications are the semiconductor sensors called LGAD. LGAD sensors are similar to standard silicon diodes, but are designed to operate at high voltages, which allows for generated electrons and holes to gain enough energy to initiate an avalanche mechanism (or multiplication). Initially, the LGADs were intended for use as radiation-hard tracking detectors. The idea was to benefit from the fact that they already exhibit charge multiplication in their unirradiated state, which can offset the signal degradation caused by radiation damage. However, it appeared to be advantageous also for the timing applications, since the detectors with intrinsic gain enhance the slew rate (rising edge), leading to the improvement of the time resolution. In recent years, thin LGAD devices have been developed specifically for good timing performance, as the detector thickness impacts timing performance.

Figure 3.14 shows the layout of a single pad of the LGAD diode. The LGAD structure is based on the standard PIN diode architecture with an n+ layer as the cathode and a p+ layer as the anode. High bias voltage is applied on the anode and charge is collected at the n+ cathode. The p substrate is the active volume where the electron-hole pairs drift. Right under the n+ layer, a special gain layer, i.e. multiplication layer, composed of acceptor-doped (p+) silicon delivers a low gain factor (10 - 20). The gain layer is a key component of the LGAD, which is optimized to provide a sufficient gain at moderate voltages. This optimization allows the active thickness of the LGAD to be depleted, enabling high drift velocities of charge carriers. For this layer, usually boron is used as doping. The electric field profile is divided into two regions: a drift volume with low electric field values (around 30 V/μm) and a few micrometers deep multiplication zone with a very high electric field (around 300 V/μm). A Junction Termination Extension (JTE) made by an n+ dopant is added at the perimeter of the cathode to shape the electric field at the electrode's edge and to protect the sensor from an early breakdown.

The better timing resolution of the LGAD requires a large signal height and a fast rise time. These two factors can be expressed by the slew rate, i.e. $\frac{dV}{dt}$. The slew rate is proportional to the gain: the more charge is generated and collected, the higher the signal amplitude is. On the other hand, the slew rate is also inversely proportional to the thickness of the sensor: the thinner the sensor is, the shorter the drift time of the charge to the electrode is. Moreover, the thinner sensors minimize

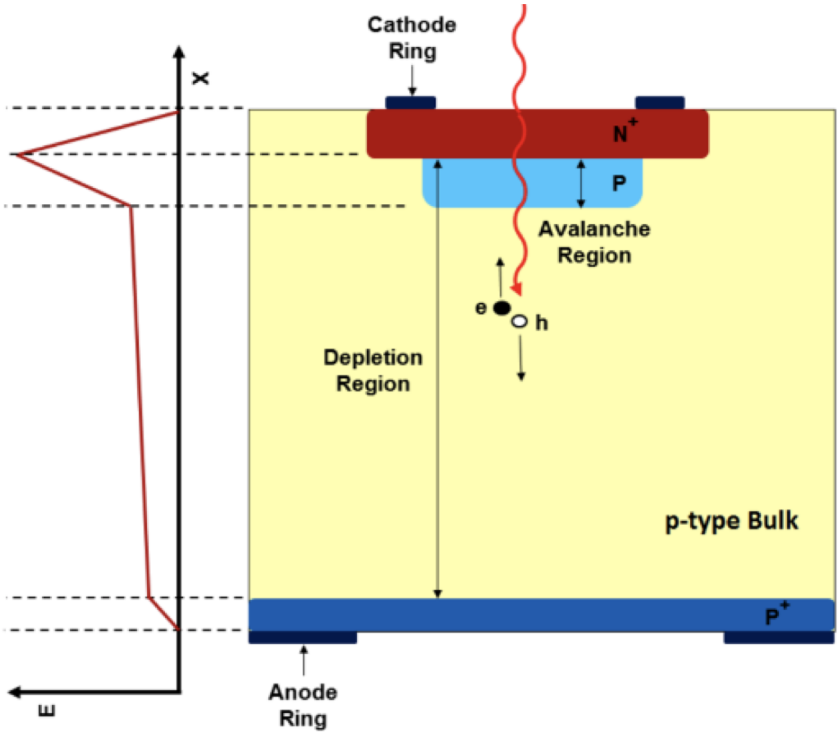


Figure 3.14: *Schematic view of a single pad LGAD diode. On the left hand of the figure, the electric field profile inside the sensor is shown. Taken from [20].*

the Landau fluctuations (non-uniformity of the charge deposition), and therefore the Landau term in Equation 3.3. Overall, thin detectors with higher gain provide the best time resolution. Figure 3.15 shows the contributions of the primary and gain electrons/holes to the total pulse (a) and the time of the pulse for different sensor thicknesses (b).

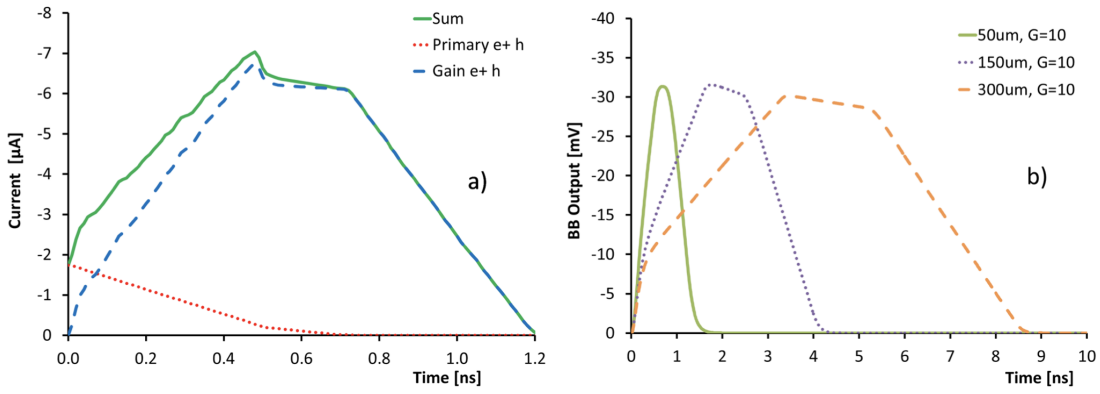


Figure 3.15: *Pulse shapes of LGAD simulated with WeightdField 2 version 3.5. (a): detector current for a MIP traversing a 50 μm thick LGAD; (b): voltage output from a x100 broad-band amplifier (BB) with 50 Ω input for LGADs with gain of 10 and thickness 50, 150, 300 μm. Taken from [62].*

To be noted, that the LGAD has a much lower gain than other timing detectors such as Avalanche Photodiode (50-500) or Silicon Photo-Multipliers (10^4), that is why the name holds "low" gain. However, high gain levels can bring drawbacks such as the increase of the sensor noise, difficulties in the sensor segmentation and high power consumption [63].

For HGTD, the LGAD sensors with an active thickness of 50 μm and gain of 20 has been chosen as a baseline. This thickness gives the best compromise between on one hand capacitance and deposited charge, both favouring thicker sensors, and on the other hand signal slope and Landau fluctuation, both favouring thinner sensors. As mentioned before, the LGAD for HGTD is expected to collect a charge of minimum 4 fC and have a timing resolution not worse than 35 ps per hit at the beginning of the HGTD operation and 70 ps at the end of detector lifetime. Over the last years, LGAD sensors have been produced by CNM (Spain), HPK (Japan), FBK(Italy), NDL (China), and IME (China) with different doping level, active thickness, pad size, and inter-pad gaps. The R&D of the sensors for HGTD is still ongoing.

3.4.2 Single Event Burnout

At the end of HGTD's lifetime, the LGAD sensors are expected to obtain a neutron equivalent fluence of approximately $2.5 \times 10^{15}\,\mathrm{n_{eq}}\ \mathrm{cm}^{-2}$. In order to operate 50 μm sensors in these conditions and get the required performance, a bias voltage of at least 700 V at -30 C° is required. Indeed, laboratory performance tests using a strontium-90 electron source have demonstrated that sensors can gather sufficient charge and achieve the desired time resolution when operated for extended periods in such conditions.

In 2018-2020 HGTD beam test campaigns at CERN-SPS using 120 GeV pions and DESY using 5 GeV electrons attempted to replicate the laboratory measurements. For most of the sensors, achieving the necessary operating bias voltage was failing. These sensors suffered from destructive breakdown at bias voltages approximately 100 V lower than those used in successful laboratory tests. In the affected sensors, the penetrating particle was leaving a distinctive star shaped burn mark, see Figure 3.16.

In 2021, I participated in the several test beams at DESY and SPS to study the mortality of different LGADs and to define the bias voltage range for safe detector operation. It had been concluded that in all the breakdown cases, a single beam particle hitting the detector was responsible for sensor destruction. It was possible to associate the signals from such breakdown events and the locations of the craters with the hit position reconstructed by the beam telescope, as shown in Fig. 3.17.

The observed sensor mortalities are most likely caused by a phenomenon known as Single Event Burnout (SEB). While laboratory tests use the lower energy electrons from a strontium-90 source, i.e. maximum 2.3 MeV, highly energetic beam particles

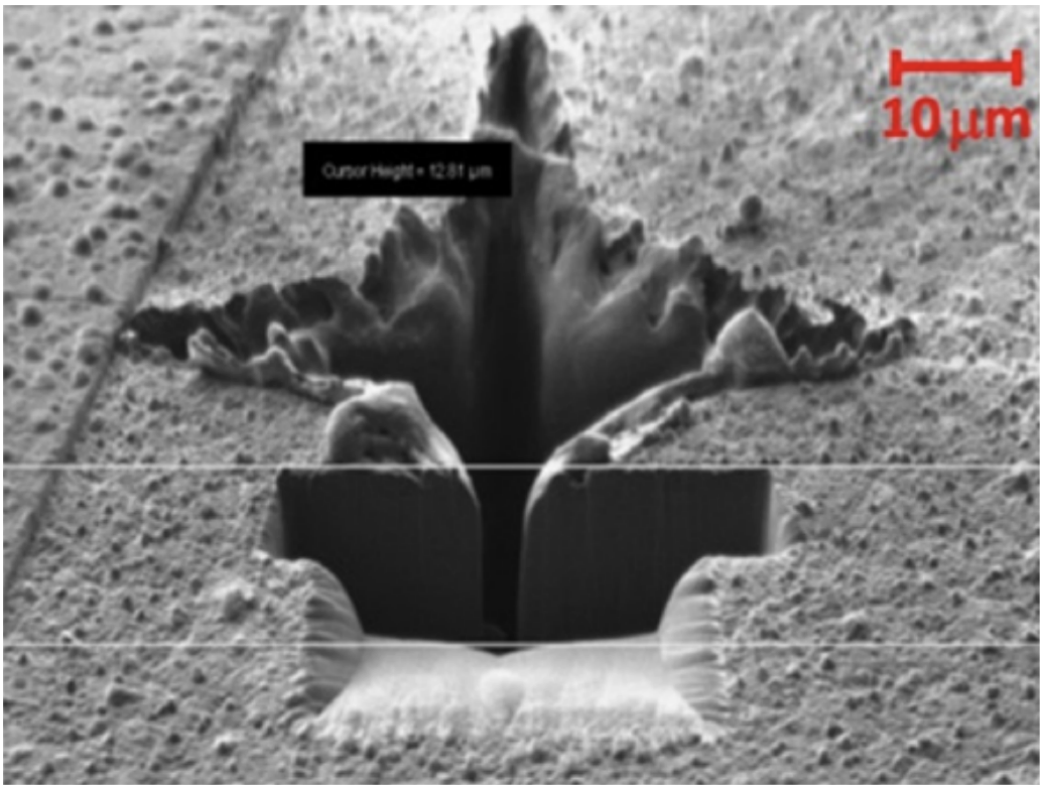


Figure 3.16: *Microscopic photo of a typical burn mark, observed in ATLAS proton beam tests in 2018. Taken from [64].*

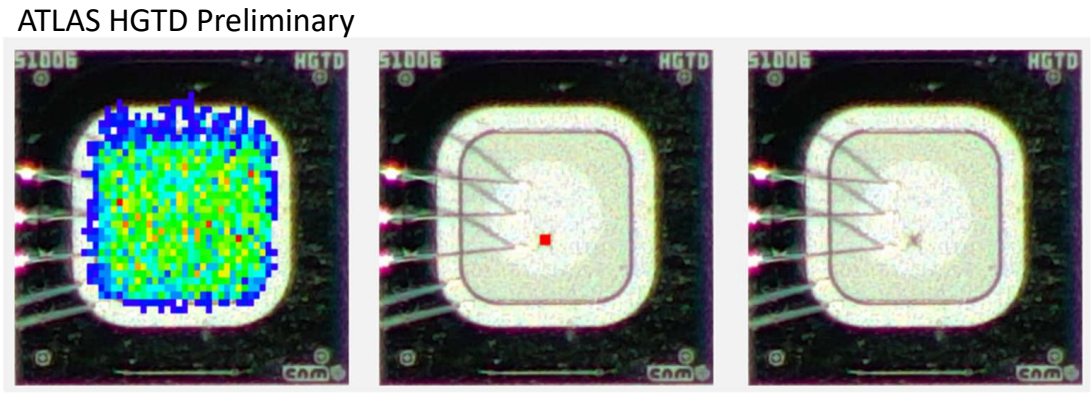


Figure 3.17: *Left: All the reconstructed tracks distribution across the detector before Single Event Burnout occurs. Middle and Right: The reconstructed track in the Single Event Burnout event pointed to the location of the burn mark. Taken from [64].*

in the active zone of the LGAD detector can deposit much larger amounts of charge. Geant4 [39] simulations show that a single charged hadron can deposit up to 100 MeV, creating a high density of carriers that can cause a screening effect, preventing them from being swept away. This leads to a change in the resistivity in that part of the sensor, making it conductive and causing the field to collapse in the area of high free

carrier density. This collapse results in an increase in voltage drop in the lower-density region, leading to avalanche breakdown when the field exceeds the critical level. As a result, the charge stored on the sensor electrodes and the high voltage filtering capacitor (typically 10 nF) is discharged through the sensor, generating enough energy to melt the silicon and create a crater that damages the sensor. Although the breakdown is eventually quenched, the sensor is permanently damaged.

The key parameter to avoid the SEB was found to be the electric field, or ratio between the applied bias voltage and the thickness of the sensor. In the mentioned 2021 test beams, 74 sensors were studied. It was concluded, that by keeping the electric field lower than 11 V/μm, one can avoid the SEB process, as shown in Figure 3.18. It was also noted, that the sensors with carbon infused gain layer were able to deliver the required performance and sustain the radiation. In order to operate the sensor at a safe bias voltage and to meet the project requirements, the latest LGAD designs implements the carbon enriched gain layer. Carbon infusion helps to achieve a good sensor performance at lower bias voltages, mitigating the risk of SEB occurrence.

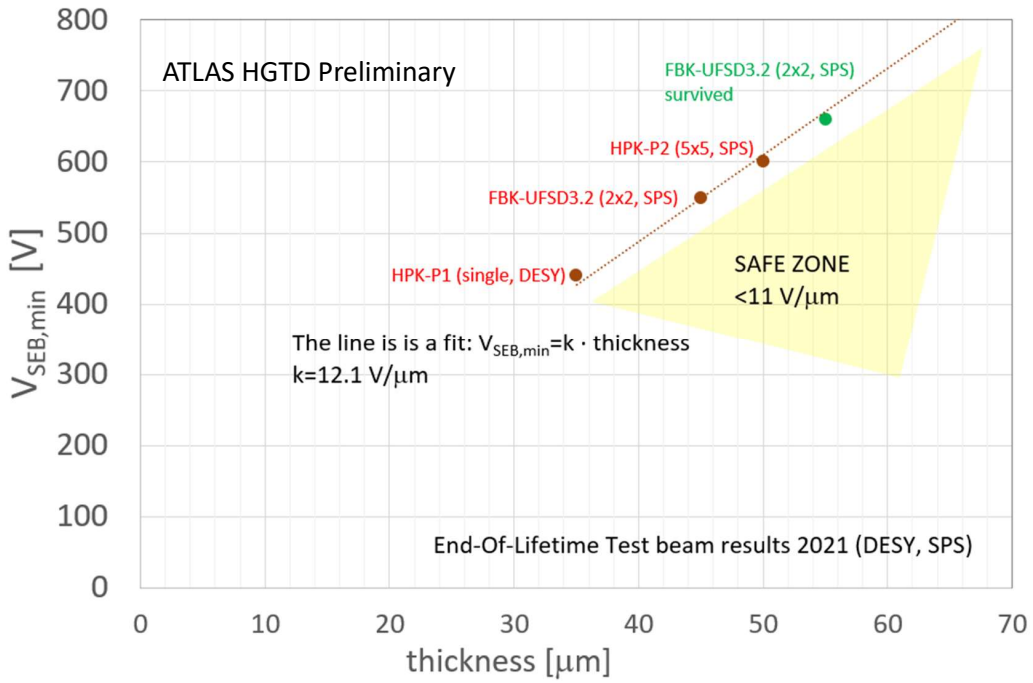


Figure 3.18: *Single Event Burnout voltage dependence on sensor thickness. The minimum voltage at which SEB was observed after several* 10^6 *particles/pad for each thickness in 2021 HGTD end-of-life test beams is shown (manufacturer-run, type, test-beam). Overall 74 sensors (single-pad, 2×2, 5×5 arrays) were tested. The sensor indicated in green survived the voltage point. The dashed line represents the critical average electric field of 12.1 V/mm where SEB occurs. The safe zone of 11 V/mm where no SEB was ever observed is indicated in yellow.*

3.5 Front-End electronics

The performance of LGAD sensor is strongly correlated with the performance of the read-out ASIC ALTIROC. ALTIROC matrix consists of 15×15 channels and it is designed using the 130 nm TSMC technology [65].

3.5.1 Single channel readout

The analog Front End electronics of each channel plays a crucial role in achieving low jitter (improtant for timing resolution, see Section 3.5.3). A conceptual schematic for the single-channel readout is presented in Figure 3.19. To amplify the sensor signal, a

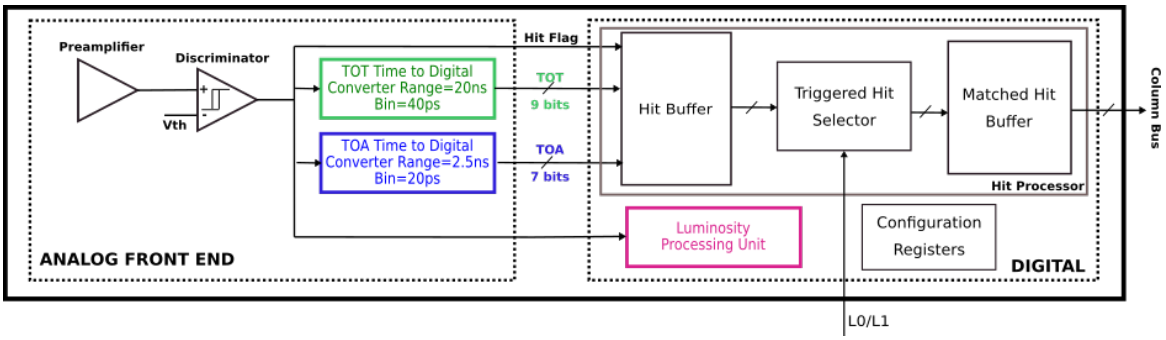


Figure 3.19: *Schematic of the single-channel readout electronics. Two main blocks are identified, the analog and the digital part. The input pulse from the sensor enters the preamplifier on the left. The TOA and TOT data are read out by the column bus on the right. Taken from [20].*

voltage preamplifier is utilized with a bandwidth of approximately 1 GHz, which is sufficient for the duration of the LGAD signal (around 1 ns). Two Time-to-Digital Converters (TDCs) digitize the Time of Arrival (TOA) and Time Over Threshold (TOT) measurements, which are then stored in a local memory at channel level. A sketch with the pulse including TOA and TOT is shown in Figure 3.20 (b). The preamplifier is followed by a fast discriminator, where the leading edge of the output (TOA) triggers the start of a Time to Digital Converter (TDC). The stop is given by the clock. The start-stop structure, minimizes power dissipation when there are no hits present [65]. The bin width of the TDC for TOA is 20 ps, which does not contribute significantly to the expected time resolution. TOA measurements are limited to a 2.5 ns window centered on the bunch crossing. Taking into account the time dispersion of the hits (with an r.m.s of 300 ps), the 2.5 ns time window contains all collisions' hits if centered with about 100 ps accuracy using a phase shifter. The falling edge of the discriminator output provides the stop of a second TDC (which uses the leading edge as the start signal as well) with a 40 ps bin width to measure the TOT, an estimate of the signal amplitude. TOT information is used offline to correct the TOA for the time walk effect described in Section 3.5.3. The digital front end stores the time data until

the reception of a trigger and buffers the data to be read by the end-of-column cells. This buffer is necessary to handle event-to-event fluctuations in the number of hits and random trigger arrivals [20], i.e. it acts as a derandomising buffer.

3.5.2 General ASIC requirements

The ALTIROC requirements include the operational environment of the ASIC, its powering and electrical connections, and the performance. All these are listed in the Table 3.2.

Pad size	1.3×1.3 mm^2
Voltage	1.2 V
Power dissipation per area (per ASIC)	300 mWcm^{-2} (Total: 1.2 W)
e-link driver bandwidth	320 Mbit s^{-1}, 640 Mbit s^{-1}, or 1.28 Gbit s^{-1}
Temperature range	-40 °C to 40 °C
TID tolerance	2.0 MGy
Full Chip SEU Upset probability	$< 5\%$/hour
Maximum leakage current	5 µA
Single pad noise (ENC)	$< 3000\ e^- = 0.5$ fC
Cross-talk	$< 5\%$
Threshold dispersion after tuning	$< 10\%$
Maximum jitter	25 ps at 10 fC
	70 ps at 4 fC
TDC contribution	< 10 ps
Time walk contribution	< 10 ps
Minimum threshold	2 fC
Dynamic range	4 fC–50 fC
TDC conversion time	< 25 ns
Trigger rate	1 MHz L0 or 0.8 MHz L1
Trigger latency	10 µs L0 or 35 µs L1
Clock phase adjustment	100 ps

Table 3.2: *Performance requirements for the HGTD ASIC. The values given for the noise, minimum threshold, and jitter have been specified considering a detector capacitance $C_d = 4$ pF. Taken from [20]*

The ALTIROC will have to withstand high radiation levels (Section 3.3.2.2) and it is mainly sensitive to the TID (or ionizing radiation). Each ALTIROC readout channel needs to fit within the sensor pad (1.3×1.3 mm^2). To ensure the ASIC's optimal performance, each readout channel is connected to a sensor pad that can handle up to 5 μA of leakage current. However, irradiation can cause degradation in sensor performance, so a discriminator threshold can be configured for small input charges. A minimum threshold of 2 fC should provide a hit efficiency of over 95% for an input

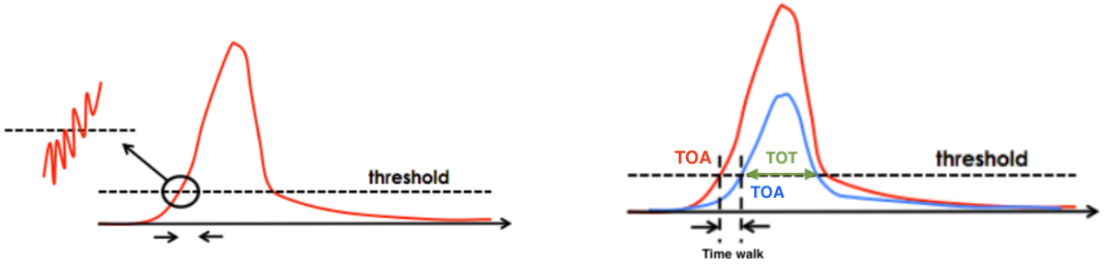
charge of 4 fC. The electronics must read out signals from 4 fC to 50 fC throughout the HGTD lifetime, and the electronics jitter must be less than 25 ps for a charge of 10 fC, i.e.smaller than the dispersion induced by the Landau fluctuations on the deposited energy. This charge is equal to the deposited charge of a MIP in a 50 μm-thick LGAD with a gain of 20. The contribution to the time resolution from the TDC should be negligible and leads to a 20 ps TDC bin for the TOA measurement and a 40 ps TDC bin for the TOT measurement. The time walk must be less than 10 ps over the range after correction. Both TOA and TOT information is transferred to the data acquisition system only upon L0/L1 trigger reception, which has a latency of up to 35 μs and requires a large memory. The clock's global phase adjustment must have a precision of 100 ps to center the 2.5 ns measuring window at the bunch-crossing. ALTIROC must also compute the number of hits on a bunch-by-bunch basis for luminosity measurement in the range of $2.4 < |\eta| < 3.5$. Finally, minimizing power dissipation is crucial to limit the size of the cooling system required [20].

3.5.3 Contribution to the time resolution

The ALTIROC time resolution contribution (term σ^2_{elec} in Equation 3.3) depends on three components:

$$\sigma^2_{\text{elec}} = \sigma^2_{\text{jitter}} + \sigma^2_{\text{time walk}} + \sigma^2_{\text{TDC}}. \tag{3.4}$$

The jitter term comes from the electronic noise (see Figure 3.20 (a)) and should be smaller than 25 ps. The time walk effect originates from the readout signal amplitude variations. Since the TOA is defined when the pulse crosses a constant threshold, the larger signals cross this threshold earlier than smaller ones resulting in the smaller TOA (see Figure 3.20 (b)).



a) b)

Figure 3.20: *Jitter (a) and time walk (b) effects in the time measurement with a fixed threshold including TOA (red and blue) and TOT (green). Taken from [66].*

The two contributions can be described as:

$$\sigma_{\text{jitter}} = \frac{N}{dV/dt} \approx \frac{t_{rise}}{(S/N)}, \tag{3.5}$$

$$\sigma_{\text{time walk}} = [\frac{V_{th}}{S/t_{rise}}]. \tag{3.6}$$

where S refers to the signal amplitude which is proportional to the gain, V_{th} is the threshold voltage, N is the noise and t_{rise} is the rise time. The high signal-to-noise ratio (S/N) and small rise time minimize the noise jitter and time walk, advocating for thin sensors with higher gain. Time walk can usually be corrected using time reconstruction algorithms such as Constant Fraction Discrimination (for details, see Section 5.2.1), or amplitude or TOT corrections [65]. For HGTD, the baseline time walk correction method is a Constant Threshold Discriminator. It is done by measuring the time of the pulse above the threshold level, TOT, which is correlated with the pulse amplitude. An example of such correction is presented in Figure 3.21 including the fit between the TOA and TOT correlation. This method brings the time walk residual error to less than 10 ps and is considered negligible.

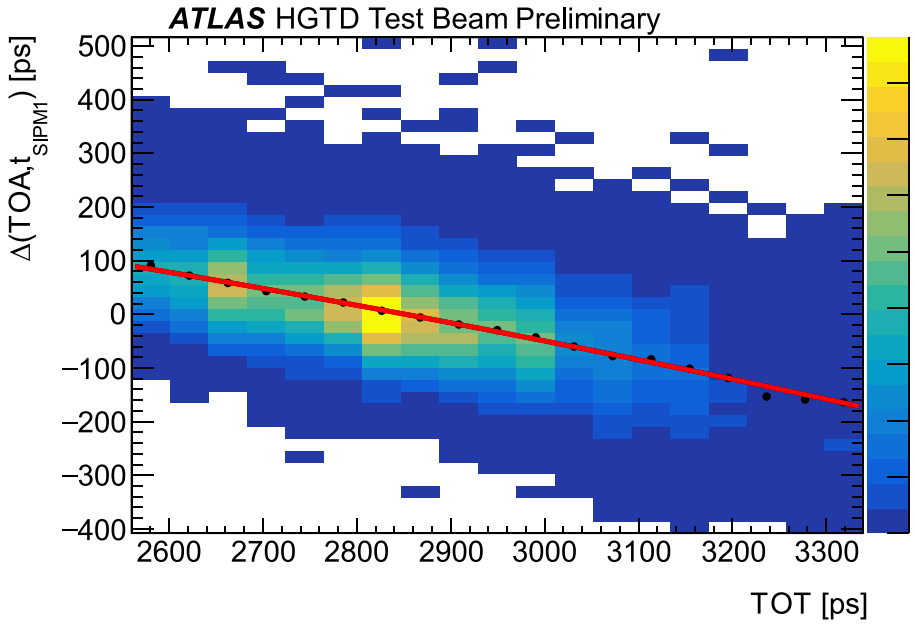


Figure 3.21: *Time walk effect illustration from the correlation between the TOA and TOT of a tested ALTIROC. The black dots display the mean value of the TOA distribution and the red line is a polynomial fit to these points used to perform the time walk correction. Taken from [67].*

For the test beams discussed in Chapter 5, the Constant Fraction Discrimination reconstruction was used, where the TOA is defined as the time when the signal crosses a constant fraction of its maximum amplitude. However, this method cannot be realistically implemented in a readout circuit, due to the fact that the maximum value is reached after the threshold has been already crossed.

The last term, TDC, represents the contribution from the binning of the TDC circuit, since the time information is converted to digital values. It depends on the time bin width of TDC. HGTD will provide around 20 ps and 40 ps fine binning for TOA and TOT, respectively, leading to a negligable uncertainty.

3.6 Conclusion

In the HL-LHC (for more details see Section 2.5), with the increasing average number of interactions per bunch crossing from 30 to about 200, the pile-up rates will also drastically increase. Such conditions make it very challenging to associate particles tracks to the correct primary vertex, which is important to study the physics processes. As was mentioned in the previous chapter, tracking reconstruction capabilities of ATLAS are worse for the tracks in the forward region than in the central detector acceptance. This results in an increased residual pile-up contamination when assigning reconstructed objects to the reconstructed vertices [20]. To address this problem, HGTD is being designed to use the difference in the collision times within a single bunch-crossing. The new detector will be able to provide the precise time measurements for tracks in the forward region, with an average time resolution of 30 ps and 50 ps per track at the beginning and by the end of HL-LHC operation, respectively. As discussed in Section 3.1, HGTD will notably enhance the objects reconstruction capabilities of ATLAS detector. In addition, HGTD will provide the high precision luminosity measurements.

A comprehensive developement of this detector is ongoing and is presented in this chapter including the project requirements and the key design features. The following chapters will be dedicated to the HGTD R&D work in which LPNHE is involved and which is the scope of my PhD: the mechanical R&D (Chapter 4), the sensors performance studies in test beams (Chapter 5) and the software developement for HGTD (Chapter 6 and Chapter 7).

Chapter 4

Mechanical R&D for the HGTD

As discussed in Section 3.3.1, one instrumented disc of HGTD consists of a cooling plate with the sensitive modules on both sides of it. The HGTD modules, each consisting of two ASICs, two LGAD sensors, and a module flex, need to be mounted to the cooling plates in readout rows (see Section 3.3.1.4). This is done using the support units screwed to the cooling plate, on which the modules are glued. The extensive R&D is still ongoing in order to define the most sufficient geometry of the support units and a procedure of modules assembly onto them. The following chapter is dedicated to this R&D, in which the LPNHE is heavily involved. In addition, the realisation of the heater demonstrator as part of the mechanics R&D is discussed in Section 4.3.

4.1 Detector layout design

4.1.1 Modules placement

Overall, HGTD will be assembled with 8032 identical modules, 1004 modules per disc organised in readout rows as mentioned in Section 3.3.1. The longest rows have 19 modules. Each disc consists of four identical quarters that are different for the front and the back side of a disc. The current (May 2023) placement of the modules in one quarter is shown in Figure 4.1. The positioning of the modules is driven by the project requirement on the overlap between the two sides of one HGTD disc, which is 20%, 54% and 70% for the inner, the middle, and the outer ring, respectively. This overlap gives a good compromise between the coverage, that affects the overall detector efficiency, and the cost. The HGTD disc is thus sectorized in the three independant areas: inner ring (radius 120-230 mm), middle ring (radius 230-470 mm), and outer ring (radius 470-660 mm).

4.1.2 Support units design

To ensure mechanical stability, the groups of modules will be glued onto thin support units (SU), which will be screwed onto the cooling plate. A SU with the modules creates a detector unit (DU). In the current detector layout (May 2023), there are 24 DUs (or SUs) per disc quarter, as shown in Figure 4.2. The design was taking into account the fact that the inner and middle disks will be replaced after every 1000 fb^{-1} and 2000 fb^{-1} accumulated, respectively. The SUs are thus grouped into three groups according to the rings. There are three, eleven and ten SUs in the inner, middle, and outer rings of each quarter disc, respectively.

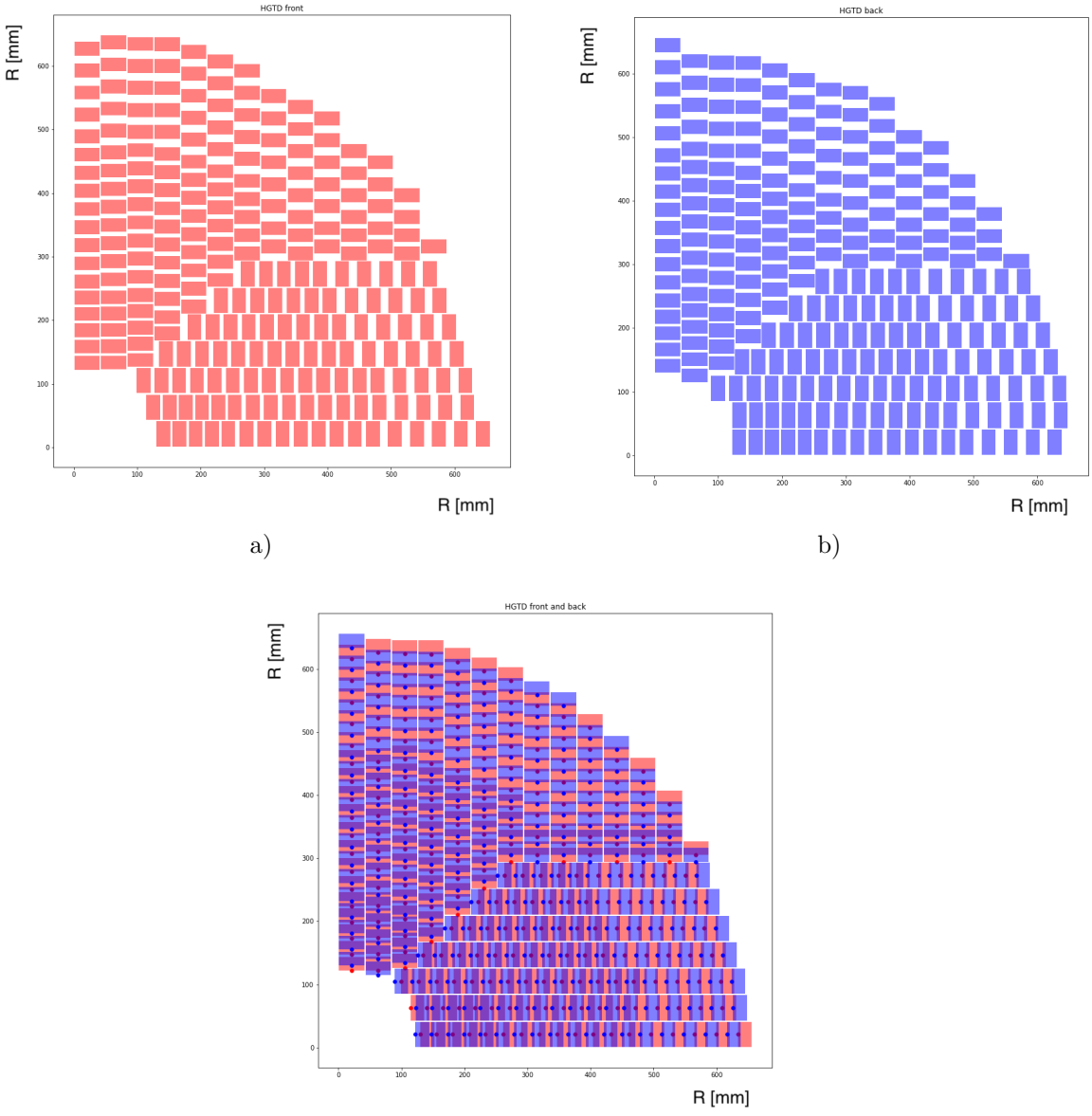
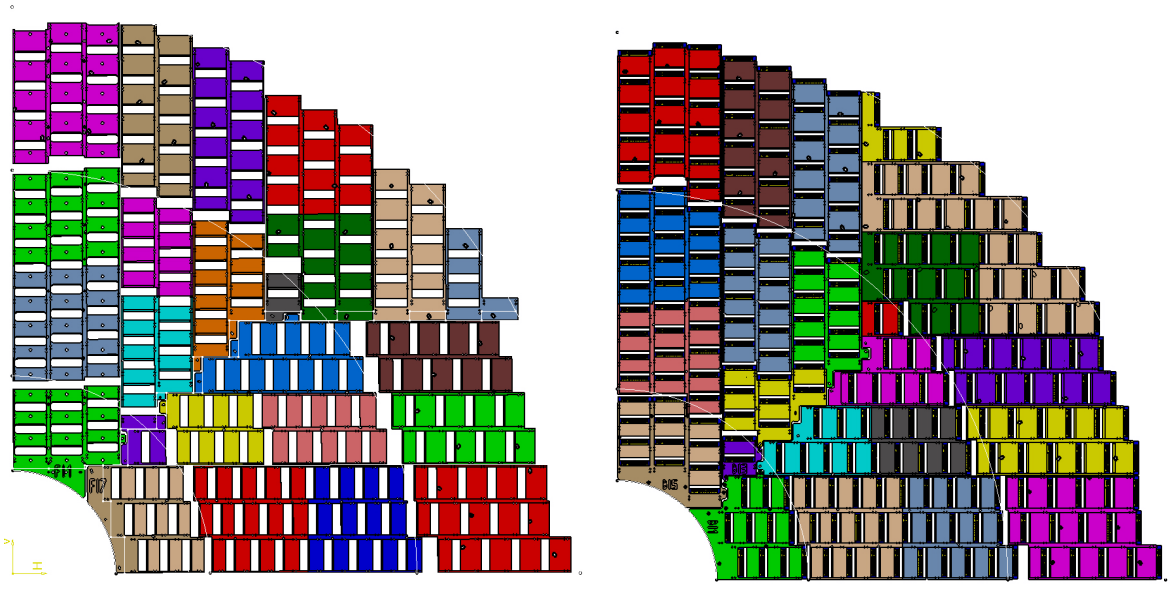


Figure 4.1: *Placement of the modules on the quarter of the front (a) and back (b) sides of the HGTD disc as well as their overlap (c).*

This design has been developing with time and underwent a lot of changes. For example, one of the previous solutions was to use 13 SUs per quarter disc with a maximum of 30 modules per SU (September 2022).The 24 SUs per quarter disc design has several advantages over the previous designs. First of all, the reparation of the smaller DUs is easier. For example, in case one of the modules needs to be replaced, the extraction of the module from a smaller SU is an easier and a safer option for several reasons. When a module is pushed out from an SU, it creates a shock and vibration across the SU, which may also push out other modules. Second, smaller SUs make it easier to control an adequate fabrication in terms of fragility and flatness. With the smaller SUs, also the gluing of the modules on each support goes much faster and easier (see Section 4.2). Another reason is that any unscrewing of the DU from the cooling plate brings a risk of damaging SU or modules. The less modules are involved, the lower the risk is. Additional advantage of the design with 24 DUs per quarter disc is the higher production rate of each SU. However, there are also the downsides for such a layout: more different and diverse supports may lead to more errors in production and more tools are needed for the DUs assembly (see Section 4.2).

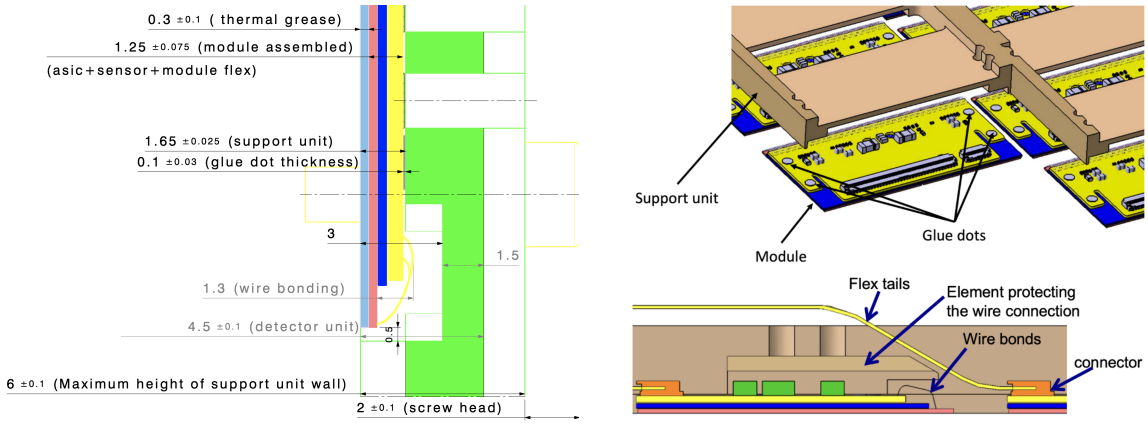


a) b)

Figure 4.2: *Placement of the 24 SUs on the quarter of the front side of the disc (a) and 24 DUs (SUs with modules) on the back sides (b). The different DUs (and SUs) are maked with different colors.*

As discussed in Section 3.3.1, the 1.25 mm thick, 40.4 mm wide and 2.6 g heavy HGTD module consists of two ASICs bump-bonded to two LGAD sensors and wire-bonded to the module flex. The thicknesses of each component of the DU are shown in Figure 4.3 (a). The module is glued with four 0.1 mm thick glue dots onto rectangular strip of SU. Currently, the baseline glue is ARALDITE 2011 [68] (also used for the sensor to flex attachment). The maximum thickness of SU is 6 mm and the current baseline

material is PEEK (Polyether Ether Ketone). PEEK was chosen due to the excellent radiation hardness, relatively easy machining, heat resistance, and a good experience of usage in other CERN experiments [69]. Figure 4.3 (b) presents the sketch of the module fit in the SU. The SU shape is made in a way, that protects the ASIC wire bonds, enables the connection of the flex tail with the module flex and allows to detach a module with the four holes on opposite sides of the SU (per module). The SU edges make contact with the cooling plate, and the height is greater than the thickness of the module. This arrangement ensures thermal contact without causing any damage due to compression. Before the modules are loaded onto the SUs, each unit will undergo inspection using a coordinate measuring machine. Once the DU is securely screwed to the cooling plate, the modules establish thermal contact with the plate. To enhance the thermal contact between the modules and the cooling plate, a thermally conductive material like thermal grease will be used.



a) b)

Figure 4.3: *(a): Cross section with thicknesses and tolerances of DU elements. (b): Sketch of the module with glue dots for the fixation to the SU including the side view of modules loaded on a SU. Taken from [70].*

The SUs have been designed and various prototypes have been manufactured in laboratory workshops or by companies. This allowed to establish the acceptance criteria for the production of the SUs. To optimize the balance between quality and cost, the mechanical manufacturing tolerance of ±0.025 mm for the height of the support in the gluing areas was chosen. When determining the amount of glue to be applied, one should consider the available surface area and the gap that needs to be filled between the module and the SU. If the thickness variations of the modules (including the substrates, bump-bonds, module flex, and glue) in the gluing areas fall within the range of ±0.075 mm, the height of the glue should accommodate a variation of ±0.150 mm to effectively fill the gap, while keeping the glue dot diameter of approximately 2 mm [70]. Additionally, it is necessary to take into account the flatness of the SUs. The tolerances on the dimensions of the SUs align with the

ISO 2768 standard [71]. Therefore, the variation in the flatness of the surfaces in contact with the cooling plate is ±0.200 mm. Considering these factors, the maximum total gap that the glue needs to cover is calculated as follows: 0.050 mm (minimum glue thickness) + 0.150 mm (variation of modules) + 0.200 mm (variation of SUs), resulting in a total of 0.400 mm. The thermal media between a module and a cooling plate has a thickness of 0.3 mm to absorb modules level variation, while the tolerance of this media is 0.1 mm.

To create sufficient space for the components of the module flex, the SUs will undergo machining. Currently, there is an anticipated minimum available space of 1.35 mm as depicted in Figure 4.3 (a). The wire bonding is expected to take 1.30 mm in thickness. If necessary, the design of the SU can be adjusted to allow for a nominal space of 2 mm with a tolerance of 30 μm.

The overall thickness of the DUs, once the modules are loaded, comprises the module envelope and the SU material on top of the module. In addition, there is the flex tail stack that contains up to 19 cables for the longest read-out rows. These components must fit within a total thickness of 9 mm [70], leaving 1 mm of free space for assembly. Considering the thickness of each flex tail to be 210±10 μm, the maximum thickness would be 8.2 mm, resulting in a clearance of 0.8 mm. Furthermore, the walls of the SUs and the screws used to attach them to the cooling plates have a combined thickness of 8 mm, with a tolerance of 0.2 mm. These components also need to fit within the same 9 mm envelope mentioned earlier, leaving a clearance of 0.8 mm.

4.2 Gluing procedure

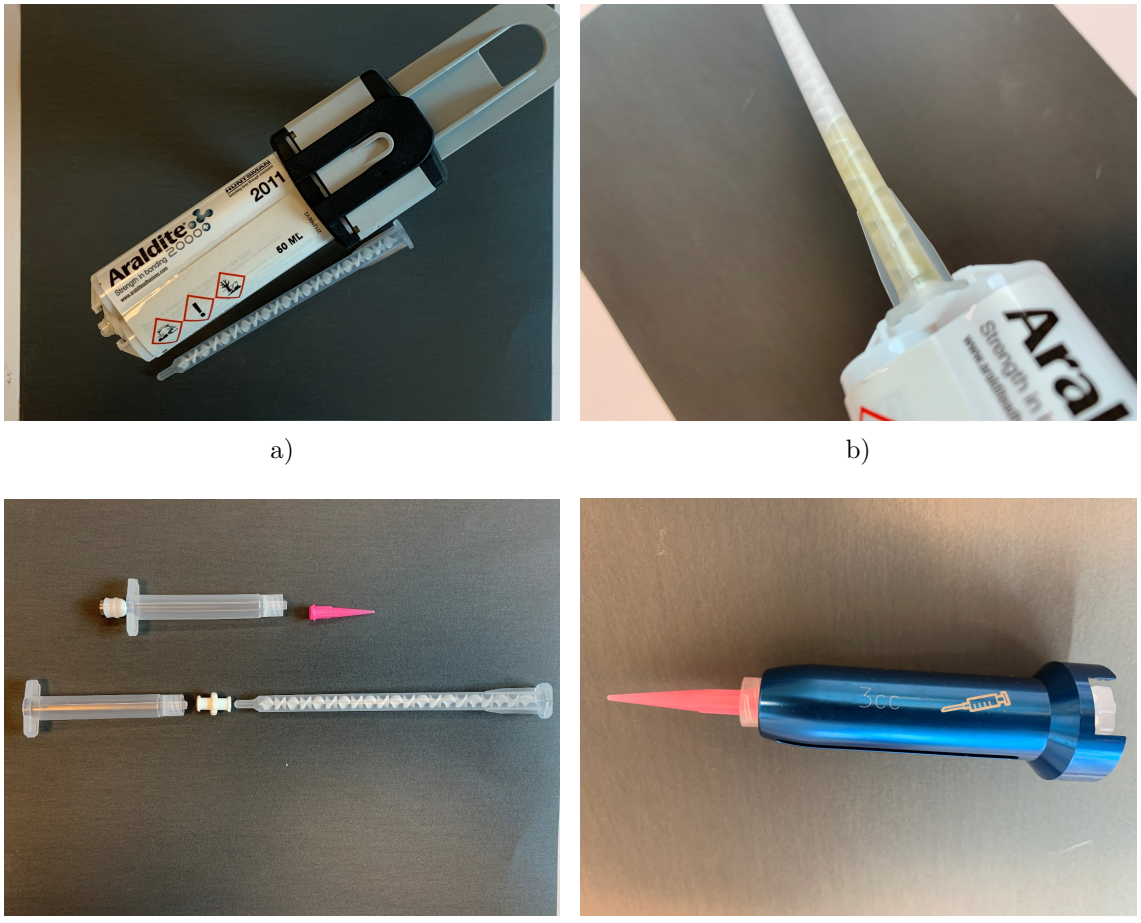
As was mentioned above, the glue picked for the project is Araldite 2011, which satisfies the project requirements in terms of radiation tolerance ($>$ 5 MGy), viscosity ($<$ 100 Pa s), and the push-off strength ($\sim$1 MPa).

Other parameters taken into account were: fluidity, life time, duration and temperature of the polymerisation, which can be found in [68]. Since the dimensions of a glue dot are strictly specified it is important to know and control the parameters for the glue applications precisely.

Until the summer of 2023, the gluing tests were done with a gluing robot, that was initially purchased for another project LPNHE is involved in. The specific robot for HGTD (from FESTO [72]) installation in the laboratory is planned in summer 2023. The glue dots are deposited on the modules by the volumetric dispenser Precifluid from Poly Dispensing Systems [73]. The dispenser controls a fluid drop volume (in cm^3) and a drop push strength for different viscosities (in $g.cm^{-1}s^{-1}$). The gluing itself is done on a vacuum plate, that ensures stable placement of the modules by pumping

out the air under each module in the places of contact with plate. The robot is given the trajectory, which it should follow to deposit the glue dots onto the modules one by one. After the glue dots are in place on the modules, the SU is put on the modules.

The full procedure of a detector unit assembly is presented on Figures 4.4, 4.5, 4.6. The gluing procedure starts with preparing the glue itself. First, the glue is put into the gluing gun, see Figure 4.4 (a), to which the syringe for mixing two Araldite components is attached, see Figure 4.4 (b). The well mixed glue is pushed by the gun into the syringe, which serves as the dispenser, that is closed from one end by plastic-metal cap in order to minimize the amount of air bubbles in the glue. This syringe with glue is then closed from the other end with a plastic tapered tip (pink cap in Figure 4.4 (d,e)) allowing a precise glue distribution and is put into the dispenser holder, blue device in Figure 4.4 (e). The tapered tip with a diameter of 0.61 mm [73] allows for rapid and regular application of medium to high viscosity fluids.



a) b)

c) d)

Figure 4.4: *Tools used for gluing including a gluing gun (a), a syringe for mixing the two components of Araldite 2011 (b), a glue container of the dispneser with a cap for glue transport from the mixing syringe (d), pink tapered tip for precise glue distribution (d), blue dispenser holder (e).*

Once the glue is prepared, the dispenser is attached to the robot, see Figure 4.5 (a). The modules (or mockups like the glass dummies in Figures 4.5 (b, c)) are placed on the vacuum plate and their position is adjusted with the metallic pins, see Figure 4.5 (b). When the positions are fixed, the air is pumped out from the vacuum plate and the modules are held still. After that, the glue dispenser is calibrated to provide the glue dots of a correct size, 2 mm diameter with the volume of 0.0003 cm^3, and regular round shape. The glue robot is then set up for desired trajectory, speed, and delays. The robot is following the preset trajectory, see Figures 4.5 (c, d), and disposes the glue dots at the predefined coordinates on the modules one by one.

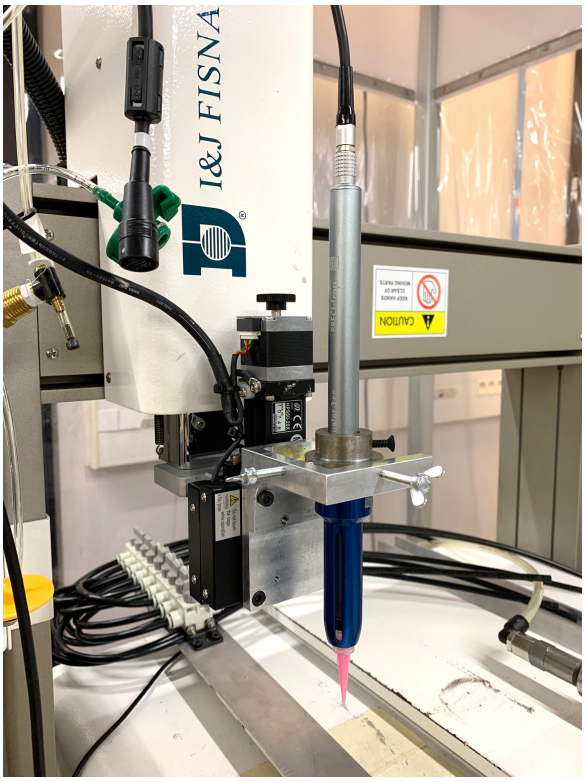
Once all the glue dots are put in place, the modules are covered with the SU. This is done with the help of the metalic pins inserted in the vacuum plate to ensure, that the SU will be placed in the correct position without smearing the glue dots, see Figure 4.6 (a). To ensure a good contact of the SU with the modules and glue dots, the heavy metallic weight is put on top of the structure, as shown on Figure 4.6 (b). The setup is left for minimum ten hours to cure at room temperature.

In addition, a specific tool for a module removal was developped in case a module is damaged and needs replacement. This device is shown in Figure 4.6 (c).

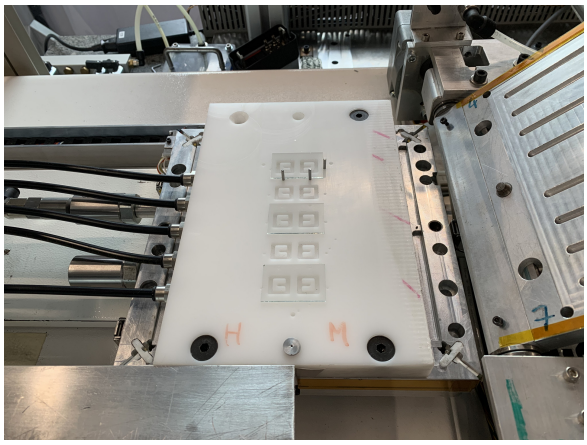
4.2.1 Gluing parameters

As was discussed in Section 4.2, the glue dots have the certain specifications. First of all, the diameter should be around 2 mm after curing. Second, the thickness is required to be 0.1 mm after curing. These two parameters correspond to the dispenser setting on the pushed out glue drop volume of 0.3 μL. Last, but not least, it should be enough so that the attachment force between the glued modules and the SUs between 1 and 2 kg [20]. It is crucial to ensure that the minimum value of 1 kg is maintained consistently after the DUs are placed on the cooling plate and throughout the detector operation. On the other hand, it should be not too strong to allow removing a non-functional module from the SU.

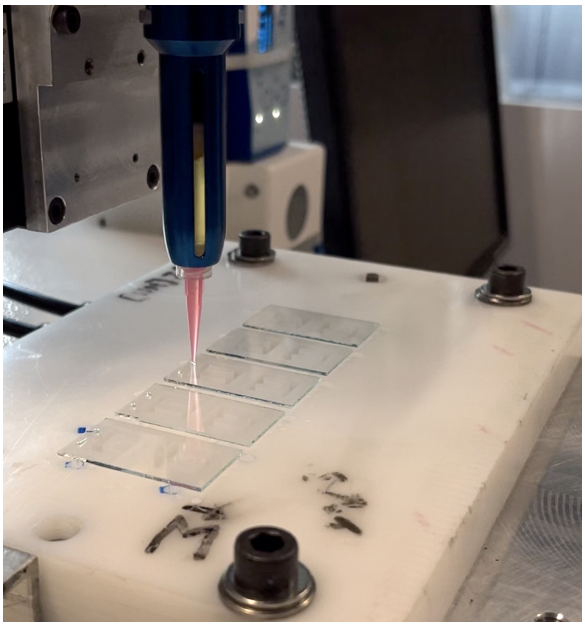
The dimensions of the final glue dot depend not only on the dispenser setting, but also on the robot settings. Since the glue is fluid, two effects take place: it constantly flows out of the syringe due to gravity and it changes the dot shape depending on the time of contact of the syringe and surface. This may lead to the higher quantity of glue deposition, than the value set with the disposer. To address the first effect, after pushing out the required amount of glue, the dispenser is programmed to release the pressure on the glue and pull it back to partially compensate for the gravity. The second effect can be regulated by optimising the gluing robot time delays described in the following text.



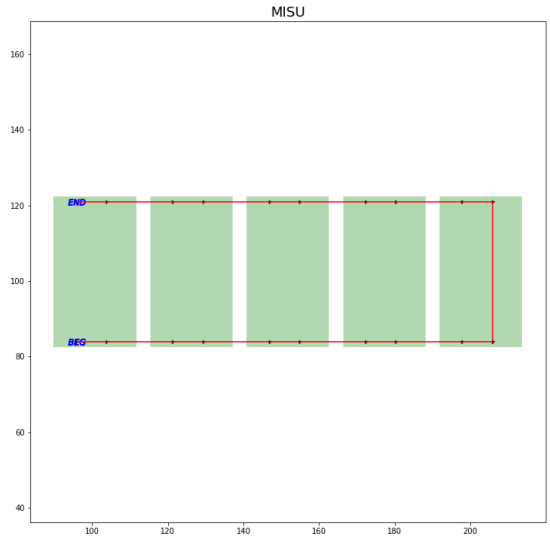
a)



b)

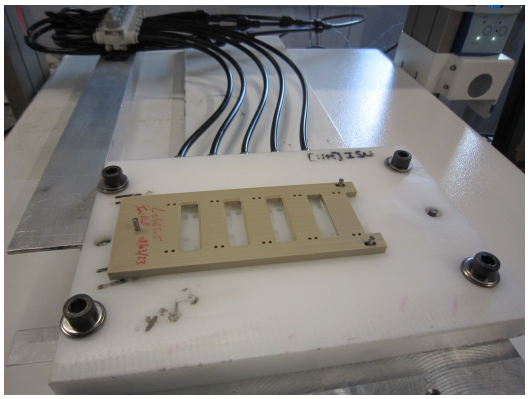


c)

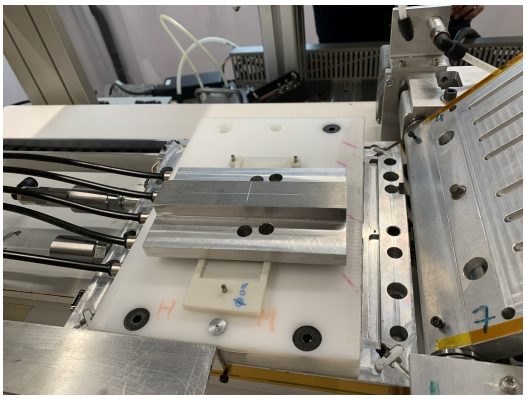


d)

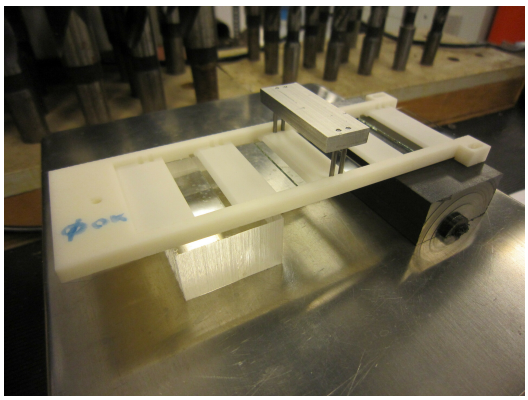
Figure 4.5: *Tools used for gluing including a gluing gun (a), a syringe for mixing the two components of Araldite 2011 (b), a glue container of the dispenser with a cap for glue transport from the mixing syringe (c), a pink tapered tip for precise glue distribution (c), blue dispenser holder (d).*



a)



b)



c)

Figure 4.6: *(a): support unit placed onto the modules with glue fixed by three metal pins. (b): heavy weight on the SU ensures a good mechanical contact between the SU and modules during the glue curing. (c): a device for the modules removal with four teeth inserted in the special holes in SU, that are pushing the module out. The expected strength applied to this device to remove a module is between 1 and 2 kg.*

During the gluing, the robot moves from point to point, see Figures 4.5 (c, d), 20 mm above the modules. The glue dot deposition can be divided in the three steps, where the time delays are set:

1. Once the robot reaches the x-y position where the glue dot should be deposited, it pushes out a drop (still 20 mm above the module). After the drop is pushed out, a delay (later called *before time*) of around 3 s is set.

2. In the next time range, the syringe moves down to the module. Once the module is reached, 0.1 mm above the module, the second time delay (later called *bottom time*) of around 2 s is set when the syring with a dot is in contact with the module.

3. The third delay starts (later called *after time*) after the robot goes up and reaches 20 mm height above the module. The robot moves to the next glue dot point coordinate after this last delay.

The delays should be studied carefully. I conducted several tests for the gluing parameters studies which are presented in the Section 4.2.2.

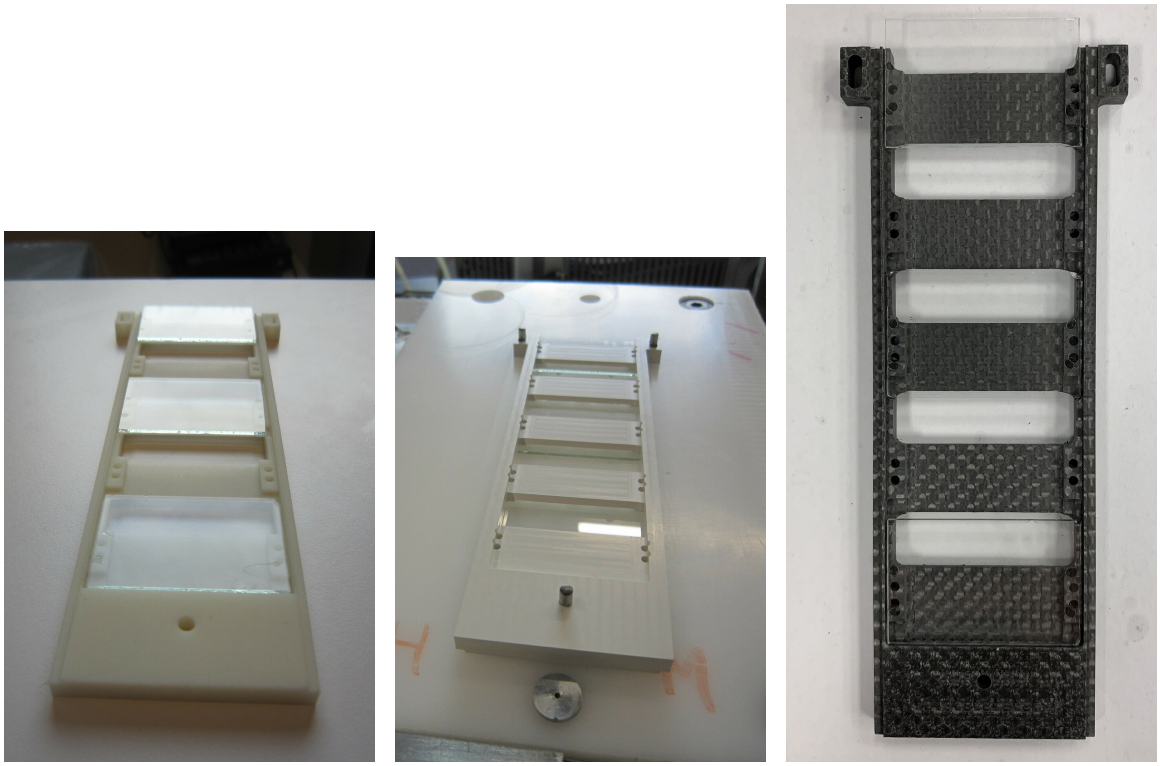
4.2.2 Tests

4.2.2.1 Tests on the attachment strength

Several tests have been done with gluing and removing the module in order to check the module attachment strength depending on the glue quantity. On one hand, the modules should be fixed strongly, so they don't detach naturally. On the other hand, the higher the force needed for a module detachment, in case of a module replacement, the higher the mechanical shock is, i.e. mechanical stress followed by vibration. This may lead to detachment or damage of other modules.

In 2021 tests with the two different glue dot volumes were performed. In the beginning of the year, the gluing tests were done with ∼2 g glass mockup with the dimensions of a real module and with the three different candidate support units materials: Accura 25 plastic [74], Carbon fiber T300 [75], and PEEK (Polyether ether ketone) [69]. The glue dots size was selected to be 0.6 mm^3 in volume corresponding to 2 mm in diameter right after depositing. The dot will increase in diameter and decrese in height due to the fluid nature and under the pressure of SU. The gluing procedure was the same as described in the Section 4.2. All the support units had three modules attached (see Figure 4.7).

After curing, detachment tests were executed. An SU, with the modules attached, is placed on top of two volumes on the scale. Then, the metal device from Figure 4.6 (c) is put in the dedicated holes in SU, that are machined for each module envelope. For



a) b) c)

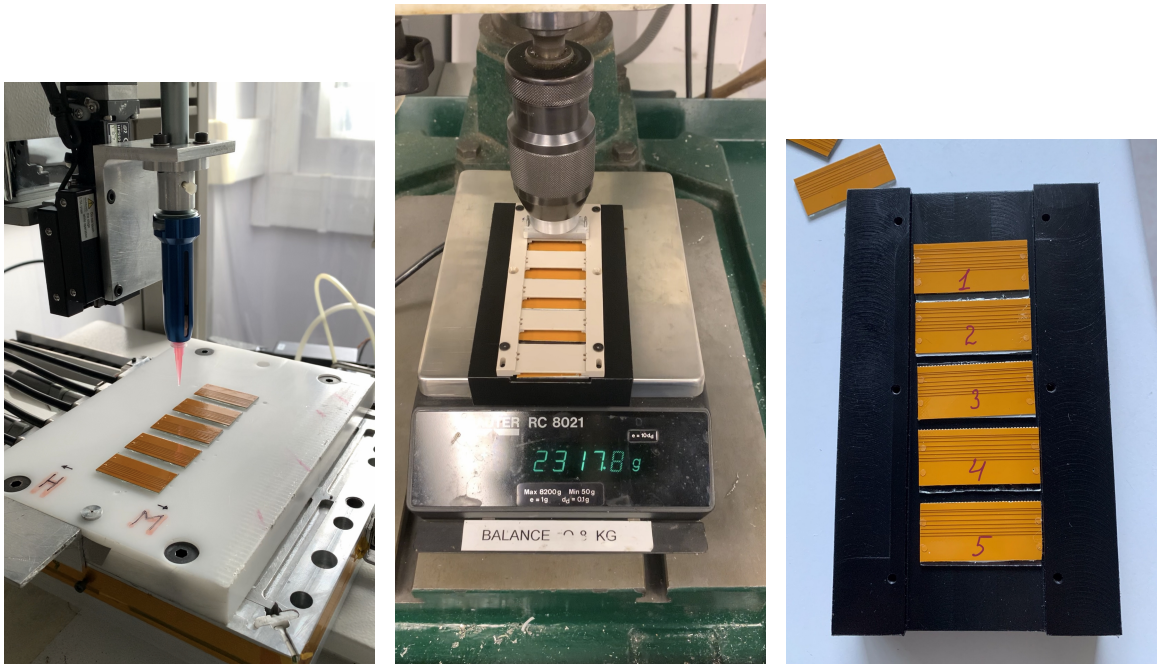
Figure 4.7: *The SUs made of Accura 25 (a), PEEK (b) and carbon fiber T 300 (c) with the glass module mockups glued onto them. The detector units were after tested for the detachment strength.*

detaching each module, the force was applied to this device (by hand) and measured on the scale.

Overall, for nine modules (three on each SU), between 4.5 and 8 kg, with the mean of 6.8 kg, were applied in order to detach a module from the SU. Additionally, for every, SU at least one module got detached while another module was being removed. This is due to mechanical shock vibration, since the force applied to push out a module was very high. After the modules were removed, it was possible to measure the glue dots size left on the SUs, which was around 2.5-3 mm. Overall, these tests showed that the glue dots should be decreased to minimize the mechanical shock coming from a module removal from an SU. Therefore, the next tests were done with the smaller (1 mm right after deposition) glue dots. Several procedure upgrades were implemented for these tests. First of all, the flex tail was glued onto the glass dummy modules in order to mimic the realistic contact between the modules and the glue dots as it is shown in Figure 4.8 (a). Second, the SUs were designed and machined to fit five modules instead of three. Also, a special box holding the SU was machined, which enbled a more comfortable and stable detachment tests comparing to the one from Figure 4.6 (c). Last, a press machine was used to push the modules out of the SU, see Figure 4.8 (b), guarantying a steady and uniform force distribution on the module. All in all, three tests with this setup have been done with 15 modules (five modules per SU). No modules detached due to mechanical shock. The mean force applied to remove an individual module from an SU is 1.9115±0.226 kg. After the detachment of the modules, it was possible to check the glue dots sizes after the curing, which were of a 2 mm diameter. The tests proved that the glue dot of 1 mm diameter, 0.3 mm^3 in volume, which becomes 2 mm after curing, meets the project requirements.

4.2.2.2 Test for the most loaded SU

Another test was performed in order to validate the gluing procedure of the most loaded SU, which had 34 modules at the time. If the glue dots deposition procedure is continious, it takes around 25 minutes to deposit the glue dots on all the modules. The physical characteristics (such as viscosity) of the glue dots deposited in the beginning of the procedure may change before the gluing is completed and the SU is placed onto the modules. This increases the risk of the lower SU attachment quality. Therefore, test on the longest gluing process was executed. In this test, the four glass module mockups covered with the flex were used. The idea was to mimic the duration of the real gluing by depositing multiple dots on each module, so that the overall time for all the modules will be 25 minutes. Each module had 38 glue dots of 1 mm in diameter (see Figure 4.9) and it took 6.5 minutes to deposit the glue dots on each module. The gluing procedure was done according to the one described in Section 4.2. Only the first and the last modules were attached to the SU for the further detachment test. After 21 hours of curing, the modules were removed with the same process as



a) b) c)

Figure 4.8: *Gluing (a) and detachment tests with the press (b) together with the modules after the gluing (c).*

described in Section 4.2.2.1. The two modules detached with 601.5 and 712 g of force applied. On one hand, the result is not satisfactory, given the attachment strength for both is less than 1 kg. On the other hand, the two modules have almost 20 minutes of difference between the dots deposition and the results for both are very similar. This means, that the properties of the glue dots from the first and the last module do not differ much. The reason for such result may be from the scratched surface of the flex on the modules. The modules with flex and the SUs were reused for several tests and each time the glue dots were removed by scratching them out with blade. This increased the surface roughness and decreased the uniformity of the deposited glue dots. Morover, shortly after this test, the baseline geometry of HGTD was changed to the current one, where the most loaded DU has 16 modules.

4.2.2.3 Test for the glue dots size and shape

As was mentioned in Section 4.2.1, the glue dots size and shape doesn't only depend on the volume of the glue drop pushed by the desposer, but also on the time delays between neighbouring dots that are set for the gluing robot. In the following study, the different delays were implemented after which the glue dots were measured. Three settings of *before time* and *bottom time* were tested. For the *before time*, the delay was set to either 4 s, 5 s, or 6 s, while the *bottom time* was set to 2 s, 3 s, or 4 s. The *after*

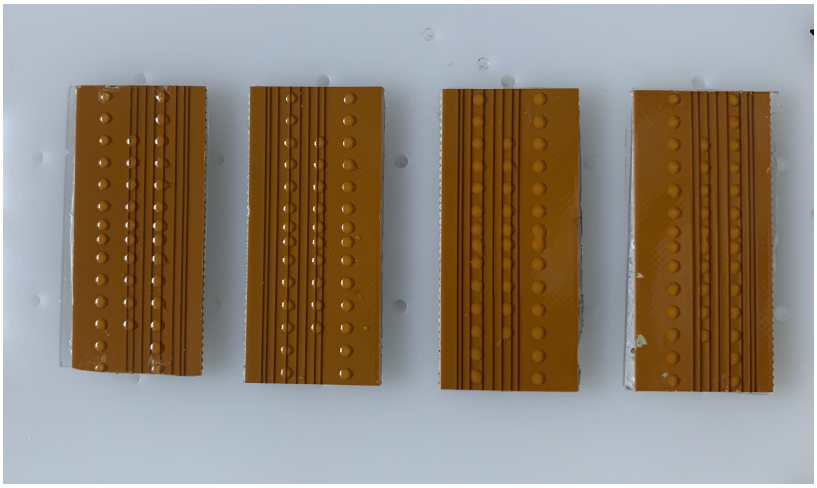


Figure 4.9: *The four modules with 38 glue dots each, used in the test for the most loaded SU.*

time was kept at 2 s, defined as the sufficient delay in the previous tests conducted at LPNHE.

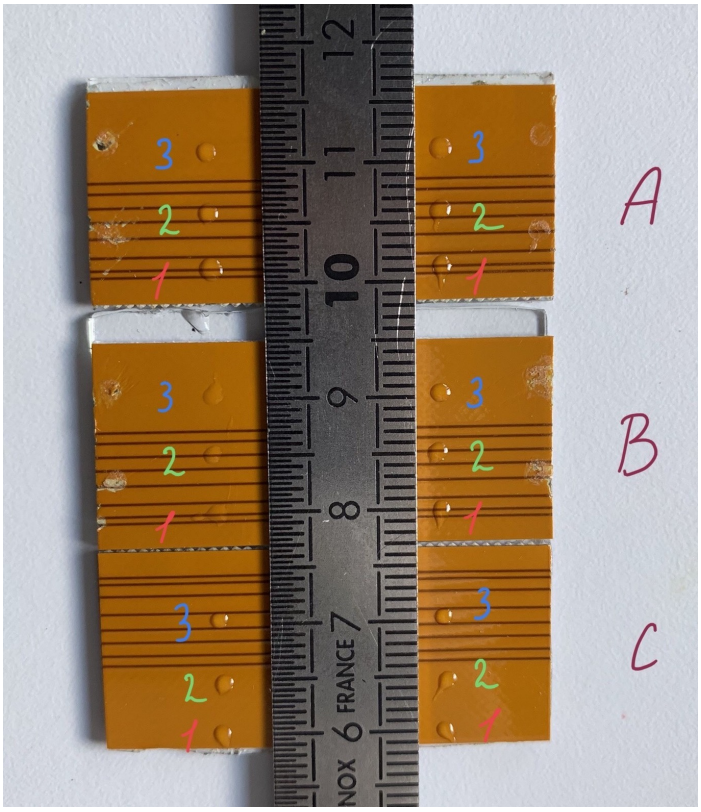
The results of the study are summarized in the Table 4.1 and Figure 4.10, where three modules were used marked as A, B, C and each having three rows (1, 2, 3). From the table it is seen, that the *before time* setting, which corresponds to the time window, when the robot is still 20 mm above the modules, does not really influence the glue deposit for the tested delays. On the other hand, the glue dots deposited with the various *bottom time* does make a difference. With the smaller *bottom time*, the glue dot is bigger and the shape is less regular (less round, with the tales). This is due to the viscous nature of Araldite 2011. When the glue dot comes in contact with the surface of the module, if it doesn't have enough of time to deposit the sufficient mass at the given point, some glue will be pulled up by a moving syringe and will form an unwanted tail on the surface (see dots in the first and the second rows in Figure 4.10). The test showed that the time when the syringe is in contact with the module surface influences the shape of the glue dots the most. The longest delay, 4 s, was selected for the more regular round shape of the deposited glue dots.

4.3 Heater demonstrator

In order to design and validate the key detector aspects, the HGTD R&D program involves the comprehensive realistic demonstrator studies. These studies include building of two separate systems: the heater demonstrator and the full demonstrator. The purpose of the heater demonstrator was to study the mechanical and cooling aspects of HGTD using a silicon-based heater substrate emulating real modules. The full demonstrator, on the other hand, will be equipped with the HGTD modules to study the electronics and DAQ. The heater demonstrator has been built and studied

Module	Row	*before time* [s]	*bottom time* [s]	Glue dot diameter [mm]	Regular shape
A	1	4	2	1.9	no
	2	4	3	1.5	no
	3	4	4	1.4	yes
B	1	5	2	1.9	no
	2	5	3	1.6	no
	3	5	4	1.4	yes
C	1	6	2	2	no
	2	6	3	1.6	no
	3	6	4	1.4	yes

Table 4.1: *Measurements of the glue dots size and shape for different time delay settings of the gluing robot. The correspondance between the module and the row can be found in Figure 4.10.*



a)

Figure 4.10: *Test for the glue dots size and shape depending on different glue robot delays. The ruller is presented only for scale.*

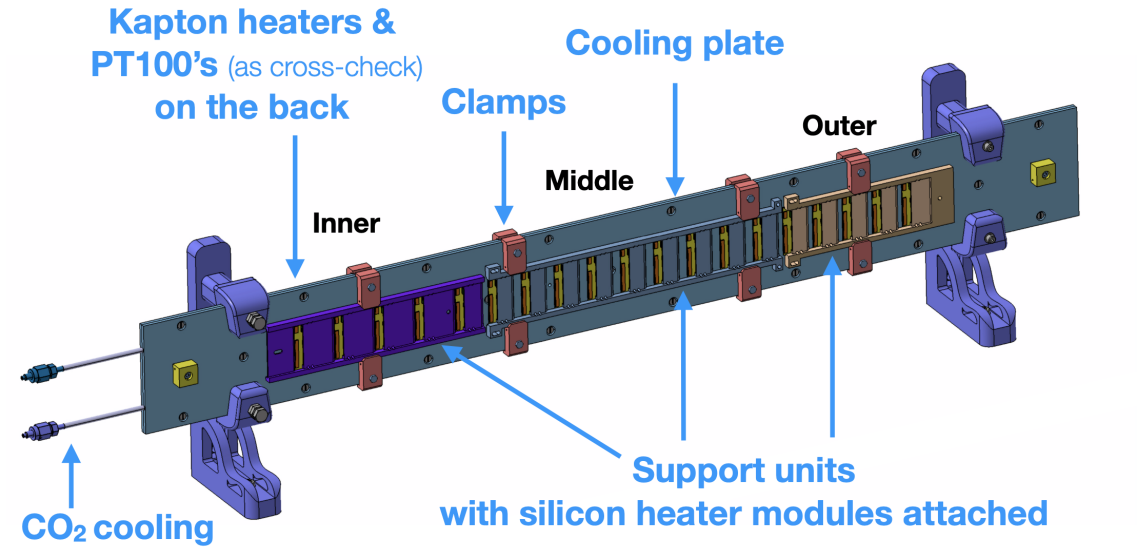
in 2021-2022, whereas the full demonstrator assembly is expected by the end of 2023. I took part in all the activities connected to the heater demonstrator described in this section: the heaters calibration, the heaters metrology measurements, the assembly of SUs, the demonstrator assembly and the data-taking.

4.3.1 Introduction

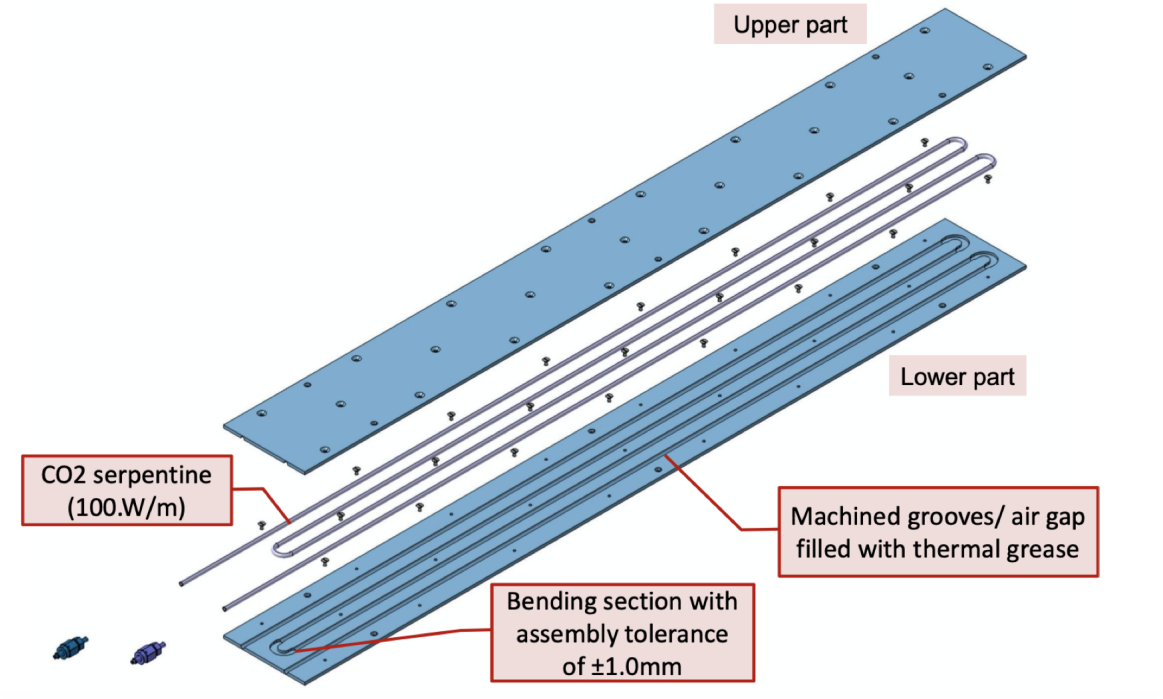
There are two main objectives of the heater demonstrator. First, to use a straightforward cooling plate system to verify the CO_2 cooling capabilities, which will be employed in the final design of the HGTD cooling loops. Second, to select and validate the procedure for module loading: intermediate plate placement, gluing, flex cable stacking, etc. The demonstrator is equipped with heaters arranged in a configuration similar to the HGTD modules [20]. In addition, since it is impossible to ensure a completely flat surface and uniformity of the detector units, it is essential to incorporate a more flexible medium in between the modules and the cooling plate. The demonstrator served as a study ground for the search of such medium.

The heater demonstrator layout is shown in Figure 4.11 and it corresponds to the longest read-out row of HGTD. It consists of a cooling plate with a CO_2 filled serpentine pipe embedded in it, see Figure 4.11 (b), and mutiple module-sized silicon heaters glued on SUs. The SUs are mounted and mounted onto the plate with clamps and Kapton heaters [76] with several PT100 sensor [77] for temperature measurements. Due to unavailability of the HGTD modules, the silicon heater devices were used to simulate the expected radial heat dissipation in HGTD. The demonstrator is divided into three regions depending on the heater placement relatively to each other: inner, middle and outer. The interdistance of heaters follows the placement scheme of the 19-modules row in HGTD : smaller in the inner part and larger in the outer part.

The heaters are composed of a silicon substrate that shares a similar geometry with the modules (20.2 mm×38.4 mm) and has a thickness of 300 μm, see Figure 4.12 (a). To dissipate power, a current is applied through a thin continious metal TiW layer embedded in the silicon substrate. The amount of generated heat can be controlled by adjusting the supplied current. To monitor the temperature of the heaters, five Resistance Temperature Detectors (RTDs) are implanted on top of the thin metal layer, with an oxide layer separating them. When the temperature of an RTD metal wire increases, the resistance to the flow of electricity increases as well. Therefore, by measuring the resistance, the temperature in the substrate can be determined. The precise resistance-voltage relationship is defined via a calibration process described in Section 4.3.2. The RTDs are controlled via a flexible cable, which also supplies current to the heater element. The flex PCB, see Figure 4.12 (b), mimicing the HGTD module flex, is glued onto the heater, and its pads are wire-bonded to the heater. The PCB also incorporates a connector enabling power supply to the heaters and



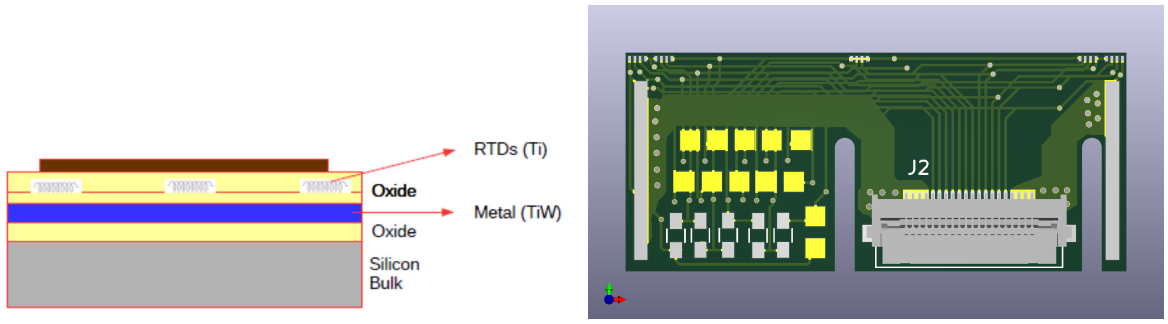
a)



b)

Figure 4.11: *(a): sketch of the heater demonstrator including the cooling plate, SUs with heaters, clamps and the cooling pipes. Taken from [78]. (b): cooling plate with the serpentine layout. Taken from [79].*

individual readout lines for the RTDs on each heater. The flex cables are layered on top of each other, extending towards the peripheral readout boards. External power supplies control the system, supplying the required operational thermal range [20]. The nominal power dissipation in the innermost elements of the heater demonstrator is 400 mWcm^{-2}, but variations from this value are also explored, see Section 4.3.6. To maintain the desired temperature conditions and ensure a dry atmosphere, the entire heater demonstrator is placed in an isolated container box. The box maintains temperatures close to -30°C while the nitrogen atmosphere prevents condensation. The Kapton heaters, Polyimide heaters on the back side of the demonstrator are added to give an equivalent amount of heat dissipation to the estimated one of the modules on the inner serpentine.



a) b)

Figure 4.12: *(a): Silicon heater transverse view. (b): Heater flex PCB layout. Taken from [20].*

4.3.2 Heaters calibration

As mentioned in the previous section, the heater modules implement five RTDs in order to precisely measure the temperature. Each heater has an internal resistance of around 20 Ω, that was measured individually (see Table B.1 in Appendix B.1).

By design, each RTD should have 1 $k\Omega$ resistance at 25°C, however the calibration of each individual one is needed in order to define an accurate resistance-temperature relation. The temperature dependence of the resistance of each RTD can be described by a linear equation $a \times R + b$, where a represents the slope, R is resistance and b represents the offset. The calibration was therefore performed in order to determine the slope and offset for each RTD. Overall, 40 heaters were glued and wire-bonded to flex PCB at IFAE institute in Barcelona. Out of these, 31 heaters were successfully calibrated. Unfortunately, one heater had a defective RTD, while the remaining 8 heaters had issues with wirebonding.

The calibration was performed in batches of three heaters using a climate chamber at CERN. Inside the climate chamber, the three separate locations were organised for

each heater, see Figure 4.13(a). The chamber was equiped with six PT100 sensors and two humidity sensors. The heaters were connected to Intermediary Boards providing power and DAQ via a flex tail, see Figure 4.13(b).

For each batch, eight different temperatures were measured, from 35°C to -35°C in steps of 10°C. After setting one of the temperature points in the climate chamber, the data taking was starting once the environment inside was stable. For each temperature point, the temperature from the PT100s would be recorded together with the RTD resistances. These data were then used to calibrate the heaters. In this way, for each RTD in each heater, eight temperature-resistance points were recorded and fitted to obtain a calibration curve. From this curve it is then possible to deduce the slope and the offset from the linear equation described above. Table 4.2 and Figure 4.14 show the results of the calibration for each RTD of the heater $W04_3$ as an example. Knowing the calibration curve slope and offset it is possible then to calculate the temperature inside the heater by measuring the RTDs resistances. The calibrations for all the heaters are presented in Tables B.2 to B.8 in Appendix B.1.

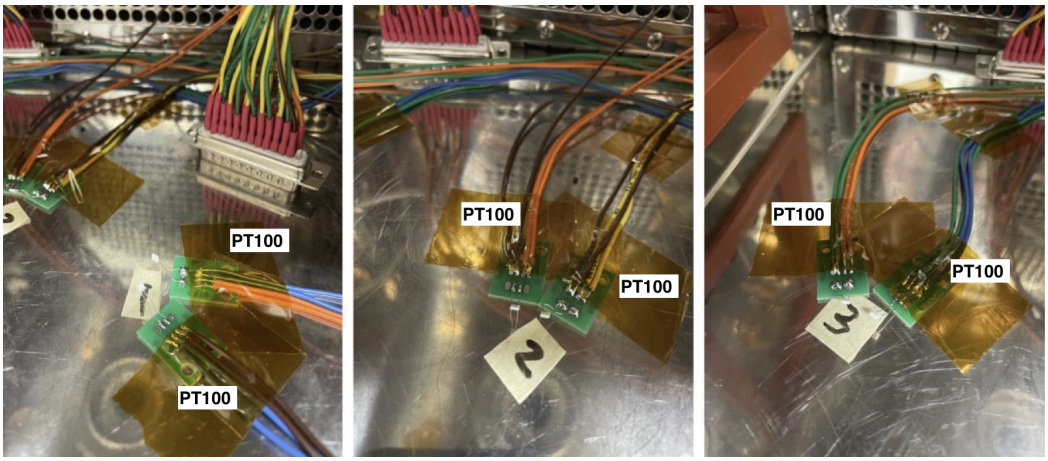
4.3.3 Heaters metrology

After the calibration of the heaters was completed at CERN, in the end of August 2021 they were sent to LPNHE for the assembly on SUs. Even though the special SUs were designed for the heaters, the gluing procedure did not work out of the box. Since the heaters were glued to PCB flex by hand, the thickness of the heaters was varying from 0.696 mm to 0.870 mm. Therefore, the SUs had to be reworked to fit each heater. It was necessary to measure the thickness of all the heaters and group them according to their thickness and the inner resistance for assembly.

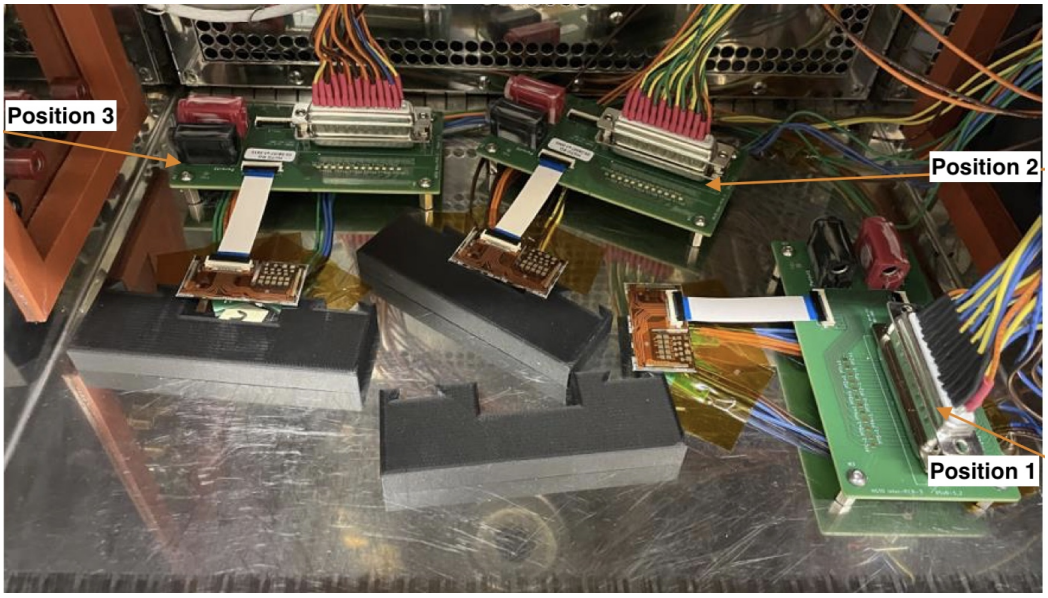
Each heater was measured with the height measurement instrument TESA-Hite with the 0,001 mm resolution [80], see Figure 4.15 (a), in four points where the glue was supposed to be deposited, see blue dots in Figure 4.15 (b). The metrology measurements were taken twice per point and the average was used. An example of such measurements for heater $W04_3$ can be seen in Table 4.3, while all the

RTD	Slope [°CΩ^{-1}]	Slope error [°CΩ^{-1}]	Offset [°C]	Offset error [°C]
1	1.433	0.00069	-1274.7	0.61
2	1.404	0.00051	-1293.7	0.47
3	1.369	0.00052	-1284.4	0.49
4	1.304	0.00053	-1338.7	0.55
5	1.281	0.00045	-1359.7	0.48

Table 4.2: *The slope and the offset extracted from the calibration curves in Figure 4.14 for 5 RTDs of the heater $W04_3$.*



a)



b)

Figure 4.13: *(a): the three locations with PT100s in the climate chamber. (b): heaters inside the climate chamber on their positions for measurement.*

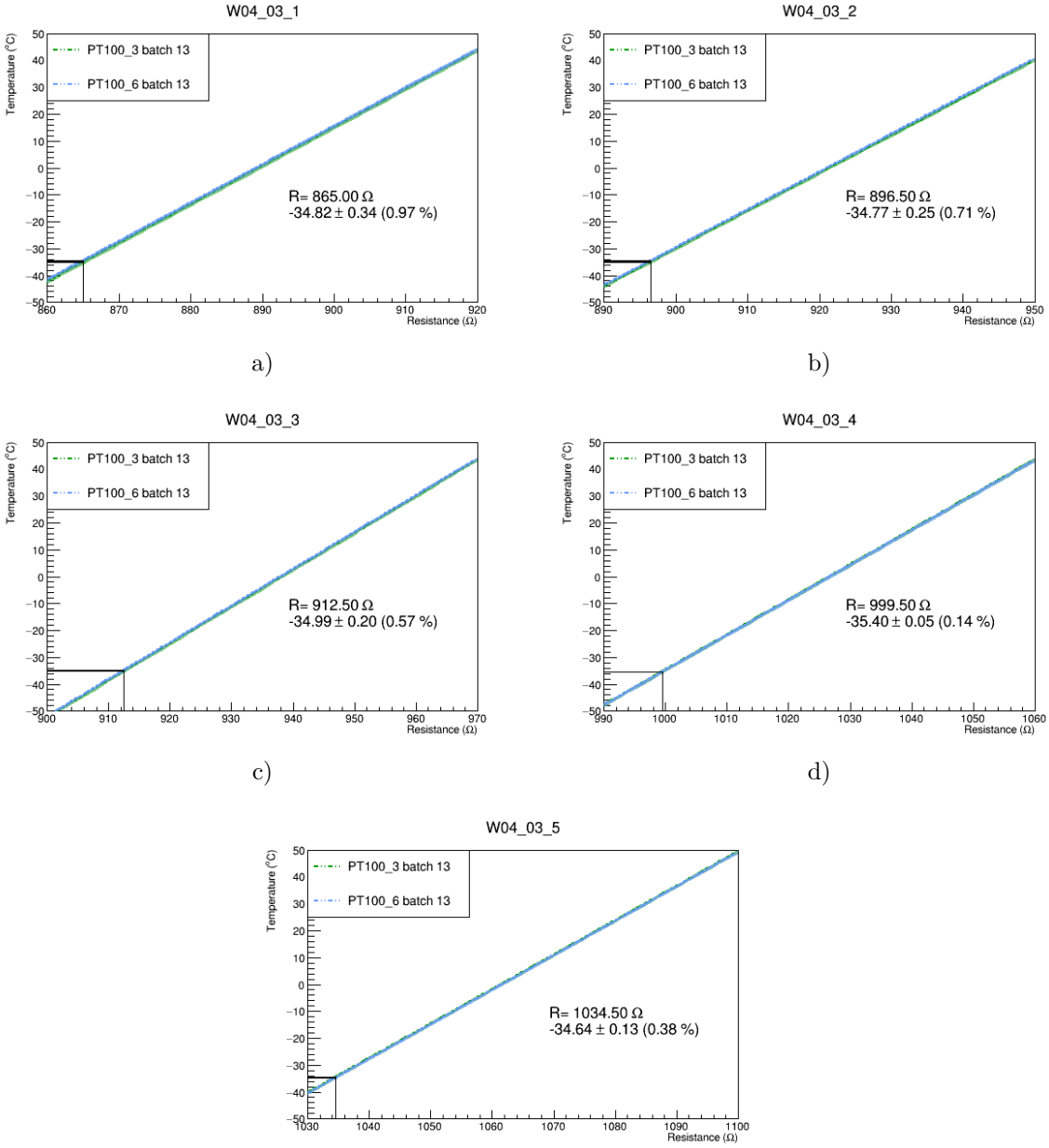


Figure 4.14: *Calibration curves for all five RTDs of the heater W04_3. Five graphs show the dependence of the temperature measured by two PT100 devices depending on the RTD resistance. The resistance around 35° C is pointed out.*

measurements are presented in Tables B.9 and B.10 in Appendix B.1. Before and after the tests, the internal resistance of each heater was measured in order to check that the device was fully functional.

4.3.4 SUs for the heaters

The devices with the similar characteristics were assigned to the three SUs: five heaters were selected for each of the inner and the outer SUs and nine heaters for the middle SU. The SUs were then machined according to the heaters thickness. Figures 4.15 (c, d) show the initial and the final design of the SU, respectively. The latest one has a limited contact with the heater, only in the places of the glue dots (blue dots in Figure 4.15 (d)), which increases the flatness of the detector unit.

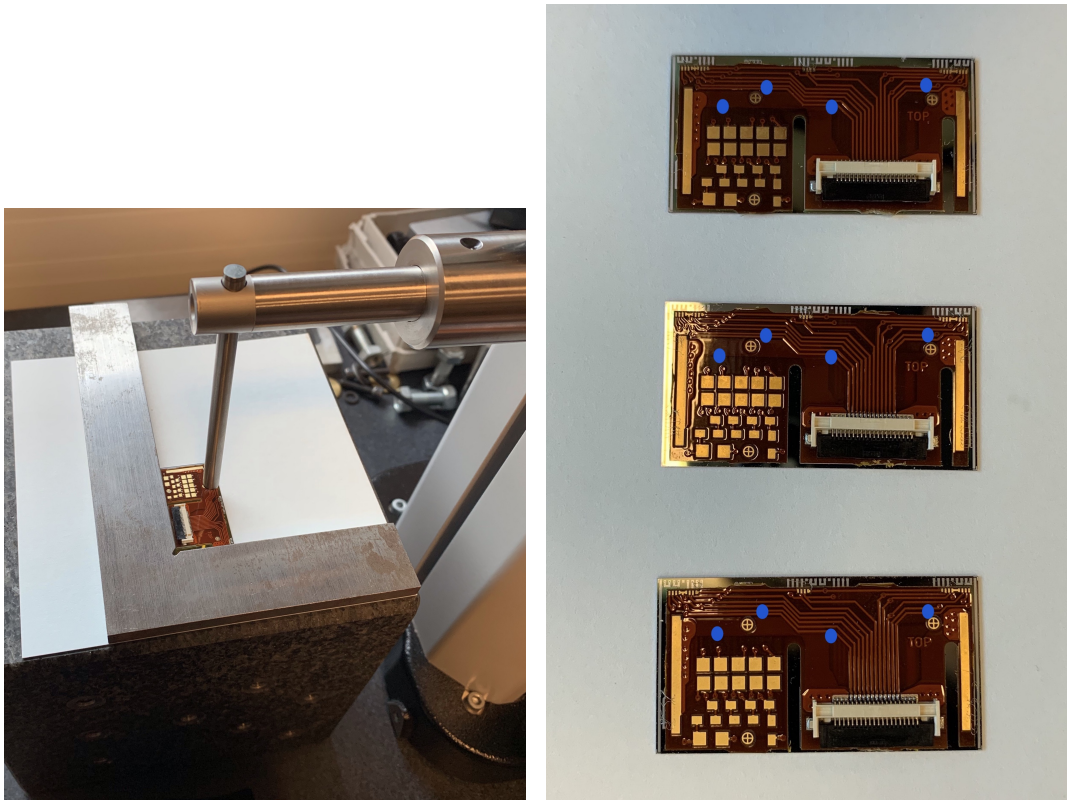
4.3.5 Gluing

Before gluing the selected heaters onto the SUs, it was crucial to validate the gluing parameters. Since the thicknesses of the heaters were varying not only between each other, but also throughout the single module, as shown in Table 4.3, it is important to deposit the glue dots with the sufficient thickness so that all the glue points get in contact with the SU. Tests were performed with different dimensions of the glue dots starting from the volume of 0.5 mm^3 to 0.8 mm^3. The tests were done with the three damaged heaters following the procedure described in Section 4.2. The best glue dots, ensuring a good contact between the heaters and a SU together with the regular shape, were found to be of 0.8 mm^3 in volume and of 2 mm in diameter. The following gluing robot delay settings were used: *before time* of 8 s, *bottom time* of 5 s.

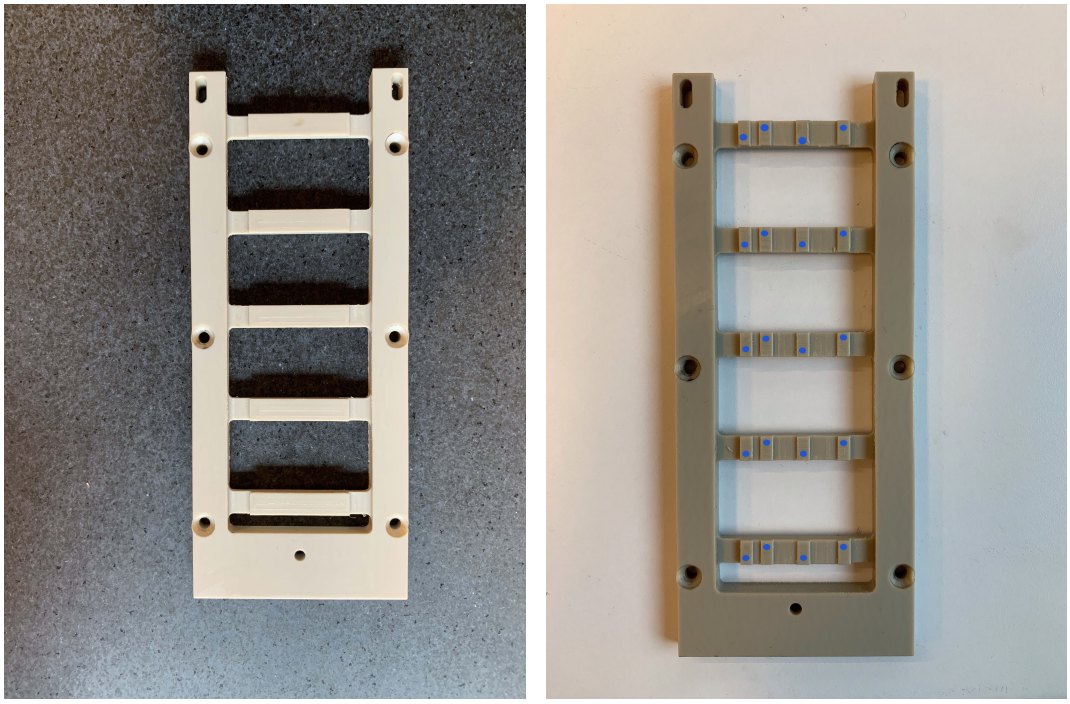
After the settings were validated, the heaters were glued, see an example in Figures 4.16 (a, b). After gluing and curing, all the SUs with heaters were placed in the special transporting box, in which SU was fixed with the screws, see Figure 4.16 (c). Before and after gluing, the internal resistance of each heater was measured to make sure that the heaters are fully functional. No heaters were damaged during the gluing.

Measurement	Point 1 [mm]	Point 2 [mm]	Point 3 [mm]	Point 4 [mm]
1	0,739	0,735	0,794	0,737
2	0,733	0,728	0,802	0,748

Table 4.3: *The thickness measurements in four points for the glue deposition of the heater W04_3.*



a) b)



c) d)

Figure 4.15: *(a): thickness measurement of a heater. The metal frame used to fix the position of the heater and the height measurement instrument TESA-Hite are also shown. (b): three heaters with the glue points positions marked with blue circles. (c): initial design of one of three SUs for heater demonstrator. (d): final design of a SU that takes into account the thickess variation of heaters.*



a) b) c)

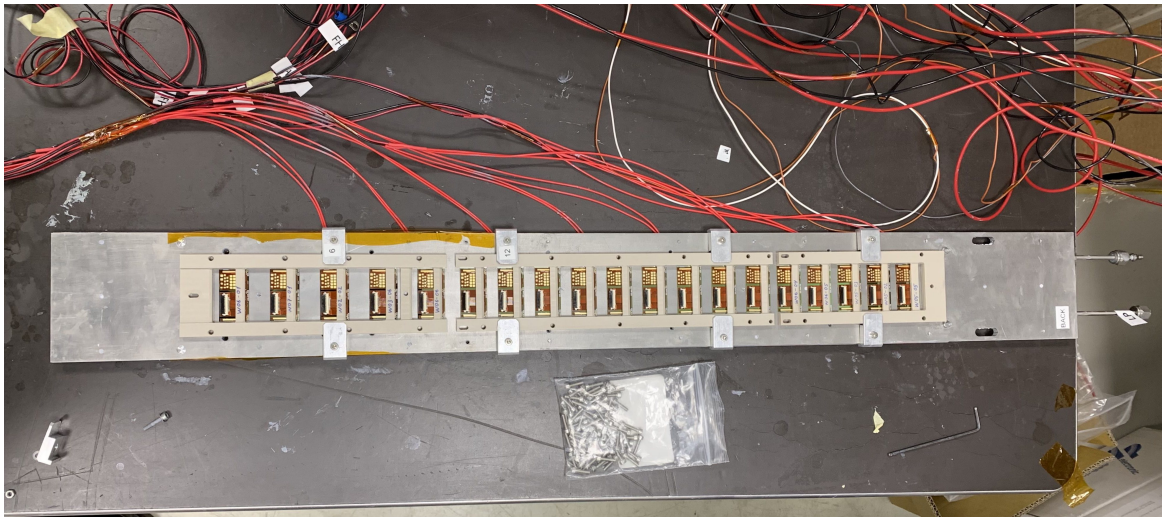
Figure 4.16: *(a): the heaters on the vacuum plate after the glue dots were deposited. SU positioning pins are shown. (b): heaters glued to the SU after curing. (c): SU with heaters in the transporting box fixed with the screws.*

4.3.6 Demonstrator assembly and tests

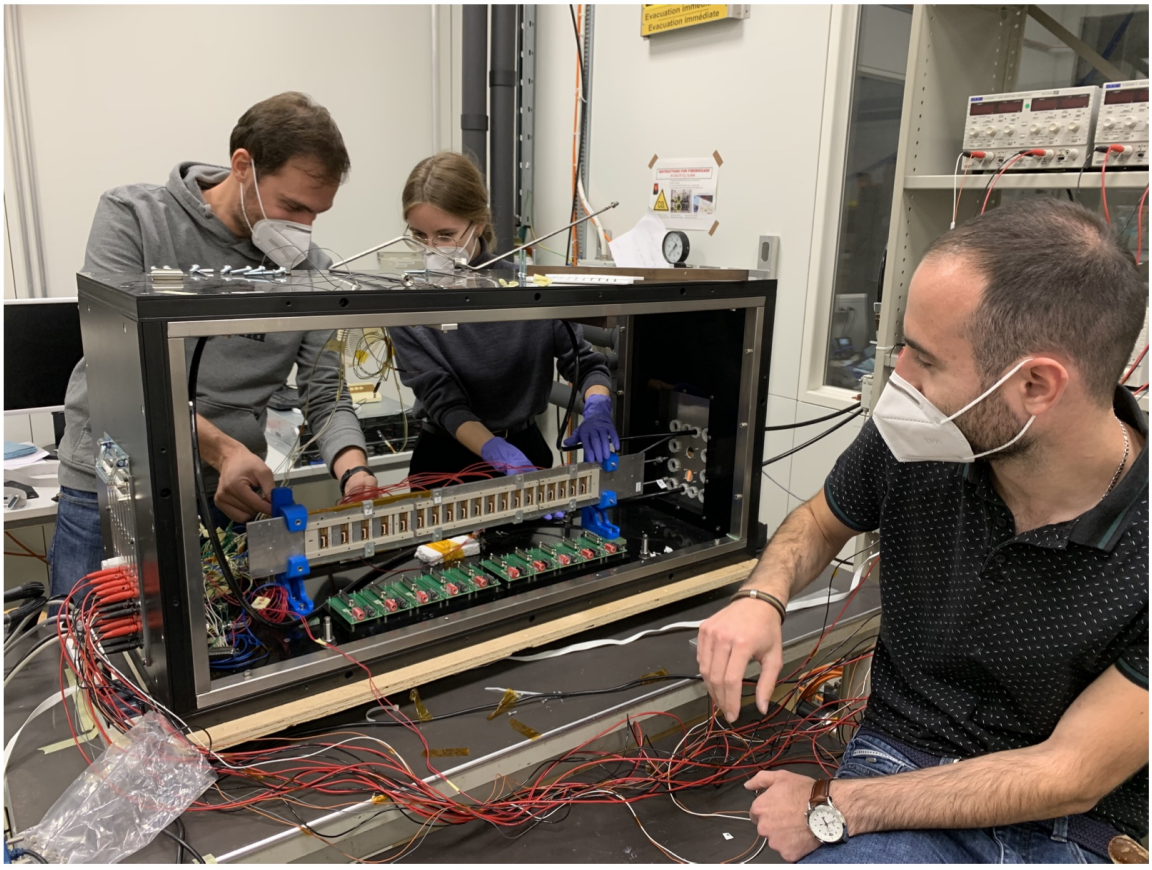
In November 2021, the successfully assembled SUs with the heaters were transported to CERN, where the assembly of the heater demonstrator took place. Figure 4.17 (a) shows all the three SUs with 19 heaters placed on the demonstrator cooling plate and fixed with the special metal clamps. In Figure 4.17 (b), the assembly process of the demonstrator in the climate chamber is pictured. During the assembly, the connector of one heater was damaged ($W06_1$ from the inner SU), making it impossible to read out its RTDs.

The plate was put on the special holder inside the climate chamber behind the row of Intermidiary Boards, Figure 4.18 (a). Each board was connected to two heaters (ten RTDs) via flex tails, to power supply via banana plugs and to DAQ via flat cables. The setup was also equipped with ten PT100 devices for the temperature measurements in the different places of the climate chamber, Kapton heaters sticked to the back side of the demonstrator (powered and read-out), five humidity sensors and nine NTC temperature sensors.

The tests objective was to collect the temperature measurements (by RTDs), while providing different power to heaters. The constant CO_2 flow of around 2 g/s was provided during the data-taking. The powering range was selected such that the power dissipation was varying from 0 to 750mW/cm^2, whereas the nominal one is 400mW/cm^2. The first tests showed a huge temperature spread throughout the whole demonstrator

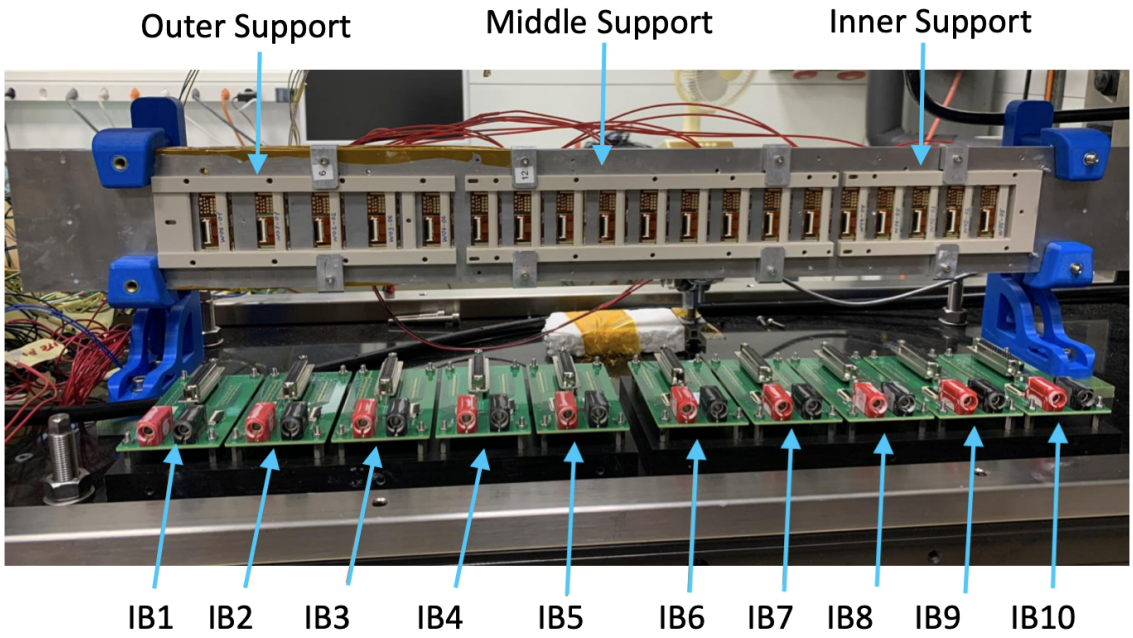


a)

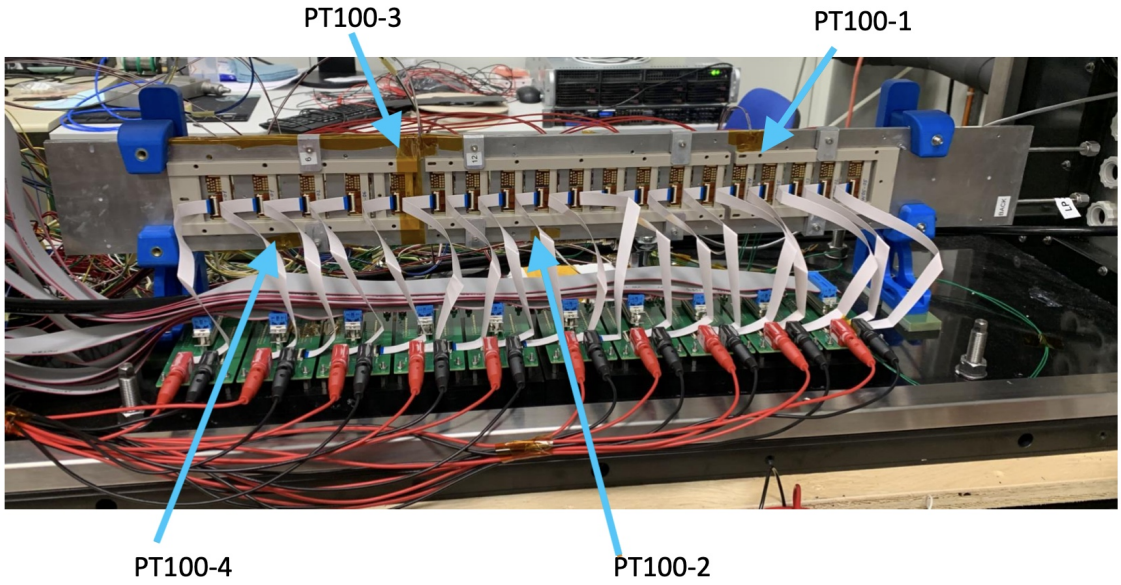


b)

Figure 4.17: *(a): cooling plate with SUs and heaters attached to it with the metal clamps. (b): process of the heater demonstrator assembly inside the climate chamber.*



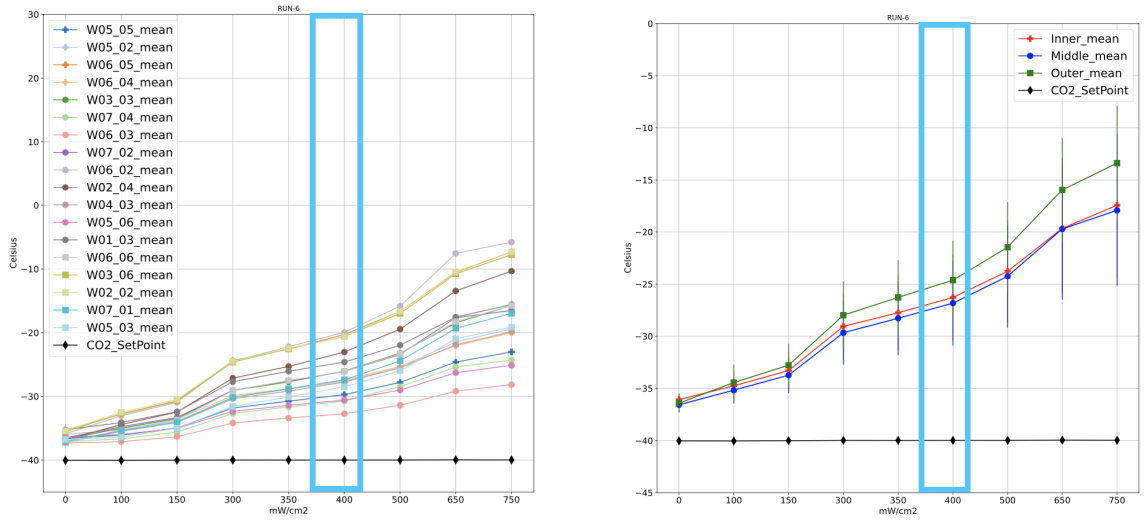
a)



b)

Figure 4.18: *Front side of the demonstrator with the heaters, ten Intermidiary Boards marked as IB1-IB10 (a), cables (b) and temperature sensors PT100 (b).*

with a more than 10° difference with the CO_2 setpoint (-40°) (see Figure 4.19). This was atributed to the poor thermal contact between the heaters and the cooling plate caused by the non-planarity of the DUs. At the power of 400mW/cm^2, the average temperature raised above -30°, with the CO_2 set-point of -40°.



a) b)

Figure 4.19: *The first results from the heater demonstrator showing the dependence of the measured temperature by each heater (a) and DU (b) on the power dissipation by the heaters. A blue rectange represents the expected power dissipation in HGTD.*

The following tests were performed with different thermal media between the cooling plate and the heaters including 1 mm thick thermal foam, thermal grease, copper foil, glue graphite sheet and their combinations. Figure 4.20 shows the results of the three most promising configurations. The Inner Detector unit was placed on thermal grease with copper foil, the middle one on graphite sheet with thermal grease, while the outermost heaters were on top of the combination of graphite sheet + thermal grease + graphite sheet. The best thermal performance was achieved with the configuration: graphite sheet + thermal grease + graphite sheet. The configuration provided a good contact between the heaters and the cooling plate ensuring the cooling well below -30° even at the 750mW/cm^{2}s. At the 400mW/cm^2, the temperature inside the outermost DU was below -35°, while for others it was slightly above -35°.

4.4 Conclusion and outlook

The extensive R&D is ongoing in order to define the most sufficient geometry of the SUs, assembly procedure, and cooling. The LPNHE laboratory is heavily involved in this process by providing the SUs and the detector units assembly. In this chapter, the evolution of the SU design was discussed together with the detector unit assembly

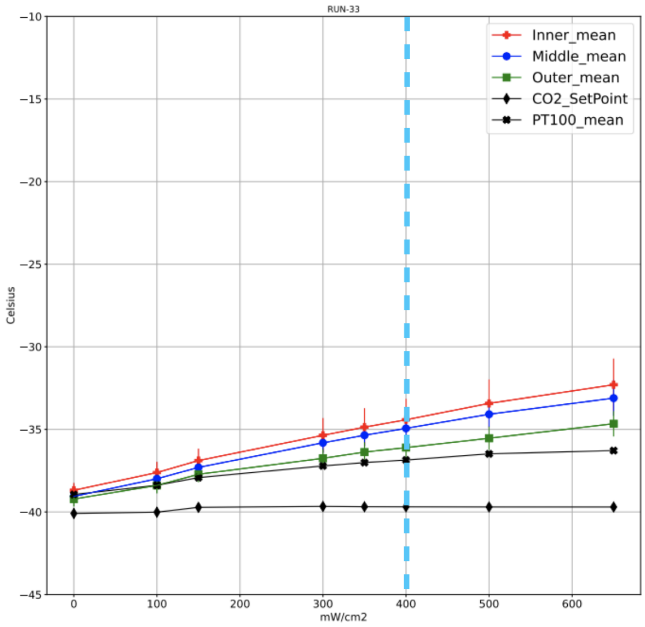


Figure 4.20: *Temperature measurements taken with three different configurations: thermal grease+copper foil for the inner, graphite sheet+grease for the middle and graphite sheet + thermal grease + graphite sheet for the outer detector unit together with the CO_2 set point and the PT100s mean measurement. Taken from [81].*

procedure and gluing optimisation, for which I conducted several tests. The tests defined the sufficient glue dot size and the optimal assembly procedure.

Big part of the mechanical R&D work in the scope of this thesis was dedicated to the heater demonstrator. The purpose of this demonstrator was to study the mechanical and the cooling aspects of HGTD using the silicon-based heater substrate emulating the real modules. I contributed to all the activities related to the demonstrator: the calibration of the heaters, the metrology tests of the heaters, the gluing of the heaters onto support units, the demonstrator assembly, and data taking and analysis. The demonstrator work uncovered some bottlenecks of the module assembly and the cooling. For instance, the importance of planarity of the SU and the modules. This triggered a SU design modification to be able to accomodate more screws in order to increase the planarity. The demonstrator also revealed the importance of the precise metrology measurements for each module and the gluing tests. The heater demonstrator assembly served as a training for the future real modules assembly. It is difficult to work with fragile devices such as modules. Last, but not least, the tests showed that an additional thermal medium between the cooling plate and the modules is needed in order to achieve a better cooling. The full demonstrator with the real HGTD modules instead of heaters is being developed and takes into account the experience gained during the heaters demonstrator assembly.

Chapter 5

Performance studies of Low Gain Avalanche Detectors

A common way to evaluate the performance of a sensor for High-Energy Physics use is to test it with a beam of particles. In such tests, the Device Under Test (DUT) is put in a focused flux of high-energy particles and its response is read out and further analysed. Since 2016, the HGTD collaboration has been conducting test beam campaigns at CERN SPS and at DESY in order to study the performance of LGAD sensors. Apart from testing the non-irradiated sensors, it is crucial to study also the irradiated sensors. As the fluency increases, the gain of LGAD tends to decrease at a fixed voltage due to the removal of initial acceptors in the gain layer. This performance degradation can be compensated by tunning the applied bias voltage with the increasing irradiation level. Therefore, in the HGTD test beam campaigns, both non-irradiated and irradiated sensors are studied with different bias voltages applied.

In this chapter, the results of the two crucial HGTD test beam campaigns for which I performed the analysis are presented: at DESY in 2020 (further called "DESY 2020") and at DESY in 2022 (further called "DESY 2022"), where I also took part in the data taking. The DESY 2020 campaign was an important milestone for the studies of LGADs for HGTD, since the issue of Single Event Burnout (SEB) described in Section 3.4.2 was observed and investigated. After the SEB was studied in details by the HGTD collaboration, the new design of the LGAD sensors was developed. The new LGADs implement carbon enriched gain layer, that is not only proved to be more radiation hard, but also requires a lower voltage to achieve the required performance. The new generation of the sensors from different producers was tested in the DESY 2022 campaign and at CERN SPS in 2021 (further called "CERN SPS 2021").

This chapter will describe the test beam setups, the analysis strategy, the tested sensors and the results. In addition, the comparison of the results from DESY 2022 and CERN SPS 2021 campaigns will be discussed.

5.1 Test Beam Setup

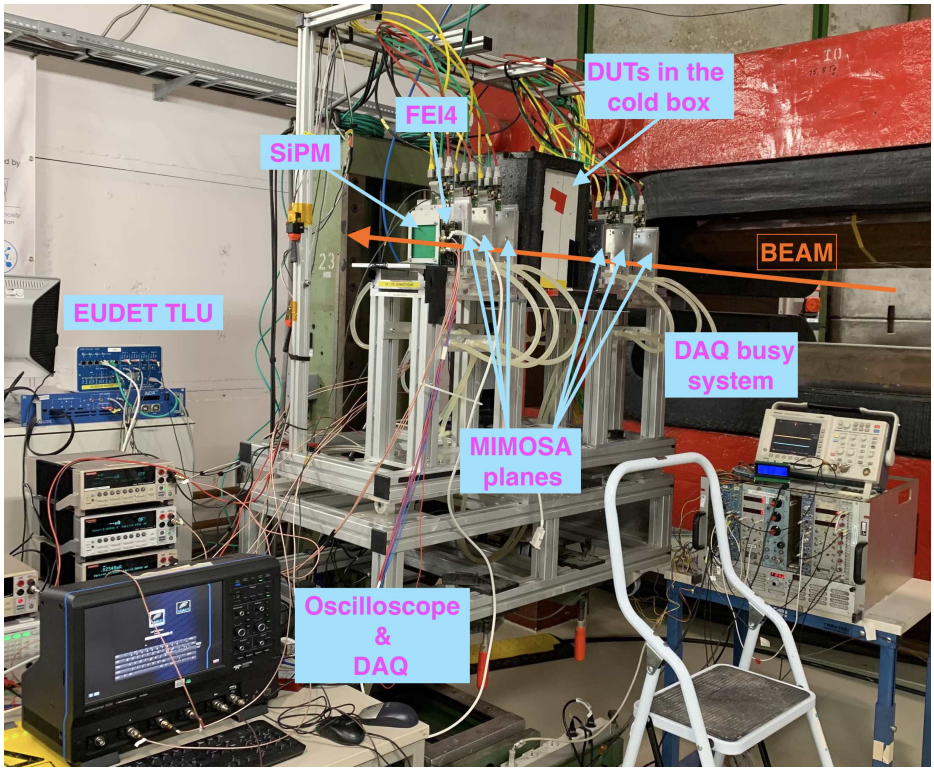
The setups at CERN and DESY facilities are similar, they consist of six telescope planes to perform the tracking and two or three DUTs, which are read out by oscilloscope. For the tests at CERN, the 120 GeV pions were used, while at DESY, the 5 GeV electrons were used. The very detailed description of both setups may be found in the dedicated papers [82], [83].

5.1.1 DESY

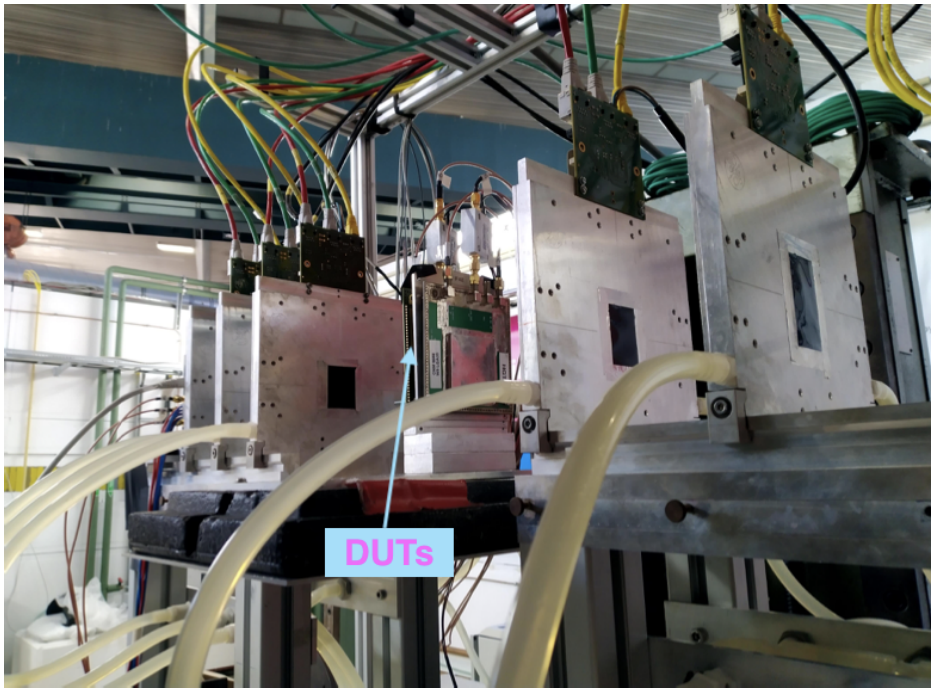
As was mentioned earlier, the test beams conducted at DESY, were using the 5 GeV electron beam. The beam profile size was about 2×2 cm^2. Figure 5.1 shows the setup from the test beam campaign. Since the cooling of LGADs was done with dry ice, which was evaporating, the temperature was varying from -40 °C to -25 °C during the data-taking. Two LGAD sensors were placed in a styrofoam box with a separate compartment for dry ice and tested simultaneously. Additionally, the temperature and humidity (PT100 [77]) sensors were in this box. Each LGAD was studied with the several bias voltages applied. The measurements of each couple of DUTs were done in batches, where in different batches different bias voltages were applied to the LGADs. The tested ranges of bias voltage were defined depending on the safe from SEB voltage limit defined with the laboratory tests of the sensors.

An EUDET-type DATURA telescope was used for the particle position measurements. The telescope consists of two arms (upstream and donwnstream) with three pixel planes called "MIMOSA" [84] on each side. MIMOSA chips have a dimension of 10.6×21.2 mm^2 and a pixel size of 18.5×18.5 μm^2, providing a few micrometers resolution. In front of the upstream telescope planes, two scintillators were placed perpendicular to each other for triggering. After the downstream arm of the telescope, a 16.8×20.0 mm^2 big FE-I4 plane [85] and Silicon Photomultiplier (SiPM) combined with a quartz bar [82] were placed. The FE-I4 is a pixel detector consisting of a 3D CNM Silicon sensor with a pixel size of 50×250 μm^2 and a FE-I4 readout chip. This device served for triggering and was configured to record only signals in the region of interest (ROI) $\approx 3 \times 3$ mm^2 representing the DUT geometry. The SiPM coupled with 10 mm long Cherenkov-light emitting quartz bars provided an independent time reference to the data acquisition (DAQ) system with an average time resolution of 62.6±0.6 ps for an operating voltage of 27 V.

The DUTs were mounted on custom readout boards with an internal and external amplification stage to enhance signals [86] and placed between the two arms of the telescope. The position of the DUTs was controlled by a micrometric x−y motor stage perpendicular to the beam axis.



a)



b)

Figure 5.1: *The experimental setup at the DESY T21 beamline including DATURA telescope, TLU, DAQ, FE-I4 chip, SiPM and DUTs with/without the cold box (a), (b), respectively.*

The trigger and DAQ architecture is shown in Figure 5.2. A four-channel oscilloscope was used to sample the waveforms recorded by the DUTs and the SiPM. A trigger system was used to initiate the DAQ of the oscilloscope and the MIMOSA planes. The scintillator signal, AUX output from oscilloscope via NIM modules [87] and the HitOr signal from the FE-I4 plane were the input to the EUDET Trigger Logic Unit (TLU) [88]. The NIM logic circuit was implemented to generate a busy signal (20 s-long veto pulse) covering the time the oscilloscope needed to read out its data buffer ($\sim$ 4096 events) that is sent back to TLU.

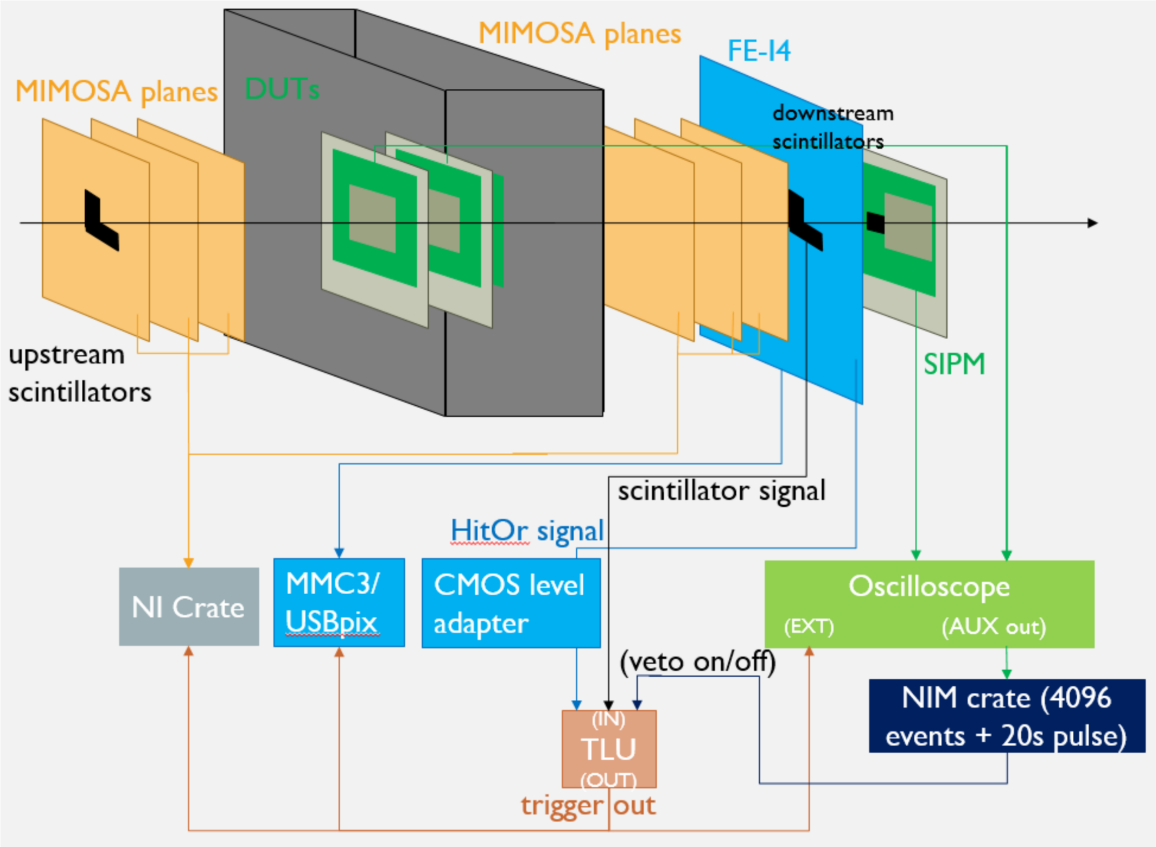


Figure 5.2: *DAQ and trigger scheme explained in the text. Taken from [82].*

5.1.2 CERN

At CERN SPS, the 120 GeV pion beam was exploited. The setup at CERN used a MALTA telescope [89] consisting of six MALTA chips, monolithic pixel detectors fabricated in TowerJazz 180 nm CMOS technology. With a 3 μm pixel collection electrode, the chip has a small capacitance, which helps to minimize the noise and achieve a low power dissipation in the active region. For the timing reference, an unirradiated calibrated LGA35 sensor (placed outside the cooling box) with a time resolution of 54.8 ps (at room temperature) was used. For triggering, one of the MALTA chips is used together with a scintillator, placed at the back of the telescope. The DUTs were placed in the climate chamber, with a stable temperature of -20°C.

5.2 Data processing

The two independent data types were recorded to study the LGADs performance: the LGADs and SiPM waveforms registered by the oscilloscope and the particles track information from the telescope and FE-I4. These data streams are processed and then joined in a single file and analysed.

5.2.1 Waveform processing

For the waveform processing, the first step is to convert the oscilloscope binary data into a ROOT [90] file containing the raw pulse information of each DUT and SiPM which were sampled with a time bin of 25 ps (see Figure 5.3). Then using the first 400 samples of an event where no signal contribution is expected, the pedestal and the noise are extracted from the mean and standard deviation of the measured voltage, respectively. The average pedestal was ∼3 mV depending on the run conditions and oscilloscope settings and is subtracted from the measured pulses event-by-event. The average noise was calculated to be ∼1.5 mV.

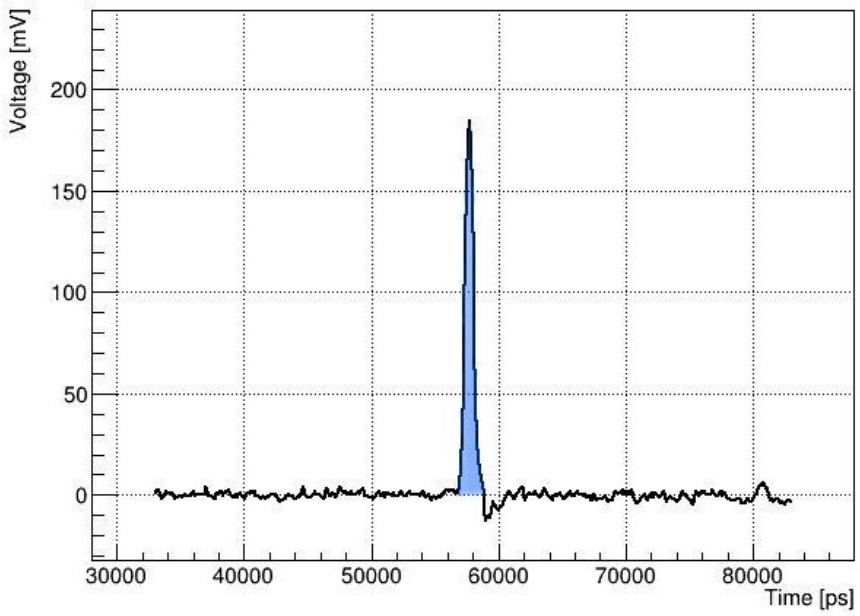


Figure 5.3: *A waveform example of one event from the Test Beam at DESY in 2022 for one of the tested sensors. The blue area represents an integral over time for calculation of the collected charge.*

The maximum of the pulse amplitude is then estimated after pedestal subtraction from a quadratic polynomial fit around the sample with the highest amplitude in a 400 ps window. The collected charge for each event q is defined as follows:

$$q = \frac{\int_{t_1}^{t_2} V_{sig}\, dt}{R_b \times G_{ampl}}, \tag{5.1}$$

where V_{sig} is the signal voltage after pedestal subtraction (blue area on Figure 5.3), R_b is the transimpedance of the readout board and G_{ampl} is the gain of the voltage amplifier. The integral of V_{sig} over time is computed in a window $t_1 - t_2$ centered around the time where the pulse is maximal and wide enough to fully contain the pulse.

The gain is then obtained from the ratio of the collected charge and the expected charge from a MIP in a silicon sensor without gain (0.46 fC for a 45 μm thick sensor). The estimated systematic uncertainty of gain is 20% due to the uncertainty on the board transimpedance.

For the reconstruction of the Time of Arrival (TOA), the Constant Fraction Discriminator (CFD) technique was used in the following analysis. The CFD method defines the TOA as the time at which the waveform crosses a constant fraction (f_{CFD}) of the signal amplitude value (see Figure 5.4 (b)), which minimises the time walk effect discussed in Section 3.5.3. However, since the threshold is crossed before the maximum amplitude is reached, this method cannot be implemented in the readout electronics for the future HGTD. Instead, the Constant Threshold Discriminator (CTD) will be used, which defines the TOA as a time when the pulse crosses a constant threshold (see Figure 5.4 (a)). The studies on optimization of the fraction f_{CFD} to be used for

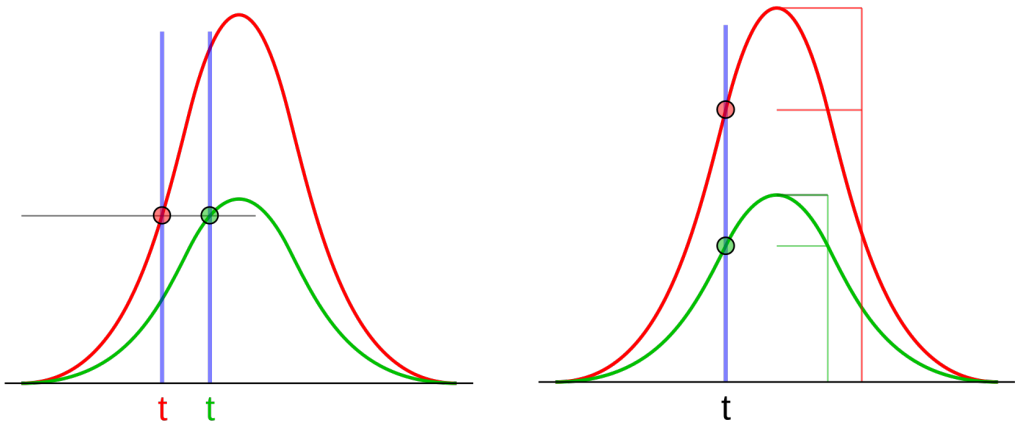


Figure 5.4: *Two methods of the TOA reconstruction (taken from [91]). (a): Constant Threshold Discriminator (CTD) method defines TOA as the time when signal crosses a constant threshold. (b): CFD method defines TOA as the time when signal crosses a constant fraction of the pulse maximum.*

different devices is described in [82]. To obtain the time resolution, the TOA value at $f_{\mathrm{CFD}} = 20\%$ is used for the time reference (SiPM) and at $f_{\mathrm{CFD}} = 50\%$ for the DUTs to minimize the noise contribution to the pulse.

5.2.2 Track reconstruction

The reconstruction of the track procedure using the EUDET telescope is done in five steps: removal of “hot” pixels from the MIMOSA planes, grouping of hits into clusters, alignement of the telescope planes, track fitting and extrapolation to the DUT. The tracking capability of the EUDET-type telescope was provided by six MIMOSA planes as explained in Section 5.1.1. The positions of the MIMOSA, FE-I4, and DUT planes were measured with a precision of 1 mm in the z-direction along the beam line.

The "hot" pixels are the ones that have an occupancy ten times higher than the average. Once the hot pixels are removed, the remaining pixels are then grouped into clusters in each MIMOSA plane. Only clusters with a maximum of six pixels were used for tracking. The cluster coordinates are the mean values of the pixels coordinates in x and y. In order to select events with only one particle traversing the DUTs, only events with exactly one cluster in the FE-I4 plane were considered. The MIMOSA planes are then aligned by iteratively shifting the planes' coordinates in x and y direction with respect to a reference plane.

Given the z-position of the MIMOSA planes along the beam axis and the x- and y-positions of the hits in these planes, the three-dimensional (3D) tracks were built. As shown in Figure 5.5, two separate 3D-proto-tracks are reconstructed from three MIMOSA planes: before the DUTs along the beam trajectory (upstream triplets), and after the DUTs (downstream triplets). The downstream triplets must coincide with a hit in the FE-I4 plane. For each event, all possible downstream and upstream triplets are reconstructed and a complete track is considered to be found if a downstream triplet matches an upstream triplet in the central region with a minimal distance of approach of 150 μm. Only events with a single complete track through the six MIMOSA planes are considered. Since the electrons passing through the telescope are undergoing scattering, the track reconstruction using two separate triplets is more efficient than the straight line track reconstruction.

Once the tracks have been reconstructed, their trajectory was interpolated at the z coordinate of the DUTs, to determine the (x, y) coordinates of the hit. The precision on the position of the track was extracted from the fit of the difference between reconstructed track position and the measured hit position in the MIMOSA planes and was about 3 μm.

5.3 LGAD studied characteristics

The following LGAD properties were studied: the hit reconstruction efficiency, the collected charge and the time resolution. Before the calculation of these characteristics, a selection (or cuts) is applied in order to remove the noise or background events. The

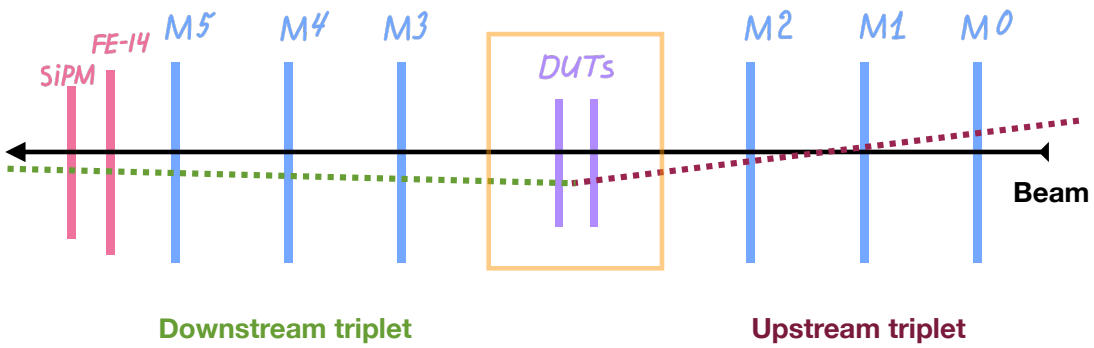
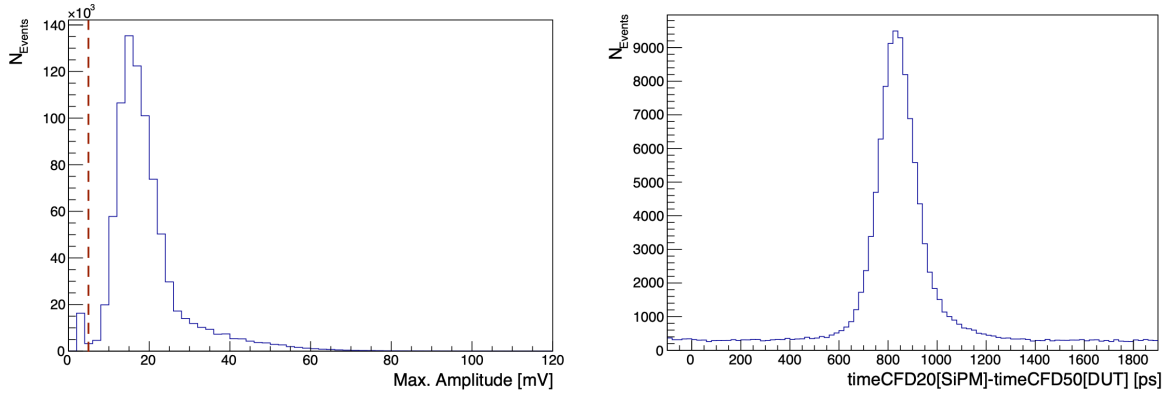


Figure 5.5: *Sketch of the track reconstruction procedure including the formation of the upstream triplet and the downstream triplet.*

first constrain was applied on the maximum pulse amplitude of the SiPM that has to be three times higher than the noise i.e. around 5 mV (see Figure 5.6 (a)). Next selection is set on the time difference between the TOA of the DUT and SiPM pulses to insure that the events are in-time. The allowed time coincidence window was set to 2 ns, see Figure 5.6 (b).

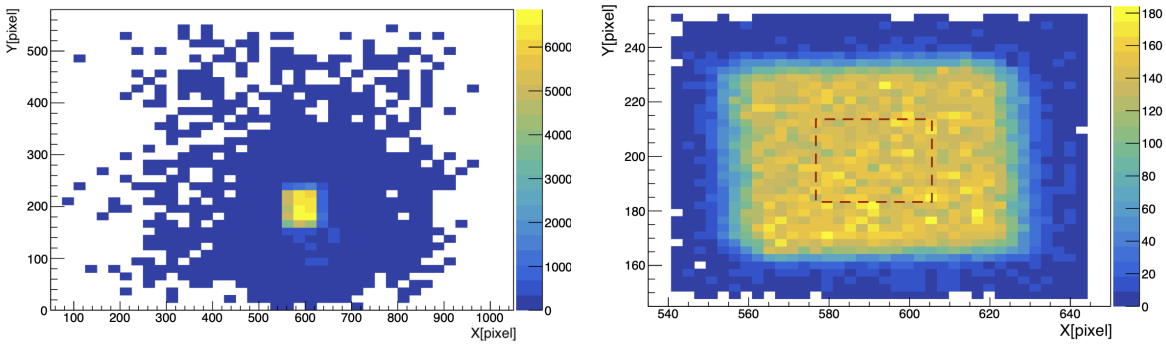


a) b)

Figure 5.6: *(a): example of distribution of the SiPM maximum pulse heights in a single batch (one bias voltage point) of collected data. The background is removed with a cut at 5 mV (red dashed line). (b): Distribution of the TOA coincidence between SiPM and DUT reconstructed with CFD method.*

Additionally, a geometrical cut based on the position where the DUTs were located inside the FE-I4 ROI is applied for the calculation of mean efficiency and mean charge collection. Since the ALTIROC discriminator threshold is set at 2 fC, the time resolution was computed only for events with the collected charge greater than this value. For the efficiency and the collected charge calculation, only the central region

0.5×0.5 mm^2 of the DUTs is considered (see Figure 5.7) to avoid the edge effects caused by the imperfection of tracking and running conditions (see Section 5.6.5).



a) b)

Figure 5.7: *(a): Occupancy map of reconstructed tracks on the DUT's $x-y$ plane in the full ROI of FE-I4 projection for a single batch. (b): Zoom-in of the same projection centered around the center of the sensor. The red dashed square represents the area where the efficiency and the collected charge is calculated. To be pointed out, that the sensor has a square shape, while on the figure it has a rectangular shape due to the scaling.*

5.3.1 Efficiency

The hit reconstruction efficiency is defined as a ratio between the number of reconstructed tracks for which the collected charge is higher than 2 fC and the total number of reconstructed tracks crossing the sensor:

$$\varepsilon = \frac{\#\text{Reconstructed tracks with } Q > 2 \text{ fC}}{\#\text{Total reconstructed tracks}} \tag{5.2}$$

Figure 5.8 shows an example of the 2D map of the efficiency as a function of the hit position for a single-pad sensor irradiated at $1.5\times10^{15}\text{n}_{\text{eq}}\text{cm}^{-2}$. As was mentioned before, the final efficiency is calculated in the central region of the pad (marked with the red rectangle on the plot) as an average. The efficiency is around 100% in the central region and drops at the edges of the pad. This drop is caused by the edge effects of the sensor. The smeared edges is the consequence of the non-uniform temperature distribution (the dry ice was melting throughout the data taking) and other factors such as the beam density profile non-uniformity.

5.3.2 Charge

The collected charge of the DUT is also calculated in the center of the pad (red square in Figure 5.8). The distribution of the charge collected for all the events is then fitted

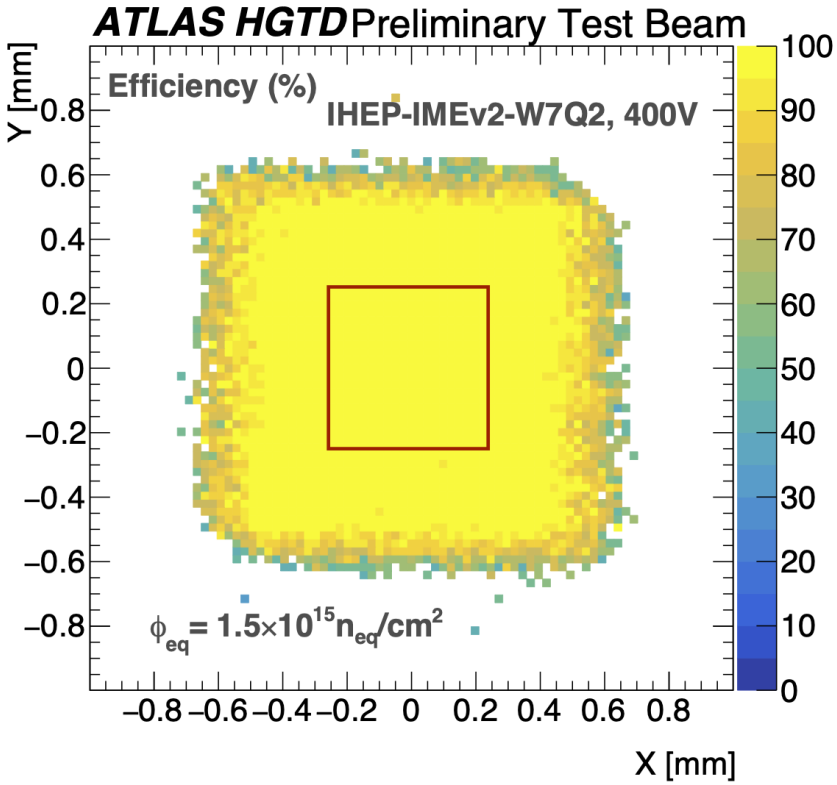


Figure 5.8: *Example of efficiency 2D map as a function of the hit position in the sensor plane with the region of interest of the pad (red square).*

with Landau-Gaussian convolution and collected charge of the DUT is defined as the Most Probable Value (MPV) from this fit as shown in Figure 5.9.

5.3.3 Time resolution

The time resolution is the key performance parameter studied. To calculate the DUT's time resolution, the distributions of the TOA differences between the DUTs, labelled as 1 and 2 in the Equation 5.3, and the time reference device (SiPM) are used:

$$\begin{cases} t_1 - t_2 \\ t_1 - t_{SiPM} \\ t_2 - t_{SiPM} \end{cases} \tag{5.3}$$

These three distributions $(t_i - t_j)$ are fitted with Gaussian function and the standard deviation σ_{ij} of each is extracted from the fits. An example of such distribution with fit is shown in Figure 5.10. Assuming that time resolutions of the devices are independent, the three measured resolutions σ_{ij} correspond to

$$\sigma_{ij} = \sigma_i \oplus \sigma_j \tag{5.4}$$

where σ_i and σ_j are the resolutions of the devices i and j respectively. This gives a system with three equations and three unknowns which can be easily solved analytically.

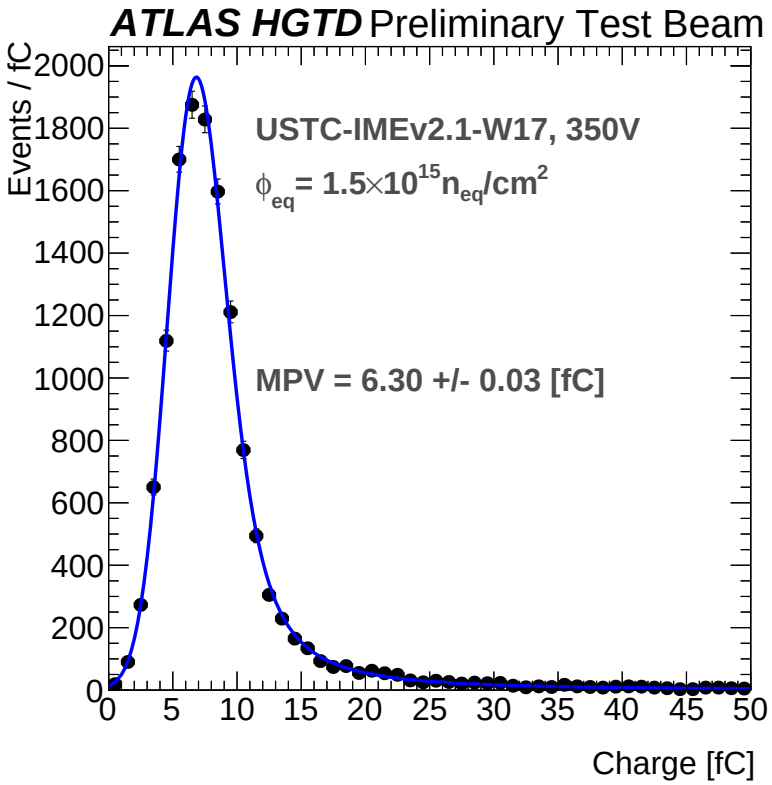


Figure 5.9: *Example of a charge distribution. The distribution is fitted with a Landau-Gaussian convolution. For this sensor, the collected charge, defined as the Most Probable Value, is* 6.30 ± 0.03 *fC.*

For example, considering two DUTs and a SiPM, the time resolution of the DUT1 (σ_{DUT1}) can be extracted as:

$$\sigma_{DUT1} = \sqrt{\frac{\sigma^2_{(SiPM-DUT1)} + \sigma^2_{(DUT1-DUT2)} - \sigma^2_{(SiPM-DUT2)}}{2}}, \tag{5.5}$$

where $\sigma_{(SiPM-DUT1)}$, $\sigma_{(DUT1-DUT2)}$ and $\sigma_{(SiPM-DUT2)}$ stand for the σ of the corresponding time difference distributions between SiPM, DUT1 and DUT2.

For DESY 2020, CERN SPS 2021 and some batches in DESY 2022 campaigns, this method was not sufficient, because one of the three devices was either too noisy or had technical problems (broken wire, readout board, TLU problems). In such cases, the resolution was calculated from the knowledge of the time resolution of the reference SiPM:

$$\sigma_{DUT1} = \sqrt{\sigma^2_{SiPM-DUT1} - \sigma^2_{SiPM}}\,. \tag{5.6}$$

The SiPM time resolution is supposed to be the same for all the tested DUT configurations. In DESY 2020 campaign the time resolution of SiPM was measured with a set of runs using Equation 5.5 and evaluated to be 50.8±0.1 ps. For DESY 2022, the SiPM time resolution was measured 24 times (in 24 batches) using Equation 5.5 and

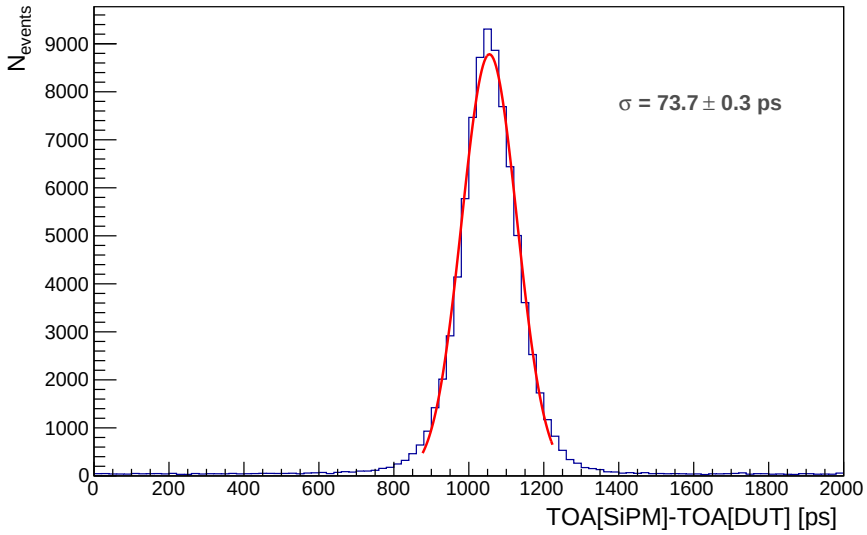


Figure 5.10: *Example of a TOA difference distribution between the SiPM and the DUT used for the time resolution calculation. The TOAs are calculated with the CFD method. The standard deviation σ is extracted from the Gaussian fit showed in red.*

its average resolution was found to be $\sigma_{SiPM} = 64.15 \pm 3.01$ ps and variations up to 10 % (see Figure 5.11) due to differences in running conditions (for example due to the current intensity fluctuations).

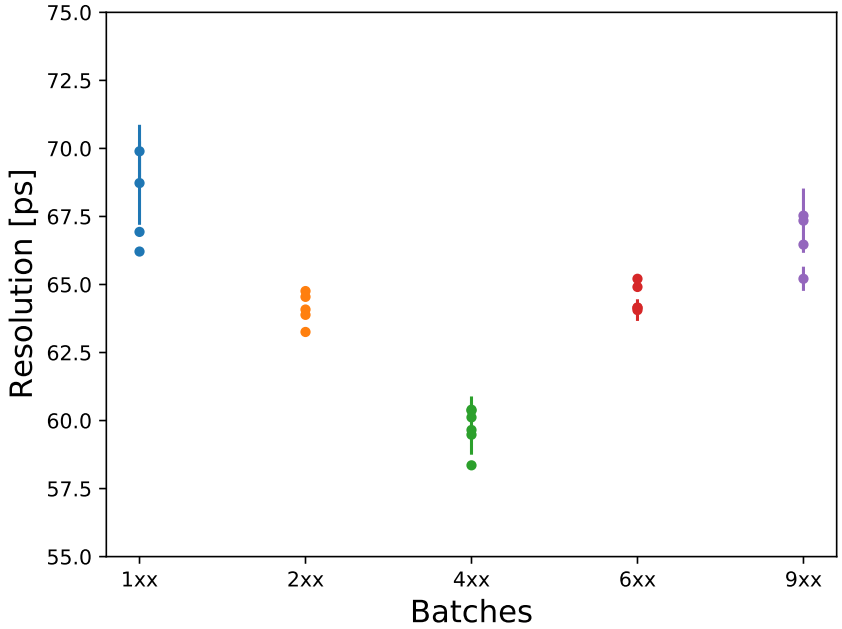


Figure 5.11: *The time resolution of SiPM measured batch by batch and calculated with Equation 5.5.*

5.4 Tested Sensors

The LGAD prototypes tested in the presented test beams were provided by different vendors: Novel Device Laboratory (NDL) of Beijing Normal University in China, Hamamatsu (HPK) in Japan, Fondazione Bruno Kessler (FBK) in Italy, Centro Nacional de Microelectrónica (CNM) in Barcelona, Institute of High Energy Physics (IHEP) in China and University of Science and Technology of China (USTC). The 2 latter ones were produced by Institute of Microelectronics of the Chinese Academy of Sciences (IME). The sensors also differed in geometry: they consisted either of a single pad or arrays of pads (1×3, 2×2, etc.). The schematic sketches of a single pad and a 2×2 array LGADs are shown on Figure 5.12. The overall active area of a pad was (1.3×1.3) mm^2 ± (0.15) mm^2 depending on the vendor. Another characteristic of the prototypes was the gain layer implant kind (boron, gallium, etc.) and its concentration (which can not be disclosed due to the agreement with vendors). Last, but not least, the tested prototypes had different irradiation levels. The irradiation of the sensors was done at the TRIGA reactor in Ljubljana with fast neutrons.

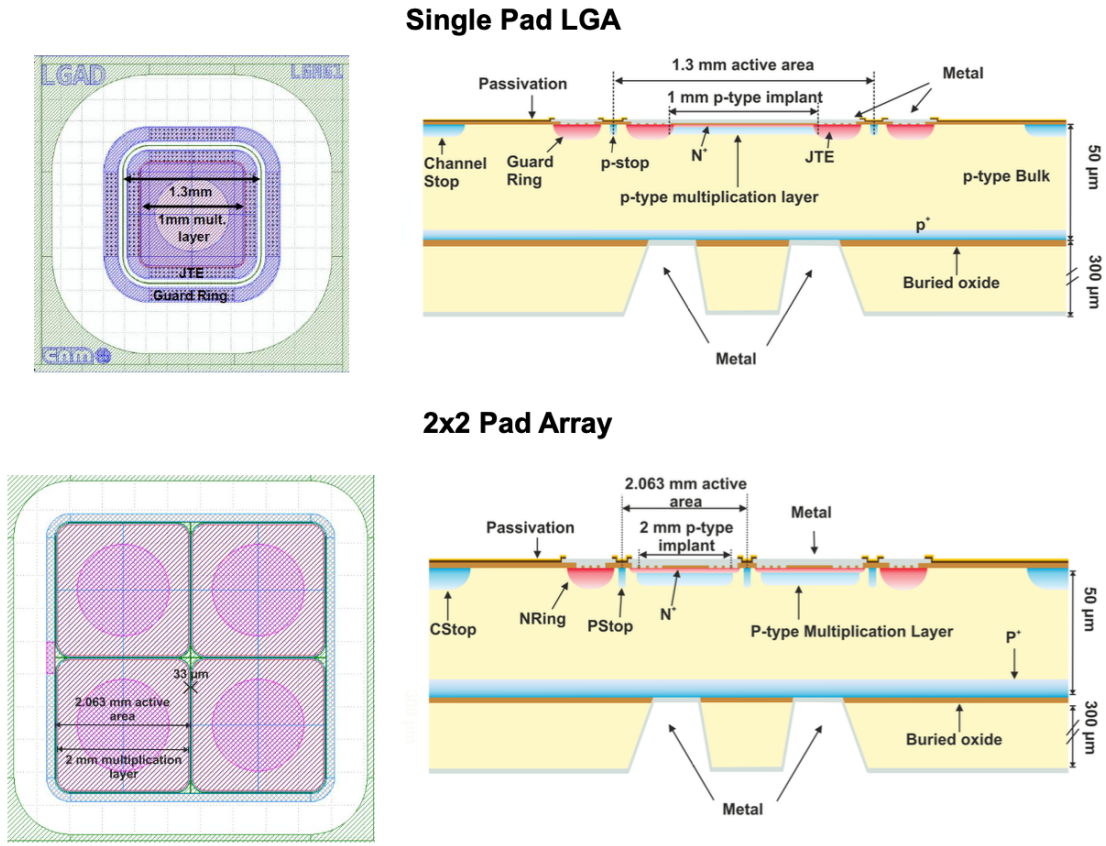


Figure 5.12: *Sketches of the single pad (top) and 2×2 array (bottom) LGAD sensors. A top view is shown on the left and a side view on the right (taken from [82]).*

5.4.1 DESY 2020 campaign

In the DESY 2020 campaign, overall 14 sensors were tested, however due to problems with TLU and FE-I4 operation, majority of the runs had an extremely poor statistics. Thus, the analysis is restricted to five sensors from four different vendors with a single bias voltage applied. In Table 5.1, the characteristics of the analysed sensors are presented.

Vendor	Sensor ID	Implant	Geometry	Fluence [$n_{eq}cm^{-2}$]
NDL	v3 B14	boron	single pad	0
FBK	UFSD3.2 W14	boron + carbon	single pad	1.5×10^{15}
HPK	P2 W28	boron	single pad	1.5×10^{15}
CNM	run12916 W1	boron	single pad	2.5×10^{15}
HPK	P1 Type 3.2 W11	boron	single pad	2.5×10^{15}

Table 5.1: *List of LGAD prototypes studied in the DESY 2020 test beam campaign. The information on the implant of the multiplication layer, the geometry and the irradiation level are given in the 3rd, 4th and 5th column respectively.*

5.4.2 DESY 2022 campaign

Overall, 11 sensors were tested during the test beam campaign. The tested sensors had three different geometries: single pad, 2×2 arrays, and 1×3 array. To be noted that the arrays had only one pad wire bonded and connected to read out, which allows to study only one pad. The studied LGADs with different geometry, irradiation and from different vendors are presented in Table 5.2.

Vendor	Sensor ID	Implant	Geometry	Fluence [$n_{eq}cm^{-2}$]
FBK	UFSD3.2 W19	boron + carbon	single pad	0
FBK	UFSD3.2 W19	boron + carbon	single pad	4×10^{14}
FBK	UFSD3.2 W19	boron + carbon	single pad	1.5×10^{15}
FBK	UFSD3.2 W19	boron + carbon	2×2 (1 bonded)	2.5×10^{15}
USTC-IME	v2.1 W17	boron + carbon	single pad	0
USTC-IME	v2.1 W17	boron + carbon	single pad	1.5×10^{15}
USTC-IME	v2.1 W17	boron + carbon	single pad	2.5×10^{15}
USTC-IME	v2.1 W19	boron + carbon	single pad	2.5×10^{15}
IHEP-IME	v2 W7 Q2	boron + carbon	1×3 (1 bonded)	0
IHEP-IME	v2 W7 Q2	boron + carbon	1×3 (1 bonded)	8×10^{14}
IHEP-IME	v2 W7 Q2	boron + carbon	1×3 (1 bonded)	1.5×10^{15}

Table 5.2: *List of LGAD sensors studied in the DESY 2022 test beam campaign. The information on the implant of the multiplication layer, the geometry and the irradiation level are given in the 3rd, 4th and 5th column respectively.*

5.5 Results of the DESY 2020 campaign

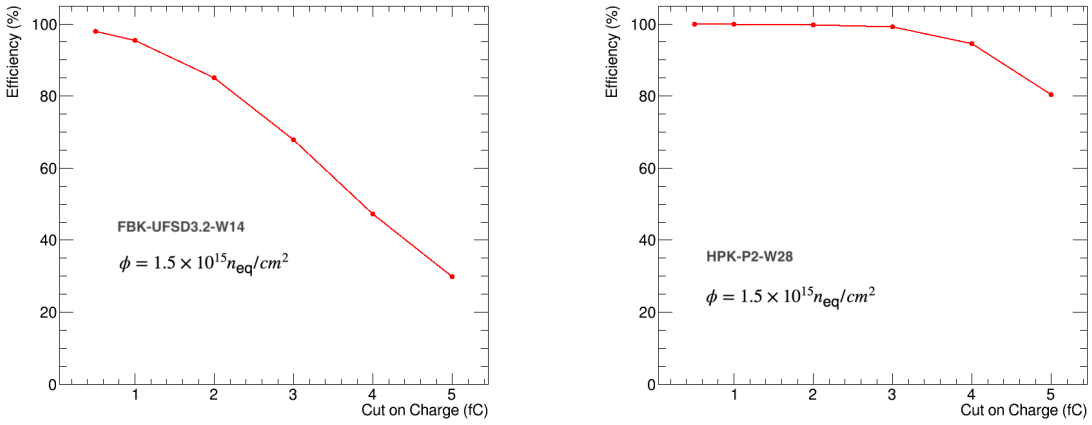
In the following subsections, the detailed LGAD performance results for irradiated sensors are presented with an overview of all the sensors in the end of the section. The uncertainties on the resolution were calculated from the error propagation composed of the standard deviation errors of the fits contributed in Equation 5.6 (see Figure 5.10). The uncertainty of the mean efficiency was calculated using the standard deviation. The uncertainty on the collected charge is taken from the fit uncertainty (see Figure 5.9).

5.5.1 Sensors irradiated at fluence of $1.5\times10^{15}\mathrm{n_{eq}cm^{-2}}$

Two sensors irradiated with a fluence of $1.5\times10^{15}\mathrm{n_{eq}cm^{-2}}$ were studied: FBK-UFSD3.2-W14 and HPK-P2-W28. The applied bias voltages for two sensors are significantly different. FBK-UFSD3.2-W14 was operated at 400 V, while HPK-P2-W28 was operated at 650 V. Thus, the performance differs a lot: the time resolution of FBK-UFSD3.2-W14 and HPK-P2-W28 is 50.4 ps and 43.2 ps respectively. Figure 5.13 shows the efficiency calculated with the different cuts on charge (0.5, 1, 2, 3, 4 and 5 fC) for FBK-UFSD3.2-W14 (a) and HPK-P2-W28 (b). The efficiency of FBK-UFSD3.2-W14 sensor drops drastically depending on the collected charge cut. At 4 fC, the charge required for the good ASIC operation (see Section 3.5), the efficiency is lower than 50 % (see Figure 5.13 (a)). Also, the efficiency of HPK-P2-W28 sensor is less than 95% at 4 fC (see Figure 5.13 (b)). At a 2 fC cut on charge (see Section 3.5), the efficiency of FBK-UFSD3.2-W14 reaches 85.05%, while for HPK-P2-W28 it is 99.79%. In terms of charge collection, both sensors show a relatively bad result for such fluence: 3.08 fC and 5.66 fC. Taking into account the project requirements for irradiated sensors at $2.5\times10^{15}\mathrm{n_{eq}cm^{-2}}$, FBK-UFSD3.2-W14 and HPK-P2-W28 do not show sufficient results in terms of efficiency and charge collection.

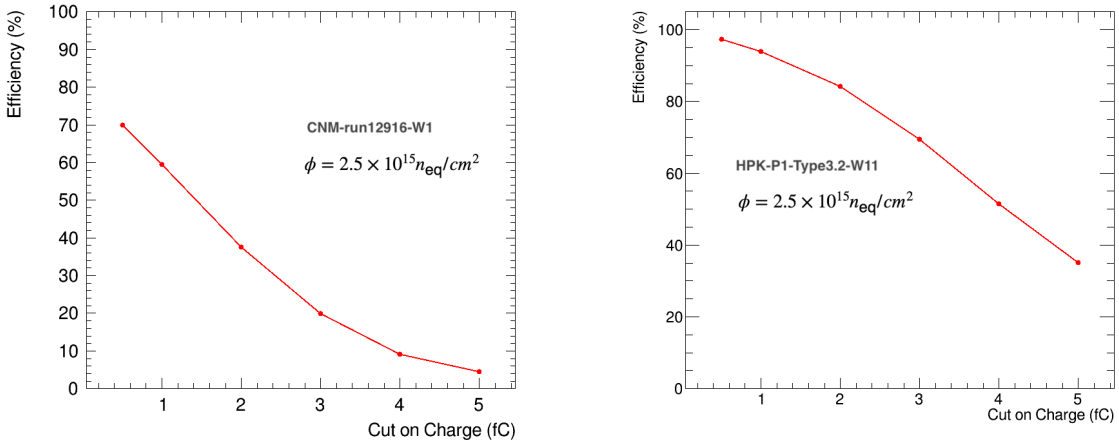
5.5.2 Sensors irradiated at fluence of $2.5\times10^{15}\mathrm{n_{eq}cm^{-2}}$

Sensors CNM-run12916-W1 and HPK-P1-Type3.2-W11 were irradiated at $2.5\times10^{15}\mathrm{n_{eq}cm^{-2}}$ and were analysed at bias voltage of 680 V and 750 V respectively. The CNM-run12916-W1 showed a very poor performance: efficiency of 37.59% (at a 2 fC cut on collected charge), time resolution of 100.6 ps and a collected charge of 1.19 fC. The HPK-P1-Type3.2-W11 showed a better performance having an efficiency of 84.3%, time resolution of 64.3 ps and a charge collection of 3.21 fC. However, it should be noted, that the HPK-P1-Type3.2-W11 was operated with a 70 V higher bias voltage. From Figure 5.14, showing the efficiency dependence on the charge cut applied, we clearly see the rapid efficiency drop with the higher collected charge requirement. At 4 fC, the CNM-run12916-W1 has an efficiency lower than 10% and HPK-P1-Type3.2-W11 lower than 55%, which is far away from the project requirement of 95 % at minimum.



a) b)

Figure 5.13: *Efficiency vs. collected charge cut for the sensors FBK-UFSD3.2-W14 at 400 V (a) and HPK-P2-W28 (b) at 650 V with fluence of* $1.5{\times}10^{15} n_{eq} cm^{-2}$.



a) b)

Figure 5.14: *Efficiency vs. collected charge cut for the sensors CNM-run12916-W1 at 680 V (a) and HPK-P1-Type3.2-W11 (b) at 750 V with fluence of* $2.5{\times}10^{15} n_{eq} cm^{-2}$.

In Table 5.3, the performance of the studied sensors is summarized including the information about temperature, bias voltage and fluence.

Sensor	**Temperature** [°C]	**Bias Voltage** [V]	**Efficiency** [%]	**Time Resolution** [ps]	**Charge** [fC]	**Fluence** [$\mathbf{n_{eq}cm^{-2}}$]
NDLv3-B14	20	200	100 ± 0	27.5 ± 2.5	13.5 ± 0.14	0
FBK-UFSD3.2-W14	-35	400	85.05 ± 0.42	50.4 ± 1.2	3.08 ± 0.03	1.5e15
HPK-P2-W28	-35	650	99.79 ± 0.05	43.2 ± 1.2	5.66 ± 0.03	1.5e15
CNM-run12916-W1	-30	680	37.59 ± 0.57	100.6 ± 1.5	1.19 ± 0.02	2.5e15
HPK-P1-Type3.2-W11	-30	750	84.3 ± 0.4	64.3 ± 1.2	3.21 ± 0.03	2.5e15

Table 5.3: *The results from the DESY 2020 beam test campaign in terms of efficiency, time resolution and charge collection, including the information on the temperature, bias voltage and fluence.*

5.5.3 Summary

The sensors studied at DESY 2020 campaign were operated at a very high bias voltage, which is far beyond the planned operational voltage of 550 V for the sensors with fluence of $2.5\times10^{15}n_{eq}cm^{-2}$ [20]. Moreover, six out of eight tested sensors irradiated at a fluence of $2.5\times10^{15}n_{eq}cm^{-2}$ underwent the SEB discussed in Section 3.4.2. Overall, these results showed that none of the studied sensors with boron diffused gain layer (see Table 5.1) satisfy the HGTD for the LGAD sensor. Thus, due to performance and mortality issues, the design of the LGAD for HGTD had to be reevaluated and new solutions for the gain layer implant had to be found. The solution seems to be a carbon enriched gain layer implementation that has been tested in DESY 2022 test beam campaign and discussed in the next section.

5.6 Performance of the carbon enriched sensors

As it was mentioned in Section 5.4.2, in DESY 2022 overall 11 sensors were studied from three various vendors at different fluences (see Table 5.2). The results of the studies are presented in the following subsections for each sensor separately. The uncertainties on the resolution were calculated from the error propagation composed of the standard deviation errors of the fits contributed in Equation 5.5 or Equation 5.6 (see Figure 5.10). The uncertainty on the efficiency was calculated using the standard deviation, while the uncertainty on the collected charge is taken from the fit uncertainty (see Figure 5.9).

Different sensors are studied with different bias voltages. The higher the accumulated fluency of the sensor is, the higher the bias voltage is needed to be applied in order to

compensate for the radiation damage of the sensor causing the degradation of the gain and performance. In Appendix A.1.6, the radiation damage effects on=f the silicon detectors including LGADs are described in more details.

5.6.1 FBK-UFSD3.2-W19 sensors with different irradiations

The sensor FBK-UFSD3.2-W19 was tested with four different irradiation levels (see Table 5.2). The performance of the sensors depending on the applied bias voltage in terms of time resolution, efficiency, and collected charge are shown in Figures 5.15, 5.16, and 5.17, respectively.

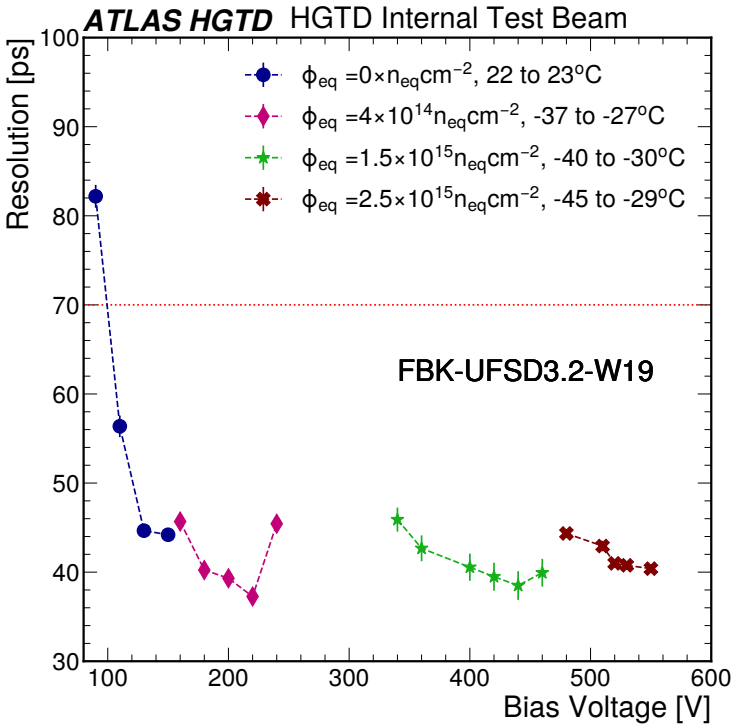


Figure 5.15: *Time resolution as function of applied bias voltage for the non-irradiated (blue circle) FBK-UFSD3.2-W19 and irradiated at fluence of 4×10^{14} (pink diamond), 1.5×10^{15} (green star) and 2.5×10^{15} (red cross) [$n_{eq}cm^{-2}$]. The red dashed line corresponds to the project requirement of at least 70 ps time resolution for the sensor irradiated at 2.5×10^{15}$n_{eq}cm^{-2}$. The project requirement on time resolution for the non-irradiated sensor is 35 ps.*

For time resolution, the general trend is an improvement when the bias voltage is increased (see Figure 5.15). Even at the highest irradiation, the sensor is able to reach 40.3±0.1 ps at bias voltage of 550 V. At irradiation with lower fluences, the device provides a resolution lower than 40 ps. Taking into account the project requirement of a time resolution being less than 70 ps for the highest irradiation level (at a fluence of

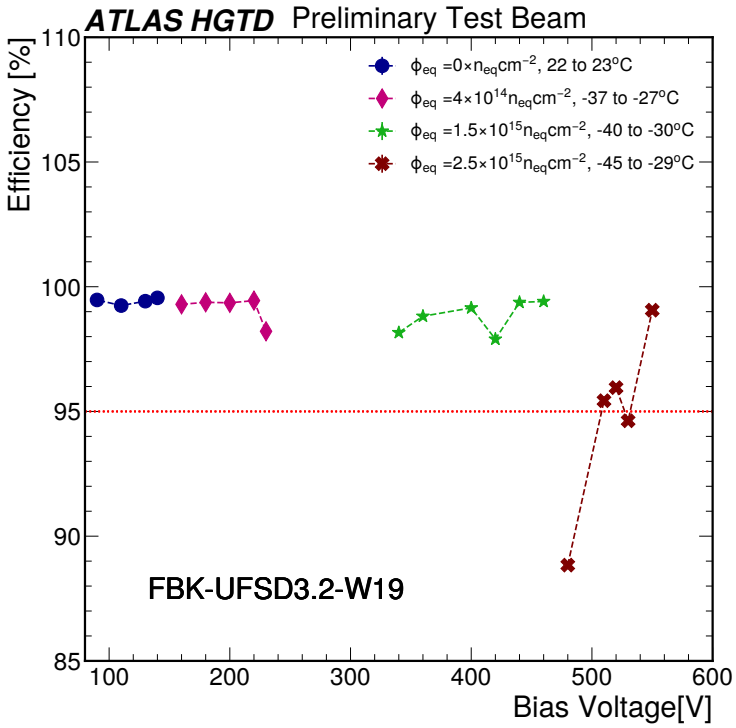


Figure 5.16: *Efficiency as function of applied bias voltage for the non-irradiated (blue circle) FBK-UFSD3.2-W19 and irradiated at fluence of 4×10^{14} (pink diamond), 1.5×10^{15} (green star) and 2.5×10^{15} (red cross) [n_{eq}cm^{-2}]. The red dashed line corresponds to the project requirement of minimum 95% efficiency for the sensor irradiated at 2.5×10^{15}n_{eq}cm^{-2}. The project requirement on efficiency for the non-irradiated sensor is above 99%.*

2.5×10^{15}n$_{eq}$cm^{-2}), the FBK-UFSD3.2-W19 sensor does meet the requirements at all tested bias voltages. To be noted that the time resolution is also influenced by the temperature conditions in which LGAD was tested. The non-irradiated sensor (blue circles in Figure 5.15) has significantly worse performance than the irradiated sensors because it was tested at the room temperature, while other sensors were tested at temperatures from -46°C to -27°C. Figure 5.18 shows the temperature record in each run throughout the data-taking for all irradiated sensors. For the sensor irradiated at a fluence of 4×10^{14} n$_{eq}$cm^{-2}, the last bias voltage point (240 V) was taken at the temperature higher than -29 °C (last 7 points in Figure 5.18) and the resolution for these runs goes up to 48 ps violating the general trend. Same effect can be seen for the last bias voltage (480 V) when the fluence 1.5×10^{15}n$_{eq}$cm^{-2} (corresponds to the last 11 temperature points in Figure 5.18), but is much less pronounced. The degradation of the time resolution of LGAD operated at the higher temperatures is a known feature. It comes from the fact, that the gain of LGAD depends on the temperature [92]. With the higher temperatures, the gain decreases leading to the worse time resolution.

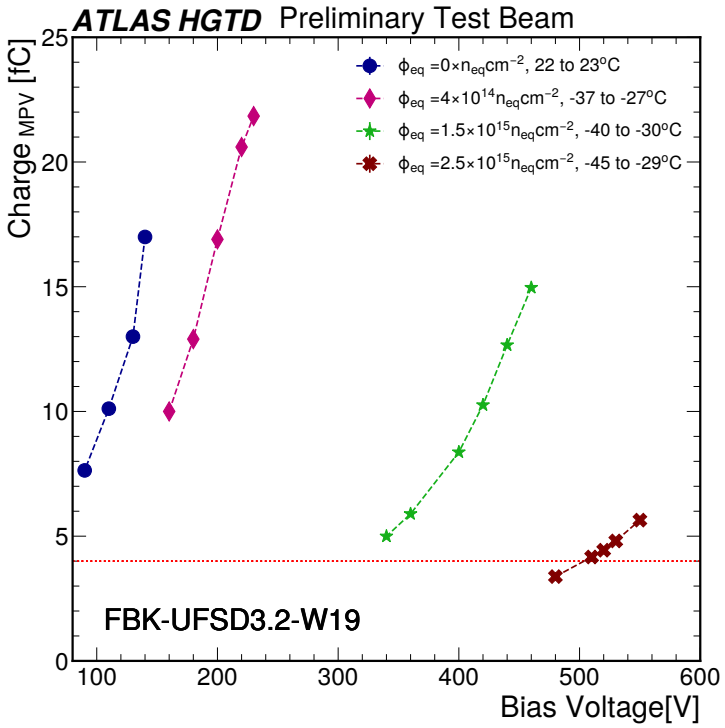


Figure 5.17: *Collected charge as function of applied bias voltage for the non-irradiated (blue circle) FBK-UFSD3.2-W19 and irradiated at fluence of 4×10^{14} (pink diamond), 1.5×10^{15} (green star) and 2.5×10^{15} (red cross) [$n_{eq}cm^{-2}$]. The red dashed line corresponds to the project requirement of at least 4 fC of collected charge for the sensor irradiated at 2.5×10^{15} $n_{eq}cm^{-2}$.*

The efficiency of the highly irradiated LGAD is expected to be higher than 95%. From the Figure 5.16, one sees that at the highest irradiation, the 95% efficiency is reached at bias voltage of 510 V, and for all the tested irradiations an efficiency of 99% and higher can be achieved. The general trend is that efficiency increases with the increased bias voltage. As for the time resolution, the efficiency performance also has outliers. In this case, the effect is not only due to the higher temperature as in case of the sensor irradiated at 4×10^{14} $n_{eq}cm^{-2}$, but also due to tracking difficulties caused by several unpleasant running conditions. One of the reasons is the evaporation of dry ice and the subsequent temperature change. Another reason is the dry ice replacement, which was changing the environment conditions. For instance, this was the case for the sensor irradiated at fluence of 1.5×10^{15}$n_{eq}cm^{-2}$. In the middle of the data taking, when the measurements with bias voltage of 420 V were being taken, the dry ice was replaced, causing the change of environment conditions and alignment. For the sensor irradiated at fluence of 2.5×10^{15}$n_{eq}cm^{-2}$, the data taking for the bias voltage of 530 V started with temperature -39 °C (see red crosses in Figure 5.18, starting from run 32), but due to the beam dump, the measurements were stopped and restarted with the beam

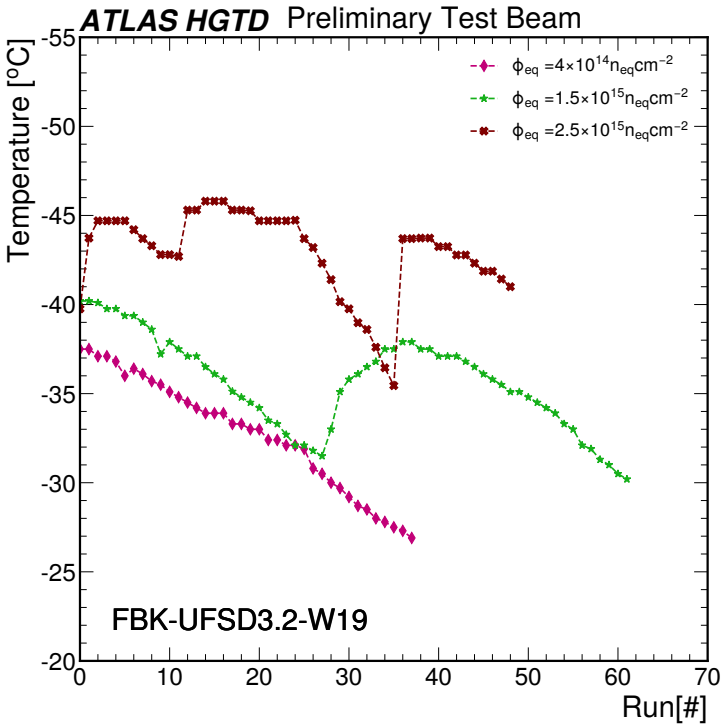


Figure 5.18: *The run by run temperature record for the sensor FBK-UFSD3.2-W19 irradiated at fluence of: 4×10^{14} (pink diamond), 1.5×10^{15} (green star) and 2.5×10^{15} (red cross) [$n_{eq}cm^{-2}$].*

recovery when the temperature in the box was -44 °C (run 34) after several hours. Another factor influencing tracking is the beam rate and beam energy fluctuations that were present from time to time.

The collected charge of the FBK-UFSD3.2-W19 meets the project target of 4 fC for the irradiation at a fluence of 2.5×10^{15}n$_{eq}$cm^{-2} already at bias voltage of 510 V (see Figure 5.17). With lower irradiation, the sensor is able to provide the charge collection of up to 15 fC (at irradiation with fluence of 1.5×10^{15}n$_{eq}$cm^{-2}) and 22 fC (at irradiation with fluence of 4×10^{14} n$_{eq}$cm^{-2}).

The statistical uncertainty of efficiency and charge are too small and are not seen under the marker (0.1% for efficiency and 0.03 fC for charge). All in all, the highly irradiated sensors have the similar performance to the non-irradiated ones at a higher applied bias voltage. The performance of the sensor irradiated at 2.5×10^{15}n$_{eq}$cm^{-2} is comparable to the non-irradiated one at the 360 V higher bias voltage and meets all the project requirements at bias voltage of 510 V.

5.6.2 IHEP-IMEv2-W7Q2 sensors with different irradiations

The sensor IHEP-IMEv2-W7Q2 performance follows the usual trend having the better time resolution, efficiency, and charge collection with the higher bias voltage (see Figure 5.19, 5.20, and 5.21). Figure 5.22 shows the temperatures for every run recorded with PT100.

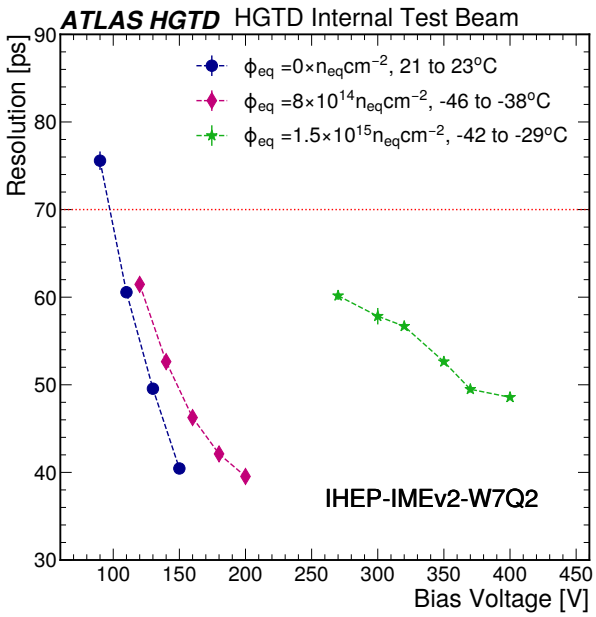


Figure 5.19: *Time resolution vs. applied bias voltage for the non-irradiated (blue circle) IHEP-IMEv2-W7Q2 and irradiated at fluence of 8×10^{14} (pink diamond) and 1.5×10^{15} (green star) [n_{eq}cm^{-2}]. The red dashed line corresponds to the project requirement of at least 70 ps time resolution for the sensor irradiated at 2.5×10^{15}n_{eq}cm^{-2}.*

At the highest studied irradiation (1.5×10^{15}n$_{eq}$cm^{-2}), the device provides the time resolution lower than 50 ps (see Figure 5.19), the efficiency > 99% (see Figure 5.20) and the charge collection of 11 fC (see Figure 5.21). In the efficiency, for 1.5×10^{15}n$_{eq}$cm^{-2} irradiation, the outlier from the trend (at bias voltage of 35 V) corresponds to the batch during which, the dry ice was replaced (run 34 on Figure 5.22). This sharp temperature difference in a single batch led to the worse tracking and decrease in efficiency. As expected, the sensors with higher irradiation reaches a performance of the non-irradiated devices at the higher bias voltage. It is important to point out that the sensor was not studied at the highest expected fluence of 2.5×10^{15}n$_{eq}$cm^{-2}. At the fluence of (8×10^{14} n$_{eq}$cm^{-2}) with the studied bias voltage, the IHEP-IMEv2-W7Q2 provides the time resolution lower than 40 ps, efficiency of around 98% and the charge > 7 fC. The non-irradiated sensor reaches the time resolution of 40 ps at the 150 V, efficiency > 99% and the collected charge of 16 fC.

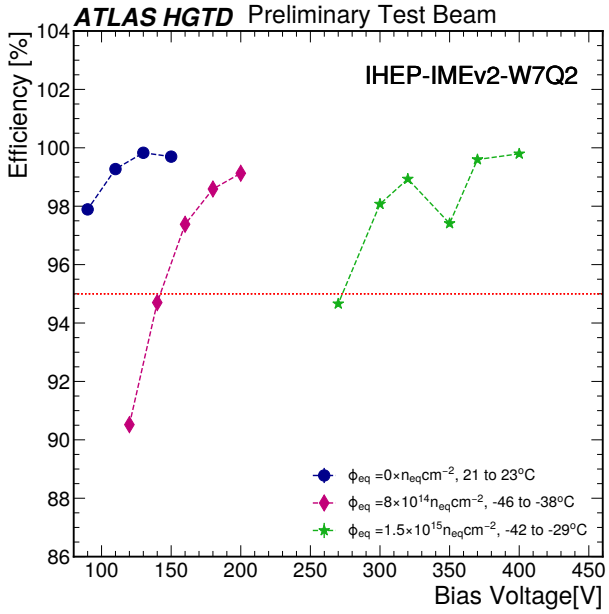


Figure 5.20: *Efficiency vs. applied bias voltage for the non-irradiated (blue circle) IHEP-IMEv2-W7Q2 and irradiated at fluence of 8×10^{14} (pink diamond) and 1.5×10^{15} (green star) [$n_{eq}cm^{-2}$]. The red dashed line corresponds to the project requirement of minimum 95% efficiency for the sensor irradiated at 2.5×10^{15}$n_{eq}cm^{-2}$.*

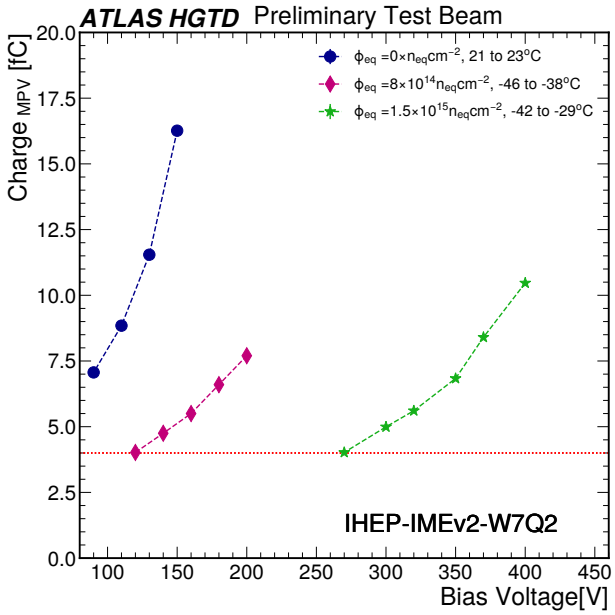


Figure 5.21: *Collected charge vs. applied bias voltage for the non-irradiated (blue circle) IHEP-IMEv2-W7Q2 and irradiated at fluence of 8×10^{14} (pink diamond) and 1.5×10^{15} (green star) [$n_{eq}cm^{-2}$]. The red dashed line corresponds to the project requirement of at least 4 fC of collected charge for the sensor irradiated at 2.5×10^{15}$n_{eq}cm^{-2}$.*

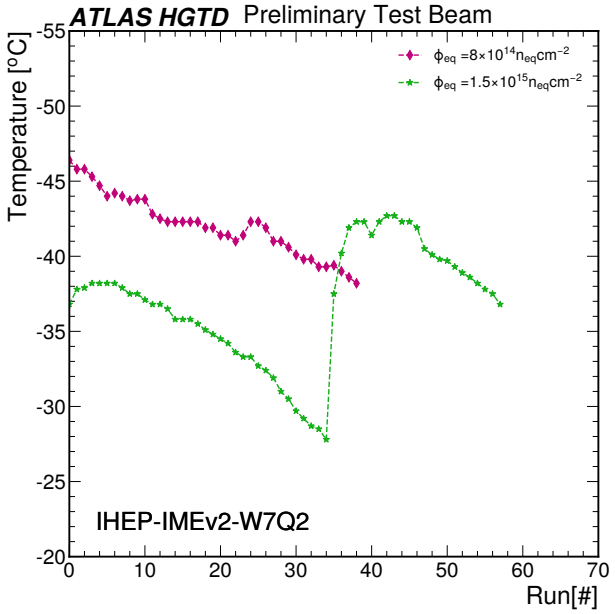


Figure 5.22: *The run by run temperature record for the non-irradiated (blue circle) IHEP-IMEv2-W7Q2 and irradiated at fluence of 8×10^{14} (pink diamond) and 1.5×10^{15} (green star) [$n_{eq}cm^{-2}$].*

5.6.3 USTC-IMEv2.1-W17 sensors with different irradiations

Based on the DESY 2022 data analysis, USTC-IMEv2.1-W17 meets the project requirements for the highly irradiated sensor. At the highest irradiation of 2.5×10^{15}n$_{eq}$cm^{-2}, its time resolution is lower than 50 ps already at 460 V (being well below the project goal, see Figure 5.23), the efficiency passes 95% at 490 V and gets up to 98.1% at 550 V (see Figure 5.24), and the charge collection is higher than 4 fC at bias voltage of 490 V reaching 5.5 fC at bias voltage of 550 V (see Figure 5.25).

The general trend of the performance enhancement with the higher applied bias voltage is present for the sensor with the exception in time resolution (see Figure 5.23) at the highest irradiation rate (2.5×10^{15}n$_{eq}$cm^{-2}). The outliers at the bias voltage of 500 V and 510 V are caused by the low statistics in data due to the technical problems during the data taking (especially at bias voltage of 500 V) and the higher temperature (runs 28–41 in Figure 5.26) comparing to the rest of the runs. Once the normal data taking was recovered and the dry ice was changed (starting from the run 42 in Figure 5.26), the expected behavior of the sensor was observed (see the bias voltage of 530 V and 550 V in Figure 5.23) Nevertheless, the time resolution variation is persistent within the error.

At the lower irradiation, the USTC-IMEv2.1-W17 is able to provide a time resolution of 43 ps, efficiency of 98.9% and the charge collection of 6.3 fC at 350 V. The non-

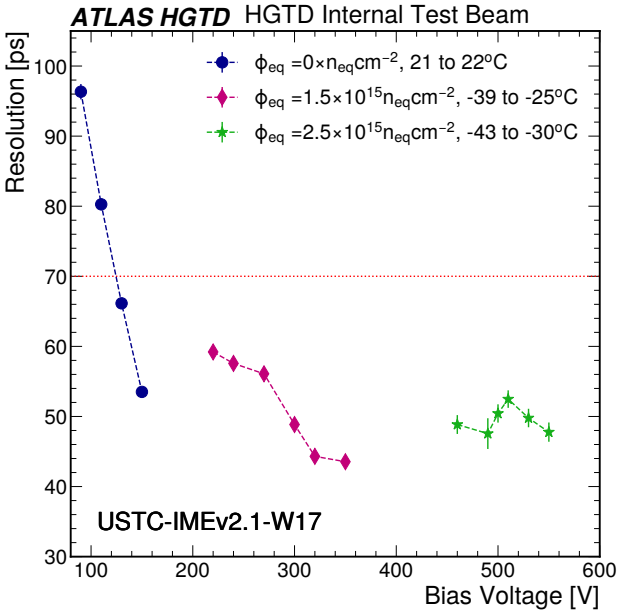


Figure 5.23: *Time resolution vs. applied bias voltage for the non-irradiated (blue circle) USTC-IMEv2.1-W17 and irradiated at fluence of 1.5×10^{15} (pink diamond) and 2.5×10^{15} (green star) [$n_{eq}cm^{-2}$]. The red dashed line corresponds to the project requirement of at least 70 ps time resolution for the sensor irradiated at 2.5×10^{15} $n_{eq}cm^{-2}$.*

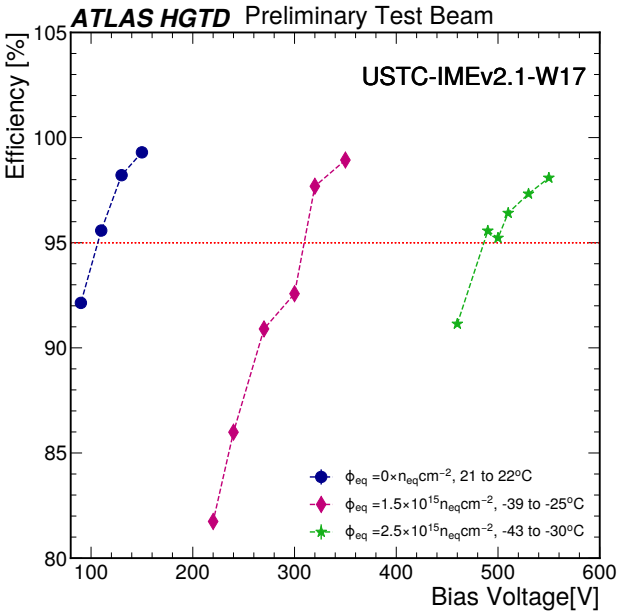


Figure 5.24: *Efficiency vs. applied bias voltage for the non-irradiated (blue circle)USTC-IMEv2.1-W17 and irradiated at fluence of 1.5×10^{15} (pink diamond) and 2.5×10^{15} (green star) [$n_{eq}cm^{-2}$]. The red dashed line corresponds to the project requirement of minimum 95% efficiency for the sensor irradiated at 2.5×10^{15} $n_{eq}cm^{-2}$.*

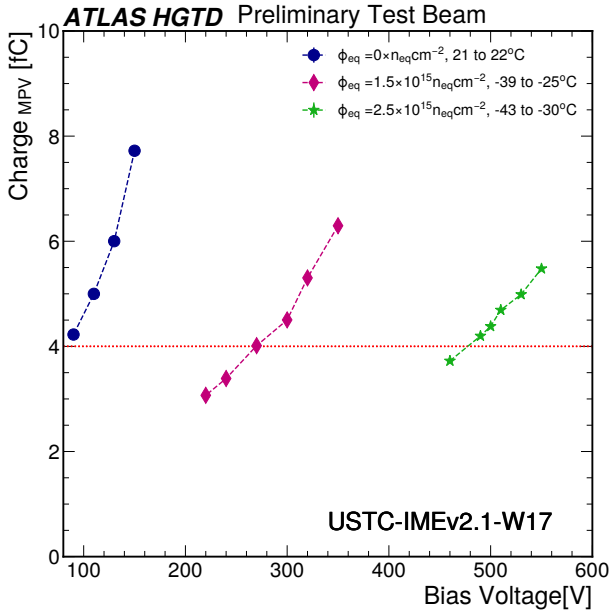


Figure 5.25: *Collected charge vs. applied bias voltage for the non-irradiated (blue circle) USTC-IMEv2.1-W17 and irradiated at fluence of 1.5×10^{15} (pink diamond) and 2.5×10^{15} (green star) [$n_{eq}cm^{-2}$]. The red dashed line corresponds to the project requirement of at least 4 fC of collected charge for the sensor irradiated at 2.5×10^{15}$n_{eq}cm^{-2}$.*

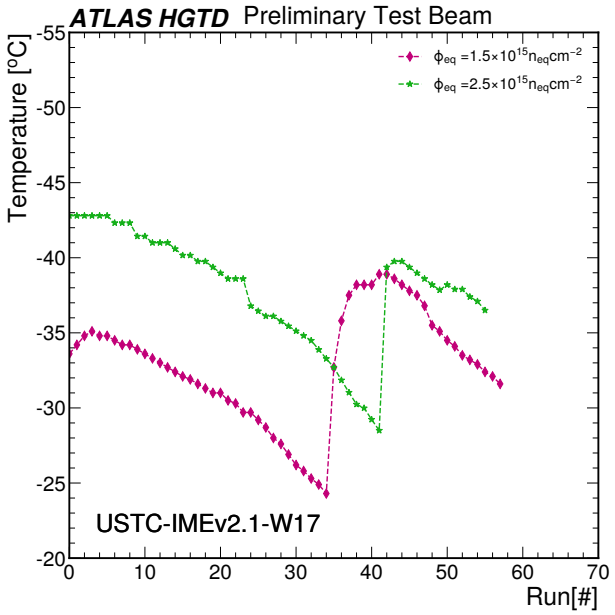


Figure 5.26: *The run by run temperature record for the non-irradiated (blue circle) USTC-IMEv2.1-W17 and irradiated at fluence of 1.5×10^{15} (pink diamond) and 2.5×10^{15} (green star) [$n_{eq}cm^{-2}$].*

irradiated sensor was tested at the room temperature, therfore its time resolution gets only up to 53 ps and collected charge up to 7.7 fC. Nevertheless, the efficiency goes above 99% at 150 V.

5.6.4 Sensor USTC-IMEv2.1-W19 irradiated at $2.5\times10^{15}\mathbf{n_{eq}cm^{-2}}$

The sensor USTC-IMEv2.1-W19 was studied at DESY with a single irradiation level of $2.5\times10^{15}\mathrm{n_{eq}cm^{-2}}$, the results of the analysis are presented in the Figure 5.27, 5.28, and 5.29.

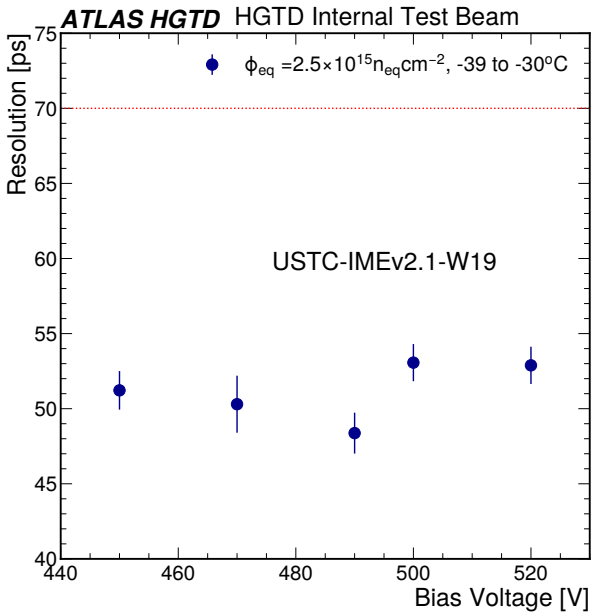


Figure 5.27: *Time resolution vs. applied bias voltage for the sensor USTC-IMEv2.1-W19 irradiated at a fluence of $2.5\times10^{15}n_{eq}cm^{-2}$ (blue circle). The red dashed line corresponds to the project requirement of at least 70 ps time resolution for the sensor irradiated at $2.5\times10^{15}n_{eq}cm^{-2}$.*

The time resolution is well below 70 ps for all the tested bias voltage from 450 to 520 V (see Figure 5.27). While running the test with bias voltage of 500 V and 520 V, the sensor was suffering from a quick raise of temperature (runs 30-38 and 39-48 in Figure 5.30 respectively), causing the worse time resolution than at bias voltage of 490 V. Nevertheless, the time resolution variation is consistent within the error.

At the tested bias voltage, which are 30 V lower than the ones USTC-IMEv2.1-W17 was tested with, the sensor does not meet the project requirements in terms of efficiency. With the bias voltage of 520 V, the device has an efficiency of 94.4% which is below the required 95% (see Figure 5.28). Therefore, the sensor does not meet the project requirements at $2.5\times10^{15}\mathrm{n_{eq}cm^{-2}}$ irradiation level.

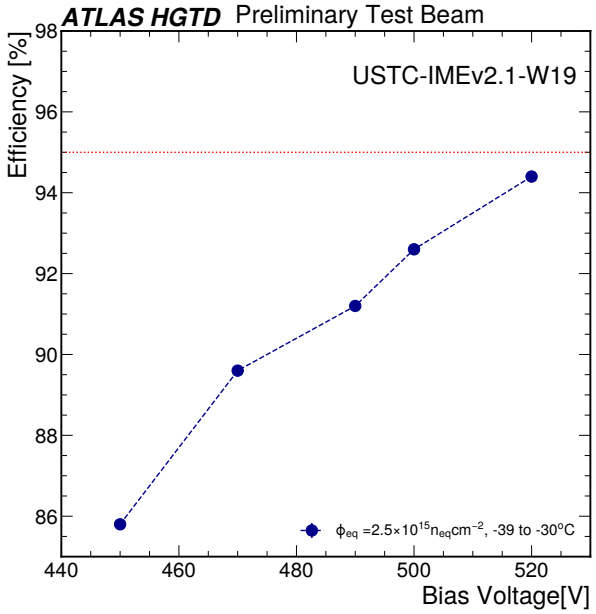


Figure 5.28: *Efficiency vs. applied bias voltage for the sensor USTC-IMEv2.1-W19 irradiated at a fluence of* $2.5\times10^{15} n_{eq} cm^{-2}$ *(blue circle). The red dashed line corresponds to the project requirement of minimum 95% efficiency for the sensor irradiated at* $2.5\times10^{15} n_{eq} cm^{-2}$.

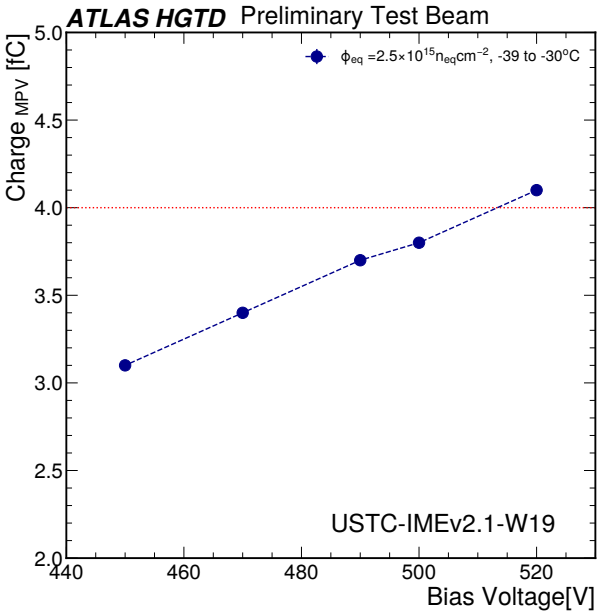


Figure 5.29: *Collected charge vs. applied bias voltage for the sensor USTC-IMEv2.1-W19 irradiated at a fluence of* $2.5\times10^{15} n_{eq} cm^{-2}$ *(blue circle). The red dashed line corresponds to the project requirement of at least 4 fC of collected charge for the sensor irradiated at* $2.5\times10^{15} n_{eq} cm^{-2}$.

The charge collection stays below the needed 4 fC with the appplied bias voltage up to 500 V anf reaches 4.1 fC at 520 V (see Figure 5.29).

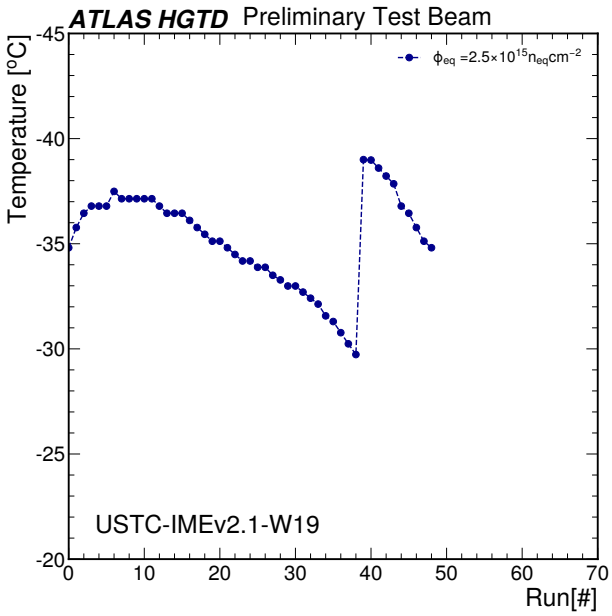
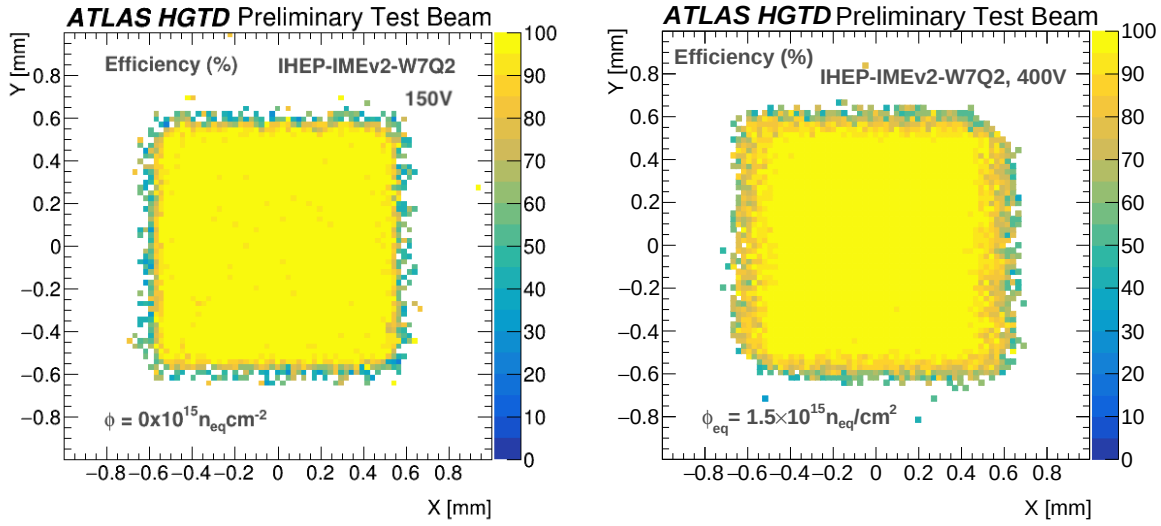


Figure 5.30: *The run by run temperature record for the sensor USTC-IMEv2.1-W19 irradiated at a fluence of 2.5×10^{15}n$_{eq}$cm^{-2} (blue circle).*

5.6.5 Efficiency uniformity

In addition to the characteristics described above, the sensors efficiency uniformity was also studied. As it is shown in Figure 5.31, the efficiency distribution for the non-irradiated sensor (a) is more uniform throughout the full pad area than the one for the highly irradiated sensor (b). The difference in the uniformities in the edges is due to the ice evaporation and the styrofoam box movement in case of the irradiated sensor. This movement caused a non-uniform temperature distribution in the cooling box and could cause a slight displacement of the sensor, degrading the track reconstruction in the DUT and subsiquentely efficiency. The non-irradiated sensor was tested at a room temperature without the cooling box.

Figure 5.32 shows the uniformity of efficiency along the y-axis for the sensors irradiated with a fluence of 1.5×10^{15}n$_{eq}$cm^{-2} (a) and 2.5×10^{15}n$_{eq}$cm^{-2} (b). The size of the efficiency plateau above 95% of the FBK-UFSD3.2-W19 is 863 μm and 1152 μm for the sensors irradiated with a fluence of 1.5×10^{15}n$_{eq}$cm^{-2} and 2.5×10^{15}n$_{eq}$cm^{-2} respectively. Their mean plateau efficiency is 99.4% and 99.1% respectively. The big difference of the plateau is not only due to the smearing of the tracking at the edges, but also due to the difference in the pad size of 2 sensors. The studied device at a higher irradiation was a 2×2 array with the bigger pads, while at a lower irradiation it



a) b)

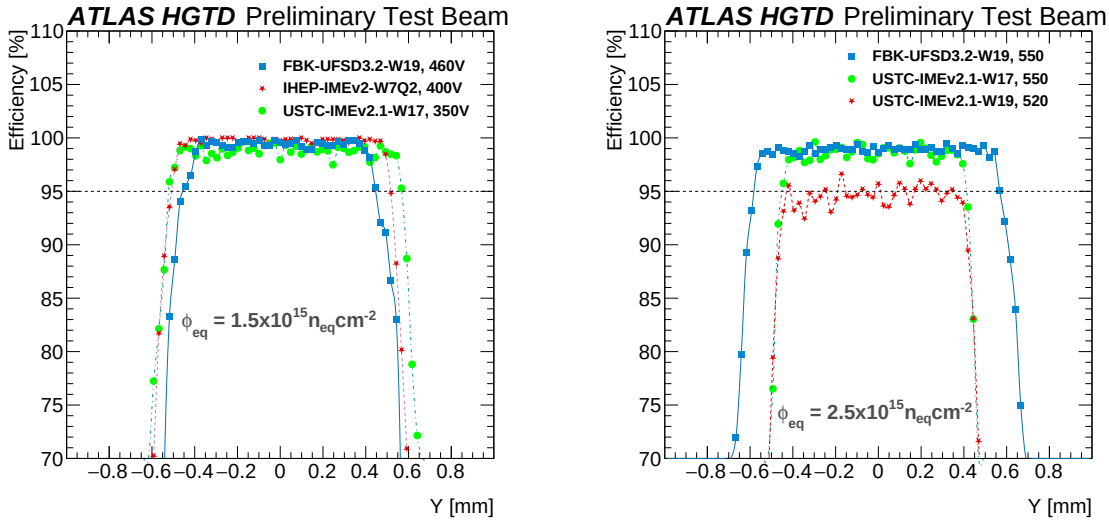
Figure 5.31: *Efficiency 2D map as a function of the hit position for the IHEP-IMEv2-W7Q2 pad non-irradiated (a) and irradiated at fluence of* $1.5\times10^{15} n_{eq}cm^{-2}$ *(b).*

was a single pad. The USTC-IMEv2.1-W17 sensor has an efficiency plateau of 1085 μm at irradiation with a fluence of $1.5\times10^{15}\mathrm{n_{eq}cm^{-2}}$ and 853 μm at $2.5\times10^{15}\mathrm{n_{eq}cm^{-2}}$, while the mean efficiency is 98.9% and 98.1% respectively. For this sensor, the plateau size difference is caused only by the worse tracking for the device irradiated at a fluence of $1.5\times10^{15}\mathrm{n_{eq}cm^{-2}}$ due to the fast temperature raise while taking the data at bias voltage of 350 V. The USTC-IMEv2.1-W17 also shows a higher variation of the mean efficiency at the plateau (1.5%) than FBK-UFSD3.2-W19 (<0.5%) for both irradiations. Sensor IHEP-IMEv2-W7Q2 irradiated with a fluence of $1.5\times10^{15}\mathrm{n_{eq}cm^{-2}}$ has a 987 μm wide plateau with the mean efficiency of 99.8%. Last, but not least, for the USTC-IMEv2.1-W19 irradiated with a fluence of $2.5\times10^{15}\mathrm{n_{eq}cm^{-2}}$ the plateau is below the required 95% (94.4%) with the variation of up to 2%.

Overall, the uniformity check showed the need of limiting the analysis of efficiency and charge collection in the center of the pad and the chosen area of 0.5×0.5 mm^2 seems to be sufficient.

5.6.6 Summary

The described results of the analysis of the test beam campaign at DESY in 2022 showed the sutisfactory performance of the tested LGAD sensors. The sensors FBK-UFSD3.2-W19 and USTC-IMEv2.1-W17 irradiated at a fluence of $2.5\times10^{15}\mathrm{n_{eq}cm^{-2}}$ do fulfill the HGTD needs in terms of time resolution (lower than 70 ps), efficiency (higher than 95%) and charge collection (at least 4 fC). The USTC-IMEv2.1-W17



a) b)

Figure 5.32: *Projections on the y-axis of efficiency for sensors irradiated at a fluence of 1.5×10^{15}n$_{eq}$cm^{-2} (a) and 2.5×10^{15}n$_{eq}$cm^{-2} (b). The dashed line at 95% corresponds to the efficiency required from the highly irradiated sensor.*

fulfills the requirements at 490 V, while FBK-UFSD3.2-W19 at 510 V. Sensors have the similar performance in terms of charge collection and efficiency taking in consideration the different running conditions like temperature, beam rate and so on. The time resolution of FBK-UFSD3.2-W19 is 40.3 ps at a bias voltage of 550 V, while the USTC-IMEv2.1-W17 time resolution is 46.9 ps at the same bias voltage. It should be taken into consideration, that the FBK-UFSD3.2-W19 was operated at a lower temperature (see Figure 5.18, 5.26) than USTC-IMEv2.1-W17. Unfortunately USTC-IMEv2.1-W19 did not meet the requirements for the efficiency at 2.5×10^{15}n$_{eq}$cm^{-2}, but it should be noted, that the sensor was operated at a slightly lower bias voltage than USTC-IMEv2.1-W17 and FBK-UFSD3.2-W19 and that the temperature conditions were worse than in the case of USTC-IMEv2.1-W17 and FBK-UFSD3.2-W19.

As for the sensors tested at 1.5×10^{15}n$_{eq}$cm^{-2}, the range of applied bias voltage for the sensors was different, being one of the reasons of different performance. The FBK-UFSD3.2-W19 was tested in the range of 340–460 V, IHEP-IMEv2-W7Q2 in the range of 270–400 V and USTC-IMEv2.1-W17 in the range of 220–350 V. The maximum achieved charge collection is 22 fC for FBK-UFSD3.2-W19, 11 fC for IHEP-IMEv2-W7Q2 and 6.3 fC for USTC-IMEv2.1-W17. The time resolution is also the best for FBK-UFSD3.2-W19, reaching 39 ps. The reason may be the higher applied bias voltage and lower operation temperature. In terms of efficiency, FBK-UFSD3.2-W19 and IHEP-IMEv2-W7Q2 also show slightly better performance (higher than 99%) than USTC-IMEv2.1-W17 which reaches a maximum efficiency of 98.9%. The performance

summary of the sensors irradiated at a fluence of $2.5\times10^{15}\mathrm{n_{eq}cm^{-2}}$ is presented in the Table 5.4.

Sensor	**Temperature** [°C]	**Bias Voltage** [V]	**Efficiency** [%]	**Time Resolution** [ps]	**Charge** [fC]
FBK-UFSD3.2-W19	-42	550	99.1 ± 0.1	40.3 ± 0.1	5.64 ± 0.03
USTC-IMEv2.1-W17	-38	550	98.1 ± 0.1	46.9 ± 0.5	5.48 ± 0.03
USTC-IMEv2.1-W19	-37	520	94.8 ± 0.1	52.9 ± 1.2	4.10 ± 0.03

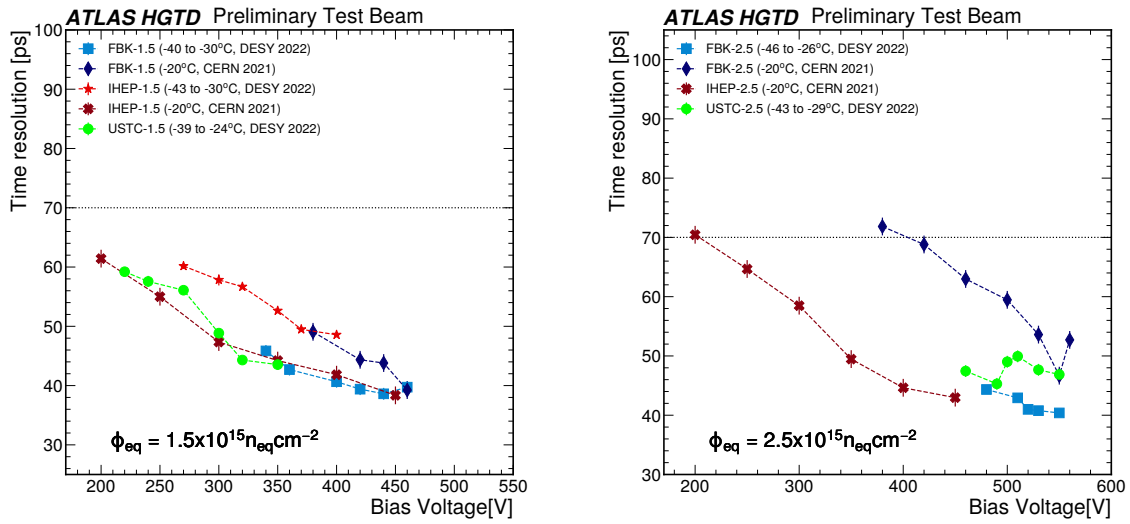
Table 5.4: *The results from the DESY 2022 beam test campaign in terms of efficiency, time resolution and charge collection at the highest measured bias voltage for the sensors irradiated at a fluence of* $2.5\times10^{15}n_{eq}cm^{-2}$.

5.7 Comparison of the results from DESY 2022 and CERN SPS 2021

As explained in the beginning of the chapter, the new generation of LGADs with the carbon diffusion of gain layer was tested both at CERN SPS 2021 and DESY 2022 campaigns. This section is dedicated to the comparison between these test beams results for two levels of irradiation: $1.5\times10^{15}\mathrm{n_{eq}cm^{-2}}$ and $2.5\times10^{15}\mathrm{n_{eq}cm^{-2}}$. On Figure 5.33, Figure 5.34, and Figure 5.35 time resolution, efficiency and charge of the sensors tested at DESY 2022 and CERN SPS 2021 for both fluences are shown. The main difference between the campaigns were the temperature at which sensors are operated and the time reference (see Section 5.1.2 and Section 5.1.1). At CERN, the temperature was stable at -20 °C and so the resolution steadily got better with the higher aplied voltage for all the sensors. At DESY, the temperature conditions were changing as discussed earlier.

For the same sensors tested both at CERN and DESY with the same bias voltage applied, the time resolution is different. This difference can reach 10 ps. This may be explained by the following factors. Different temperature conditions imply that the sensors tested at lower temperatures tend to have better time resolution. Another factor is the difference in the setup. At DESY, the time reference was a SiPM with a time resolution of 64.15 ps, while at CERN, the time reference was LGA35 sensor with a time resolution of 54.8 ps.

As shown on Figure 5.34, the difference in efficiency for the same sensors in the different campaigns reaches a maximum of 5%. This variation may be caused by the fact that the two analysis were using different tracking frameworks for the analysis (Proteus [93] for CERN and PaTrack [82] for DESY). The different running conditions may also have an impact: beam intensity, temperature stability, and so on. At the



a) b)

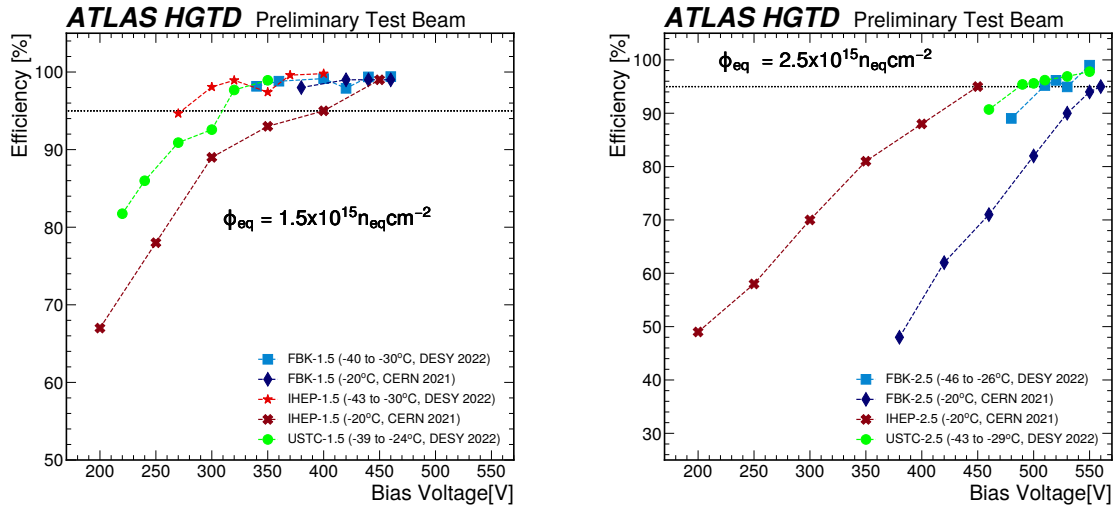
Figure 5.33: *Time resolution vs. applied bias voltage for the sensors FBK-UFSD3.2-W19 (from DESY 2022 and CERN SPS 2021), IHEP-IMEv2-W7Q2 (from DESY 2022 and CERN SPS 2021) and USTC-IMEv2.1-W17 (from DESY 2022) at fluences: $1.5\times10^{15} n_{eq}cm^{-2}$ (a) and $2.5\times10^{15} n_{eq}cm^{-2}$ (b). The black dashed line shows a project limit for the highly irradiated sensor.*

same time the collected charge shows a very good agreement for all the compared sensors (Figure 5.35).

5.8 Conclusion

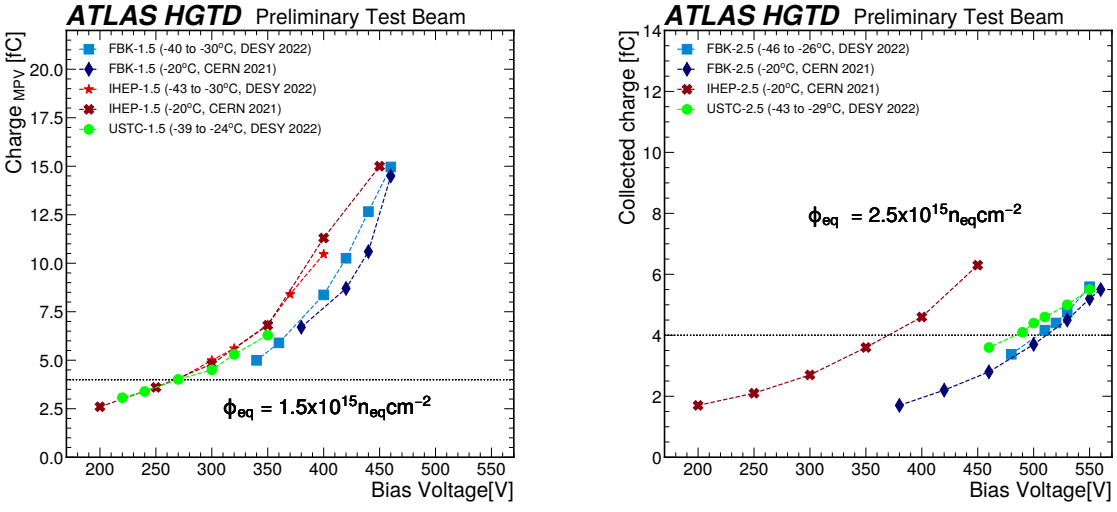
This Chapter was dedicated to the performance studies of the LGAD sensors for HGTD in test beams. The DESY 2020 campaign was an important milestone showing the issues of the highly irradiated sensors performance and the mortality problem of LGADs caused by Single Event Burnout. In Table 5.3, the performance of sensors studied at DESY in 2020 is summarized. None of the sensors fullfilled the project requirements in terms of efficiency, time resolution and charge collection. This campaign showed that the new design solution of the LGAD was needed.

The new generation of the LGADs with carbon diffused gain layer was tested at DESY in 2022 and CERN SPS in 2021 campaigns. The new design has proved to achieve the needed performance at lower bias voltage and avoid the Single Event Burnout. The performance summary of the sensors studied at DESY in 2022 irradiated at the highest expected irradiation level of $2.5\times10^{15} n_{eq}cm^{-2}$ is presented in the Table 5.4. The USTC-IMEv2.1-W17 and FBK-UFSD3.2-W19 LGADs do fulfill all the project requirements already at 490 V and 510 V respectively.



a) b)

Figure 5.34: *Efficiency vs. applied bias voltage for the sensors FBK-UFSD3.2-W19 (from DESY 2022 and CERN SPS 2021), IHEP-IMEv2-W7Q2 (from DESY 2022 and CERN SPS 2021) and USTC-IMEv2.1-W17 (from DESY 2022) at fluences: $1.5\times10^{15} n_{eq}cm^{-2}$ (a) and $2.5\times10^{15} n_{eq}cm^{-2}$ (b). The black dashed line shows a project limit for the highly irradiated sensor.*



a) b)

Figure 5.35: *Collected charge vs. applied bias voltage for the sensors FBK-UFSD3.2-W19 (from DESY 2022 and CERN SPS 2021), IHEP-IMEv2-W7Q2 (from DESY 2022 and CERN SPS 2021) and USTC-IMEv2.1-W17 (from DESY 2022) at fluences: $1.5\times10^{15} n_{eq}cm^{-2}$ (a) and $2.5\times10^{15} n_{eq}cm^{-2}$ (b). The black dashed line shows a project limit for the highly irradiated sensor.*

The sensor USTC-IMEv2.1-W19 also showed a good overall performance, however at the highest studied bias voltage of 520 V, its efficiency is 94.4 %, which is slightly lower than the project limit. It has to be noted, that the temperature was rising very rapidly while taking measurements at this bias voltage.

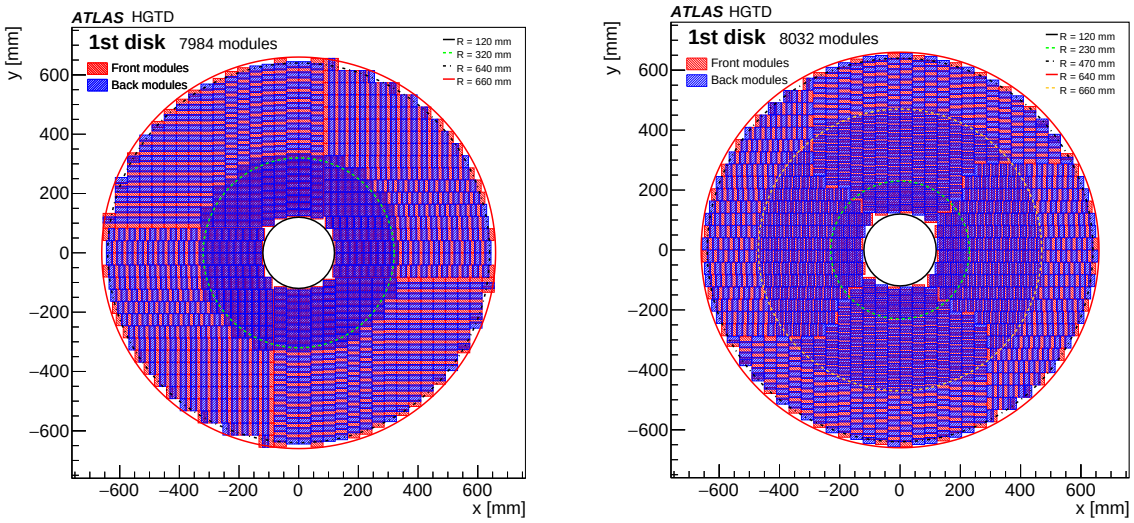
The comparison between the results from DESY 2022 and CERN SPS 2021 campaigns showed a good agreement taking into account the differences in running conditions and analysis. In addition, the IHEP-IMEv2-W7Q2 sensor irradiated at a fluence of $2.5\times10^{15}\mathrm{n_{eq}cm^{-2}}$ at CERN SPS also appeared to meet all the HGTD requirements.

Chapter 6

HGTD simulation and performance studies

This chapter is dedicated to the low-level, i.e. track reconstruction, performance studies of the HGTD. In order to mitigate the pile-up effects, the HGTD should be able to correctly associate the measured times to physics objects (or tracks). I worked on the new algorithm developement and implementation for the track-time association enhancement called *holes on track cleaning*. The first Section 6.1 is dedicated to the track reconstruction procedures in ITk and HGTD. In Section 6.2, the HGTD performance in terms of track-time association efficiency and resolution is discussed. The following Section 6.3 proposes the solutions for the HGTD tracking performance improvement, that is denoted as *TDR cleaning* and *Holes on track cleaning*.

The studies have been done with two HGTD layouts: a 2-ring geometry, see Figure 6.1 (a), that was a baseline geometry before year 2020, and the relevant 3-ring geometry, see Figure 6.1 (b) and Section 3.3.1. The two differ in the modules placement and the sensors overlap between two sides of one HGTD disc in different detector rings. For the 2-ring HGTD, the inner rings of two layers have an 80% overlap between the modules, while the outer rings overlap only 20%. For the 3-ring geometry, the levels of overlap between the layers are: 20%, 54% and 70%. For both geometries, an accurate GEANT4 simulation was used. The physics samples with the new 3-ring geometry were produced in April 2023. Hence, the vast majority of the studies and developements were done with the 2-ring HGTD geometry physics samples. Only the track-time association performance was re-evaluated with the new samples.



a) b)

Figure 6.1: *The placement of the modules in the (a) 2-ring and (b) 3-ring layouts. Taken from [20].*

6.1 Reconstruction of the charged particles trajectories

The procedure of track reconstruction involves extracting the properties of a charged particle (such as p_{T}, charge, etc.) from a series of measurements generated by its interaction with a sensitive detector. The objective is to identify the measurements that correspond to each particle, arrange them appropriately, and determine the trajectory of each particle. In many cases, these trajectories serve as the input for higher-level reconstruction procedures. Currently, the track reconstruction in ATLAS is using only spatial information. The time measurement provided by HGTD is also planned to be utilized in the future HL-LHC (see Chapter 7).

6.1.1 Track parametrization

To describe the characteristics of a particle's path accurately, it is essential to select appropriate parameters that can encompass all the relevant quantities of interest. When a magnetic field is present, it affects the charged particle's trajectory, and to fully specify its properties, the position, momentum, and charge of the particle in a global reference frame are required. Additionally, a time parameter is added after the track reconstruction in HGTD, which will be discussed in Section 6.1.4. The base parametrization used in ATLAS experiment is the following [41]:

$$\vec{x} = (l_0, l_1, \phi, \theta, q/p, t)^T, \tag{6.1}$$

where l_0 and l_1 are the local coordinates of the corresponding detector element, $\phi \in [-\pi, \pi)$ is the azimuth angle in transverse direction of the global frame, $\theta \in [0, \pi]$ is the polar angle in longitudinal direction of the global frame, q/p comprises the charge and inverse momentum of the particle and t is time. The (l_0, l_1) denote the two coordinates in the intrinsic frame of the surface and $(\phi, \theta, q/p)$ a representation of the momentum in the global frame. The (l_0, l_1) vary depending on the surface type, therefore the individual classes extending the base parametrization has been implemented for every surface type. The base parametrization is illustrated in Figure 6.2 (a, b).

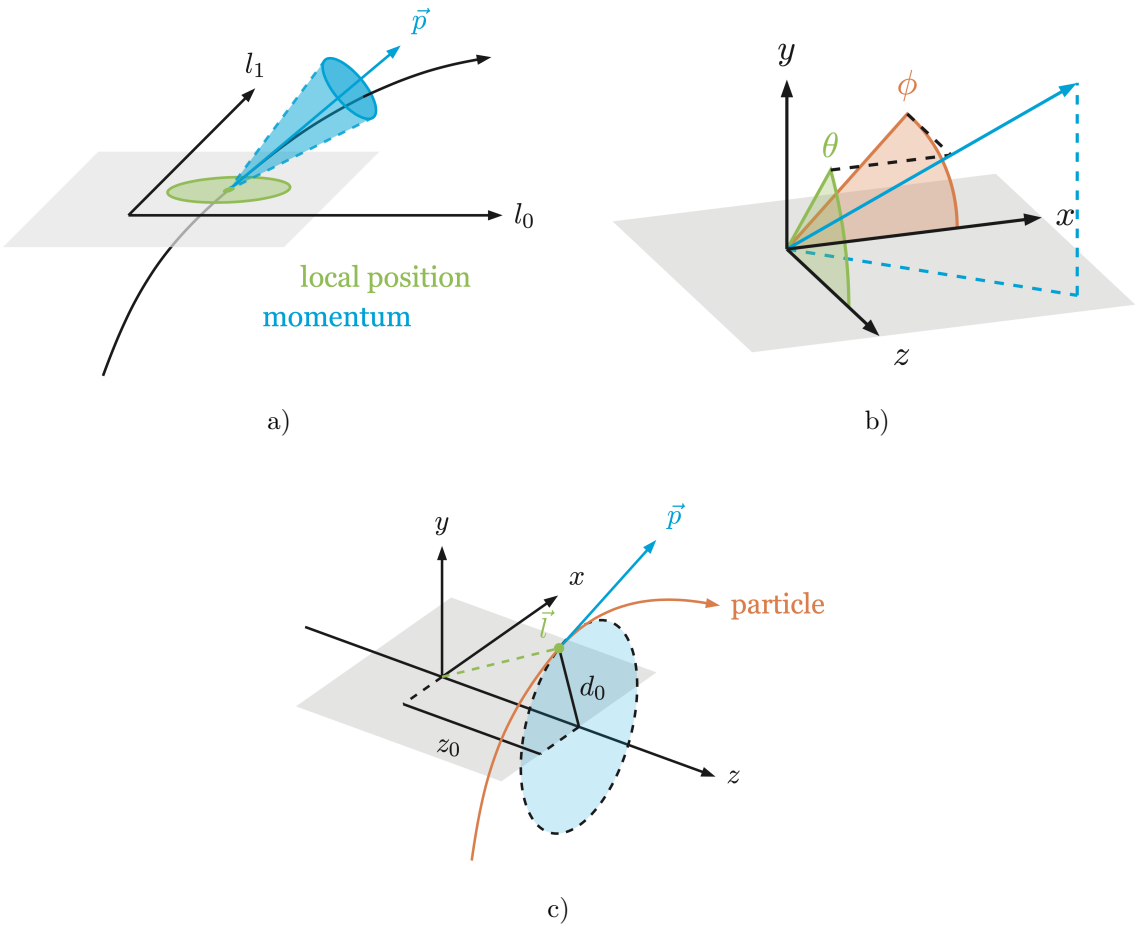


Figure 6.2: *The base (a, b) and perigee (c) parametrizations of a particle track with respect to a two-dimensional surface. (a) shows the local position, global momentum and their corresponding uncertainties (green elipse and blue cone). (b) displays the angles ϕ and θ in the transverse and longitudinal planes. (c) shows the perigee parametrization with the impact parameters d_0 and z_0, the point of closest approach $\vec{l}$ and the momentum vector $\vec{p}$. Taken from [41].*

It is also crucial to consider the uncertainties and correlations associated to the track parameters. These can be represented by the 6×6 covariance matrix, that takes into account the covariance of variables, cov(X, Y) for variables X and Y, and the

variances $\sigma^2(\mathrm{X})$:

$$C = \begin{bmatrix} \sigma^2(l_0) & \mathrm{cov}(l_0,l_1) & \mathrm{cov}(l_0,\phi) & \mathrm{cov}(l_0,\theta) & \mathrm{cov}(l_0,q/p) & \mathrm{cov}(l_0,t) \\ . & \sigma^2(l_1) & \mathrm{cov}(l_1,\phi) & \mathrm{cov}(l_1,\theta) & \mathrm{cov}(l_1,q/p) & \mathrm{cov}(l_1,t) \\ . & . & \sigma^2(\phi) & \mathrm{cov}(\phi,\theta) & \mathrm{cov}(\phi,q/p) & \mathrm{cov}(\phi,t) \\ . & . & . & \sigma^2(\theta) & \mathrm{cov}(\theta,q/p) & \mathrm{cov}(\theta,t) \\ . & . & . & . & \sigma^2(q/p) & \mathrm{cov}(q/p,t) \\ . & . & . & . & . & \sigma^2(t) \end{bmatrix}$$

6.1.2 Particle propagation

An essential component of track reconstruction is the ability to determine the trajectory of a charged particle based on its properties at a given point. This process is known as particle propagation or extrapolation and is used to predict the properties of a particle at a certain path length, usually on a detector element. The trajectory of a charged particle is determined by the magnetic field it encounters and the material effects. If a homogeneous magnetic field is applied, and there is no material interaction, the particle follows a helical path, which can be calculated purely analytically. However, numerical methods are still required to determine the intersections. In ATLAS detector, the magnetic fields are not fully homogeneous, therefore the corresponding differential equations of motions need to be solved using numerical integration techniques [41].

The numerical integration in ATLAS is done using the fourth order Runge-Kutta-Nyström method [94], that can be adopted to solve an initial value problem for the equation of motion in the magnetic field:

$$\frac{d^2\vec{r}}{ds^2} = \frac{q}{p}(\frac{d\vec{r}}{ds} \times \vec{B}(\vec{r})) = f(s,\vec{r},\vec{T}), \quad \vec{T} = \frac{d\vec{r}}{ds}, \tag{6.2}$$

where $\vec{r}$ is the global position, s is the path element, $\vec{T}$ is the normalized tangent vector and $\vec{B}(\vec{r})$ is the magnetic field at the global position.

Together with the track parameters prediction after travelling a certain distance also the uncertainties should be recalculated at each step of the extrapoaltion. The conversion between the initial and final covariance matrix from Equation 6.1.1 $C^i \to C^f$ is done using the Jacobian matrix:

$$C^f = J \cdot C^i \cdot J^T, \tag{6.3}$$

where Jacobian matrix is defined as

$$J = \begin{bmatrix} \frac{\partial l_0^f}{\partial l_0^i} & . & . & . & \frac{\partial l_0^f}{\partial (q/p)^i} \\ . & . & & & . \\ . & & . & & . \\ . & & & . & . \\ \frac{\partial (q/p)^f}{\partial l_0^i} & . & . & . & \frac{\partial (q/p)^f}{\partial (q/p)^i} \end{bmatrix}$$

Charged particles travelling through the detector interact with matter. As particles move through any material, they experience both elastic and inelastic interactions with the atomic structure of the matter, depending on the properties of the particle and may loose some energy or change the trajectories. These effects may be minimized by constructing the lighter tracking detectors and reducing the passive components, such as support structures, in the areas upfront the sensitive elements that can detect a particle.

In ATLAS tracking, there are two main methods to encounter the material interactions. The first approach employs a description that approximates the material interaction by averaging the actual material onto thin surfaces distributed throughout the detector. When particle propagation encounters one of these surfaces, it retrieves the material properties and applies the adjustments to the particle's properties and uncertainties. The second approach incorporates material effects continuously during propagation, rather than at discrete locations. This method is particularly useful for traversing volumes of dense material where the discretization of the material distribution is not as effective [41].

6.1.3 Track reconstruction in ITk

The first step of the track reconstruction in ITk is the pre-processing, where signals from the Pixel and SCT subdetector's (see Section 2.4.1) adjacent channels are combined to form clusters. These clusters are interpreted as deposits created by individual charged particles traversing through the subdetector. Following this, pairs of one-dimensional SCT clusters on each side of a sensor module or single pixel clusters are transformed into 3D space-points with position uncertainties determined by the sensor pitch and detector geometry.

Next step is the formation of track seeds consisting of triplets of space-points in the Pixel or SCT subdetectors which are likely to belong to the same track (see Figure 6.3). It is achieved by iterating the combinatorial triplets and successively filtering them. To enhance computational efficiency, track seeds undergo some basic selection criteria (cuts on momentum and impact parameters) to eliminate seeds that may generate low-quality tracks.

The initial sets of seeds are then used to build track candidates. For this, ATLAS employs the Kalman formalism, known as the Combinatorial Kalman Filter (CKF) [95], which is able to iteratively calculate a track estimate. The CKF starts from an initial track seed going outwards and consists of the following steps. First of all, the *prediction* of the track parameters on the next detection layer based on the current parameters. The predictions are then $filtered$ by incorporating the compatibile measurements on the detection element (see Figure 6.4 (a)). The compatibility of the measurement

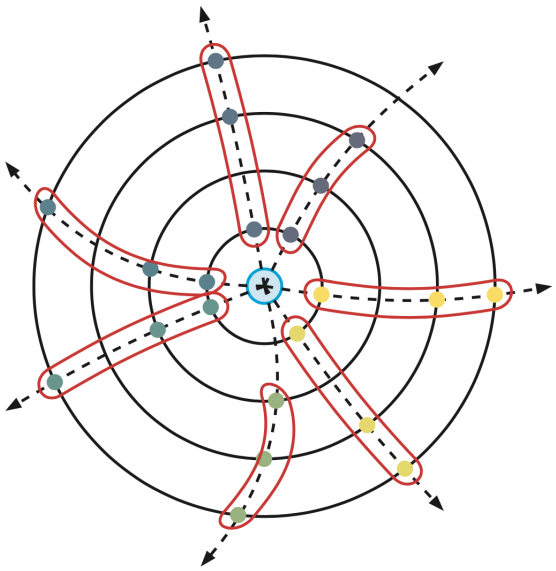
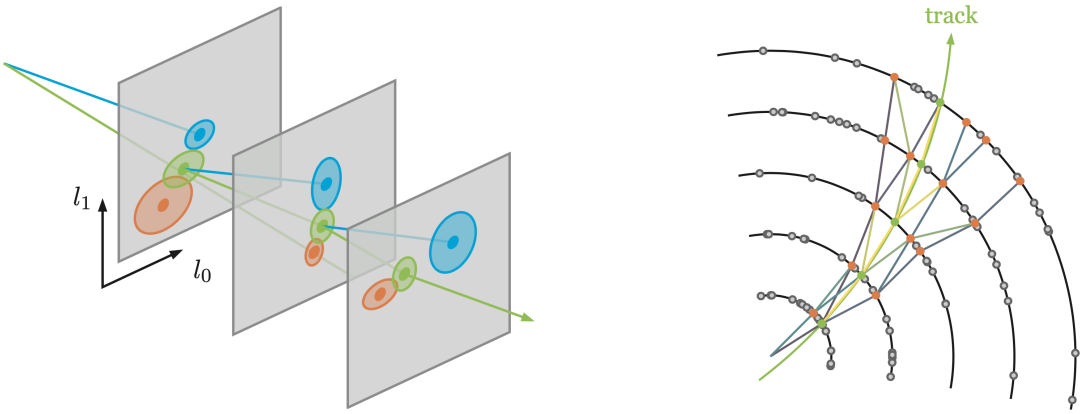


Figure 6.3: *Sketch of seeds in the transverse plane for a number of tracks on four layers. Seeds can combine hits on any three of these layers. The shown seeds appear compatible with having originated in the center of the detector, which is also drawn. Taken from [41].*

with the prediciton is estimated by the χ^2 analysis of the filtered residuals (difference between the measurement and the filtered prediction) in this step. Measurements with a large χ^2 are considered as outliers, which have low compatibility with the trajectory and therefore are discarded. Consiquently, a tree-like structure of compatible track candidates originating from a track seed is assembled, see Figure 6.4 (b).

After the tracks candidates are assembled, the *ambiguity resolution* step is run to reject the tracks that most likely don't belong to the real particles tracks. This is done by scoring the candidates based on their properties. The higher the score is, the higher the probability that the track candidate belongs to a real particle. The score of the candidate is based on the particle p_{T}, amount of the hits, whether the candidate shares or not hits with other candidates and other characteristics. One particular property accounted in scoring, which is of interest for the following studies (Section 6.3.2), is the amount of holes the candidate has. These are the track extraploation predictions on the active detector elements for which no compatible measurements were found.

Finally, the tracks that passed the ambiguity resolution are going through the final precision fit. This fit is done as part of the Kalman filter's *smoothing* phase, by walking back the steps and using information for the subsequent step $k+1$ to improve the track parameters at the current step k [41].



a) b)

Figure 6.4: *(a):The Kalman Filter steps with the prediction (blue) and the filtering (green) steps. The filtering updates the prediction with information from the measurement (orange). (b): A sketch of the way the CKF iteratively explores measurements from a seed outwards. Measurements are added successively, and can be shared between the resulting track candidates. Shown in green is a circular real trajectory.Taken from [41].*

6.1.4 Track-time association in HGTD

The track reconstruction in HGTD exploits the progressive Kalman filter and uses the tracks formed in ITk. The reconstruction starts from the track's last measurement in ITk, from which the track is extrapolated to the closest HGTD layer. The next step is the collection of the HGTD surfaces in the 4×4 cm^2 window around the prediction position, this window was selected after optimisation. After that, the extrapolations of the track on each selected surface are collected. In each surface, the HGTD hits are incorporated one by one to update the track parameters of the extrapolation (see Figure 6.5). The χ^2 of all the measurements are compared to find the best hit-prediction match. The measurement with the lowest χ^2 becomes a valid extension of the track and the procedure is repeated in the following HGTD layer. If no measurement with χ^2 lower than the threshold is found, the layer is skipped, the track extrapolation continues to the next HGTD layer and undergoes the same procedure. The maximum number of four hits can be assigned to a track (due to the HGTD geometry consisting of four layers per endcap). It is important to point out, that the hit's time measurement is not taken into account in the current track-hit association.

Once the hits in HGTD are associated to a track, it is possible to assign a time to it. The times from individual HGTD hits are aligned using the Time of Flight (TOF) correction, calculated by dividing the path length of the particle's track by the speed

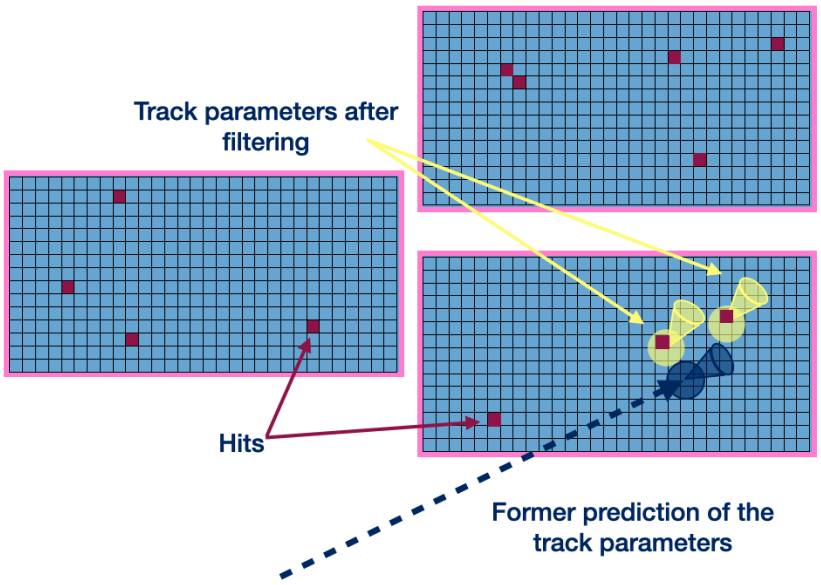


Figure 6.5: *Illustration of the track extention onto an HGTD layer (consisting of sensors, or surfaces, represented by the blue rectangles) with the track prediction on one of the surfaces (blue circle with the uncertainty cone), hits on the surfaces (red squares) and the updated track parameters (yellow sircles with the uncertainty cones).*

of light. The path length is assumed to be a straight line between the hit's position and the particle's origin $\vec{x} = (0,0,z_0)$. The time assigned to a particle is the arithmetic mean of the corrected hit's times. Additionally, the TOF correction allows to compare the reconstructed track time with truth track time (see Section 6.2.4). The resolution of the track-time σ_t^{track} depends on the number, n, of HGTD hits assigned to it and is expected to follow relation [51]:

$$\sigma_t^{track} = \sigma_t^{hit} / \sqrt[2]{n}, \tag{6.4}$$

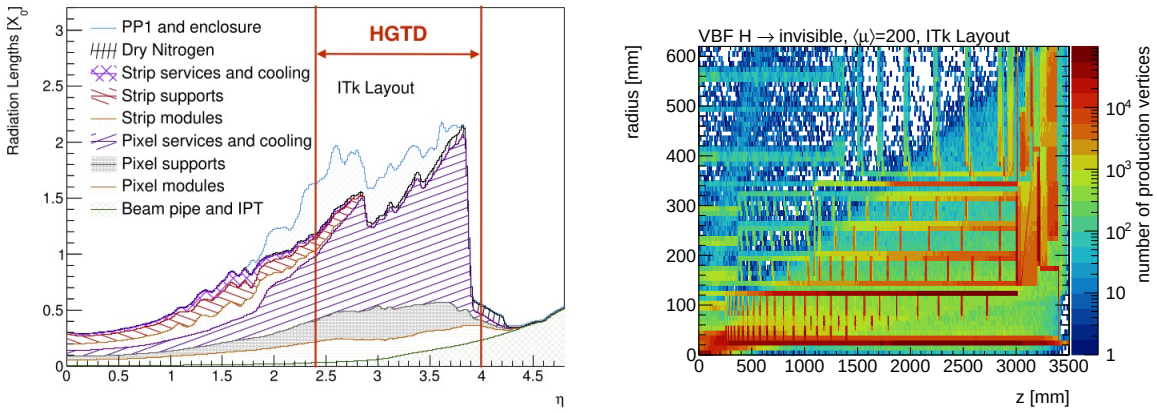
where σ_t^{hit} is the time resolution of a hit, which is 35 ps at the beginning of the HGTD operation.

6.2 Low-level performance of HGTD

6.2.1 Particles showering in ITk

The HGTD occupancy is influenced not only by the expected average number of p-p collisions per bunch crossing, but also by the quantity of material present in front of HGTD. This material induces hadronic and electromagnetic showering of particles passing through the ITk, leading to an increased number of secondary particles penetrating HGTD. The energy deposits created by these secondary particles in the HGTD's active sensor elements represent unwanted background that complicates the correct association of tracks with HGTD hits [51].

The total material budget of ITk results in a total radiation length ranging from 1.6 to 2.2 X_0 units in the entire coverage area of HGTD. Figure 6.6 (a) shows a stacked plot illustrating the different contributions to the material budget, with the largest contributions coming from the cooling equipment, supports, and services of the ITk pixel detector. The radiation length along η strongly depends on the incident angle of the particle penetrating the material. At a higher η, a particle crosses more material.



a) b)

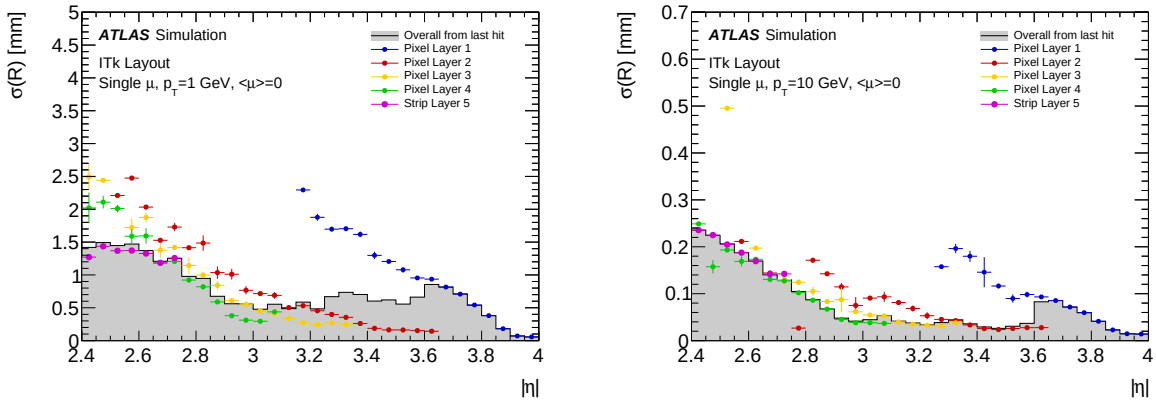
Figure 6.6: *(a): Material budget of ITk in units of radiation length X_0 as a function of the pseudorapidity η. The shown profile is used in simulation for the studies presented here, updated version can be found in Figure 2.19 (b). The two red lines show the HGTD acceptance region. (b): Position of truth associated production vertices of secondary particles that deposited energy in HGTD sensors, projected on two dimensions. Hot spots are found in the beam pipe and ITk services, notably the pixel detector services located at a radius of $r \sim 120\,\text{mm}$ [51].*

In Figure 6.6 (b), the production vertices of the secondary particles that leave hits in HGTD are shown. The truth information of the particles origin and decay is provided by the ATLAS simulation software. The structures with the highest amount of vertices correspond to the ITk active material layout (see Figure 2.18), the ITk patch panel and its enclosure [51]. The HGTD track-time reconstruction capabilities are particularly challenging in the region $|\eta| > 3.5$ due to the intensive showering in the pixel services located at a radius of roughly 120 mm.

6.2.2 Extrapolation uncertainties

The accuracy of the track extrapolation presented in Section 6.1.4 is influenced by the material budget in front of HGTD. The more material a particle penetrates before reaching HGTD, the worse the precision of extrapolation will be due to possible multiple scattering. Figure 6.7 shows the uncertainty of a track extrapolation to the HGTD depending on η for 1 GeV and 10 GeV muons. Another factor influencing the

extrapolation accuracy is the distance between the last hit in ITk associated to the propagated track and the HGTD. The resolution is worse for bigger distances. In most cases for the tracks with p_{T} higher than 1 GeV, the precision of the extrapolation is smaller than the LGAD pad size 1.3×1.3 mm^2. The extrapolation uncertainty plays a crucial role in the holes on track cleaning, a notion used for the HGTD track-time association enhancement discussed in Section 6.3.2.



a) b)

Figure 6.7: *The extrapolation on the HGTD surface uncertainty of the radius for muons with p_T =1 GeV (a) and p_T =10 GeV (b). The uncertainty is represented as a function of η. The extrapolations coming from different ITk layers are indicated with different colors. The grey area shows the overall uncertainties coming from all the locations of the last hits in ITk. The uncertainty depends on $|\eta|$ and on the layer in which the last measurement in ITk is registered, as extrapolation from layers closer to HGTD will render a smaller error. Taken from [20].*

6.2.3 Track-time association efficiency

Once a track coming from ITk is associated to the hit in HGTD, a time is assigned to it. The studies in this section evaluate the performance of track-time association using various samples, including single-muon and single-pion without pile-up, as well as a physics sample with Vector Boson Fusion produced H→Z($\nu\nu$)Z($\nu\nu$) (later mentioned as VBF H → invisible) with an expected HL-LHC pile-up of $\langle\mu\rangle = 200$. The simulation samples production can be found in the production task page [96] as part of the ATLAS Monte Carlo simulation campaign $mc15_14TeV$ using the ATLAS Software release 20.20. It was generated with Powheg v2 [97–99] interfaced to Pythia 8.186 [100] with AZNLO tune [101] and CT10 PDF set [102]. The studied tracks were required to have a p_{T} >1 GeV and be within the HGTD pseudorapidity acceptance (2.4<$|\eta|$<4.0). The simulations considered per-hit time resolution of σ_{hit} = 35 ps, corresponding to

non-irradiated LGAD sensor resolution, in the following figures denoted as Timing scenario "Initial" [51].

Since the track timing measurement is available when at least one HGTD hit is associated to the track reconstructed in ITk, the overall efficiency is identical to the efficiency of the track extrapolation (or track-time association rate, as denoted in the following figures of this chapter). The HGTD tracking efficiency is thus evaluated as a rate of the tracks with a time measurement in HGTD acceptance. In other words, it is a fraction of tracks in HGTD acceptance with a time assigned. The tracks in HGTD acceptance are divided into several categories depending on the purity (fraction of the HGTD hits originated from the primary particles, for which the maximum ratio is one) and the amount of expected hits in HGTD caused by primary particles (this information is extracted from the truth record of the simulation [1], for which the maximum number of hits is 4). First category $Prime\ frac. = 1$ includes the tracks for which all the associated HGTD hits were deposited by the primary particle. The tracks labeled $0.5 < Prime\ frac. < 1$ are the ones for which more than a half of associated HGTD hits were caused by the primary particle. The $Prime\ frac. = 0.5$ and $0 < Prime\ frac. < 0.5$ categories represent the tracks with a half and less than a half (but more than 0) of HGTD hits deposited by the primary particle respectively. For example, if a track from ITk is associated with 3 HGTD hits but only one of them is from the primary particle associated with this track, than it falls into the category $0 < Prime\ frac. < 0.5$.

Two more categories include the tracks for which all the assigned HGTD hits originate from non-primary particles. The tracks from $Confusion$ category are associated to non-primary hits, even though the truth particle associated to the track left primary hits in HGTD (minimum one and maximum four hits). The $Misassignment$ category denotes the particles tracks that does not leave any primary hit in HGTD and to which the time (or HGTD hit/hits) is assigned wrongly.

The efficiency studies were initiated with the single particle samples ($\langle\mu\rangle = 0$) including muons and pions. Figure 6.8 shows the track-time association efficiency with tracks splited into the categories described above as a function of η for 45 GeV single-muons (a) and single-pions with $p_{\mathrm{T}} \in (0.1, 5)$ GeV (b). Figures 6.8 (c) and (d) show the efficiency splited into 2 categories: $Correctly\,reconstructed$, representing the tracks with $Prime\ frac. > 0.5$, and $Misassignment$, that includes the tracks with $Prime\ frac. \leq 0.5$. The $Confusion$ category is not present due to the absence of the pile-up in these samples.

[1] The truth information available for the current studies is limited in the sense that it is only possible to differentiate primary hits and non-primary hits. Secondary hits that originate from the primary particle and likely give the correct track time can't be separated from secondary hits coming from pile-up. Thus the fraction of correct time assignment might be underestimated [51].

Figures 6.8 (a) and (c) show that for muons, the rate of correct track-time association is above 95% for majority of the η bins. This behavior is anticipated, since muons barely interact with the ITk material they pass through and do not shower before reaching HGTD. The sensors coverage in HGTD affects the efficiency: this can be seen in the small drop in the track-time association rate for $\eta < 3.0$, where the sensors overlap between two sides of one HGTD layer is smaller than that for the higher η, see Figure 6.1 (a). In the last η bin, the small efficiency decrease is caused by the fact that the sensors do not fully cover the area of the innermost radius of HGTD ~ 120 mm, see Figure 6.1 (a).

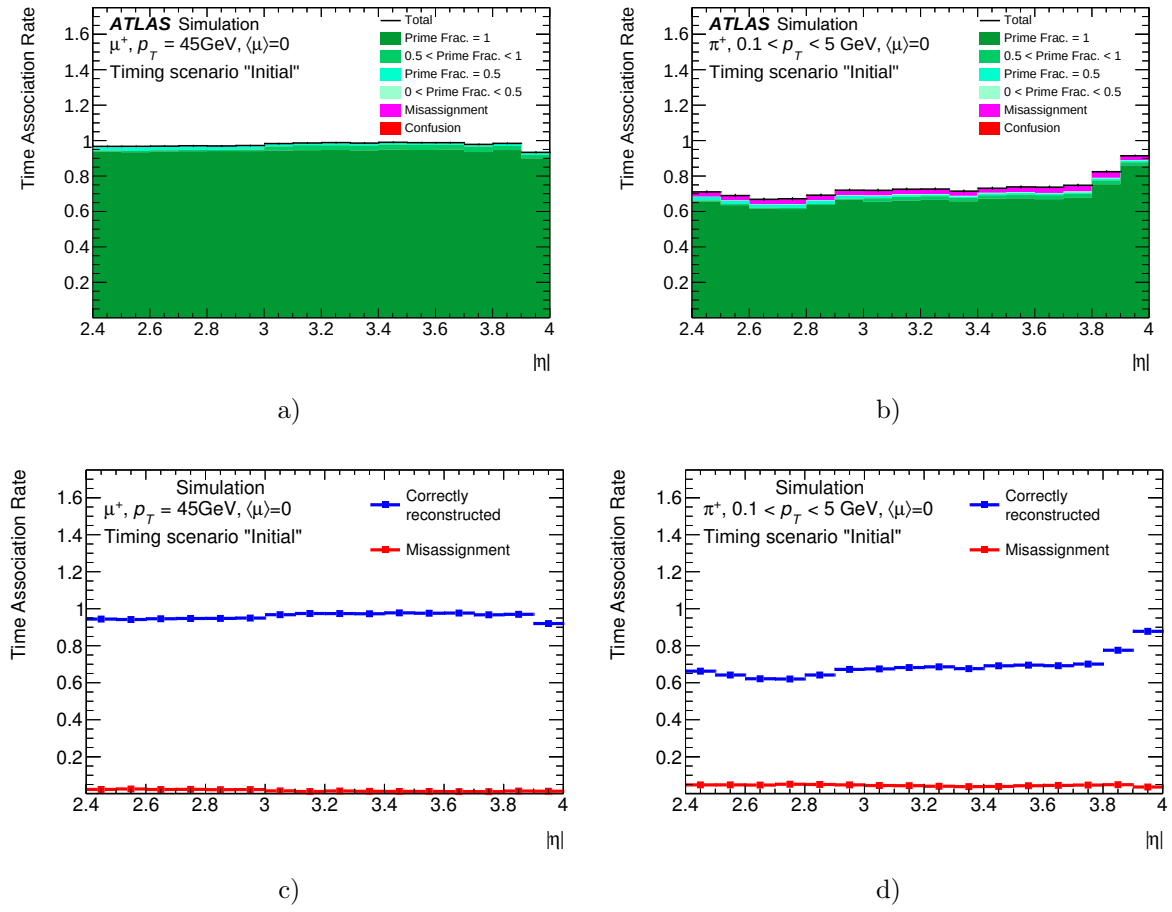


Figure 6.8: *Overall track-time association rate for tracks as function of pseudorapidity for single-muon (a, c) and single-pion (b, d) events without pile-up. The graphs (a) and (b) show the bin-by-bin breakdown of correct (green shades) and incorrect (red/magenta) hit associations described in the text. The graphs (c) and (d) show the simplified categorisation of the tracks ratio: correctly reconstructed tracks with Prime frac.* > 0.5 *(blue) and misassigned tracks with Prime frac.* ≤ 0.5 *(red). Taken from [20].*

The problem of particles shower in ITk is well represented in the case of charged pions. They actively interact with the material and about 30% of pions shower before

reaching HGTD and thus do not deposit a hit there. The products of the showering leave the hits classified as "secondary" in HGTD and are typically located too far away from the initial pion extrapolation to be accepted by the χ^2 cut used in the track extension. This leads to a significant drop in the tracking efficiency as seen on Figure 6.8 (b) and (d) [51]. The efficiency of pion track reconstruction is coherent with the material budget showed in Figure 6.6 (a). It drops in the range $2.4 < \eta < 2.8$, where the amount of ITk suports and services grows. On the contrary, in the range $2.8 < \eta < 3$, efficiency grows with the decrease of material budget. In the next η bins, the efficiency is more or less stable due to the better overlap of the sensors on both sides of one HGTD disc (and thus coverage) compensated with the rising material budget in ITk. In the innermost part of the HGTD, highest η bins, the efficiency abruptly increases because of the steep drop in ITk material budget. Overall, the fraction of correctly reconstructed pion tracks stays around 70% and of the misassigned tracks around 5% in the whole pseudorapidity range.

Even though HGTD tracking efficiency and purity show great results for the single particles, it is crucial to study the HGTD performance in the harsh high pile-up environment. The particle showering products described in Section 6.2.1 together with the pile-up particles largely increase the occupancy of HGTD. If these secondary hits are located close enough to the extrapolation point of the primary particles, they may be prefered by the χ^2 fit to the primary particle hit, resulting in a wrong time association to a track. Figure 6.9 shows the number of fired pads of an HGTD LGAD sensor as a function of the radius simulated with the expected pile-up of $\langle\mu\rangle = 200$. Even though the expected occupancy will not exceed 8%, it is still possible that the wrong hit may be associated to a track.

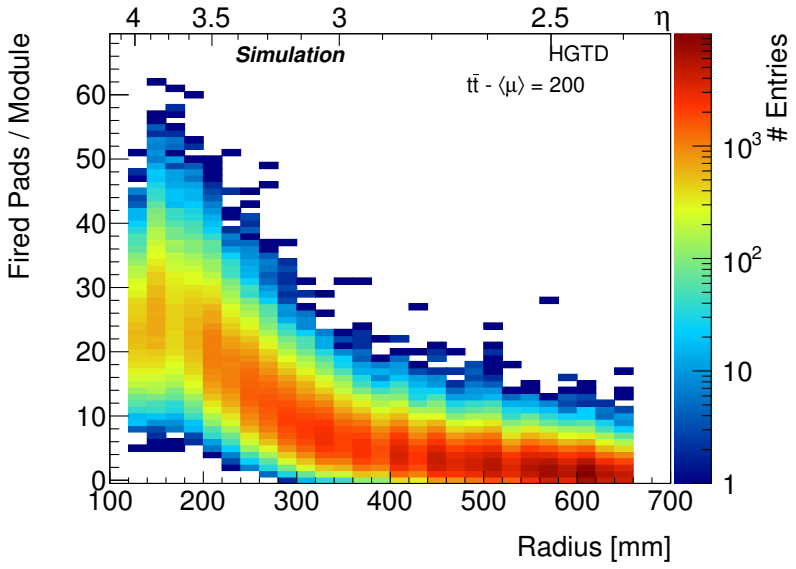


Figure 6.9: *Occupancy of LGAD sensors (i.e. the number of fired pads per module versus the radius). One module contains 450 LGAD pads in total. Taken from [51]*

Figure 6.10 shows the tracking efficiency for the physics sample VBF H → invisible as a function of η (a and b) and as a function of p_{T} (c) with $\langle\mu\rangle = 200$. The overall efficiency is on average higher than 80%. The difference in the time association for

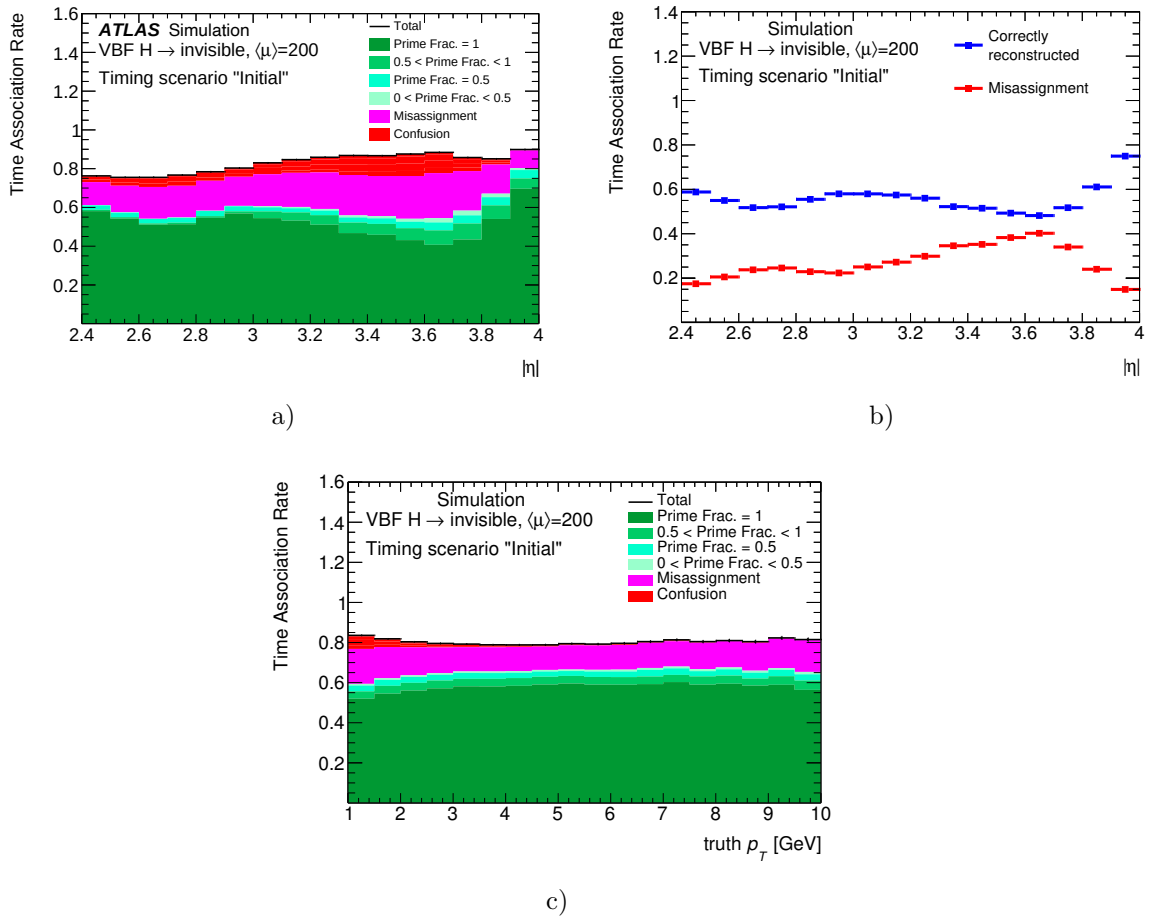


Figure 6.10: *Track-time association efficiency of HGTD for the $\langle\mu\rangle = 200$ VBF H → invisible sample as a function of η (a and b) and p_T (c). Taken from [51]*

different η bins is driven by the sensors coverage (and HGTD discs overlap) and the material amount that particles penetrate before reaching HGTD. Roughly one fourth of the tracks in HGTD acceptance falls into the categories of wrong track-time association. This is caused by the large ratio of the primary particles showering upstream of HGTD. The most significant contributions to *Misassignment* due to the particles decays are seen in the η bins 3.3-3.8, which correspond to the highest material budget and largest secondary vertices production region, see Figure 6.6. The track extension algorithm associates the secondary hits to the particles that decayed before reaching HGTD and obviously did not leave the hits. In addition, the track extension suffers not only from the particles showering but also from the multiple scattering. This effect contributes to the incorrect hit association adding the tracks to *Confusion* category. The fraction of correctly associated HGTD hits to the tracks increases with higher p_{T}, as it is shown

in Figure 6.10 (c). Such behaviour is expected, since the uncertainty of extrapolation position is decreasing for the higher particle energy.

6.2.4 Track-time association resolution

Another representative characteristic for the performance validation of HGTD is the reconstructed time resolution defined as a residual between the reconstructed time of the track, with TOF correction applied, and the truth time stored in the truth particle record.

Figure 6.11 shows the time resolution distribution for samples with single-muon (a), single-pion (b) and $\langle\mu\rangle = 200$ VBF H $\rightarrow$ invisible sample (c). On each figure the six purity categories described in Section 6.2.3 are presented. The time resolution for the single-muons follows Gaussian shape with σ around 30 ps. The vast majority of the tracks have the correct track-time assignment. For the single-pions, non-Gaussian tails in the time resolution distribution are observed. They are originated from three factors. First of all, the z_0 resolution 2.22 (b) in the forward region reaches 1 mm for low p_{T} tracks. This uncertainty may lead to the wrong track longitudinal impact parameter z_0 reconstruction, shifting the TOF correction for the time measurements in HGTD. The second factor is caused by the assumption that all the particles reaching HGTD have the speed of light, which results in overcorrection of the TOF. Last but not least, the track extension to HGTD may assign secondary hits to the primary particle's track. Since the secondary particles have lower momentum and may get trapped in the magnetic field, they reach HGTD with a delay comparing to the primary ones. The average time calculated from all the hits will then be shifted towards a higher value [51].

From Figure 6.11 (c), it is seen that with a high pile-up, the non-Gaussian tails are more significant already for the tracks associated to only primary hits $Prime\ frac. = 1$. The contributions to these tails in this case come from the z_0 mismeasurement and from the TOF overcorrection (which drastically increases the right shoulder in contribution). The main input to the non-Gaussian spread is given by the tracks from the $Misassignment$ and $Confusion$ categories, when a track got assigned to the secondary hits. The time resolution of these tracks suffers significantly from the time measurement shift due to the secondary hits assignment originating from pile-up or showering products. The reconstructed track-times will have a resolution close to the one of a total beam spread, which is $\sigma = 175$ ps according to the simulation [51].

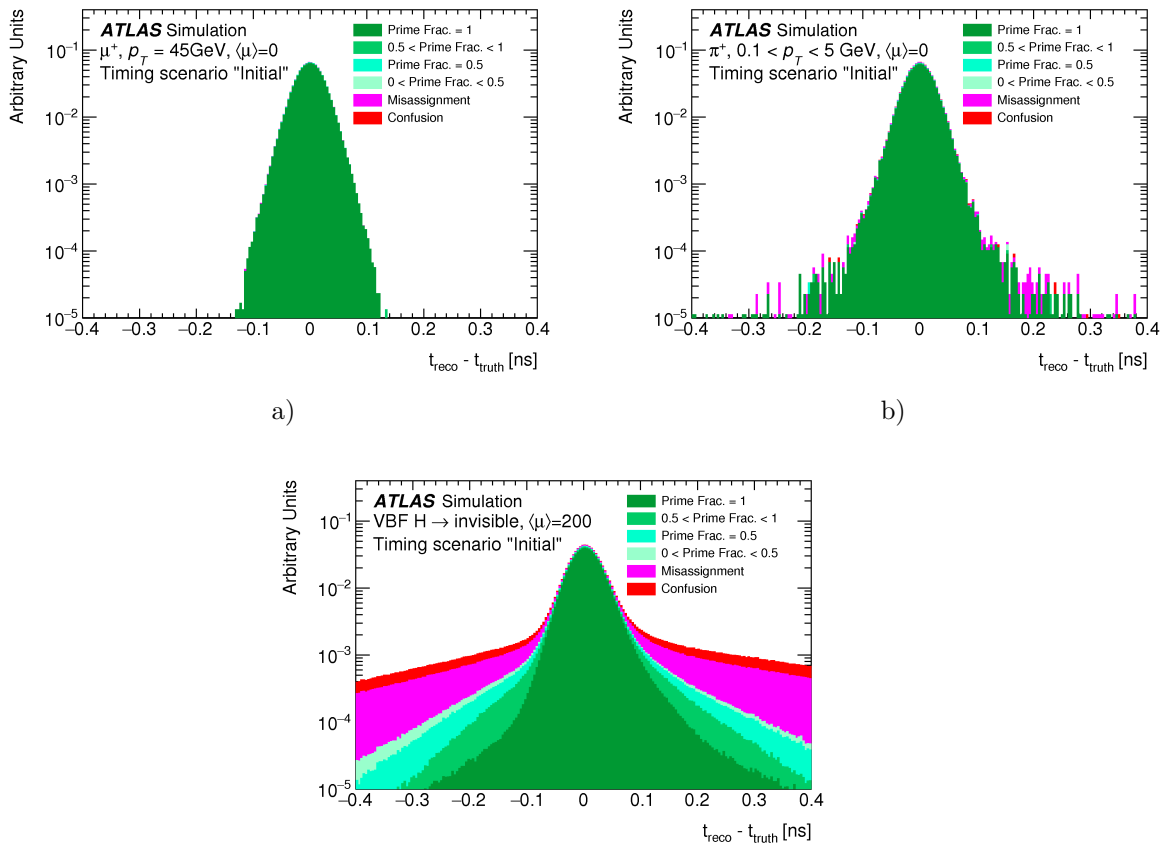


Figure 6.11: *Difference between the measured and true track-time for extrapolated tracks in HGTD for samples with single-muon (a), single-pion (b) events without pileup and VBF $H \rightarrow$ invisible events with $\langle\mu\rangle = 200$ (c). A breakdown of how correct (green shades) and incorrect (red/magenta) hit associations contribute in each bin is shown. Taken from [20].*

6.3 Enhancement of the track-time association performance

As it is shown in the previous section, the track propagation experiences a large track-time misassignement due to the particles showering and pile-up tracks. In order to improve the purity of the tracking, two tracks cleaning algorithms are available. The first one is denoted as *TDR cleaning* [51] and the second one as *Holes on track cleaning*. To be pointed out, that I developed the *Holes on track cleaning* algorithm, while the *TDR cleaning* is discussed in this section for performance comparison.

6.3.1 TDR cleaning procedure

The *TDR cleaning* procedure implements three requirements on the tracks:

1. The last ITk measurement of a track should be on a detector layer close to the HGTD in the longitudinal direction. This cut is implemented to tackle the issue of particles showering upstream HGTD.

As was already mentioned, a significant part of the particles undergo electromagnetic or hadronic showering when crossing the ITk. Particle tracks reconstructed from hits in the innermost layers of ITk that don't have measurements close to the HGTD can be considered to have undergone showering. Thus, those tracks should not be associated to a time in HGTD. The first *TDR cleaning* requirement discards the tracks, whose last measurement in ITk was outside the layers highlighted in Figure 6.12. This cut was optimized in order to ensure a good η coverage and not loose in track-time association efficiency.

2. At least two associated hits in the HGTD are required for tracks within $3.5 < |\eta| < 3.9$, in the region with a significant material upstream of HGTD, see Figure 6.6 (a). This region has also the highest overlap between the HGTD modules on the opposite sides of one disc, see Figure 6.1 (a). Thus, the stricter number of hits requirement is allowed.

This cut addresses the track-time misassignement in the most problematic HGTD region $3.5 < |\eta| < 3.9$, where the material budget before HGTD is the highest. The misassignement in this η range is especially observed for the tracks with only one associated HGTD hit. This leads to the requirement of minimum two hits per track in $3.5 < |\eta| < 3.9$ HGTD area.

3. The HGTD hits asociated to a track should be consistent in time. This cut is addressed to the non-Gaussian time resolution tails caused by a time shift due to the delayed secondary hits contribution. This applies only to tracks that have at least two hits assigned.

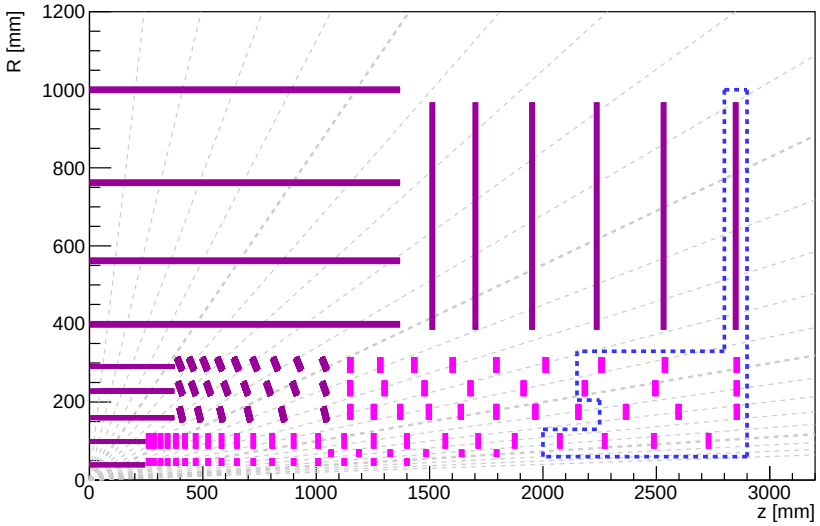


Figure 6.12: *Quadrant of the ITk detector layout in the r-z plane. The layers outlined with a blue dashed line are used to define the layers in ITk where last hits on track are required to be located for a track's time to be accepted in the cleaning procedure. Taken from [51].*

The last requirement deals with time inconcistencies between the HGTD hits. As discussed in Section 6.2.4, the secondary hits associated to a track cause a shift in reconstructed time, which then leads to the non-Gaussian tails in Figure 6.11 (c). If only two hits are associated to the track, the time consistency between them is evaluated as

$$\frac{|t_{\text{hit }1} - t_{\text{hit }2}|}{\sqrt{\sigma^2_{t,\text{hit }1} + \sigma^2_{t,\text{hit }2}}} < \alpha \tag{6.5}$$

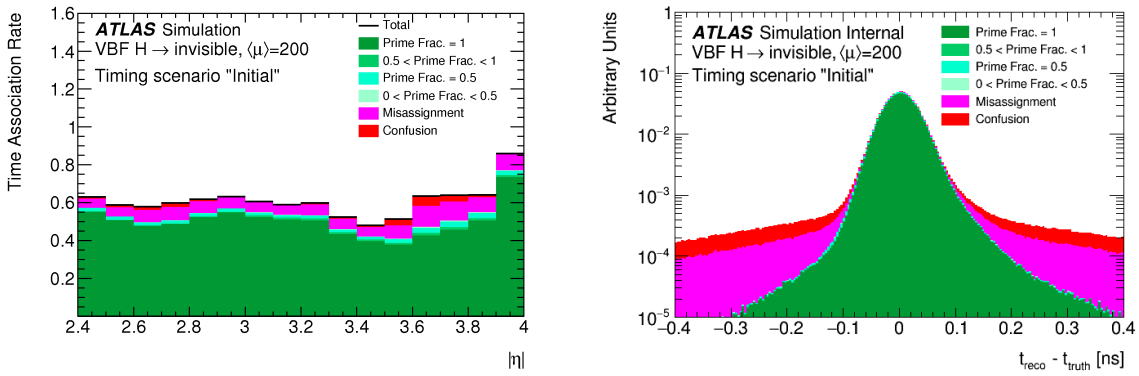
where $t_{\text{hit }1}$ and $t_{\text{hit }2}$ are the times measured for the first and the second hits respectively and α is a time difference parameter that is set to two after optimisation [51].

If more than two hits are associated to a track, the time consistency is defined via a χ^2 analysis

$$\chi^2 = \sum_{i=1}^{k} \left(\frac{\bar{t} - t_{\text{hit }i}}{\sigma_{t,\text{hit }i}} \right)^2 < \beta \tag{6.6}$$

where $\bar{t}$ is the arithmetic mean of all k hits times. Hit combinations are accepted if the combined χ^2 value does not exceed β threshold (set to 1.5 after optimisation). If the calculated χ^2 value exceeds the threshold, an attempt can be made to isolate and remove outlier hits. This is achieved by identifying the hit time t_i that constitutes the largest contribution to the total χ^2 value. By iteratively removing hits from the collection and recalculating χ^2, the largest contributing hit can be identified and rejected. This is repeated until either the χ^2 threshold is fulfilled or only two hits remain and the criterion from Equation 6.5 is fulfilled [51].

The HGTD tracking performance after applying the *TDR cleaning* procedure on the VBF H $\rightarrow$ invisible events is summarized in Figure 6.13. These cuts successfully remove up to two thirds of the tracks from the *Confusion* and *Misassignment* categories and not more than 10% of correctly reconstructed tracks. The requirement concerning the last hit in ITk appears to be the strongest cut in removing the misassigned hits (magenta and red contributions). On the other hand, enforcing the time consistency between hits removes outliers in track extensions that make the track fall into categories combining the primary and non-primary hits (light green shades). Also, this leads to a decrease in the non-Gaussian tails of the time residual distribution. Overall, after the *TDR cleaning* procedure, 39.47% of tracks have no time assigned, 49.74% of tracks have a correctly assigned time and 10.79% of tracks get a wrong track-time extension [51]. These numbers can be compared with the performance without *TDR cleaning* presented in Figure 6.10 (a): 17.09% of tracks have no time assigned, 55.72% of tracks have a correctly assigned time and 27.18% of tracks get a wrong track-time extension.



a) b)

Figure 6.13: *Performance plots at $\langle\mu\rangle = 200$ after application of the TDR cleaning procedure, splitting the result of the track extension into tracks with primaries associated (green shades), tracks that left primaries but got associated to non-primaries (confusion, red) and tracks that did not leave primaries in HGTD and random non-primaries got associated (misassignment, magenta). Figure (a) shows the tracking efficiency (taken from [20]) and Figure (b) shows the time resolution. These results can be compared with the performance without TDR cleaning presented in Figures 6.10 (a, c).*

6.3.2 Holes on track cleaning concept

The *TDR cleaning* procedure implements an empirical approach, that has to be tuned for any change in the detector operation upstream of HGTD, for instance if the ITk geometry and services change. Therefore it was important to develop an alternative method for the tracks cleaning, that would have more theoretical ground. Since a

significant fraction of track-time association impurities comes from the showering products, it is important to identify the particles that decayed upstream HGTD. If a particle crossing the detector sensitive material, doesn't leave hits in it, there is a strong evidence, that the particle no longer exists, because otherwise, the detector hits would be associated to it. The *holes on track cleaning* algorithm attempts to identify and reject such tracks. Nevertheless, the tracks selection based on time consistency between the hits (see the 3rd cut in Section 6.3.1) still needs to be applied. Indeed, the cut is addressed to the non-Gaussian time resolution tails caused by a time shift due to the delayed secondary hits contribution, that cannot be covered by the *holes on track cleaning*. Therefore, the *holes on track cleaning* is accompanied by the time consistency cut in the studies presented in Section 6.3.3 and Section 6.3.4.

Holes are defined as intersections of the reconstructed track trajectory with a sensitive detector element that does not contain a matching cluster (or hit). These are estimated by following closely the track trajectory and comparing, within the uncertainties, the traversed sensors with the associated clusters to the track. Inactive detector elements or regions, such as edge areas on the silicon sensors, are excluded from the hole definition. The *holes on track* search algorithm has been already implemented in the ATLAS Track Reconstruction algorithm descibed in Section 6.1.3.

In HGTD, the track reconstruction procedure deals with the tracks formed in ITk. Each ITk track is propagated to the HGTD surfaces and the hits are then associated to the track using progressive Kalman filter. Figures 6.14 (a, b) shows an example of a particle (green curve) crossing the ITk leaving hits in the detector elements (yellow stars). At some point the particle initiates a shower. The HGTD tracking algorithm will get the track last measurement in ITk and extrapolate it to the closest HGTD layer (green dashed line). The algorithm may associate some HGTD clusters to the initial track, even though they originate from the secondaries or pile-up, see Figure 6.10 and 6.11. By knowing if the particle has the *holes on track* (red circles), it is possible to prevent the incorrect track-time association. Hence, the *holes on track cleaning* concept is a good identifier of the particle's decay.

The algorithm of the *holes on track* search in ITk and HGTD consists of three steps:

1. check if the particle propagation (track) intersects the active detector element within a certain *tolerance level* (boundary check);

2. look for a compatible cluster in the hits collection of the detector element;

3. if such cluster is not found, the extrapolation is considered to be a hole.

The confidence in defining the extension as a hole on track depends on how certain we are that the extrapolation of this track really crosses a detector element. Having an uncertainty of extrapolation σ (taken from the first two diagonal terms in covariance

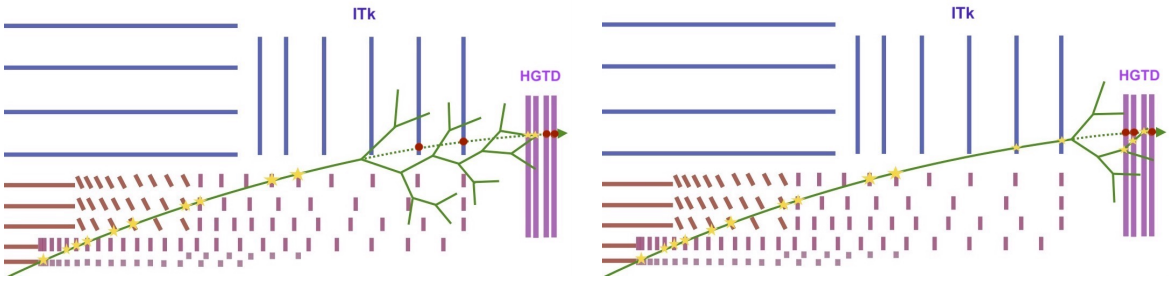
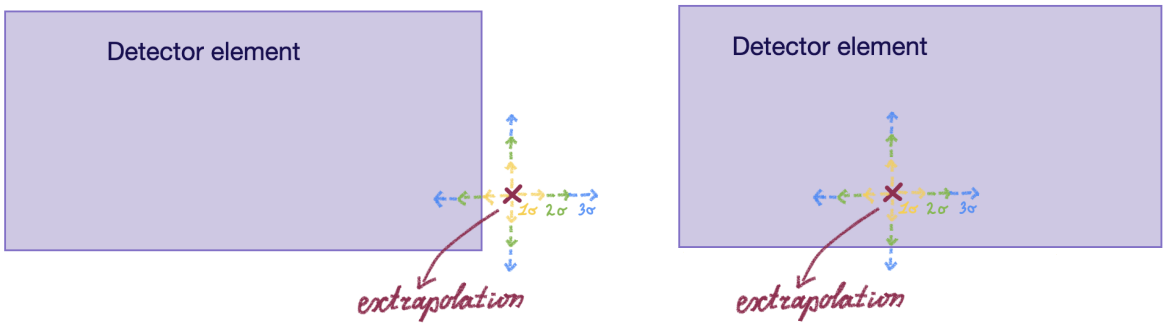


Figure 6.14: *Sketch of an ITk quadrant and four layers of HGTD in one endcap for the illustration of a particle decay in ITk (a) and between ITk an HGTD (b) when traversing through the detector elements and leaving the holes on track (red circles). The green lines represent the tracks of a primary particle and its decay products, the yellow stars are the detected hits, the dashed green line is a primary particle's track extrapolation and the red circles are the holes.*

matrix of the track parameters, see Section 6.1.1), it is possible to define a tolerance level that the extrapolation is inside the active surface as $n\sigma$. The bigger the distance between the extrapolation and the surface border is, the higher the tolerance level is and the higher the probability to associate a cluster to it is.

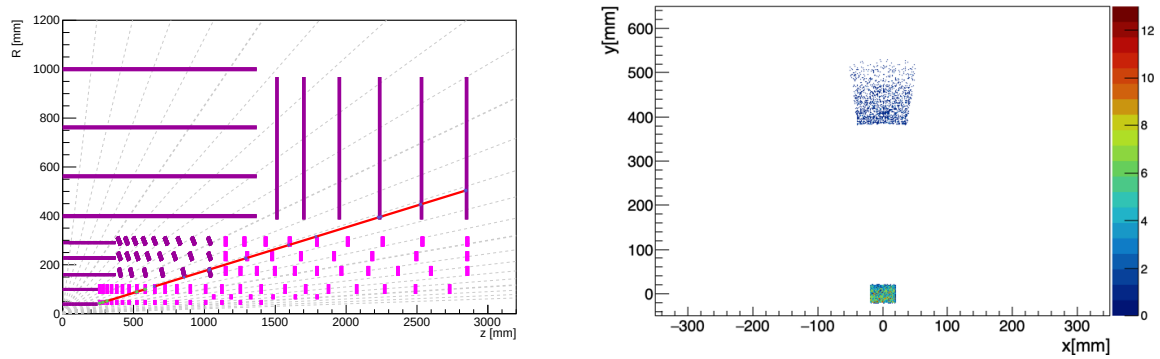
Figure 6.15 shows two scenarios of track extrapolation onto the HGTD layer. On the sketch (a), the track did not cross the detector element and in this case, if a compatible hit on this surface is not found, we do not consider it as a hole on track. On the sketch (b), the extrapolation is on the surface at 2σ tolerance level (green arrows), but not on the surface at 3σ tolerance level (blue arrows). Which means, that if we do not find a compatible hit on this surface, we consider it a hole at a 2σ tolerance level and not a hole at a 3σ tolerance level. Overall, the higher the tolerance level we accept, the less *holes on track* we should expect. The algorithm treats separately the extrapolations in ITk and HGTD. Since the tracks in HGTD acceptance are extrapolated from the last ITk measurement, all the intersections between the track and ITk surfaces after this last measurement can be considered as holes (within a certain tolerance level). The example of such propagation is shown in Figure 6.16. In Figure 6.16 (a), a track propagation (red line) through ITk is presented pointing out the measurements (green stars) and the overlaps of this track with the detector elements representing holes (blue stars). This particle most likely decayed and should not be associated to the HGTD hits. The Figure 6.16 (b) shows the local coordinates of the *holes on track* inside the ITk detector elements between the last ITk measurement and HGTD. In this example, the tolerance level of 0σ is taken, meaning that the holes found should be inside the surface border within 0 mm. The pixel sensor (4x4 cm ^{2} square in the



a) b)

Figure 6.15: *An example of two scenarios of a track extrapolation on the detector surface. (a): the extrapolation is outside the sensor. (b): track does cross the sensor at 2σ tolerance level and does not cross the sensor at 3σ tolerance level.*

bottom) and the strip detector (the petal on top) are clearly seen, prooving that the algorithm works correctly.



a) b)

Figure 6.16: *(a): a track reconstructed in ITk and further extrapolated in the direction of HGTD, the green stars in the inner part of ITk show detected hits and blue stars show the overlap of the extrapolation with the detector elements (holes). (b): the local positions in xy projection of the holes on track found in ITk for 5 GeV π^+. This checks that the holes are inside the detector elements, here, at 0σ tolerance level.*

For HGTD, the *holes on track* are identified following the three-step algorithm described above and is embedded in the track reconstruction procedure:

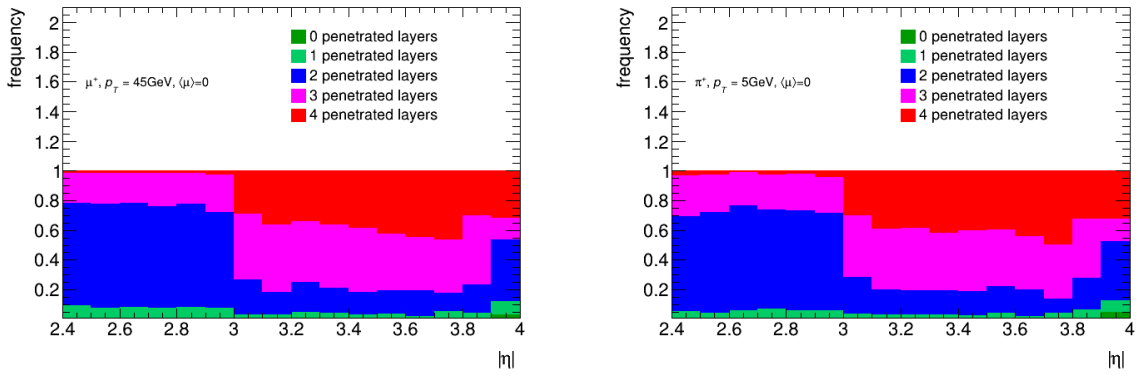
1. track propagation from the last hit in ITk to the closest HGTD layer,
2. collection of the candidate detector surfaces (modules) around the extrapolation point,
3. prediction of the track position on each preselected surface using the Kalman Filter,

4. selection of the compatible hit (on the preselected surface) for each prediciton via χ^2 analysis,
5. choose the best hit-prediction match within all the preselected surfaces,
6. if no match is found and one of the predicitons is inside the detector within the tolerance level, it is a hole,
7. best measurement with the updated track parameters becomes the new last hit (if available), go to step 2.

Figure 6.17 shows the $|\eta|$ distribution of the tracks penetrating the HGTD layers for single muons (a) and single pions (b). A track is considered to pass through an HGTD layer if its extrapolation is inside the detector element within 0σ tolerance level. The tracks are categorised depending on how many layers they penetrated (0 to 4). It should be pointed out that only track geometrical propagation is considered: the real clusters assigned to the track in HGTD are not taken into account. In the outermost η range (2.4 - 3), for both single muon and pion the majority (70%) of the tracks penetrate two layers and 20% of tracks penetrate three layers of HGTD. This behaviour is caused by the fact that the sensors density in this $|\eta|$ region is lower and also by the tracks trajectory that may cross only 2 first layers of HGTD and continue outside the detector acceptance. In the second η region (3 - 3.9), the sensors are much closer to each other and the immediate increase in the ratios of tracks penetrating three and four HGTD layers is seen. Both categories take around 40%, making up together around 80% of all the tracks. Due to the poorer sensor coverage in the last $|\eta|$ bin, the tracks crossing two layers dominate again constituting around 40%, while the tracks penetrated three and four layers compose around 50% together. These plots are in agreement with the HGTD hit multiplicity for the 2-ring geometry design, see Figure 6.18.

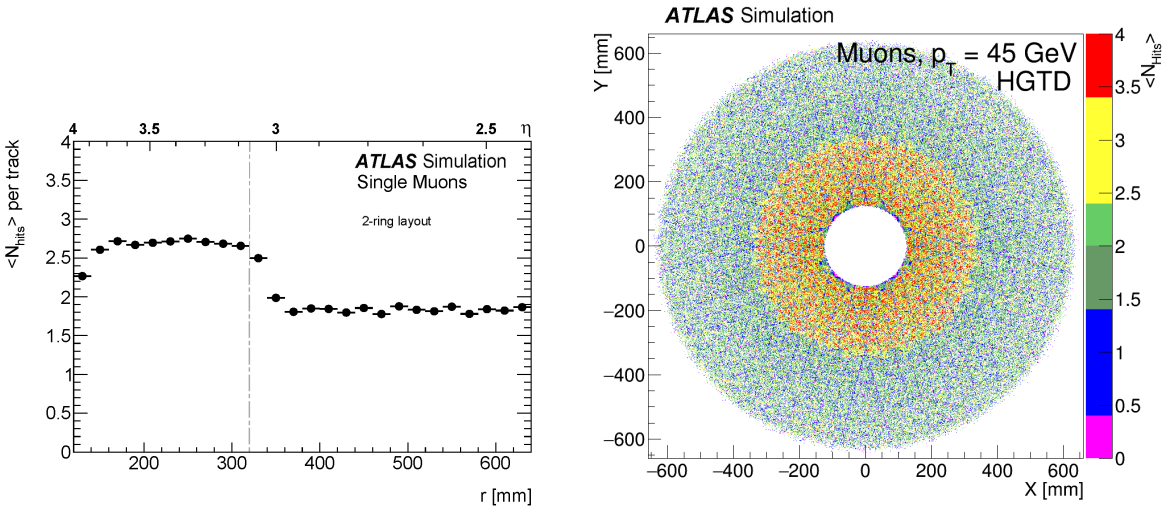
A more detailed layer per layer tracks behavior (including the hits information) is shown in Figures 6.19 and 6.20 for 45 GeV muons and 5 GeV pions respectively. Since, all the layers of HGTD share the same geometry, the tracks distributions are very similar in each layer.

According to these graphs, for both muons and pions, in each layer, around 45 % of the tracks leave no trace within $2.4 < \eta < 3$ (red area). These tracks are passing in between the sensors and consistently no HGTD clusters were associated to these tracks. For the inner ring $3 < \eta < 3.9$, such tracks constitute only about 20 % of the particles in the HGTD acceptance, since the sensors density is higher in this area. In both Figures 6.19 and 6.20, the tracks with extrapolations outside the detector elements but with the hits associated to them (magenta area) are not observed, which is a logical and expected behavior. The light green histogram represents the cases of the *holes on track*, when the extrapolation is inside the active material, but the



a) b)

Figure 6.17: *The stack plots of the particles rates vs. $|\eta|$ divided in five categories depending on the amount of penetrated HGTD layers for 45 GeV μ^+ (a) and 5 GeV π^+ (b). The particles selected for these distributions have their tracks in the HGTD acceptance.*



a) b)

Figure 6.18: *Hit multiplicity as function of radius (a) and transverse plane (b) for the 2-ring HGTD geometry. These figures were made using simplified simulations, resulting in an uncertainty of roughly 10 %. Taken from [20].*

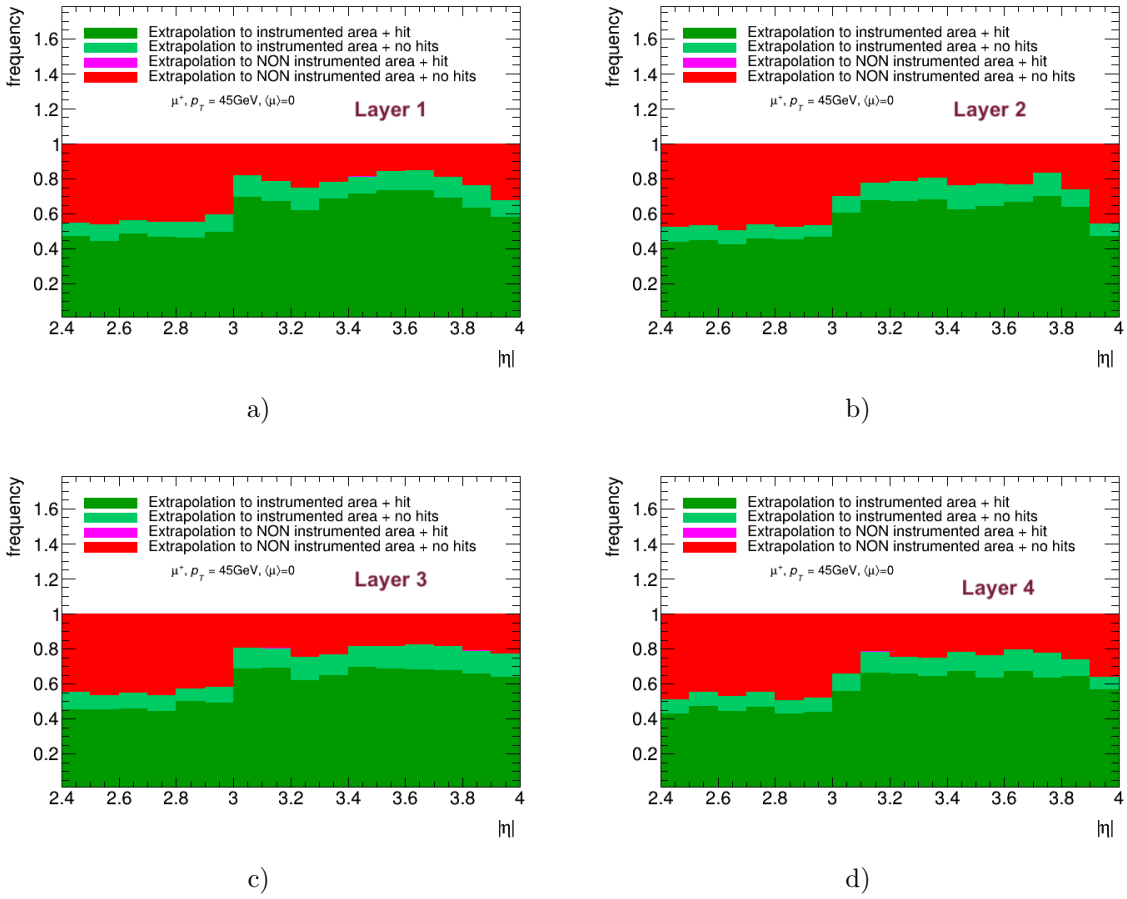


Figure 6.19: *The HGTD layer per layer tracks ratio in η for 45 GeV single μ^+ broken down by four categories. Dark green area: tracks extrapolated to the active detector element with a hit assigned to it. Light green: tracks penetrated an active detector element but no compatible hits were found, this category represents the holes on track. Magenta: extrapolations which ended up in the non-instrumented areas, but to which a hit was assigned (wrongly). These tracks are not observed, which is a logical and expected behavior. Red: tracks with extrapolations outside the active detector elements and without hits assigned to them. The 0σ tolerance level is used.*

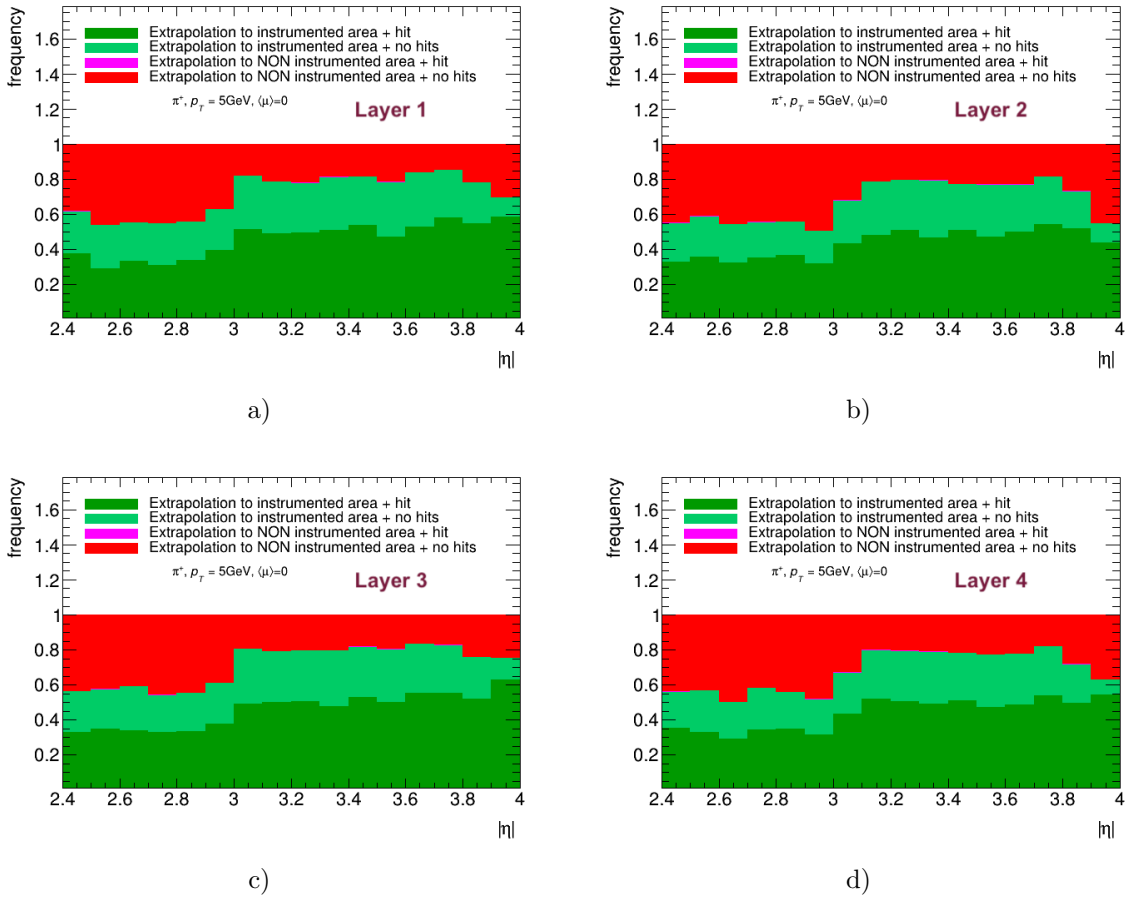


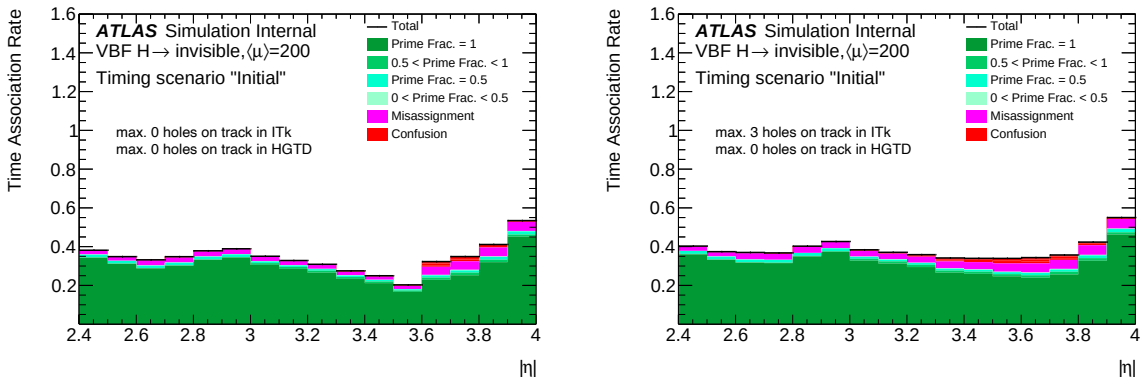
Figure 6.20: *The tracks ratio in each HGTD layer for 5 GeV single π^+ vs. pseudo-rapidity broken down by four categories described in Figure 6.19. The same 0σ tolerance level is used for deciding if the extrapolation is on the active detector element.*

hit was not associated to it. For muons, throughout the whole $|\eta|$ range, the *holes on track* take place in 10 - 15% of the cases. Whereas for pions, the holes are present in 25 - 30% of the tracks. This difference can be explained by the fact that pions decay before the HGTD much more frequently than the muons and consequently do not leave the hits in HGTD.

6.3.3 Holes on track cleaning for the 2-ring HGTD geometry

Overall, the *holes on track* efficiency in misassignment mitigation depends on two factors: the amount of holes accepted for the track-time association and the tolerance level for the extrapolation boundary check (how deep is the extrapolation inside the active sensor). The tolerance is given in units of σ described in the previous section. Intuitively, the stricter the cut on the allowed amount of holes is, the more tracks will be refused for the track-time association, which will lead to the decrease of the tracking efficiency. On the other hand, with a higher tolerance level in the boundary check, less extrapolations will be considered as holes, since more of them will be classified to be outside the sensor. As a reminder, in the following results, the time consistency cut is applied in addition to the cut on amount of the *holes on track*.

Figure 6.21 shows the track reconstruction efficiency for VBF H $\rightarrow$ invisible sample after implementing the *holes on track cleaning* with two different configurations. For both graphs in Figure 6.21, the maximum allowed amount of holes in HGTD is 0 and from 0 (a) to 3 (b) in ITk. The cut on number of holes is done with the boundary check tolerance level of 0σ for all the figures (a,b), meaning that the extrapolations are considered to be on surface if they are inside the detector element and are at least 0 mm away from the border. The overall efficiency trend is following the material budget distribution before HGTD. With the most stringent cut on holes, maximum



a) b)

Figure 6.21: *The HGTD track-time association rates after implementing the holes on track cleaning at 0σ tolerance level. The number of maximum allowed holes on track in HGTD is set to 0 and in ITk to 0 (a) and 3 (b).*

0 holes in ITk and HGTD, the tracking efficiency is around 30% over the whole η acceptance range going down to 20% at the 3.5 η bin. As the amount of holes in ITk is increased to 3, the efficiency of track-time association also raises. However, misasignment also increases, since more decayed tracks are accepted for the extension to HGTD. Overall, the efficiency for correctly associated hits is about 20% less than the one for the pure HGTD performance without any cuts, see Figure 6.10 (a).

If the tolerance level is set too loose, the requirement for an extrapolation to be considered as a hole on track will be too easy to meet and too many tracks will be discarded. Indeed, Figure 6.22 shows the track reconstruction efficiency for the same cuts on holes as in Figure 6.21, but with the boundary check tolerance level of 9σ. It means that the extrapolations are required to be inside the sensor and at least 9σ mm away from the borders. The track-time association efficiency is 15-20% higher with respect to the one with 0σ tolerance level, but a misassignement also increases drastically, especially for the more loose cut on holes in ITk (maximum 3 holes in ITk). This is an anticipated result, since with the too tight 9σ tolerance, less extrapolations are considered to be inside the detector elements and less tracks are assigned the holes. Therefore it is important to define a sufficient tolerance level to discard only the tracks with holes without loosing efficiency and purity.

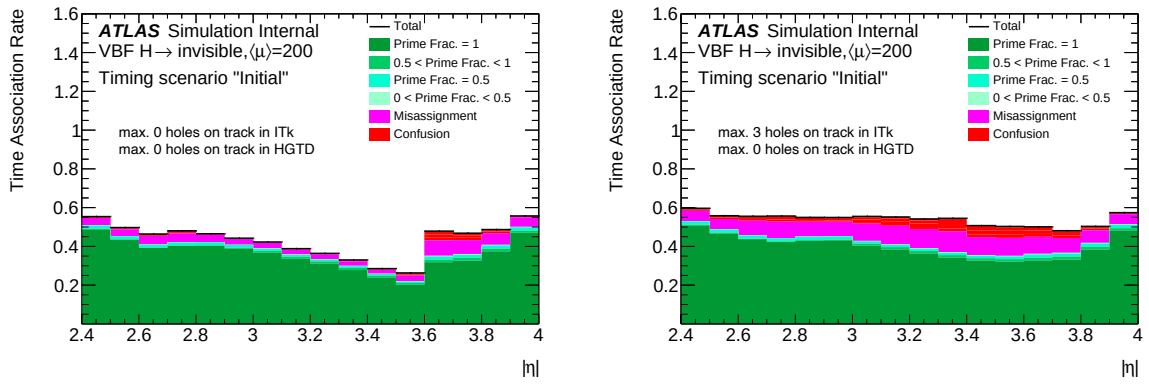


Figure 6.22: *The HGTD track-time association rates after implementing the holes on track cleaning at 9σ tolerance level. The number of maximum allowed holes on track in HGTD is set to 0 and in ITk to 0 (a) and 3 (b).*

The described cases use a very strict cut on holes in HGTD and different cuts on holes in ITk. Figure 6.23 shows instead the tracking performance with maximum 1 allowed hole in ITk and with different cuts in HGTD. The boundary check tolerance level is set to 3σ in all three figures, which proved to be a good compromise between the efficiency and purity. As in the previous cases, the looser the cut on the maximum allowed amount of holes in HGTD is set, the higher the efficiency. If already 1 hole is allowed for the tracks in HGTD (see Figures 6.23 (b)), the overall efficiency increases

by 50%. The wrong track-time assignment increases by maximum 30% in all the η bins except for the most problematic range of 3.5-3.9, where the misassignement gets up to 15% (see Figures 6.23 (c)).

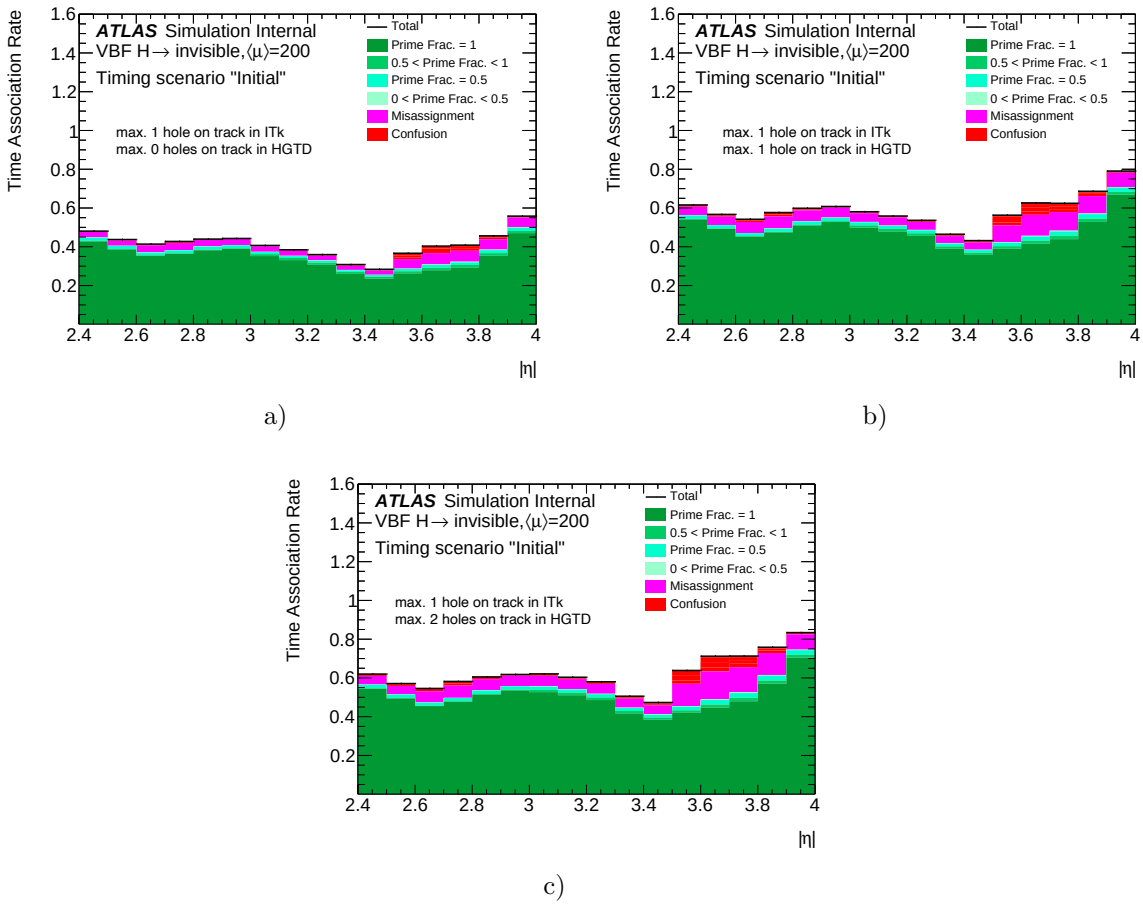


Figure 6.23: *The HGTD track-time association rates after implementing the holes on track cleaning at 3σ tolerance level. The number of maximum allowed holes on track in ITk is set to 1, while in HGTD to 0 (a), 1 (b) and 2 (c).*

Table 6.1 summarizes the integrated over η rates for the correct track associations, which include the tracks with $Prime\ frac. > 0.5$, and the misassigned track-times ($Prime\ frac. \leq 0.5$) for 6 different *holes on track* configurations. If the cut on HGTD holes is set to 0, the efficiency doesn't exceed 47% and the misassignment rate constitutes almost 10% of the tracks in HGTD acceptance (or 25% of the tracks with time assigned) even if a maximum of 5 holes in ITk is allowed. A cut of 1 hole on track in HGTD seems to improve the efficiency significantly. The configuration of maximum 1 hole in HGTD and 2 holes in ITk makes the performance of *holes on track* algorithm similar to the TDR cleaning, that has 49.74% of tracks correctly assigned to the hits and 10.79% misassigned. It should be pointed out that the significantly high misassignment rate in the 3.5-3.9 $|\eta|$ range is caused by the considerable material

budget upstream HGTD and the high secondary particles density in this region as discussed in 6.3.1.

	0 ITk holes		2 ITk holes		5 ITk holes	
	Correct	Misassigned	Correct	Misassigned	Correct	Misassigned
0 HGTD holes	33.01%	5.47%	35.98%	7.25%	36.59%	9.75%
1 HGTD hole	45.99%	8.52%	50.17%	11.82%	50.99%	15.95%
2 HGTD holes	48.01%	9.78%	52.42%	13.96%	53.28%	18.82%

Table 6.1: *The ratios of correctly assigned and misassigned track-times for different amount of maximum allowed holes on track. The 3σ tolerance level is applied. To be noted that the sum of Correct and Misassigned categories does not sum up to 100% because some tracks in the HGTD acceptance did not get any hit assigned to.*

Figures 6.24 and 6.25 show the ratios of the correctly associated track-times and misassigned tracks respectively with different number of *holes on track* configurations and for a range of tolerance levels from 0σ to 9σ. Additionally, the TDR cleaning results are shown in the figures. Overall for the best compromise of efficiency and purity, the lower the boundary check tolerance level is, the stricter the cuts on holes should be. With the higher tolerance level, the looser cut on amount of holes is more sufficient. The best options appear to be the following configurations for 3σ and 4σ tolerance level: 1 hole in ITk and 1 hole in HGTD or 2 holes in ITk and 1 hole in HGTD or 1 hole in ITk and 2 holes in HGTD. The performance of these selected cuts are presented in Table 6.2. In Figure 6.26, the efficiency and time resolution broken down by the purity categories are shown. The cuts on *holes on track* and time consistency are able to deliver the same performance as the TDR cleaning cuts and better. The advantage of the *holes on track cleaning* method is that it offers the possibility of tunning the cuts depending on the desired efficiency-purity ratio.

	1 ITk hole		2 ITk holes	
	Correct	Misassigned	Correct	Misassigned
1 HGTD hole	48.62%	9.95%	50.17%	11.82%
2 HGTD holes	50.78%	11.61%	52.42%	13.96%

Table 6.2: *The ratios of correctly assigned and misassigned track-times for different amount of maximum allowed holes on track. The 3σ tolerance level is applied.*

The figures with more examples on the *holes on track* cuts for the 2-ring HGTD geometry can be found in Appendix C.1.

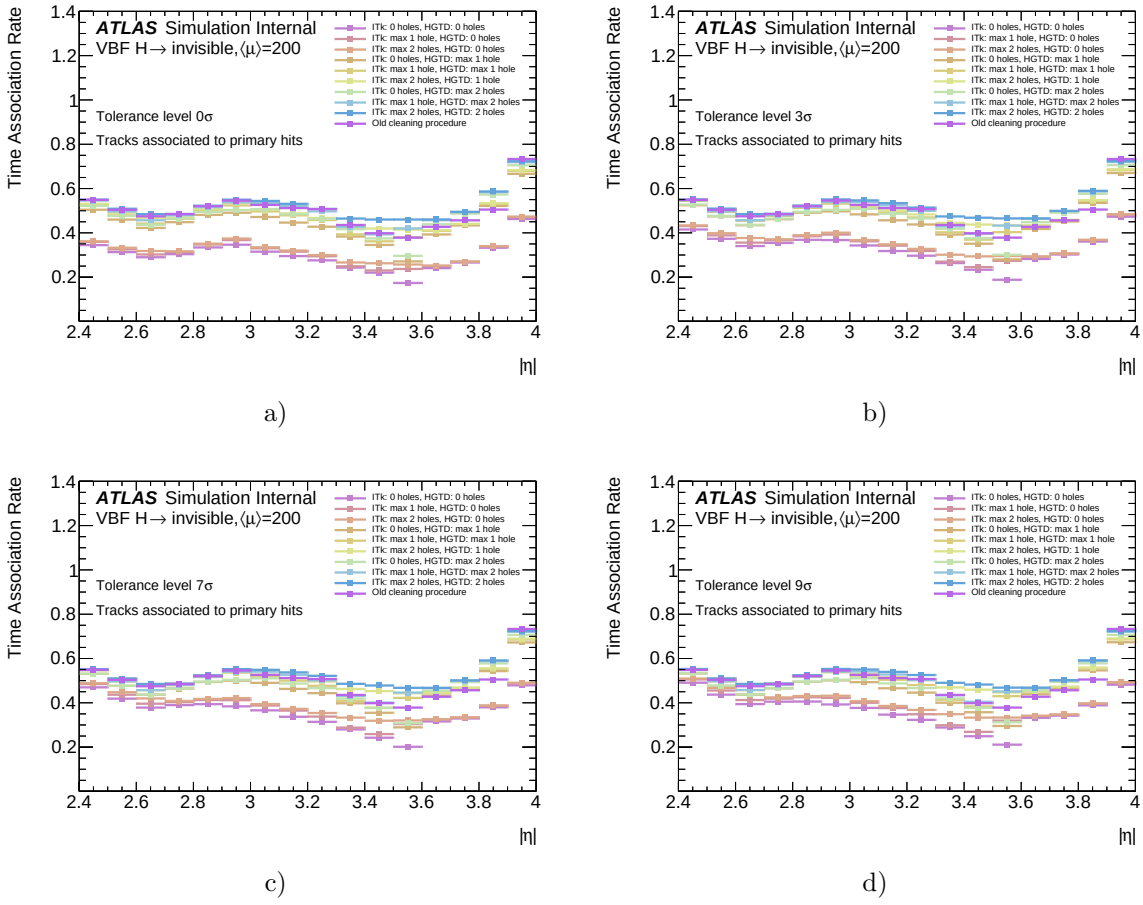


Figure 6.24: *Correct track-time association rates in the HGTD acceptance as function of η. Different configurations for the cuts on the number of holes in ITk and HGTD with tolerance levels from 0σ (a) to 9σ (d). The results from TDR cleaning procedure marked as "Old cleaning procedure" are presented for the comparison.*

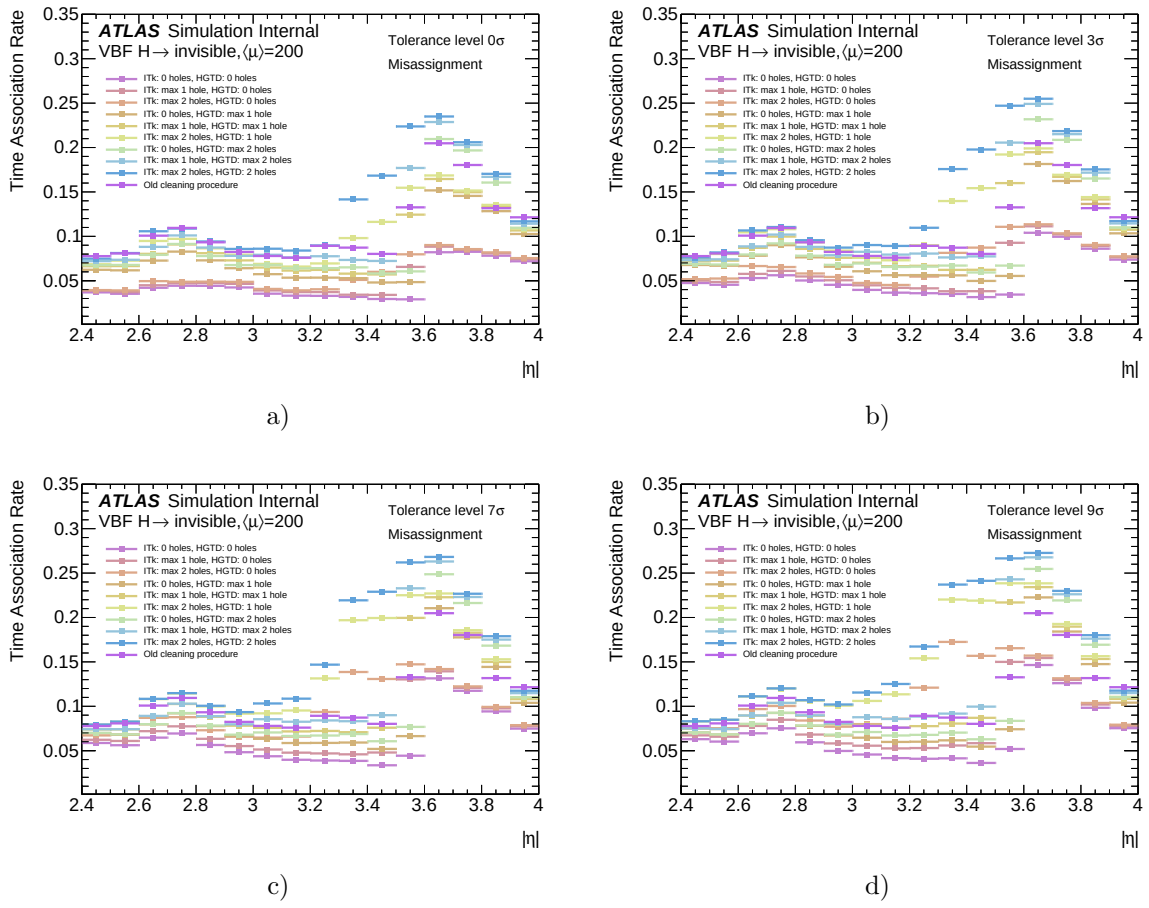


Figure 6.25: *Misassigned track-time association rates in the HGTD acceptance as function of η. Different configurations for the cuts on the number of holes in ITk and HGTD with tolerance levels from 0σ (a) to 9σ (d). The results from TDR cleaning procedure marked as "Old cleaning procedure" are presented for the comparison.*

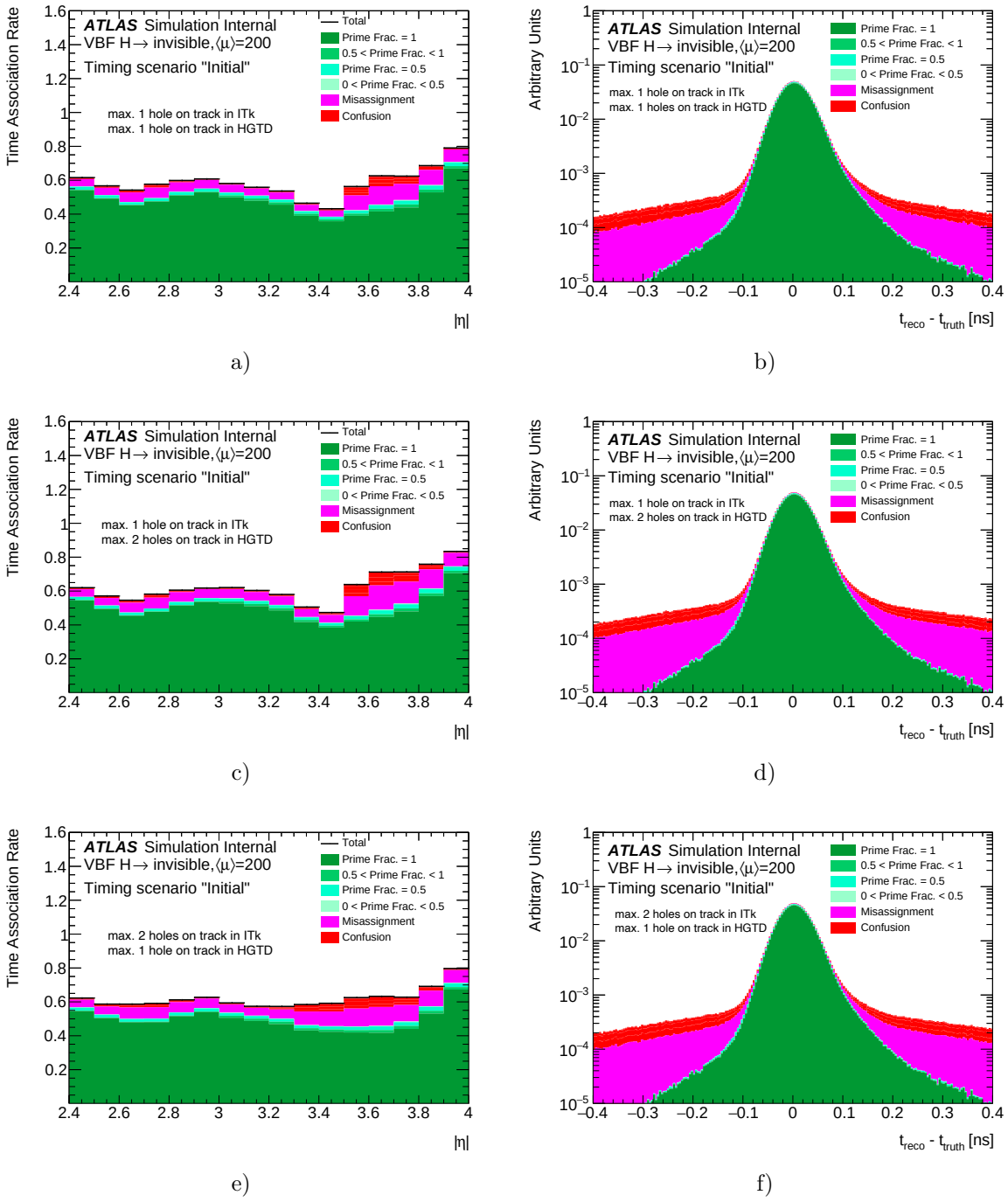


Figure 6.26: *Performance plots at $\langle\mu\rangle = 200$ for the 2-ring HGTD geometry, splitting the result of the track extension into different purity categories described in Section 6.2.3. The holes on track cleaning is implemented with different cuts on number of holes on track at 3σ tolerance level.*

6.3.4 Track reconstruction performance of the 3-ring HGTD

In 2023, the 3-ring HGTD geometry performance has been studied with the $t\bar{t}$ production samples simulated using Powheg [103] as generator, Pythia8 (v8.230) [104] for the showering and A14 tune [102] for the hadronisation. The *holes on track cleaning* procedure has been implemented and tested with this samples and is presented in this section.

Figures 6.27 (a,b) and (c, d) show the 3-ring HGTD performance in terms of efficiency and time resolution respectively without any tracks cleaning and with TDR cleaning implementation. The HGTD performance without any cleaning shows that 19.12% of tracks do not get the time assigned, 53.50% of tracks have the correct time assigned to them and 27.38% have misassigned times. The $(t_{reco} - t_{truth})$ distribution has a large non-Gaussian contribution to the tails which has already been seen in case of the 2-ring HGTD performance. These tails are caused by the TOF overcorrection, the TOF shift due to the poor z_0 resolution and the wrong average time calculation due to the track-hit misassignments. The TDR cleaning does enhance the performance, bringing the ratio of correctly assigned track-times to 49.45% and misassigned to 12.71%. The rate of misassigned tracks thus drops more than two times.

With the implementation of the time consistency cut together with the *holes on track* cleaning, it is possible to get the similar performance as TDR cleaning already with the configuration that allows maximum 1 hole in ITk and 1 hole in HGTD at 3σ tolerance level, see Figure 6.27 (e, f). With this setting of maximum number of *holes on track*, the ratio of correctly assigned tracks is reaching 49.48% and misassigned is 12.40%. The time resolution is mostly influenced by the cut on the time consistency, therefore the distribution is very similar to the one delivered by the TDR cleaning, see Figure 6.27 (d).

As mentioned before, a big advantage of the *holes on track* cleaning method is that it is tunable. The two parameters affecting the performance of the algorithm is the amount of holes allowed in ITk and HGTD and the boundary check tolerance level in ITk and HGTD. So far, the tolerance level was kept the same for ITk and HGTD, however it can also be treated separately for the two detectors. Tables 6.3 and 6.4 show the correctly assigned and misassigned track-time ratios for different holes and tolerance level configurations. The tolerance level of 3σ in ITk is kept in both tables while for HGTD, a tolerance of 2σ is shown in Table 6.3 and of 3σ in Table 6.4. The 3σ tolerance is the default setting in the tracking for ITk, therefore this value is kept. The HGTD extrapolations have higher uncertainty than the ITk ones, thus the tolerance level for holes may be kept slightly smaller. According to the tables, the lower tolerance level in HGTD brings a lower overall efficiency including the lower misassignement rate. All in all, the *holes on track* cleaning method implemented with

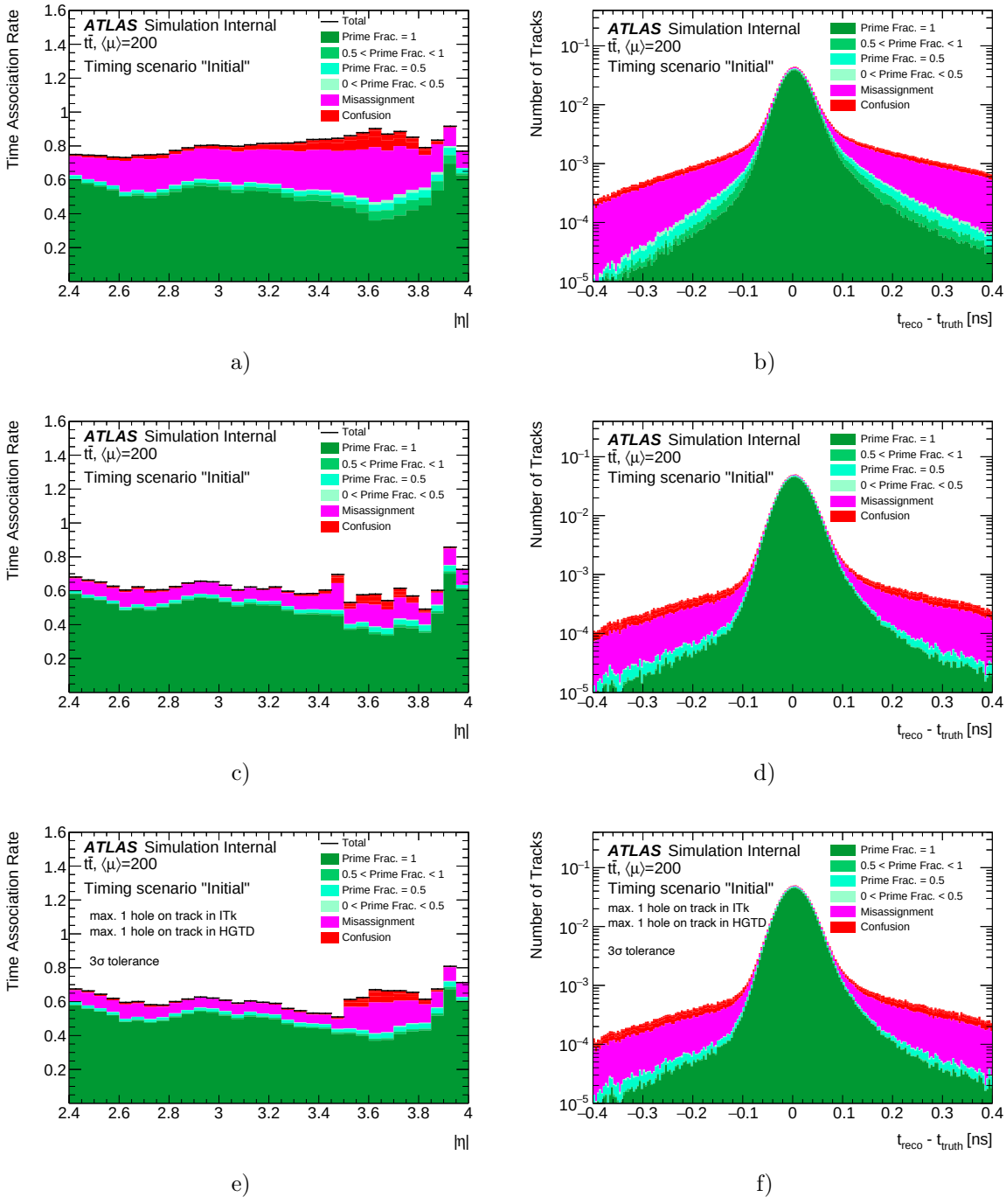


Figure 6.27: *Performance plots at $\langle\mu\rangle = 200$ for the 3-ring HGTD geometry, the result of the track extension is splited into different purity categories as described in Section 6.2.3. Figure (a) shows the tracking efficiency and Figure (b) shows the time resolution for the HGTD performance without cuts. Figures (c) and (d) show the tracking efficiency and the time resolution after implementing the TDR cleaning cuts. Figures (e) and (f) show the tracking efficiency and the time resolution after implementing the holes on track cleaning with a maximum of 1 hole in ITk and of 1 hole in HGTD for a boundary check tolerance level of 3σ.*

the time consistency cut is a good alternative to the TDR cleaning procedure as it proved to achieve a better performance with more options for tuning.

	1 ITk hole		2 ITk holes	
	Correct	Misassigned	Correct	Misassigned
1 HGTD hole	49.36%	12.17%	49.85%	13.90%
2 HGTD holes	50.72%	14.31%	51.13%	16.42%

Table 6.3: *Ratios of correctly assigned and misassigned track-times for different amount of maximum allowed holes on track. The 3σ and 2σ tolerance levels are applied for ITk and HGTD respectively.*

	1 ITk hole		2 ITk holes	
	Correct	Misassigned	Correct	Misassigned
1 HGTD hole	49.48%	12.40%	50.74%	14.47%
2 HGTD holes	50.74%	14.47%	51.25%	16.76%

Table 6.4: *The ratios of correctly assigned and misassigned track-times for different amount of maximum allowed holes on track. The 3σ and 3σ tolerance levels are applied for ITk and HGTD respectively.*

6.4 Conclusion and outlook

The low-level performance of HGTD was studied in terms of track-time association efficiency and resolution for two geometries of HGTD: the 2-ring and the 3-ring geometries. The HGTD performance without any cuts shows an overall efficiency of 82.9% and 81% for the 2-ring and the 3-ring geometry, respectively. However, the ratio of the wrong track-time associations are 27.2% and 27.4% for the 2-ring and the 3-ring geometry, respectively. Such a low purity is caused by the material budget upstream of HGTD and the consequent particle showering. The time resolution suffers from the major non-Gaussian contributions in the tails of the distribution, which can be reduced by implementing the time consistency cut.

It has been shown that the purity can be enhanced by applying cleaning procedures: *TDR cleaning* and *holes on track cleaning*. The first one was developed in 2019 in preparation for the HGTD Technical Design Report. For the 2-ring HGTD, the TDR cleaning is able to reduce the misassignment by 16.4% keeping the correct track-time association rate at 49.7%. For the 3-ring HGTD, the misassignment rate reaches 12.7% and the correct track-time association rate 49.45%.

The second method *holes on track cleaning* was developed in the frame of this thesis. It provides the oportunity to tune the performance by changing the boundary check

tolerance level and the allowed amount of *holes on track* both in ITk and HGTD, thus, the performance depends on the settings chosen by the user. Another advantage of the method is the independence from the ITk's operation conditions. The *holes on track* cleaning algorithm takes into account the status of detector elements (whether they are active, damaged, etc.) crossed by a track. Three optimal cuts were chosen that are comparable with or better than the *TDR cleaning* performance: 1 hole in ITk and 1 hole in HGTD, 1 hole in ITk and 2 holes in HGTD, or 2 holes in ITk and 1 hole in HGTD. For these cuts in the 2-ring HGTD geometry, if the tolerance level of 3σ in ITk and HGTD is set, the misassignement varies from 9.95% to 13.96%, while the correct assignement rate is between 48.62 and 52.42%. The same configurations for the 3-ring geometry shows the misassignement from 12.4% to 16.76% and the correct assignement of 49.48-51.25%.

The most problematic $3.5 < \eta < 3.9$ range due to the major particle showering upstream of HGTD still shows a poor purity for both cleaning procedures. A possible solution may be to tune the *holes on track* cuts depending on η and puting the stricktest cut (0 holes in ITk and HGTD) for $3.5 < \eta < 3.9$. The efficiency can be improved by not discarding the particles that left some hits in HGTD and then decayed. This is possible by applying the cut on the number of holes only in the last HGTD layers.

Finally, the purity definition can be redefined, since the secondary particles coming from the primary's decays may provide the correct timing to the track. Thus, the assignement of the secondary hits (coming from the primary's decay) to the track may be considered as correct association. This could not be tested in the scope of this thesis because the difference between the secondary particles and the pile-up particles was not available in the simulation truth record so far, but will be implemented in the future simulations.

Chapter 7

HGTD integration in A Common Tracking Software

Athena (see Section 2.4.6), just like any large software project, has gradually become less structured over time, with maintainability and clarity of code taking a backseat to working code. This is particularly true for the tracking software, which suffered from a lack of maintenance due to frequent changes of contributors. The ATLAS software has moved to a new concurrent execution model for reasons explained in Section 2.4.6. This transition required that the existing code is compatible with the new model. However, this is a very complicated task given the size and complexity of the codebase and requires testing and verifying various approaches and additional developments before committing to global migration. To simplify this process, in 2016 the tracking code was extracted from the ATLAS software framework and released first on CERN's instance of GitLab [105] and later on GitHub [106] (from 2020). The resulting decoupled code formed the basis of the ACTS (A Common Tracking Software) project (in the beginning ATLAS Common Tracking Software), which has since undergone significant development. The ACTS code was used as an environment for prototyping thread-safety approaches, which are essential for concurrent execution. Moreover, at the time of the extraction, the ATLAS software, built using Configuration Management Tool (CMT) [107] and version controlled using Subversion (SVN) [108], was planning to migrate to more modern and industry-standard solutions. ACTS was used to prototype the usage of Git [109] as a version control system and the CMake [110] as a build system. Nowadays ACTS is an experiment-independent toolkit for track reconstruction, developed to serve the needs of the HL-LHC experiments (including ATLAS).

In the HL-LHC era, ATLAS is planning to use the ACTS toolkit for track reconstruction, thus its reintegration in the Athena software framework is ongoing. As described in Section 6.1, currently in Athena the time is not used in track fitting, hence limiting

the physics potential of the HGTD. ACTS will allow to exploit 4D-tracking algorithms in order to achieve the best physics performance.

This chapter is dedicated to ACTS and its implementation in Athena. Section 7.1 gives an overview of the ACTS project, Section 7.2.3 provides the roadmap of the ACTS toolkit integration into Athena, in particular for HGTD and Section 7.3 describes the implementation of ACTS HGTD Tracking Geometry in Athena. The project is considered a longer-term work than a PhD research period. Therefore, in the scope of this thesis, I worked only on the implementation of the HGTD tracking geometry and material mapping with ACTS.

7.1 The ACTS project for HL-LHC

7.1.1 Overview

The ACTS project has three main objectives. First of all, it aims to preserve and enhance the extensively-tested code bases of the LHC experiments, while facilitating the preparation for the HL-LHC data-taking and other experiments in particle and nuclear physics. This necessitates the use of an advanced software development environment including modern programming language standards and development workflows. Secondly, the project serves as a research and development testing ground for new algorithms and techniques (including machine learning), as well as adaptability to accelerated hardware. Last but not least, the ultimate goal is to provide a complete track reconstruction toolkit, capable of being a foundation for the rapid development of tracking applications for future tracking detectors. In order to prepare ACTS for such general use, the framework design complies with the following concepts [111]:

- minimal dependency of the core components on external software packages,
- abstraction of the Event Data Model and geometry description from the specific details of any experiment,
- general mathematical formulations of algorithms independent of specific detector geometry, magnetic field, or detector technology,
- customizable connection to the algorithm configuration,
- transparent import and handling of experiment-specific contextual conditional data, such as detector calibration and detector alignment,
- facilitation of integration of core functionality typically governed by the event processing framework, e.g., message logging,
- a plugin mechanism to extend the toolkit with external software packages.

ACTS is specifically developed to meet the requirements of the heterogeneous computing environment with parallel execution. Consequently, all algorithmic modules can be executed concurrently during event processing and in between the processing of multiple events, without encountering any interference. The ACTS modules are designed so that each function call is entirely governed by the flow of data input and output, while back channel communication to caller functions is forbidden [1] [111].

ACTS targets modern many-core, general-purpose CPUs, used in ATLAS and other LHC experiments (both x86 [112] and ARM [113] architectures were tested). The hardware accelerators such as GPUs and FPGAs are actively explored by the ACTS developers.

ACTS is implemented in modern C++ (17), a programming language widely employed in the particle and nuclear physics community. Being a compiled language with minimal implicit runtime features and enabling extensive control over low-level hardware, C++ provides a good execution performance. However, it is recognized to be challenging to learn and use correctly, particularly in terms of memory management. To address this, ACTS incorporates guidelines and implementation choices that facilitate effective memory management. These measures include strict ownership handling through the move and value-like semantics. Additionally, ACTS adopts best software development practices such as unit tests and continuous integration.

The project limits the external packages dependencies to two libraries: Eigen [114] for linear algebra and Boost [115] for unit testing, file system handling, and a few key containers. The dependency management and building of the software are done with CMake. ACTS favours data-oriented programming over object-oriented programming. In data-oriented design, the communication between different parts of the code is done through sharing common data structures rather than predefined interfaces. The ACTS repository comprises the core components (always part of the installation) and the optional components (each one can be turned off during the build time) such as plugins (for building the detector geometries, digitization of particle charge deposits, etc.), the fast track simulation Fatras [116], and the test and validation code. The toolkit can be integrated into the frameworks of various experiments softwares as shown in Figure 7.1.

7.1.2 The ACTS core components

The ACTS core library is structured into modules, each one collects tools and algorithms with similar functionality. Figure 7.2 provides an overview of the core components, such as *Event Data Model*, *Geometry*, etc., that are described in the following subsections.

[1] In C++, this is enforced by restricting methods to follow a const-correct signature and by forbidding mutable data members [111].

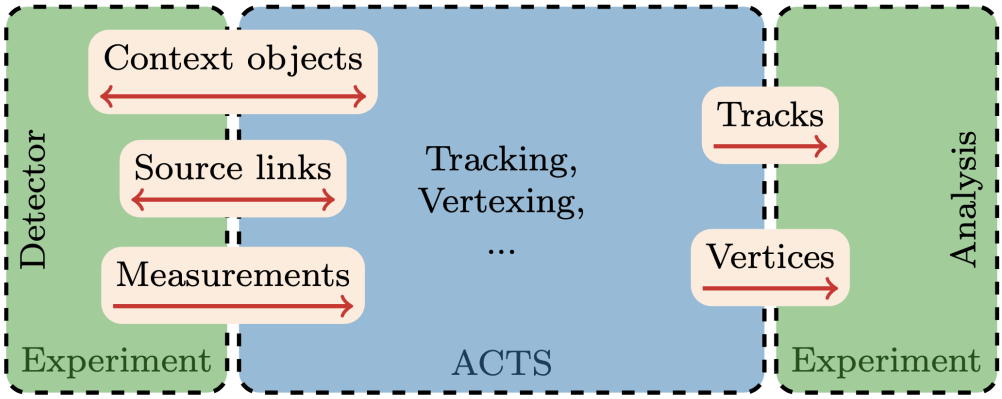


Figure 7.1: *Example of the integration of ACTS (blue square) into an experiment's software framework. The experiment- and detector-specific code (green squares) is expected to handle low-level data preparation and provide Source links and Measurements as input to ACTS algorithms. ACTS provides tracks and vertices as output for further experiment- specific reconstruction and analysis. Taken from [111].*

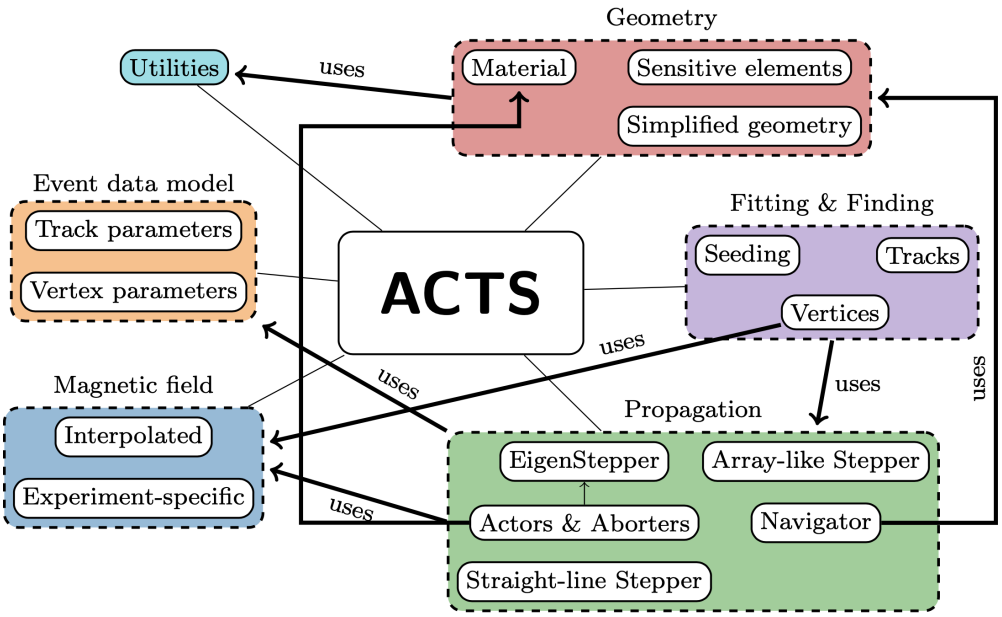


Figure 7.2: *Overview of the core modules in the ACTS repository and their interactions. The components are categorized into modules (marked with the different colors), such as Geometry, Propagation, or Event data model. A non-exhaustive number of relationships where one component "uses" other components in different modules are indicated by arrows. For example, the Propagation module components are connected to the Magnetic Field module, because the Propagation steppers need the magnetic field information. Taken from [111].*

7.1.2.1 Event Data Model

The algorithms communicate through the shared event data structures, Event Data Model (EDM), provided by the *Event Data Model* module. EDM plays a crucial role in facilitating communication between various steps of the reconstruction chain. Therefore, it needs to be both generic enough to incorporate all potential event data types and lightweight. The ACTS EDM includes measurements, track parameters and vertex parameters represented as vectors. ACTS defines two distinct types of track parameters: bound and free track parameters. Bound track parameters are represented by a reference surface for a single track, while free parameters do not rely on a reference surface and use a generic definition. The measurements vector space is a strict subvector of track parameters. It is always bound to a surface (detector element) and has at least one surface local position [111].

7.1.2.2 Geometry

The *Geometry* module handles the tracking geometry, which logically and geometrically groups detector surfaces into layers and volumes. The *Surfaces* component implements various types of detector surfaces and boundaries, while the *Material* component contains tools describing material for surfaces and volumes, along with algorithms for creating the material mapping. The ACTS reconstruction uses a simplified version of the comprehensive detector description utilized in Monte Carlo simulation programs like Geant4 [39]. While the sensitive detector elements necessitate precise depiction (including information on misalignments, damages, etc.), certain approximations are made for the non-sensitive detector elements. The detector material effects are included in the reconstruction process either deterministically or stochastically.

The reconstruction geometry is entirely built using surface objects. Composite layer objects and volume objects are all based on the surface class. Volume shapes are compounded of boundary surfaces, which are also referred to as portal surfaces since they join the volumes. Layers consist of bounding surfaces and contained surfaces, that can be sensitive (detection elements) or passive material surfaces. Navigation within the detector occurs either through portal surfaces or by performing a local search of layer surfaces after entering its bounding surfaces.

Tracking detectors are usually constructed using physical layer structures holding the modules, on-detector electronics, power cabling, cooling units, and other elements. ACTS implements the logical division into layer structures to constrain the local navigation to specific areas of interest rather than attempting to navigate through the entire detector. Each layer is assigned with a set of approach surfaces and a representative surface. The approach surfaces define the boundaries of the layer and serve as the entry points into the local layer navigation. They are used in track propagation to identify potential surface candidates within the layer, which are then

examined for intersection with the trajectory. The representative surface is a single surface representing the layer in a fast navigation search [111]. Figure 7.3 provides a sketch of the various surface types.

The generic geometry description can be extended with experiment-specific information, the detector geometry can be translated from an existing representation (DD4Hep [117], GeoModel [118], TGeo [90]).

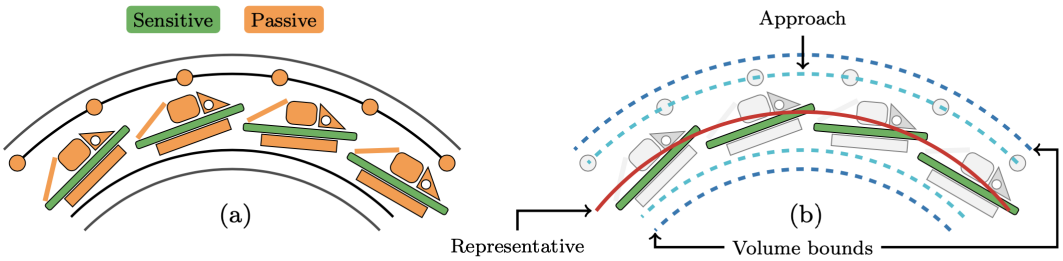


Figure 7.3: *Illustration of the layer geometry for planar detection modules. (a) Highly detailed geometry, in which both sensitive (green) and passive (orange) elements are present. (b) Simplified version, where all passive elements are discarded (grayed out). Instead, various virtual surface approximations of the detailed structure are shown and used in the modeling. The representative surface is the closest to the sensors on layer locations, while the approach surfaces form an envelope around them. A volume surrounds the layer, which also features boundary surfaces. Taken from [41].*

Apart from specifying the precise locations and shapes of the sensitive devices, the detector geometry description must also encompass a sufficient depiction of the detector material. Since passive and active materials contribute significantly to uncertainty in track reconstruction, it is crucial to have an accurate description of the quantity, type, and distribution of material within the detector volume. The handling of passive material can be done either through deterministic adjustments to the trajectory estimate or through stochastic additions to the covariance matrix. The material within the detector can be usually approximated using average material mixtures. This is done using an effective amount of traversed radiation length to evaluate contributions from multiple scattering, bremsstrahlung, and ionization loss. Simplified geometry accelerates track reconstruction by reducing the computational workload. Navigating and propagating through such geometry requires fewer CPU cycles, primarily because there are fewer intersections with surface candidates and fewer calculations for material integration. It is essential to optimize the trade-off between accuracy and speed based on the requirements of each specific experimental setup.

In ACTS, each surface and volume can have an associated material description, including auxiliary layer surfaces and volume boundary surfaces. Depending on the specific environment, corrections must be applied during the track propagation

step, which requires a precise material description. To achieve this, ACTS utilizes a dedicated mapping algorithm to project the detailed material description (homogeneous or binned) onto a selected set of surfaces or volumes. The material integration methods are called once the track propagator reaches a surface or volume that has material attached [111].

7.1.2.3 Propagator

The *Propagator* module provides tools for particle parameters propagation on surfaces along their trajectories in magnetic fields. The propagator must ensure reliable navigation through all detector elements and perform the mathematical transport of track parameters and their corresponding covariance matrices. The propagation is composed of two key components: a *Stepper* module, which is responsible for performing the mathematical transport through the magnetic field and a *Navigator* module, which predicts potential intersected candidate surfaces within the detector geometry and regulates the associated step size for the *Stepper*.

ACTS includes two steppers that utilize a fourth-order Runge-Kutta-Nyström method [94]. One employs an array-like mathematical implementation, while the other is based on the Eigen math library. Both steppers require the magnetic field as an input. Additionally, a straight-line stepper is available for use when no magnetic field is present.

The propagator is controlled by a dedicated options object that is provided for each propagation call. This options object consists of two lists: actors and aborters. Each actor defines a result type depending on the track state after *Stepper* and *Navigator*. The aborters can specify a dependency on any of the actors' result types. The client code has the ability to extend both lists during compilation and is called after each propagation step. This actor/aborter model configures the propagator in a wide variety of ways: from the on-the-fly search for missing expected hits to Kalman Filter (or Combinatorial Kalman Filter) implementation.

The magnetic field in ACTS is accessed through a dedicated provider that is passed to the stepper. The implementation of the magnetic field, both in terms of memory and conceptual design, can be modified, and several standard implementations are available. One method to provide magnetic field data involves interpolating between a grid of known field vectors. In this case, the map of the magnetic field is divided into cells with interpolated fields. Since particle propagation often involves multiple consecutive calls to the magnetic field, the steppers optimize the lookup and potential reuse of magnetic field information in one cell by accessing the field through a thread-local cache. Thus, subsequent calls to the field interface either result in the retrieval of the previous interpolation (if the call remains within the same field cell) or the retrieval of a neighbouring field cell.

Figure 7.4 shows an overview of the propagation steps in ACTS.

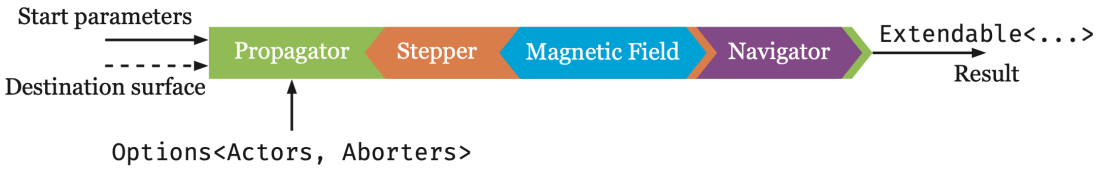


Figure 7.4: *Diagram showing the architecture of the ACTS propagator. It shows the inputs, starting parameters and an optional destination surface, and the extendable output. The functionality is controlled by the client provided options containing actors and aborters, and a number of mandatory components. Taken from [41].*

7.1.2.4 Track finding and fitting

The track reconstruction in ACTS follows the same steps as the ATLAS track reconstruction procedure described in Section 6.1.3. It starts from the track seeding, that provides a rough estimate of potential track candidates and their properties. The following steps are the track finding and track filtering, both using Kalman filter algorithms and its extension, the Combinatorial Kalman filter (CKF) technique (performs the measurement search at the same time as performing the fit).

ACTS provides a flexible and efficient primary vertex reconstruction tool, which includes various components that form a complete chain from vertex seeding to precise vertex parameter estimation. The vertexing module includes two key algorithms: the Iterative Vertex Finder (IVF) and the Adaptive Multi-Vertex Finder (AMVF) [119]. IVF performs iterative fitting of individual vertices, using a vertex seed and a collection of seed tracks. On the other hand, the AMVF simultaneously fits multiple vertices and dynamically assigns tracks to candidate vertices during the fitting. AMVF demonstrates excellent performance in high vertex density environments, such as the HL-LHC, and has been selected as the default vertex reconstruction tool for the ATLAS experiment in Run 3.

Both the *TrackFinding* and *TrackFitting* modules utilize the *Geometry* and *Propagator* modules. The *Vertexing* module, while mostly independent, relies on input from other modules and the propagation infrastructure. The *Seeding* module incorporates a geometry-independent seeding algorithm that work only with the global three-dimensional points.

7.2 Integration of ACTS into the ATLAS software framework

As mentioned in the previous section, ACTS components have been extracted or derived from the ATLAS software, with the aim of eventually reintegrating them into the ATLAS framework. To leverage ACTS tools within Athena software, several steps need to be taken for all the ATLAS subdetectors including HGTD.

7.2.1 Athena environement

First of all, the ACTS code should be available within the ATLAS Athena environment. Like ACTS, Athena employs the CMake build system implementing additional configurations to meet the specific requirements of ATLAS. As explained in the beginning of the chapter, ACTS was used as a test environement for the Athena transition from CMT to CMake. The CMake infrastructure in ATLAS encompasses an extensive collection of sophisticated custom code, designed to facilitate a logical build model for the project. In the previous build infrastructure based on CMT, the build process was relying on the numerous packages [107]. Each package was saved in a dedicated folder and consisted of C++ implementation and header files and auxiliary files like Python job configurations. CMT allowed for defining dependencies between packages, which were then transformed into a dependency tree used to coordinate the build. Each package was managed individually in source control, initially using Concurrent Versions System (CVS) and later SVN. They followed individual version strategies, resulting in complex version requirement structures and difficult packages update [41].

Given the extensive size of the codebase, comprising approximately 7 million lines predominantly composed of C++ and Python code, the build process requires a significant amount of time. Athena carries out a nightly build [34] of the entire project to ensure reasonable build times for individual developers. Developers can check out a local copy of the source code, activate a specific nightly build and choose to rebuild only selected packages on top of this build. This model facilitates a development process for such a big collaboration as ATLAS.

During the transition to CMake, it was necessary to support the existing package usage pattern. CMake handles dependencies by defining targets [110] (rather than packages), such as executables and libraries. By importing targets, it is possible to model the cases where these targets are compiled separately. The special CMake configuration code was implemented in ATLAS [41] to support the workflow of building selected packages against a complete shared build. Currently, the dependencies are defined using CMake targets instead of the package concept, keeping the logical model of a package for organizational purposes. All packages are merged into a single repository

in Git, where any change applied must ensure that the entire project still builds. This requirement is enforced by the GitLab continuous integration[2].

In addition to the main packages, Athena relies on several external projects that are essential to the build process. One of the most important examples is the Gaudi framework, which provides the event loop and various infrastructure components for the events processing. Other dependencies include linear algebra libraries like Eigen [114], the simulation toolkit Geant4 [39], the analysis framework ROOT [90] and others. These external dependencies are built from a separate repository prior to the main Athena build, ensuring that all Athena packages can use them.

7.2.2 ACTS specific packages

Since the beginning of 2018, ACTS has been included in the ATLAS Externals project. Initially, the ATLAS build process was synchronized with the master development branch of ACTS. However, it was later modified to specify an explicit version to avoid any unforeseen build issues caused by changes in the ACTS code. While this integration allows the shared libraries and headers of ACTS to be accessible from ATLAS packages, separate code development is still required for utilizing ACTS functionality.

Figure 7.5 illustrates an overview of the Athena and Externals projects and pointing out their package structure with some examples. One of the packages included in the Externals is the ACTS package, responsible for building the ACTS library. Another external package of interest for this Section is the GeoModel, which was extracted from Athena. The Athena Detector Description packages uses the GeoModel package to deliver a comprehensive description of the ATLAS detector geometry.

In order to construct the ACTS-specific instances of its geometry classes, the ActsGeometry package, inside Athena, pulls information from GeoModel and the Detector Description packages. These ACTS classes form the tracking geometry, which can be utilized by the ACTS tools and algorithms. The construction of the HGTD tracking geometry is described in Section 7.3. Additionally, the package includes a magnetic field provider, that leverages the ATLAS magnetic field service. The ActsGeometryInterfaces package defines the Application Programming Interface (API) for these components and tools.

The ActsInterop package provides a unified log handling that utilizes the logging structures of Athena. The ACTS logging solution offers extensive configuration and customization options. With this package, the ACTS logger instances can be configured to pass log messages to an Athena logging component utilizing the settings specified in

[2]the feature insuring that each change submitted to an application is built and tested automatically and continuously [105]

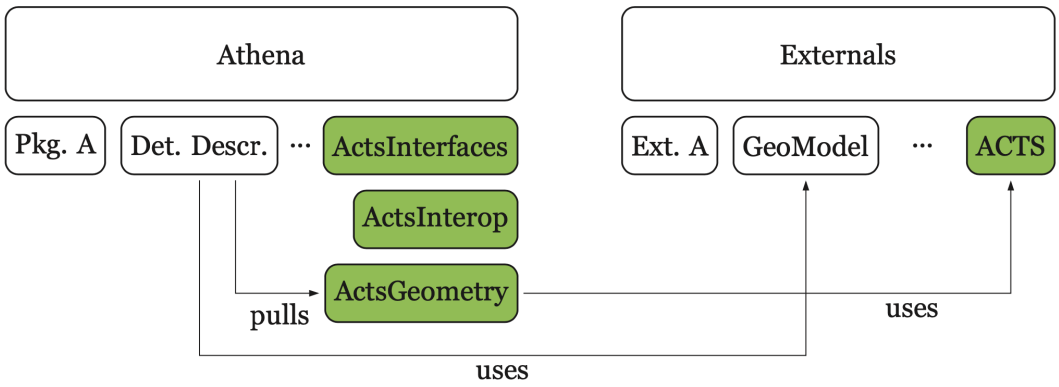


Figure 7.5: *Overview of the build structure of ACTS in the ATLAS software. The Athena and Externals projects are shown, alongside some packages contained in them. A number of Athena packages aware of ACTS are shown under Athena label, and the ACTS package is located within the Externals label. Taken from [41].*

the Athena Python configuration. Other ACTS related packages integrated in Athena such as ActsTrkAlgs, ActsTrkTools and others are out of the scope of this thesis.

7.2.3 ACTS-HGTD reconstruction roadmap

The 4-dimensional (4D) tracking with an excellent spatial resolution of the order of μm and time resolution of the order of ps represents a promising direction for charged-particle tracking in future experiments including ATLAS in the HL-LHC. Incorporating high-precision time stamps to particle tracks has a significant effect on pile-up rejection in proton-proton collisions, since it gives an information uncorrelated to the three-dimensional spatial measurements. The current HGTD track finding algorithm in Athena is based on the progressive extrapolation of tracks reconstructed in ITk to HGTD surfaces using only the spatial information. Since ACTS embeds time measurement as one of the 6 track parameters used in combinatorial Kalman filter, it is possible to include the HGTD time measurement in the pattern recognition algorithm to associate timing hits to forward tracks. The full HGTD ACTS integration is comprised of 4 major steps:

- implementation of ACTS HGTD Tracking Geometry in Athena ActsGeometry package,
- implementation of xAOD-based EDM for HGTD clusters (the ACTS compatible event data model),
- move tracking algorithm components to ACTS counterparts (extrapolator, updator etc.),
- investigation of alternative 4D-tracking approaches (exploiting time in CKF).

The first integration step was conducted by me and is described in more details in the following section. Work on further steps is still in progress involving other members of the ATLAS collaboration.

7.3 Construction of ACTS tracking geometry for HGTD

This section is dedicated to the description of the construction process of the ACTS representation of HGTD tracking geometry. This geometry serves as the foundation for various track reconstruction tasks.

For the tracking, a simplified model of geometry is used, differing from the more detailed simulation geometry (as in Geant4). Although the detailed information is crucial for accurately modeling small effects in simulations, during reconstruction, it is generally sufficient to approximate these effects, since most calculations rely on averaged material properties.

7.3.1 GeoModel geometry

In ATLAS, the GeoModel [118] is the fundamental source of geometry description used for simulation, digitisation, and reconstruction. Dedicated converters change this description into either Geant4 or a tracking geometry. The GeoModel description employs a tree structure of volume nodes, where each node contains a transformation matrix relative to its parent. To determine the absolute transformation of a node in the global frame, the tree must be traversed upwards until the root volume is reached, and the transformation matrices are accumulated along the way. The top volume represents the global frame. GeoModel incorporates mechanisms for parameterizing these transformations, which is particularly beneficial when multiple instances of an element are repeated, each with a slightly modified rotation, for instance. In this way, the elements can be described by the product of transformations applied to the prototype (or logical) node, thus avoiding the copy of essentially equivalent elements and precomputing of the transformation matrices [118].

Apart from this nominal transformation matrix, a complementary modification matrix can be included and is marked as "alignable". This feature allows the geometry tree to adapt to slight changes in the position of individual detector components over time.

The construction of the GeoModel geometry hierarchy in Athena is initiated by the component (`GeoModelSvc`), configured with a set of detector factory tools, each corresponding to one subdetector (ITk, HGTD etc.). These factory tools, in turn, call recursive factory classes responsible for building up the geometry. These factories represent physical assemblies, such as endcap wheels or ladders of modules, and

register newly created volumes in the GeoModel tree at each stage. Eventually, the construction reaches the individual sensitive sensor elements that are of interest for track reconstruction. In addition, domain-specific information needs to be incorporated, which is handled in the readout geometry step.

7.3.2 Readout geometry

ATLAS tracking software uses an additional layer of geometry information, built on top of GeoModel description, called the Readout Geometry. It represents the way in which the sensitive elements are read out. The code responsible for this discription is located in the *HGTD_ReadoutGeometry* package of Athena. The `HGTD_DetectorElement` class serves as the base class for the HGTD sensitive elements. The class inherits from a GeoModel volume class within the GeoModel hierarchy. Instance of this class combines the geometry information from the associated GeoModel element with specific details about the design of the sensor.

In contrast with GeoModel that models sensor elements as volumes, the readout geometry represents them as surfaces with a small, non-zero thickness and includes additional design parameters. These parameters capture specific aspects such as sensor segmentation or the precise shape of the sensor in a surface representation (planar surface in case of HGTD). During the GeoModel build process, the readout geometry elements are constructed when a sensitive element is encountered. These elements are created by passing the GeoModel volume, an object detailing the design and a unique identification number of the sensor. The resulting elements are stored in a flat collection [3] and indexed using the identification number. The identification number is represented by a 64-bit integer that is encoded using a specific bit range scheme. The helper class (`HGTD_ID`) enables the access to the encoded information from the identification number. Additionally, each readout geometry element stores pointers to neighbouring elements, enabling navigation between them.

7.3.3 Tracking geometry

To facilitate navigation and logical grouping in track reconstruction, a specialized hierarchy is constructed from the readout geometry. This hierarchy is designed to efficiently access and organize the elements. In the ATLAS track reconstruction library, this process involves iterating over the collection of elements and sorting them into convenient logical structures (layers for HGTD). A layer represents a two-dimensional surface that groups together multiple silicon sensors under assumption that a traversing particle will intersect with a single sensor per layer. The grouping of sensors into layers

[3] In software developement, flattening is the process of converting several collections into one single collection

is based on their identification numbers and information from the HGTD detector manager, known as numerology. The numerology contains relevant information, such as the number of disk layers in the endcap or the number of rotated sensors within a disk. This information is populated during the creation of the GeoModel hierarchy.

The readout geometry directly creates instances of the `Trk::Surface` base class (in the ATLAS tracking library), which serves as the foundation of the tracking geometry. In contrast, the tracking geometry builder in ACTS is responsible for constructing the corresponding `Acts::Surface` classes on its own. Since the ACTS version closely follows the structure of the `Trk::Surface` version, the process of extracting and converting parameters is similar in both frameworks.

The ACTS tracking geometry building starts when the configured instance of the ACTS tracking geometry service (`ActsTrackingGeometrySvc`) is initialized. The service provides configuration options for building the Pixel (ITk and Inner Detector, see Section 2.4), SCT (ITk and Inner Detector, see Section 2.4), TRT (for Inner Detector only, see Section 2.4), HGTD and the calorimeter separately or all together. Depending on the configuration, the service retrieves the corresponding detector manager instances for each subdetectors. The majority of the work is done by three implementations of the `Acts::ILayerBuilder` interface. This interface defines a factory that creates layers, which serve as the foundation for the rest of the geometry. One implementation is used for the Pixel and SCT (ITk and ID) detectors, second one is used for the TRT and the third one builds the HGTD layers. The layer builder instances rely on the respective detector managers (`HGTD_DetectorManager` in case of HGTD).

The layer builders retrieve the readout geometry elements from the corresponding detector manager and iterate over them. Each element is wrapped in an `ActsDetectorElement` instance. The class implements the `Acts::DetectorElementBase` interface, which serves as the main bridge between the experiment-aware geometry and the experiment-independent view in ACTS. Figure 7.6 shows the `Acts::DetectorElementBase` interface virtual methods that must be implemented by each detector element class. These methods enable tasks such as retrieving the element's transformation matrix and obtaining a reference to its surface representation.

The ATLAS specific implementation of this base class takes a readout geometry element and extracts its shape information to construct a corresponding surface. The ACTS detector element in Athena supports translation of several shapes (rectangular, trapezoidal, line). HGTD implements the rectangular shape modules (since the HGTD modules are 2×4 cm^2 rectangles), that are defined by two half-lengths, in the x and y directions (approximately 1 cm and 2 cm).

```
class DetectorElementBase {
 public:
  DetectorElementBase() = default;
  virtual ~DetectorElementBase() = default;

  /// Return the transform for the Element proxy mechanism
  ///
  /// @param gctx The current geometry context object, e.g. alignment
  virtual const Transform3& transform(const GeometryContext& gctx) const = 0;

  /// Return surface representation - const return pattern
  virtual const Surface& surface() const = 0;

  /// Non-const return pattern
  virtual Surface& surface() = 0;

  /// Returns the thickness of the module
  /// @return double that indicates the thickness of the module
  virtual double thickness() const = 0;
};
```

Figure 7.6: *The `Acts::DetectorElementBase`, required for all detector element classes in ACTS, with its methods.*

After obtaining a list of translated detector elements, they need to be grouped into layers. The grouping is done using the information from the identification number. In HGTD, the identification number encodes the disc layer and the endcap to which a specific element belongs.

Following the elements grouping, the layer builder (detector specific implementations of `Acts::ILayerBuilder`, for example `HGTD_LayerBuilder`) iterates over the layer groups, determining an appropriate size for each layer and assembling the required surface representations. To enable fast queries for compatible surfaces based on a given position on the surface representation of the layer, a binned structure is employed [41]. The binning scheme is automatically determined by the layer builder, taking into account the positions and sizes of the modules within the layer. Each bin in the binning structure can accommodate multiple surfaces, and the navigation procedure also gathers surfaces from neighboring bins. As a result, some level of flexibility in the binning can be achieved, provided that the binning structure approximately aligns with the geometrical arrangement of the sensors.

The layer builders are part of a series of ACTS helper classes that organize groups of layers into volumes and establish suitable connections for particle navigation. For example, for each subdetector designated for construction, a helper class `CylinderVolumeBuilder` is initialized. The resulting list, ordered from the innermost to the outermost layers, is passed to the top-level helper in this chain, the `TrackingGeometryBuilder`. This helper acts as a factory, instructing the configured builders to generate their volumes

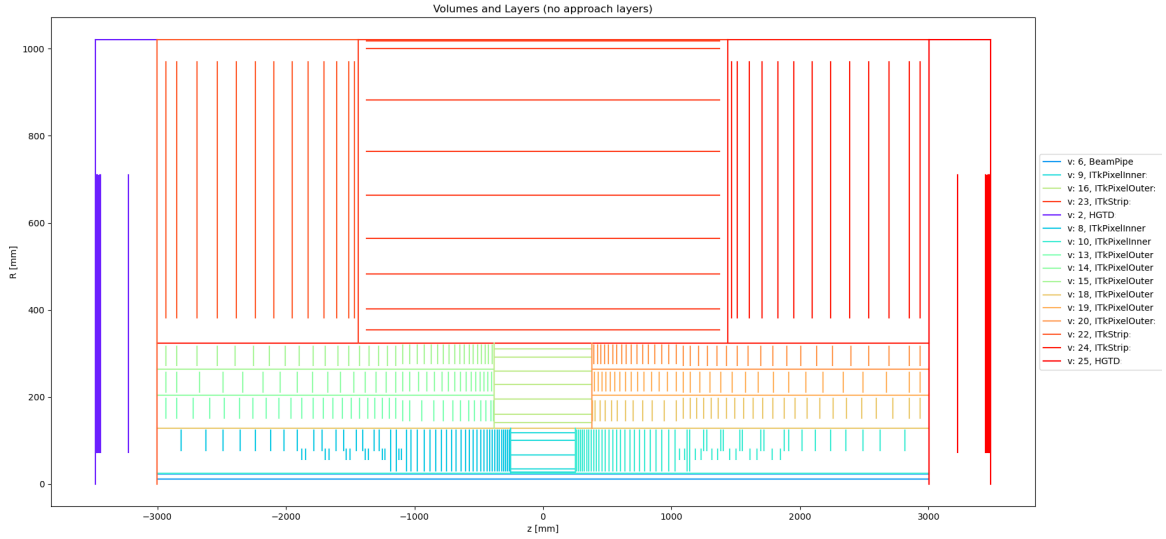
and establish connections, effectively join the subdetectors together. The final output is an instance of `Acts::TrackingGeometry`, encompassing the entire detector hierarchy, including individual sensitive modules.

Following the procedure described above, the full HGTD detector was implemented in ACTS tracking geometry. Several python scripts for plotting are available in Athena ACTS package for the built geometry cross check validation. Figure 7.7 shows the tracking geometry of both HGTD and ITk (a) and of HGTD only (b,c). In Figure 7.7 (a), the HGTD layers are located at the both endcaps (purple and red layers at the distance around ±3450 mm from the center). The surface representations of the 4 HGTD discs can be seen in Figure 7.7 (b) and (c) and can be compared to the geometry implemented in Athena (Figure 6.1).

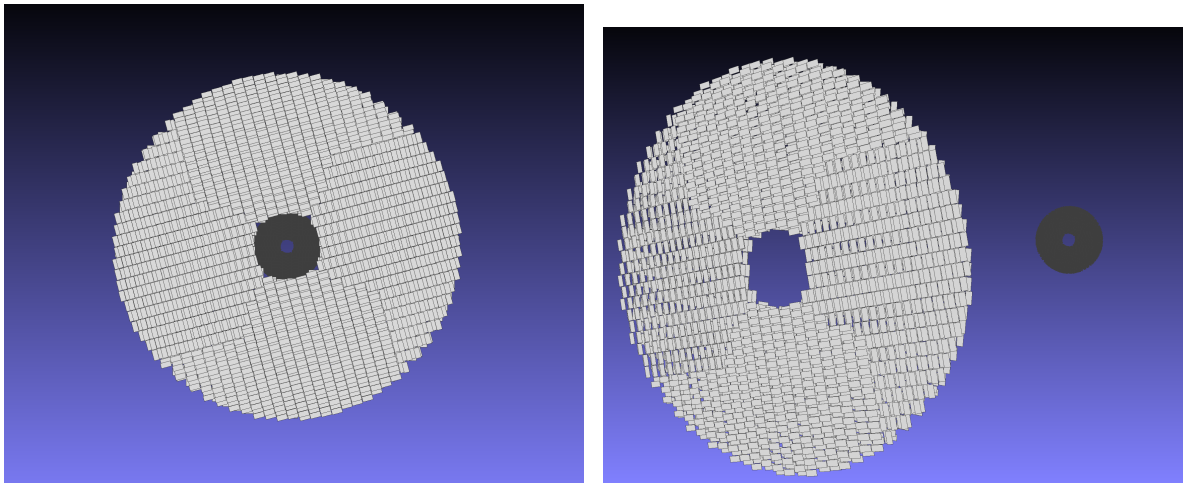
7.3.4 Propagation test

In addition to visual check of the geometry using a 3D representation based on individual sensors, it is also important to evaluate the construction by probing the navigation process. This can be accomplished through particle propagation. Numerous extrapolations of particle trajectories with different random directions were used. At each extrapolation step, information about the current state of the extrapolation was recorded. These steps are created whenever a Runge-Kutta-Nyström snapshot of the particle properties is generated, either within an empty volume or onto different types of surfaces forced by the navigation. Boundary surfaces serve as targets for navigating between volumes, layer surfaces are encountered when approaching a layer, and sensitive surfaces when intersecting a sensor. By plotting the distribution of the locations of these steps, the accuracy and effectiveness of the navigation can be verified, and potential issues can be detected. Figure 7.8 shows such particles extrapolation steps in the sensitive surfaces of HGTD in the positive endcap in the x-y plane. The propogations are shown for each layer separately (0, 1, 2, 3), only the positive endcap is presented, since the results for the negative endcap are equivalent.

As was discussed in the Section 7.1.2.2, it is crucial to include the passive material in the tracking geometry in order to correctly make predictions on the particle properties after surface intersection. For HGTD, the surface based maps were created, in which the material is averaged onto surfaces. The material was mapped on each approach surface before every HGTD disc. The discrete integration of material effects is then taken into account when the surface is crossed. In order to validate the material mapping for the ACTS tracking geometry, the comparison with the Geant4 material distribution is done for the current ATLAS geometry version ATLAS-P2-RUN4-01-01-00 [34]. The result of the comparison is shown in Figure 7.9. The material mapping with ACTS shows a good overall agreement with the Geant4 simulation. However some optimizations are needed and forseen for the future work. In particlular, the η



a)



b) c)

Figure 7.7: *The ACTS tracking geometry layer represention of part of ITk and HGTD above the beam line at R=0 mm (a) and surface representation of HGTD alone (b, c). (a): the HGTD corresponds to the 4 purple layers on the far left (negative endcap) and 4 red layers on the far right (positive endcap). (b,c): the view of HGTD detector in 3D projection without the rest of the ATLAS detector is shown, where all HGTD discs are present. The surfaces of the endcap closer to the viewer are shown in light grey, while the second endcap discs are shown in dark grey further away.*

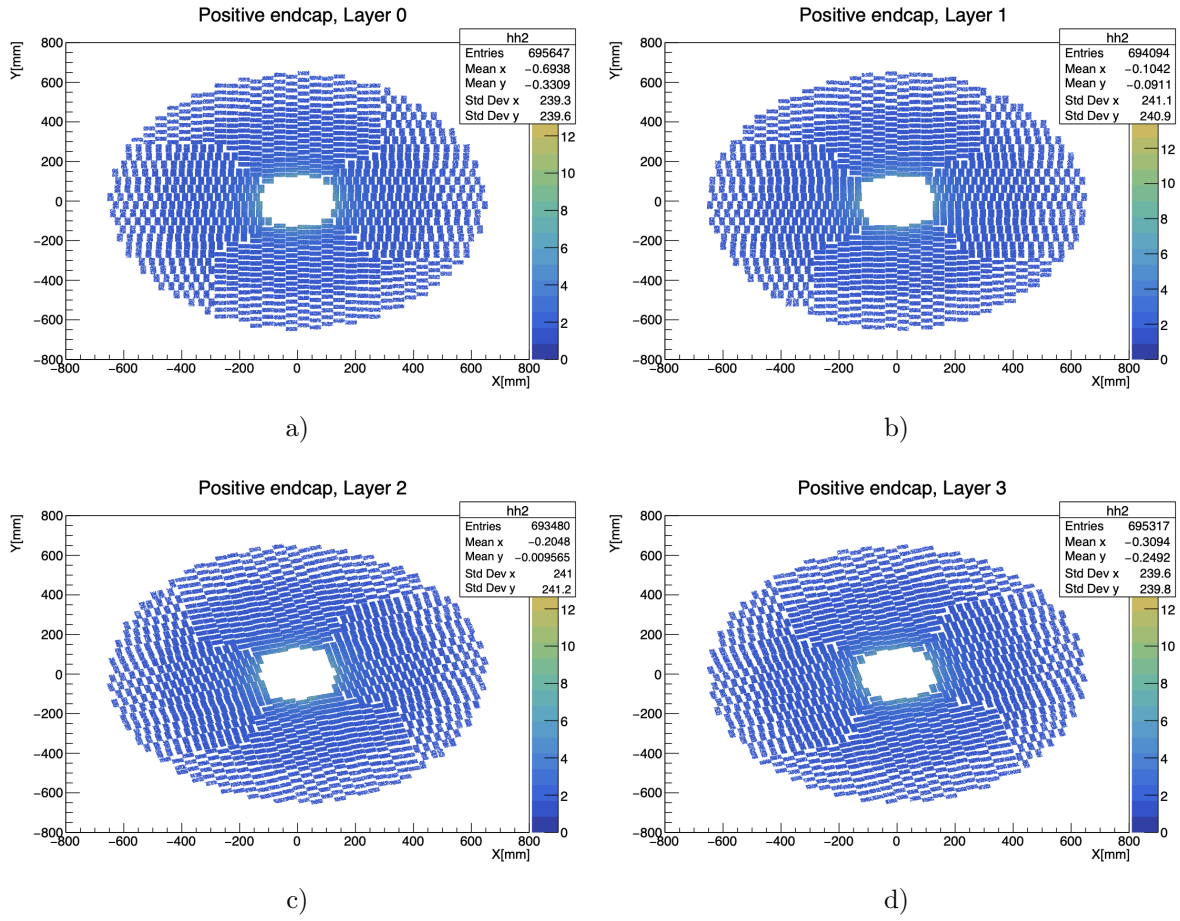
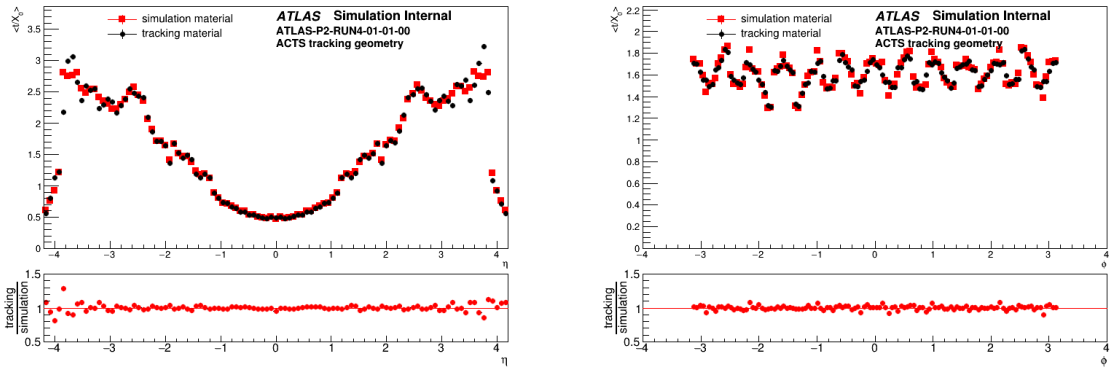


Figure 7.8: *The steps of the ACTS propagation through the tracking geometry of the four HGTD discs in the x-y plane in the positive endcap. The propagation on each HGTD layer separately is shown.*

region between 3.6 and 3.9 suffers the most from the upstream material budget and requires the more precise mapping. This can be achieved by adjusting the material binning for the problematic pseudorapidity range or adding the extra surfaces with material, for example.



a) b)

Figure 7.9: *Comparison of the material budget (ITk+HGTD) as a function of pesudorapidity (a) and azimuthal angle (b) in units of radiation length X_0 between Geant4 and the mapped ACTS material.*

7.4 Conclusion and outlook

The ATLAS track reconstruction software (Athena) has demonstrated excellent physics performance and has been highly effective as the foundation of the ATLAS offline reconstruction between Run 1 and Run 3 of the LHC data taking. The foundation of the existing ATLAS tracking software was developed approximately 20 years ago, and over time, certain concepts and design patterns have become outdated. Maintaining and updating this codebase, especially in the context of potential heterogeneous computing applications, is a challenging and risky path for ATLAS.

First of all, the core code of the ATLAS tracking software was developed before the parallel processing (MP) [42] or the multi-threaded (MT) [33] execution became part of the ATLAS reconstruction strategy (see Section 2.4.6). As a result, components enabling MP and/or MT-capable reconstruction were added to the existing codebase, leading to suboptimal implementations due to the limitations of the original code and interface structure. The ATLAS tracking code extensively relies on virtual inheritance in its design, which typically leads to a decrease in performance and raises challenges for supporting non-CPU architectures. The virtual call chain in the codebase is often very deep, and there are instances where virtual interfaces exist even when only one implementation is actually utilized. In a study exploring the feasibility of implementing a GPU-accelerated Kalman fitter [120], it was found that the polymorphism resulting

from virtual inheritance was a significant obstacle for such effort. Moreover, the key components of the code, such as the complete track fitting suite, are no longer actively maintained as the original authors and experts are no longer part of the ATLAS collaboration.

The development of the ACTS track reconstruction toolkit began in late 2016 as a prototype initially encapsulating the event data model and geometry from the existing ATLAS software. Over the years, it has evolved and expanded in functionality, becoming an experiment-independent track reconstruction software. Many of the concepts and code components, although often refurbished and modernized, have their roots in the ATLAS tracking software. Therefore, ACTS largely reflects the conceptual functionality available in the ATLAS track reconstruction code. To this day, developers from the ATLAS collaboration remain the largest group of contributors to the ACTS project.

Nowadays, the ACTS toolkit is a complete component library, offering logical track reconstruction components such as propagation engines, various fitters, and clusterization modules. These components operate at a generic mathematical level, providing a flexible and modular approach to track reconstruction. The software is written in the modern C++, favoring small compile-time interfaces and variadic templating over virtual interfaces for better performance and greater implementation flexibility. The data-oriented programming is chosen instead of object-oriented programming, meaning that the communication between different parts of the code occurs through sharing common data structures rather than predefined interfaces [111]. This enables the MT execution and the use of heterogeneous architectures.

ATLAS is planning to make extensive use of ACTS in Run 4. Therefore, work on the ACTS integration into the Athena software is ongoing. All the ATLAS subsystems participating in the tracking should adapt to the new ACTS environment, including HGTD. In addition, ACTS provides a possibility to make use of the HGTD time measurements in the 4D-tracking. This will largely improve the physics object reconstruction capability in the harsh pile-up environment during the HL-LHC era. Even though, this work is considered as long-term project, I made the first steps of the ACTS integration of HGTD. The successful ACTS HGTD tracking geometry implemention in Athena and propogation tests were described in this chapter. The tracking geometry is also supplied with the material map, which shows a good overall agreement with the Geant4 simulation, but can be further tunned in some η bins. The next steps of the ACTS integration into the HGTD reconstruction chain are: conversion of the HGTD measurements into an xAOD-based data format (the ACTS compatible event data model), transfer of the tracking algorithm components one-by-one to ACTS counterparts (extrapolator, updator etc.), investigation of alternative 4D-tracking approaches exploiting time in CKF.

Chapter 8

Conclusion

The large increase of pile-up interactions is one of the main experimental challenges for the ATLAS physics programme during High-Luminosity LHC (HL-LHC). A new promising way to mitigate the effects of pile-up contamination is to use high-precision timing information to distinguish between collisions occurring close in space but well-separated in time. A High-Granularity Timing Detector (HGTD), based on Low Gain Avalanche Detectors (LGAD) technology, is therefore being developed for the ATLAS Phase-II upgrade. Covering the pseudorapidity region between 2.4 and 4.0, HGTD will improve the ATLAS detector physics performance in the forward region. The detector design was optimized so that the target average time resolution per track for a minimum-ionising particle is between 30 and 50 ps at the beginning and the end of the operation, respectively. In addition, the HGTD offers unique capabilities for online and offline luminosity determination, an important requirement for precision physics measurements. The thesis is dedicated to the research and development of HGTD in several aspects: mechanics and assembly, LGAD performance study and software development. Chapter 2 presents an overview of LHC and the ATLAS experiment, including the HL-LHC and the corresponding ATLAS upgrade overview.

Chapter 3 is dedicated to HGTD. It gives a brief overview of how the high-precision timing information improves the pile-up reduction to enhance the forward object reconstruction, complementing the capabilities of the upgraded Inner Tracker (ITk) detector in the forward regions of ATLAS. The chapter also provides the key detector requirements and the technical design aspects.

In Chapter 4, mechanical R&D, in which LPNHE is deeply involved, is presented. In this scope, I have conducted several gluing tests of the modules and support units to define an effective gluing procedure. A big part of the mechanical R&D work was dedicated to the heater demonstrator meant to study the mechanical and cooling aspects of HGTD using the silicon-based heater substrate mimicking the real modules. I contributed to all the activities related to the demonstrator: the calibration of the

heaters, the metrology tests of the heaters, the gluing of the heaters onto support units, the demonstrator assembly and data taking. The heater demonstrator tests uncovered some bottlenecks in the module assembly procedure, such as the importance of support units flatness, and the cooling. This work provoked several detector design changes. The full demonstrator with the real HGTD modules instead of heaters is being developed and takes into account the experience gained during the heaters demonstrator assembly.

Chapter 5 is dedicated to the performance studies of several LGAD sensors from various vendors in the test beams. I took part in several test beam campaigns and analysed the data. The test beam campaign at DESY in 2020 revealed the problem of Single Event Burnout, which causes the sensors non-revertable damage. It showed the need in the new LGAD design, that will allow usage of the lower bias voltages, while keeping the required LGAD performance. The new carbon enriched LGADs, tested at DESY in 2022 and presented in this chapter, showed a good performance in terms of efficiency, time resolution and charge collection. It was proven, that the highly irradiated LGADs can deliver efficiency higher than 95%, resolution below 70 ps and the charge collection higher than 4 fC. The results of the analyses served as an important milestone in defining the baseline LGAD design for HGTD.

Chapter 6 describes a comprehensive study on the HGTD track reconstruction performance. I developed and implemented a new algorithm, *holes on track cleaning* that addresses the problem of the wrong track-time assignment and significantly improves the purity of the tracking efficiency. The optimal cuts were chosen that are comparable with or better than the *TDR cleaning* performance. For these cuts in the 3-ring HGTD geometry, if the tolerance level of 3σ in ITk and HGTD is set, the misassignement varies from 12.4% to 16.76%, while the correct assignement is between 49.48-51.25%. It can be compared with the HGTD performance without any cleaning: 19.12% of tracks do not get the time assigned, 53.50% of tracks have the correct time assigned to them and 27.38% have misassigned times.

In chapter 7, the novel tracking software ACTS (stands for A Common Tracking Software) is discussed. Since ATLAS is planning to make extensive use of ACTS during the HL-LHC data-taking, it is crucial to integrate it into the ATLAS analysis software (Athena). Even though, this work is considered as long-term project, I made the first steps of the ACTS into the HGTD reconstruction chain including the implementation of the ACTS tracking geometry for HGTD and the material mapping. The next steps of the ACTS integration are conversion of the HGTD measurements into the ACTS compatible event data model, transfer of the tracking algorithm components one-by-one to ACTS counterparts (extrapolator, updator etc.), investigation of alternative 4D-tracking approaches that use time.

The described work was crucial for the HGTD development to be used in the HL-LHC era.

Appendix A

A.1 Silicon detectors overview

One of the most common solid-state detectors in High Energy Physics are the semiconductor detectors, which are based on a crystalline semiconductor material, in particular silicon (Si). The energy needed to create an electron-hole pair in a semiconductor material is very small comparing to the gas detector, e.g. 3.6 eV for Si [58]. The advantages of the semiconductor detectors are:

- high density, which allows achieving large energy loss per traversed distance and allows to make the detector thin and having a lower material budget;
- high mobility of charge carriers (the mobility of electrons in silicon is about 1400 $\text{cm}^2 V^{-1} s^{-1}$ and of holes is around 450 $\text{cm}^2 V^{-1} s^{-1}$ [58]);
- excellent mechanical rigidity.

A.1.1 The Band theory

The fundamental theory used to describe the energy spectrum of electron levels in a crystalline lattice and to optimize the detectors performance is the band theory. According to quantum mechanics, when isolated atoms are brought together on a crystalline lattice, the discrete energy levels of their electrons evolve into energy bands. In these bands, the energy levels of electrons are so closely spaced that they can move between them with minimal energy, which can be obtained e.g. from thermal motion. The two main energy bands are the valence band, which contains the electrons that participate in chemical bonding, and the conduction band, which contains the electrons that are free to move and conduct electricity. The forbidden band to be occupied by electrons is called a band gap. It separates the valence band and the conduction band.

Energy bands have different relative positions in different materials, which can be classified into three categories based on their band configuration: insulators, conductors, and semiconductors (see Figure A.1). Insulators have a wide band gap of more than 2 eV, while conductors do not have a band gap at all. In contrast, semiconductors

have a narrow band gap. The width of the band gap in semiconductors is typically less than 2 eV, meaning that even small thermal excitations can provide enough energy for electrons to overcome the band gap. For instance, at a temperature of 273 K, the band gap of Si is around 1.1 eV. To be pointed out that in silicon 3.6 eV are required to create an *electron-hole* pair, i.e. e-h pair, due to the indirect band-gap that requires the creation of phonons for momentum conservation law [58].

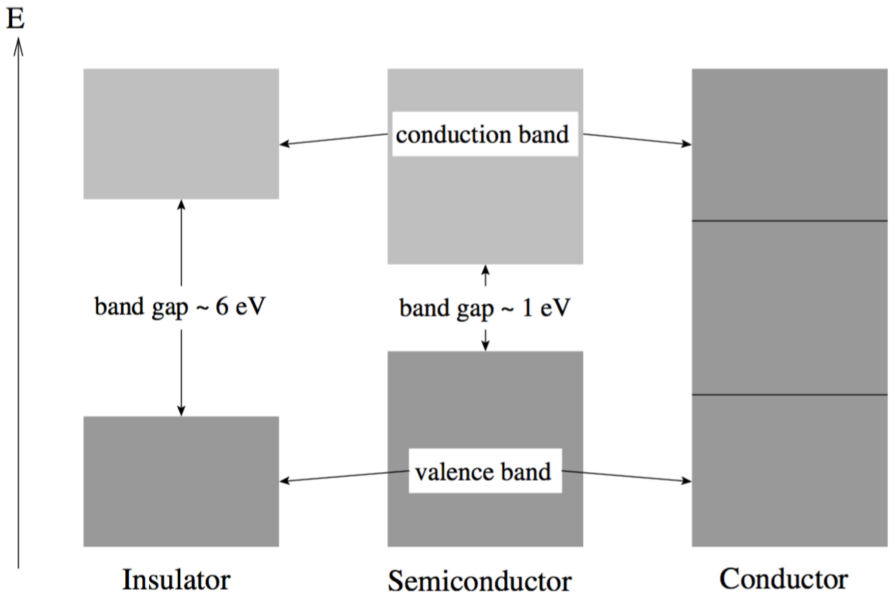


Figure A.1: *Energy band diagrams for insulator, semiconductor and conductor, taken from [59].*

The excitation of an electron in the valence band leads to a creation of a vacancy (or a hole) in the valence band and a free electron in the conduction band, together forming an e-h pair. If an electric field is applied to the semiconductor, the free electrons and holes move in opposite directions. The probability for a fermion to have energy E is described by the Fermi-Dirac distribution $f(E)$:

$$f(E) = \frac{1}{1 + e^{(E-E_F)/k_B T}}, \tag{A.1}$$

where E_F is the Fermi level, denoted as the energy level which electrons occupy with the 50% probability, k_B is the Boltzmann constant, and T is the temperature [58]. The e-h pairs are continuously generated through thermal excitation and get destroyed through the recombination process. In general, the charge carriers density can be calculated by integrating the product of Fermi-Dirac distribution (see Equation A.1) and density of states (i.e. how many electron/hole energy states are possible in conduction or valence bands) over energy range. For electrons density n_e in the conduction band, the integral is taken from the minimum energy level of conduction band (E_C) to infinity, resulting in:

$$n_e = N_C e^{-\frac{E_C - E_F}{k_B T}}, \tag{A.2}$$

where N_C is the effective density of states in the conduction band. For the holes density n_p in the valence band, one integrates from zero to the maximum energy level (E_V) in the valence band and obtaines:

$$n_p = N_V e^{-\frac{E_F - E_V}{k_B T}}, \tag{A.3}$$

where N_V is the effective density of states in the valence band [59].

In a pure semiconductor with no impurities, e-h pairs are produced by thermal excitation, the number of electrons in the conduction band (e) and holes in the valence band (p) is equal:

$$n = p = n_i, \tag{A.4}$$

where n_i is the intrinsic concentration. Such materials are called ideal intrinsic semiconductors [58].

However, ideal semiconductors do not exist in nature, they have different impurities and defects. These imply the addition of energy levels within the band gap and a change of conduction properties of a material. In these case, the electron and hole densities do not have to be in equilibrium. Material with impurities is called extrinsic semiconductor. The proccess of adding the impurities is called doping.

There are two kinds of impurities depending on the kind of increased charge carriers. If the impurity causes an increase of the number of holes, it is called acceptor impurity. On the other hand, the impurity that increases the density of electrons is the donor impurity [59]. Generally, for the radiation detectors, the extricnsic semiconductors with small impurity density are used. For example, in silicon-based semiconductors typically for each impurity atom, there are about 10^{10} atoms of Si [59]. When density of majority carriers (in the case of n - type semiconductor carriers are electrons) increases, the density of minority carriers decreases [58]:

$$np = n_i^2. \tag{A.5}$$

A.1.2 P-type semiconductors

When an impurity with fewer valence electrons than in the host semiconductor is added (for instance boron or gallium for the silicon semiconductor), it will form less covalent bonds than the intrinsic semiconductor. This leads to the creation of extra holes in the material, making it an extrinsic p-type semiconductor. P-type semiconductors have additional acceptor-type energy levels close to the valence band. For example, adding boron to silicon generates an acceptor level with an energy of $E_A = E_V + 0.045$ eV [59],

where E_V is the valence band energy, see Figure A.2, left. The energy of 0.045 eV is small enough that even thermal energy can ionize the impurity atom. Figure A.2(right) illustrates the acceptor doping of silicon by boron.

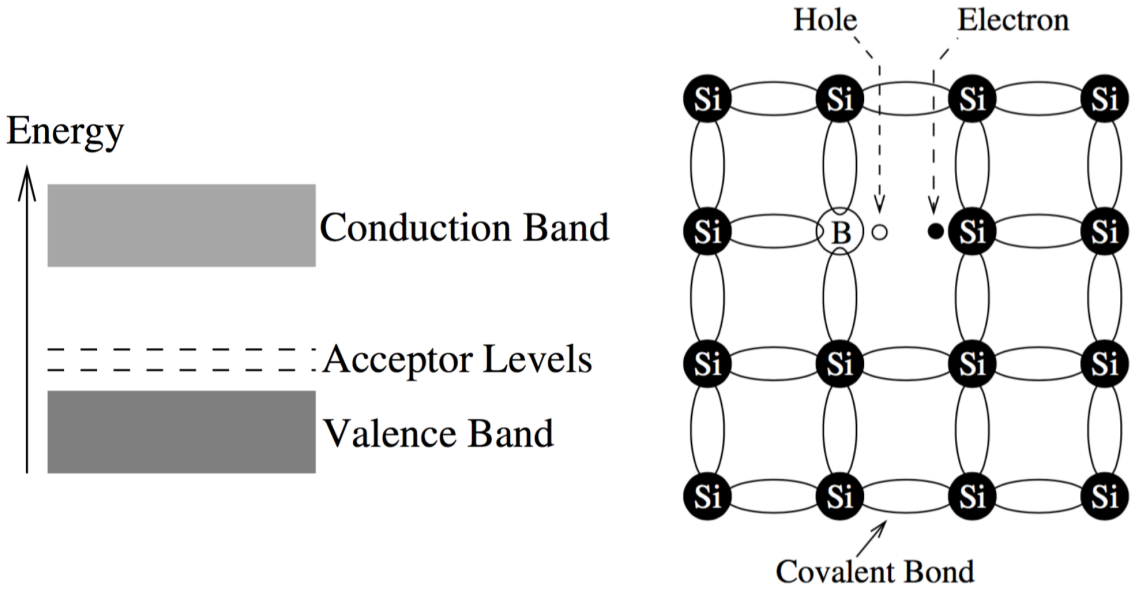


Figure A.2: *Left: energy band diagram with the additional acceptor levels. Right: Si lattice doped with boron. Since boron has one electron less, it can form only three covalent bonds with neighboring Si atoms. The fourth unfilled band behaves as a hole since it attracts free electrons. If this hole is filled by a neighboring electron, it will appear at the initial place of this electron. Taken from [59].*

A.1.3 N-type semiconductors

When an impurity element in a semiconductor material has more valence electrons than the semiconductor atoms, these extra electrons cannot form covalent bonds with the atoms and become free. This type of semiconductor material with a donor impurity is called an n-type semiconductor. Doping with a donor impurity results in the creation of new donor energy levels near the conduction band. For example, in silicon doped with phosphorus, a donor level with energy $E_D = E_C - 0.054$ eV is created, where E_C is the conduction band energy, as shown on the left diagram of Figure A.3. These additional energy levels reduce the band gap effectively, which enhances the conductivity of the material. Figure A.3 on the right shows the donor doping of silicon with phosphorus.

A.1.4 The p-n junction

The fundamental component of all semiconductor detectors is the p-n junction, which is formed by joining p-type and an n-type semiconductors. When a p-type and n-type

semiconductors are connected, electrons will move into the p region, and holes will move into the n region, in order to compensate for the charge imbalance across the junction. The diffusion and recombination processes lead to a decrease in the concentration of negative charge at the boundary of the n region, causing it to become positively charged. Likewise, the concentration of holes at the boundary of the p region will decrease, leading it to become negatively charged. This results in the creation of an electric field that opposes further diffusion, forming a depletion zone, which is a region free of mobile carriers, with a potential between the p and n regions, known as the built-in voltage V_{bi}, as shown in Figure A.4:

$$V_{bi} = \frac{kT}{q} \ln \frac{N_d N_a}{n_i^2}, \tag{A.6}$$

where N_d and N_a are donor and acceptor concentrations on the n and p sides and q is the unit elementary charge [121].

In semiconductor detectors, the depletion zone is a sensitive region, where the incident radiation (or traversing particle) generates the electron-hole pairs which are separated by the presence of the electric field. The width of the depletion region can be regulated by an external voltage. By applying a positive potential to the p-region and a negative potential to the n-region (forward bias voltage), the potential barrier decreases, causing the current across the junction to increase. Conversely, when the polarity is reversed (back/reverse bias voltage), the potential barrier increases, causing the width of the depletion region to expand. The external electric field causes the charges to

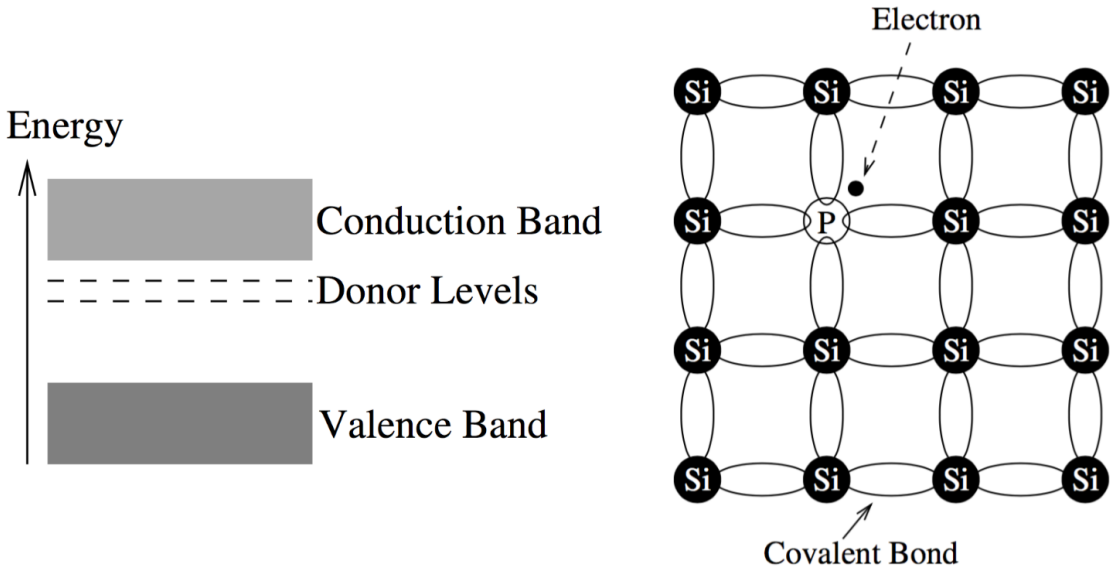


Figure A.3: *Left: energy band diagram with the additional donor levels. Right: Si lattice doped with a phosphorus atom. Since phosphorus atom has 5 available electrons for bonding, and silicon has only 4 valence electrons, one extra electron from phosphorus outer shell becomes free. Taken from [59].*

move, resulting in the production of a current, called leakage current, that creates an associated voltage drop that can be measured, see Figure A.5. The later mode of operation is used in detectors. The width of the depletion zone depends mainly on the donor and acceptor concentrations, V_{bi}, and the applied bias voltage.

The leakage current depends linearly on the depleted width, increases with $\sqrt{V}$ and is lower at lower temperatures. As the reverse bias of the junction increases, the electric field also increases, causing an expansion of the depleted region, which enhances the junction's capability as a particle detector. However, after reaching the breakdown voltage (V_{bd}), the detector will break down and become conductive. This threshold marks the maximum bias that can be applied to the junction.

A.1.5 Signal generation in silicon sensors

Charged particles crossing material interact with the atoms of the material losing part of their energy. They energy loss may be due to the particle's interaction with the electrons of the atoms (ionizing energy loss) or with the nuclei (non-ionizing energy loss). The ionizing loss is responsible for the creation of the e-h pairs, while the non-ionizing one causes defects in the crystal and is the origin of radiation damage.

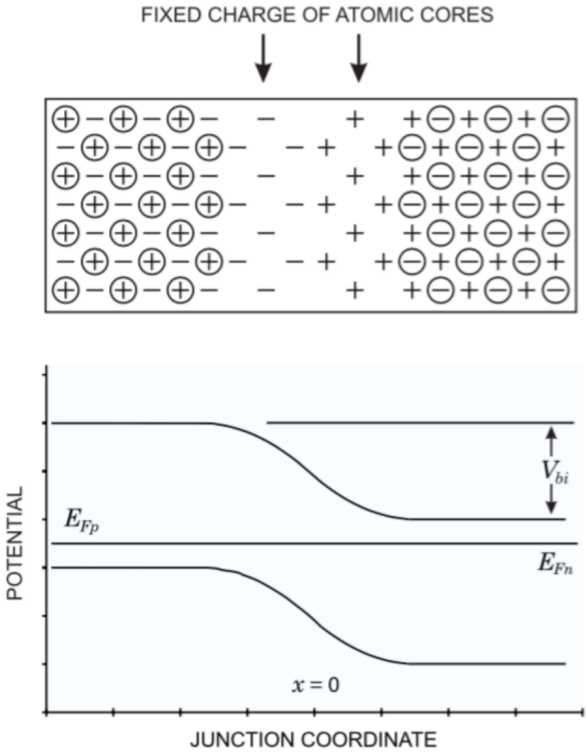


Figure A.4: *Diffusion of electrons and holes across the p-n junction forms a depletion zone with a built-in potential V_{bi} between the p and n regions, E_{Fn} and E_{Fp} are Fermi energy levels of n and p regions. Taken from [121].*

Charged particles crossing material deposit a part of their energy via scattering processes with electrons of the medium. The mean energy loss per unit traversed length is described by the Bethe-Bloch formula:

$$\langle -\frac{dE}{dx} \rangle = K z^2 \frac{Z}{A} \frac{1}{\beta^2} \left[\frac{1}{2} \ln \frac{2 m_e c^2 \beta^2 \gamma^2 T_{\max}}{I^2} - \beta^2 - \frac{\delta(\beta\gamma)}{2} - \frac{C}{Z} \right], \tag{A.7}$$

where E is the energy loss per unit length, x is the distance traveled, $K = 4\pi N_A r_e^2 m_e c^2$, z is the charge of the incident particle, Z is the atomic number of the target material, A is the atomic weight of the target material, $\beta = v/c$ is the velocity of the incident particle relative to the speed of light, $\gamma = (1-\beta^2)^{-1/2}$ is the relativistic Lorentz factor, $T_{\max}$ is the maximum energy transferable to an electron in a single collision (i.e. the kinetic energy of the incident particle divided by 2), I is the mean excitation energy of the target material, $\delta(\beta\gamma)$ is the density effect correction, and C is the shell correction term [16]. The energy loss in a detector depends on the energy of the passing particle and on the detector thickness. The energy deposited by ionization generates a number of e-h pairs proportional to the detector thickness (a Minimum Ionising Particle particle creates 70-100 e-h pairs/μm) and inversely proportional to the energy needed to create an e-h pair. The probability distribution function describing the energy loss in a detector of a certain thickness is described by Landau distribution.

The free charge carriers generated by ionizing particles, drift through the sensitive (or depleted) area and are collected by the heavily n and p doped regions (n+ and p+ respectively) that act as electrodes. The movement of the charge in the electric field induces a current in the readout electrode that is described by the Schockley-Ramo

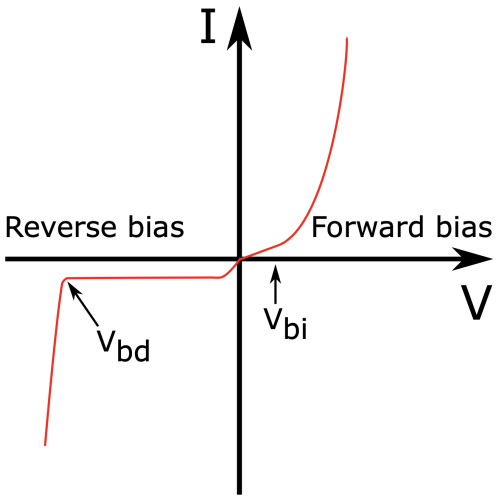


Figure A.5: *Current in a p-n junction as a function of the bias voltage . In reverse bias, the leakage current does not change over a voltage range until the breakdown voltage, V_{bd}, where it rises exponentially. In forward bias, when the current overcomes the V_{bi}, the current rises exponentially. Taken from [63].*

theorem [58]. The total charge collected by the electrode can then be calculated by integrating this current from the starting time of the carriers movement until the carriers are trapped or have arrived to the electrode. The most basic silicon detector, without any segmentation is called a pad diode and is shown in Figure A.6.

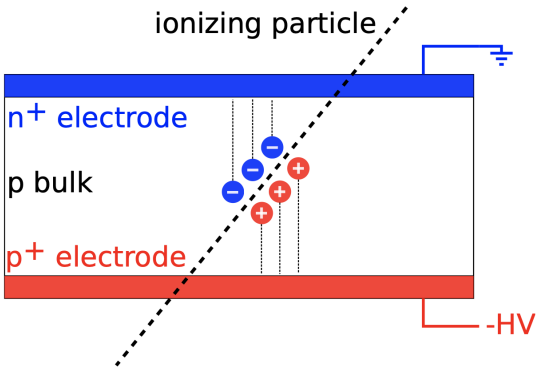


Figure A.6: *Sketch of an n-on-p pad diode with an ionizing particle creating e-h pairs in the bulk that are collected by the electrodes. Taken from [63].*

A.1.6 Radiation damage in the silicon detectors

Understanding the impact of radiation on the performance of silicon detectors in hadron collider experiments is crucial due to their exposure to high radiation levels. The radiation damage is classified as either *bulk effects* or *surface effects*. The surface effects are caused mostly by the ionizing radiation and are more significant for the embedded electronics in the sensor.

The bulk effects are the primary contributor to performance deterioration in silicon sensors. The effects of radiation damage in the silicon bulk are primarily caused by the inelastic scatterings of the particles undergoing the Non-Ionizing Energy Loss. Such interactions cause atoms to be displaced in the crystalline lattice.

High-energy particles that interact with the nuclei of silicon atoms and transfer over 25 eV of energy cause bulk effects. Such defects can be scattered or clustered around the particle trajectory. The isolated atomic displacements away from each other are called point defects, whereas a cluster of atomic displacements close to each other is called a cluster defect [58].

A.1.7 The NIEL scaling

In contrary to the ionizing energy loss (responsible for the e-h pairs creation), the NIEL is not proportional to absorbed energy, but it depends on the type of radiation and particle energy. To effectively compare the bulk defects caused by different particles

with different energies, a practical approach is to normalize and parametrize these effects. One method of achieving this is by utilizing the NIEL hypothesis to express the bulk radiation damage [121]. The NIEL hypothesis operates on the assumption that the damage caused by any particle at a particular fluence Φ, number of particles per unit area, can be scaled to that of a reference particle at a specific energy. Typically, a 1 MeV neutron is utilized as the reference particle.

The Non-Ionizing Energy Loss (NIEL) damage $D(E)$ measured in MeVmb can be expressed as:

$$D(E) = \sum_i \int_{E_{min}}^{E_{max}} Q(E_R)\, E_R\, (\frac{d\sigma(E)}{dE_R})_i\, E_R, \tag{A.8}$$

where E is the energy of impinging particle, E_{min} and E_{max} are the minimum and maximum energies of the particle spectrum, E_R is the energy given to recoil atom, $\frac{d\sigma(E)}{dE_R}$ is differential partial cross section for a particle with energy E to create a recoil atom with energy E_R in the i-th reaction and QE_R is the partition factor giving the fraction of E_R that is going into further displacements [122]. In Figure A.7, the dependence of NIEL damage function on the energy of the initial particle for different particles is shown. A reference value of 1 MeV neutron equivalent n_{eq} was fixed to 95MeVmb [121].

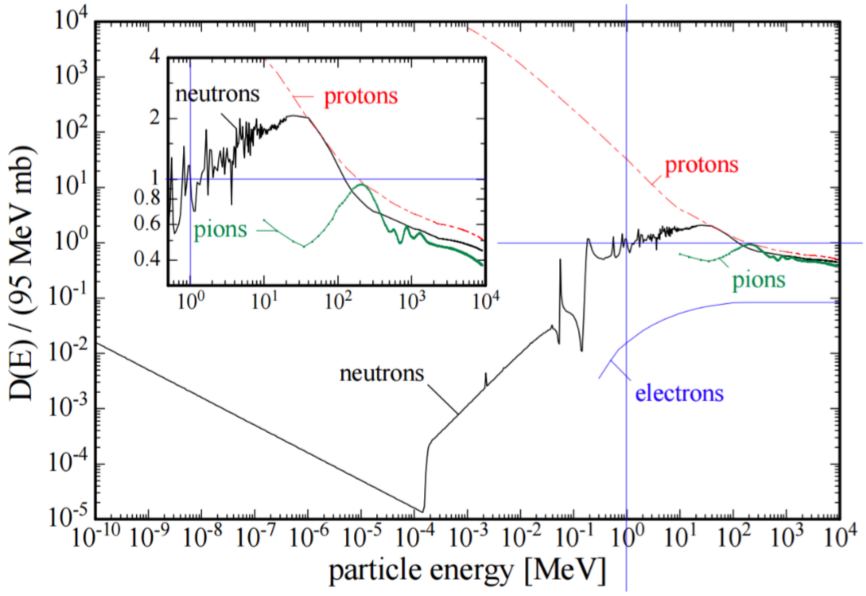


Figure A.7: *The Non-Ionizing Energy Loss (NIEL) damage $D(E)$ function normalized to 95 MeVmb for neutrons, electrons, protons and pions. The value 95 MeV corresponds to the NIEL of 1 MeV n_{eq}. Taken from [123].*

Appendix B

B.1 The heaters measurements

This appendix includes the measurements of the internal resistance of the heaters, calibration results and the metrology measurements described in Section 4.3.

Batch ID	Heater_module_id	Internal Resistance [Ohm]
Batch 2 & 4	W1-01	21.04
Batch 2 & 4	W1-03	19.84
Batch 7	W2-04	19.72
Batch 7	W2-05	19.96
Batch 7	W3-01	20.53
Batch 8	W3-02	19.53
Batch 8	W18-04	18.88
Batch 9	W3-06	20.24
Batch 9	W6-02	19.69
Batch 9	W7-01	20.57
Batch 10	W1-06	20.36
Batch 10	W03-03	19.49
Batch 10	W6-04	19.49
Batch 11	W07-04	19.53
Batch 11	W5-03	19.3
Batch 11	W6-01	20.66
Batch 12	W4-04	19.42
Batch 12	W06-03	19.6
Batch 12	W2-02	20.32
Batch 13	W05-05	19.16
Batch 13	W01-04	19.53
Batch 13	W04-03	19.8
Batch 14	W05-04	19.08
Batch 14	W05-02	19.23
Batch 14	W06-06	20.16
Batch 15	W06-05	19.46
Batch 15	W07-02	19.64
Batch 15	W04-05	19.69
Batch 16	W03-04	19.42
Batch 16	W05-06	19.8
Batch 16	W05-01	20.2

Table B.1: *The internal resistance of the heaters. The table also includes the batch number and the heaters name*

Batch	PT100	Heater	RTD	Slope	Slope-Error	Offset	Offset-Error
2	1	W1-03	1	1.422	0.00036	-1276.1	0.32
2	1	W1-03	2	1.403	0.00033	-1303.1	0.3
2	1	W1-03	3	1.369	0.00034	-1295.1	0.32
2	1	W1-03	4	1.294	0.0002	-1343.4	0.2
2	1	W1-03	5	1.268	0.00027	-1360.5	0.28
2	2	W1-01	1	1.378	0.00038	-1337.3	0.37
2	2	W1-01	2	1.296	0.0003	-1390	0.32
2	2	W1-01	3	1.346	0.00039	-1328.7	0.38
2	2	W1-01	4	1.391	0.00035	-1361.3	0.34
2	2	W1-01	5	1.277	0.00033	-1381.5	0.35
2	4	W1-03	1	1.397	0.00038	-1252.6	0.33
2	4	W1-03	2	1.371	0.00033	-1273.9	0.3
2	4	W1-03	3	1.345	0.00035	-1271.5	0.33
2	4	W1-03	4	1.275	0.00029	-1323.7	0.3
2	4	W1-03	5	1.245	0.00029	-1335.5	0.31
2	5	W1-01	1	1.4	0.00056	-1358	0.53
2	5	W1-01	2	1.259	0.00037	-1351.1	0.39
2	5	W1-01	3	1.335	0.00039	-1318.6	0.38
2	5	W1-01	4	1.379	0.00036	-1349.3	0.35
2	5	W1-01	5	1.261	0.00033	-1364.6	0.35
4	1	W1-01	1	1.344	0.00021	-1304	0.21
4	1	W1-01	2	1.247	0.00033	-1337.8	0.35
4	1	W1-01	3	1.343	0.0003	-1325.3	0.3
4	1	W1-01	4	1.355	0.00034	-1325.8	0.33
4	1	W1-01	5	1.259	0.00029	-1361.3	0.31
4	3	W1-03	1	1.455	0.00025	-1304.7	0.22
4	3	W1-03	2	1.384	0.00031	-1286.2	0.29
4	3	W1-03	3	1.366	0.00032	-1291.8	0.3
4	3	W1-03	4	1.294	0.00019	-1343.4	0.2
4	3	W1-03	5	1.274	0.00023	-1366.9	0.25
4	4	W1-01	1	1.336	0.00036	-1296.5	0.35
4	4	W1-01	2	1.229	0.00035	-1317.4	0.37
4	4	W1-01	3	1.31	0.00031	-1292.7	0.31
4	4	W1-01	4	1.334	0.0004	-1304.5	0.39
4	4	W1-01	5	1.241	0.00026	-1341.6	0.28
4	6	W1-03	1	1.445	0.00033	-1296.3	0.3
4	6	W1-03	2	1.384	0.00033	-1286.1	0.3
4	6	W1-03	3	1.358	0.0003	-1284.3	0.29
4	6	W1-03	4	1.309	0.00052	-1359.5	0.53
4	6	W1-03	5	1.264	0.00019	-1356.1	0.2
7	1	W3-01	1	1.368	0.00038	-1319	0.36
7	1	W3-01	2	1.275	0.00041	-1366.8	0.44
7	1	W3-01	3	1.345	0.00042	-1325.6	0.42
7	1	W3-01	4	1.345	0.0003	-1313.5	0.3
7	1	W3-01	5	1.266	0.00032	-1368.5	0.35

Table B.2: *The slope and the offset extracted from the calibration curves for five RTDs in each heater. The table also includes the batch number, the heaters name and the measurements uncertainties.*

Batch	PT100	Heater	RTD	Slope	Slope-Error	Offset	Offset-Error
7	2	W2-04	1	1.311	0.00043	-1363.2	0.45
7	2	W2-04	2	1.336	0.0005	-1341.2	0.5
7	2	W2-04	3	1.384	0.00043	-1283.5	0.4
7	2	W2-04	4	1.413	0.00049	-1301.9	0.45
7	2	W2-04	5	1.435	0.00047	-1276.9	0.42
7	3	W2-05	1	1.396	0.00055	-1287.3	0.5
7	3	W2-05	2	1.413	0.00054	-1257.1	0.48
7	3	W2-05	3	1.37	0.00048	-1289	0.45
7	3	W2-05	4	1.272	0.00054	-1355	0.58
7	3	W2-05	5	1.295	0.00054	-1338.9	0.56
7	4	W3-01	1	1.367	0.00041	-1318	0.39
7	4	W3-01	2	1.272	0.00044	-1363.3	0.47
7	4	W3-01	3	1.343	0.00046	-1323.3	0.46
7	4	W3-01	4	1.348	0.00042	-1316.3	0.41
7	4	W3-01	5	1.273	0.00043	-1375.4	0.47
7	5	W2-04	1	1.31	0.00041	-1362.1	0.42
7	5	W2-04	2	1.335	0.00047	-1339.3	0.47
7	5	W2-04	3	1.386	0.00041	-1285.2	0.38
7	5	W2-04	4	1.411	0.00048	-1299.7	0.44
7	5	W2-04	5	1.435	0.00044	-1277	0.39
7	6	W2-05	1	1.397	0.00051	-1288.6	0.47
7	6	W2-05	2	1.416	0.0005	-1259.9	0.45
7	6	W2-05	3	1.361	0.00035	-1281.3	0.33
7	6	W2-05	4	1.271	0.00047	-1353.5	0.51
7	6	W2-05	5	1.295	0.00048	-1338.2	0.5
8	1	W18-04	1	1.259	0.00028	-1341.1	0.3
8	1	W18-04	2	1.271	0.00027	-1310.6	0.28
8	1	W18-04	3	1.349	0.00035	-1273.9	0.33
8	1	W18-04	4	1.352	0.00023	-1265	0.21
8	1	W18-04	5	1.393	0.00036	-1255.6	0.33
8	3	W03-02	1	1.323	0.00035	-1330.2	0.35
8	3	W03-02	2	1.276	0.00028	-1329.3	0.29
8	3	W03-02	3	1.372	0.00036	-1274.6	0.33
8	3	W03-02	4	1.409	0.0003	-1251.7	0.27
8	3	W03-02	5	1.379	0.0003	-1272.4	0.28
8	4	W18-04	1	1.25	0.0003	-1331.4	0.32
8	4	W18-04	2	1.263	0.0003	-1302.5	0.31
8	4	W18-04	3	1.339	0.00036	-1264.3	0.34
8	4	W18-04	4	1.351	0.0003	-1263.4	0.28
8	4	W18-04	5	1.385	0.0004	-1248.2	0.36
8	6	W03-02	1	1.326	0.00036	-1333.1	0.36
8	6	W03-02	2	1.281	0.00032	-1334.7	0.33
8	6	W03-02	3	1.376	0.0004	-1277.8	0.37
8	6	W03-02	4	1.411	0.00034	-1254.1	0.3
8	6	W03-02	5	1.384	0.00035	-1277	0.32
9	1	W7-01	1	1.637	0.00059	-1404.4	0.5
9	1	W7-01	2	1.484	0.00049	-1468.9	0.49
9	1	W7-01	3	1.587	0.00065	-1399.4	0.58
9	1	W7-01	4	1.62	0.00068	-1402.3	0.59
9	1	W7-01	5	1.463	0.00052	-1449	0.52
9	4	W7-01	1	1.611	0.00047	-1382.2	0.41
9	4	W7-01	2	1.475	0.0006	-1459.7	0.6
9	4	W7-01	3	1.592	0.00084	-1404.2	0.74
9	4	W7-01	4	1.62	0.00088	-1401.5	0.76
9	4	W7-01	5	1.462	0.0006	-1448	0.59
9	2	W6-02	1	1.358	0.00058	-1385.5	0.6

Table B.3: *The slope and the offset extracted from the calibration curves for five RTDs in each heater. The table also includes the batch number, the heaters name and the measurements uncertainties.*

Batch	PT100	Heater	RTD	Slope	Slope-Error	Offset	Offset-Error
9	2	W6-02	2	1.305	0.00035	-1380.4	0.38
9	2	W6-02	3	1.419	0.00058	-1336.6	0.54
9	2	W6-02	4	1.453	0.00059	-1303	0.53
9	2	W6-02	5	1.424	0.00056	-1326.5	0.53
9	5	W6-02	1	1.357	0.00052	-1385.3	0.54
9	5	W6-02	2	1.335	0.00054	-1411.2	0.58
9	5	W6-02	3	1.417	0.00049	-1334.8	0.46
9	5	W6-02	4	1.451	0.0005	-1300.6	0.45
9	5	W6-02	5	1.424	0.00051	-1326.4	0.48
9	3	W03-06	1	1.29	0.00047	-1355.1	0.49
9	3	W03-06	2	1.352	0.0004	-1289.1	0.39
9	3	W03-06	3	1.359	0.00059	-1319.5	0.57
9	3	W03-06	4	1.266	0.00034	-1345.7	0.37
9	3	W03-06	5	1.365	0.0006	-1318.7	0.58
9	6	W03-06	1	1.291	0.00054	-1356.3	0.57
9	6	W03-06	2	1.367	0.00058	-1302.9	0.55
9	6	W03-06	3	1.366	0.00049	-1325.7	0.48
9	6	W03-06	4	1.281	0.00038	-1361	0.41
9	6	W03-06	5	1.347	0.00057	-1301	0.55
10	1	W3-03	1	1.451	0.00053	-1291.9	0.47
10	1	W3-03	2	1.396	0.0005	-1292	0.46
10	1	W3-03	3	1.383	0.00036	-1301	0.34
10	1	W3-03	4	1.316	0.00046	-1356.2	0.48
10	1	W3-03	5	1.273	0.00036	-1363.4	0.39
10	4	W3-03	1	1.433	0.00058	-1274.8	0.51
10	4	W3-03	2	1.388	0.00057	-1283.6	0.53
10	4	W3-03	3	1.38	0.00047	-1298.5	0.44
10	4	W3-03	4	1.293	0.0004	-1332.8	0.41
10	4	W3-03	5	1.265	0.0004	-1354.9	0.43
10	2	W6-04	1	1.312	0.00034	-1380.7	0.36
10	2	W6-04	2	1.346	0.00041	-1372.6	0.42
10	2	W6-04	3	1.432	0.00048	-1343.7	0.45
10	2	W6-04	4	1.425	0.00048	-1316.9	0.45
10	2	W6-04	5	1.445	0.00043	-1294.6	0.38
10	5	W6-04	1	1.339	0.00049	-1409	0.52
10	5	W6-04	2	1.348	0.0004	-1375.5	0.41
10	5	W6-04	3	1.433	0.00045	-1345.3	0.42
10	5	W6-04	4	1.418	0.00042	-1311.1	0.4
10	5	W6-04	5	1.436	0.00028	-1285.8	0.25
10	3	W01-06	1	1.281	0.00046	-1374.5	0.49
10	3	W01-06	2	1.363	0.00054	-1319.5	0.53
10	3	W01-06	3	1.339	0.00061	-1320.2	0.6
10	3	W01-06	4	1.277	0.00048	-1376.7	0.52
10	3	W01-06	5	1.364	0.00053	-1334.5	0.52
10	6	W01-06	1	1.279	0.00042	-1372.2	0.45
10	6	W01-06	2	1.35	0.00046	-1307.3	0.45
10	6	W01-06	3	1.366	0.00048	-1346.1	0.47
10	6	W01-06	4	1.278	0.00045	-1377.7	0.48
10	6	W01-06	5	1.367	0.0005	-1336.2	0.49
11	1	W7-04	1	1.592	0.00051	-1459.7	0.47
11	1	W7-04	2	1.608	0.00072	-1428.7	0.64
11	1	W7-04	3	1.712	0.00077	-1385.7	0.62
11	1	W7-04	4	1.74	0.00077	-1395.6	0.62
11	1	W7-04	5	1.769	0.00078	-1369.2	0.6
11	4	W7-04	1	1.58	0.0006	-1449.2	0.55
11	4	W7-04	2	1.596	0.00079	-1418.2	0.71

Table B.4: *The slope and the offset extracted from the calibration curves for five RTDs in each heater. The table also includes the batch number, the heaters name and the measurements uncertainties.*

Batch	PT100	Heater	RTD	Slope	Slope-Error	Offset	Offset-Error
11	4	W7-04	3	1.697	0.00084	-1373.6	0.68
11	4	W7-04	4	1.728	0.00085	-1385.6	0.68
11	4	W7-04	5	1.756	0.00086	-1359.1	0.66
11	2	W5-03	1	1.471	0.00048	-1339	0.44
11	2	W5-03	2	1.429	0.00059	-1350.4	0.56
11	2	W5-03	3	1.406	0.00051	-1360.2	0.49
11	2	W5-03	4	1.308	0.00058	-1382.8	0.61
11	2	W5-03	5	1.26	0.00049	-1380.5	0.53
11	5	W5-03	1	1.471	0.00046	-1339	0.42
11	5	W5-03	2	1.429	0.00056	-1350.4	0.53
11	5	W5-03	3	1.404	0.00048	-1358	0.47
11	5	W5-03	4	1.296	0.00049	-1370.2	0.52
11	5	W5-03	5	1.253	0.00037	-1372.6	0.4
11	3	W06-01	1	1.376	0.00051	-1342.5	0.49
11	3	W06-01	2	1.277	0.00048	-1378.4	0.52
11	3	W06-01	3	1.347	0.00052	-1333.9	0.51
11	3	W06-01	4	1.364	0.00063	-1336.5	0.62
11	3	W06-01	5	1.27	0.00049	-1372.2	0.53
11	6	W06-01	1	1.373	0.00048	-1339.2	0.47
11	6	W06-01	2	1.278	0.00051	-1378.9	0.55
11	6	W06-01	3	1.345	0.00055	-1332	0.54
11	6	W06-01	4	1.362	0.00065	-1334.4	0.63
11	6	W06-01	5	1.272	0.00044	-1374.6	0.47
12	1	W6-03	1	1.455	0.00059	-1307.2	0.52
12	1	W6-03	2	1.413	0.00063	-1317.3	0.58
12	1	W6-03	3	1.391	0.00055	-1317.5	0.53
12	1	W6-03	4	1.314	0.0005	-1358.5	0.52
12	1	W6-03	5	1.284	0.00056	-1373.3	0.6
12	4	W6-03	1	1.441	0.00069	-1294.3	0.62
12	4	W6-03	2	1.393	0.00057	-1298.5	0.54
12	4	W6-03	3	1.377	0.00062	-1304.3	0.59
12	4	W6-03	4	1.301	0.00058	-1345	0.6
12	4	W6-03	5	1.272	0.0006	-1359.5	0.64
12	2	W4-04	1	1.297	0.0005	-1348.1	0.52
12	2	W4-04	2	1.32	0.00054	-1331.1	0.54
12	2	W4-04	3	1.396	0.00059	-1291.3	0.55
12	2	W4-04	4	1.392	0.00055	-1279.6	0.51
12	2	W4-04	5	1.447	0.00077	-1283.2	0.68
12	5	W4-04	1	1.307	0.00036	-1358.1	0.38
12	5	W4-04	2	1.321	0.0005	-1331.2	0.5
12	5	W4-04	3	1.395	0.00057	-1290.6	0.53
12	5	W4-04	4	1.404	0.00081	-1290.4	0.75
12	5	W4-04	5	1.448	0.00071	-1283.8	0.63
12	3	W02-02	1	1.339	0.00059	-1340.5	0.59
12	3	W02-02	2	1.31	0.00057	-1355.1	0.59
12	3	W02-02	3	1.373	0.00054	-1276.9	0.5
12	3	W02-02	4	1.435	0.0006	-1278.4	0.54
12	3	W02-02	5	1.398	0.00063	-1292.3	0.59
12	6	W02-02	1	1.331	0.00063	-1332.9	0.63
12	6	W02-02	2	1.31	0.00062	-1355.6	0.64
12	6	W02-02	3	1.375	0.00052	-1278.1	0.49
12	6	W02-02	4	1.434	0.00064	-1277.1	0.57
12	6	W02-02	5	1.366	0.00059	-1262.2	0.54
13	1	W01-04	1	1.295	0.00048	-1362.7	0.5
13	1	W01-04	2	1.321	0.00048	-1344.1	0.5
13	1	W01-04	3	1.375	0.00044	-1285.6	0.42

Table B.5: *The slope and the offset extracted from the calibration curves for five RTDs in each heater. The table also includes the batch number, the heaters name and the measurements uncertainties.*

Batch	PT100	Heater	RTD	Slope	Slope-Error	Offset	Offset-Error
13	1	W01-04	4	1.407	0.00052	-1304.7	0.49
13	1	W01-04	5	1.428	0.00045	-1279.1	0.41
13	2	W05-05	1	1.48	0.00056	-1386.2	0.52
13	2	W05-05	2	1.479	0.00054	-1341.5	0.49
13	2	W05-05	3	1.435	0.0006	-1383	0.58
13	2	W05-05	4	1.301	0.0005	-1410	0.55
13	2	W05-05	5	1.304	0.0005	-1377.7	0.52
13	3	W04-03	1	1.433	0.00069	-1274.7	0.61
13	3	W04-03	2	1.404	0.00051	-1293.7	0.47
13	3	W04-03	3	1.369	0.00052	-1284.4	0.49
13	3	W04-03	4	1.304	0.00053	-1338.7	0.55
13	3	W04-03	5	1.281	0.00045	-1359.7	0.48
13	4	W01-04	1	1.284	0.00052	-1351.5	0.55
13	4	W01-04	2	1.307	0.00052	-1329.8	0.53
13	4	W01-04	3	1.368	0.00052	-1279.1	0.49
13	4	W01-04	4	1.394	0.00057	-1292.6	0.53
13	4	W01-04	5	1.415	0.0005	-1267.1	0.45
13	5	W05-05	1	1.48	0.00056	-1386.1	0.53
13	5	W05-05	2	1.48	0.00056	-1341.8	0.51
13	5	W05-05	3	1.434	0.00057	-1381.4	0.55
13	5	W05-05	4	1.303	0.00051	-1411.7	0.56
13	5	W05-05	5	1.308	0.00048	-1382.2	0.51
13	6	W04-03	1	1.428	0.00063	-1269.7	0.56
13	6	W04-03	2	1.406	0.00046	-1295	0.42
13	6	W04-03	3	1.369	0.00049	-1284	0.46
13	6	W04-03	4	1.302	0.00051	-1336.8	0.52
13	6	W04-03	5	1.282	0.0004	-1361	0.43
14	1	W05-04	1	1.346	0.00064	-1409	0.67
14	1	W05-04	2	1.355	0.00068	-1376.5	0.69
14	1	W05-04	3	1.439	0.00061	-1354.3	0.57
14	1	W05-04	4	1.471	0.00073	-1375.2	0.68
14	1	W05-04	5	1.469	0.00076	-1330.4	0.68
14	4	W05-04	1	1.344	0.00075	-1406.5	0.78
14	4	W05-04	2	1.348	0.00069	-1369	0.7
14	4	W05-04	3	1.433	0.00065	-1348.1	0.61
14	4	W05-04	4	1.463	0.00074	-1366.6	0.69
14	4	W05-04	5	1.461	0.00076	-1323.5	0.69
14	2	W06-06	1	1.322	0.00042	-1405.6	0.45
14	2	W06-06	2	1.417	0.00073	-1369.9	0.7
14	2	W06-06	3	1.394	0.00054	-1367.6	0.53
14	2	W06-06	4	1.297	0.00037	-1385	0.39
14	2	W06-06	5	1.389	0.00072	-1350.2	0.69
14	5	W06-06	1	1.319	0.00029	-1402.5	0.31
14	5	W06-06	2	1.415	0.00066	-1368.2	0.63
14	5	W06-06	3	1.391	0.00044	-1365.1	0.44
14	5	W06-06	4	1.311	0.0007	-1399.2	0.74
14	5	W06-06	5	1.39	0.00069	-1350.7	0.67
14	3	W05-02	1	1.353	0.00081	-1372.6	0.82
14	3	W05-02	2	1.31	0.00059	-1380.1	0.62
14	3	W05-02	3	1.407	0.00073	-1329.1	0.69
14	3	W05-02	4	1.442	0.00061	-1308.2	0.56
14	3	W05-02	5	1.395	0.00059	-1315.8	0.56
14	6	W05-02	1	1.348	0.0006	-1367.2	0.61
14	6	W05-02	2	1.316	0.00048	-1386.2	0.51
14	6	W05-02	3	1.408	0.00058	-1329.6	0.55
14	6	W05-02	4	1.44	0.00053	-1306.3	0.48

Table B.6: *The slope and the offset extracted from the calibration curves for five RTDs in each heater. The table also includes the batch number, the heaters name and the measurements uncertainties.*

Batch	PT100	Heater	RTD	Slope	Slope-Error	Offset	Offset-Error
14	6	W05-02	5	1.399	0.00051	-1319.7	0.48
15	1	W04-06	1	1.4	0.00042	-1283	0.39
15	1	W04-06	2	1.419	0.00041	-1256.2	0.37
15	1	W04-06	3	1.381	0.00047	-1290.1	0.44
15	1	W04-06	4	1.286	0.00044	-1358.7	0.47
15	1	W04-06	5	1.299	0.00038	-1333.7	0.39
15	4	W04-06	1	1.39	0.00046	-1274.1	0.42
15	4	W04-06	2	1.415	0.00041	-1252.7	0.36
15	4	W04-06	3	1.372	0.00048	-1282.1	0.45
15	4	W04-06	4	1.28	0.00045	-1352.4	0.47
15	4	W04-06	5	1.29	0.00042	-1324.4	0.43
15	2	W06-05	1	1.445	0.00051	-1335.4	0.48
15	2	W06-05	2	1.459	0.00045	-1305.8	0.4
15	2	W06-05	3	1.41	0.00043	-1330.5	0.41
15	2	W06-05	4	1.299	0.00033	-1380.7	0.36
15	2	W06-05	5	1.305	0.0004	-1349.1	0.42
15	5	W06-05	1	1.445	0.00052	-1335.8	0.48
15	5	W06-05	2	1.46	0.00048	-1306.6	0.44
15	5	W06-05	3	1.411	0.00046	-1331.2	0.44
15	5	W06-05	4	1.304	0.00036	-1385.5	0.39
15	5	W06-05	5	1.307	0.00042	-1350.5	0.43
15	3	W07-02	1	1.58	0.00059	-1406.3	0.53
15	3	W07-02	2	1.546	0.00064	-1451.3	0.6
15	3	W07-02	3	1.678	0.0006	-1369.6	0.49
15	3	W07-02	4	1.753	0.00074	-1358.3	0.58
15	3	W07-02	5	1.707	0.00068	-1387.7	0.56
15	6	W07-02	1	1.574	0.00054	-1401.6	0.48
15	6	W07-02	2	1.532	0.00061	-1438.5	0.58
15	6	W07-02	3	1.676	0.00055	-1368	0.46
15	6	W07-02	4	1.758	0.00063	-1362.2	0.49
15	6	W07-02	5	1.705	0.00077	-1385.1	0.63
16	1	W05-01	1	1.382	0.00058	-1355	0.57
16	1	W05-01	2	1.288	0.00041	-1401.5	0.44
16	1	W05-01	3	1.36	0.0005	-1368.1	0.5
16	1	W05-01	4	1.362	0.00051	-1363.6	0.51
16	1	W05-01	5	1.271	0.00046	-1404.8	0.5
16	4	W05-01	1	1.376	0.00033	-1349.2	0.32
16	4	W05-01	2	1.289	0.00037	-1401	0.41
16	4	W05-01	3	1.347	0.00047	-1354	0.47
16	4	W05-01	4	1.372	0.00049	-1373.8	0.49
16	4	W05-01	5	1.233	0.00035	-1362.1	0.39
16	2	W03-04	1	1.317	0.0006	-1365.6	0.62
16	2	W03-04	2	1.335	0.00055	-1342.3	0.56
16	2	W03-04	3	1.403	0.00061	-1297.7	0.56
16	2	W03-04	4	1.41	0.00057	-1291.3	0.52
16	2	W03-04	5	1.445	0.00068	-1282.5	0.6
16	5	W03-04	1	1.318	0.00054	-1367.1	0.56
16	5	W03-04	2	1.336	0.00051	-1343.4	0.52
16	5	W03-04	3	1.405	0.00057	-1298.6	0.53
16	5	W03-04	4	1.415	0.00057	-1295.7	0.52
16	5	W03-04	5	1.446	0.00062	-1283.4	0.55
16	3	W05-06	1	1.341	0.00054	-1429.9	0.58
16	3	W05-06	2	1.415	0.00066	-1372	0.64
16	3	W05-06	3	1.411	0.00065	-1400.7	0.65
16	3	W05-06	4	1.306	0.0006	-1413.5	0.65
16	3	W05-06	5	1.391	0.00049	-1376	0.49

Table B.7: *The slope and the offset extracted from the calibration curves for five RTDs in each heater. The table also includes the batch number, the heaters name and the measurements uncertainties.*

Batch	PT100	Heater	RTD	Slope	Slope-Error	Offset	Offset-Error
16	6	W05-06	1	1.34	0.00049	-1428.3	0.53
16	6	W05-06	2	1.416	0.00063	-1372.9	0.62
16	6	W05-06	3	1.41	0.00058	-1399.1	0.59
16	6	W05-06	4	1.304	0.00063	-1411.5	0.68
16	6	W05-06	5	1.393	0.00053	-1378.4	0.52

Table B.8: *The slope and the offset extracted from the calibration curves for five RTDs in each heater. The table also includes the batch number, the heaters name and the measurements uncertainties.*

Heater	Measurement	Point 1 [mm]	Point2 [mm]	Point 3 [mm]	Point 4 [mm]
W5-03	1	0,777	0,786	0,815	0,728
	2	0,779	0,800	0,817	0,742
W07-04(R=4,28)	1	0,749	0,724	0,787	0,735
	2	0,750	0,726	0,789	0,741
W06-01	1	0,703	0,734	0,778	0,727
	2	0,703	0,736	0,743	0,732
W06-04	1	0,713	0,704	0,755	0,737
	2	0,713	0,706	0,750	0,733
W03-03	1	0,768	0,729	0,748	0,731
	2	0,765	0,730	0,749	0,736
W06-02 flex!	1	0,721	0,729	0,761	0,709
	2	0,719	0,733	0,754	0,709
W07-01	1	0,728	0,701	0,784	0,715
	2	0,730	0,696	0,782	0,711
W03-06	1	0,792	0,729	0,780	0,710
	2	0,788	0,735	0,781	0,703
W06-06	1	0,736	0,739	0,770	0,779
	2	0,734	0,725	0,760	0,768

Table B.9: *The thickness measuremetns in 4 points for the glue deposition of the heaters.*

Heater	Measurement	Point 1 [mm]	Point2 [mm]	Point 3 [mm]	Point 4 [mm]
W04-03	1	0,739	0,735	0,794	0,737
	2	0,733	0,728	0,802	0,748
W05-02	1	0,806	0,775	0,800	0,741
	2	0,813	0,790	0,794	0,732
W05-05	1	0,772	0,767	0,770	0,749
	2	0,771	0,763	0,771	0,753
W01-04	1	0,756	0,748	0,772	0,731
	2	0,757	0,753	0,766	0,740
W04-04	1	0,796	0,771	0,863	0,842
	2	0,793	0,768	0,870	0,835
W06-03	1	0,761	0,737	0,811	0,755
	2	0,759	0,740	0,805	0,754
W02-02	1	0,795	0,753	0,801	0,752
	2	0,797	0,767	0,802	0,747
W03-04	1	0,771	0,746	0,843	0,733
	2	0,782	0,746	0,850	0,745
W05-01	1	0,805	0,775	0,835	0,780
	2	0,802	0,779	0,820	0,776
W07-02	1	0,730	0,716	0,765	0,721
	2	0,724	0,714	0,758	0,731
W04-05	1	0,833	0,812	0,798	0,763
	2	0,833	0,799	0,812	0,764
W05-04	1	0,741	0,772	0,839	0,790
	2	0,745	0,784	0,832	0,789
W05-06	1	0,778	0,807	0,804	0,736
	2	0,778	0,803	0,799	0,726
W06-05	1	0,768	0,775	0,827	0,779
	2	0,770	0,763	0,826	0,759

Table B.10: *The thickness measuremetns in 4 points for the glue deposition of the heaters.*

Appendix C

C.1 Holes on track cleaning performance for the 2-ring HGTD geometry

Examples of the *holes on track cleaning* performance with different configurations done with VBF H $\rightarrow$ invisible events for the 2-ring HGTD.

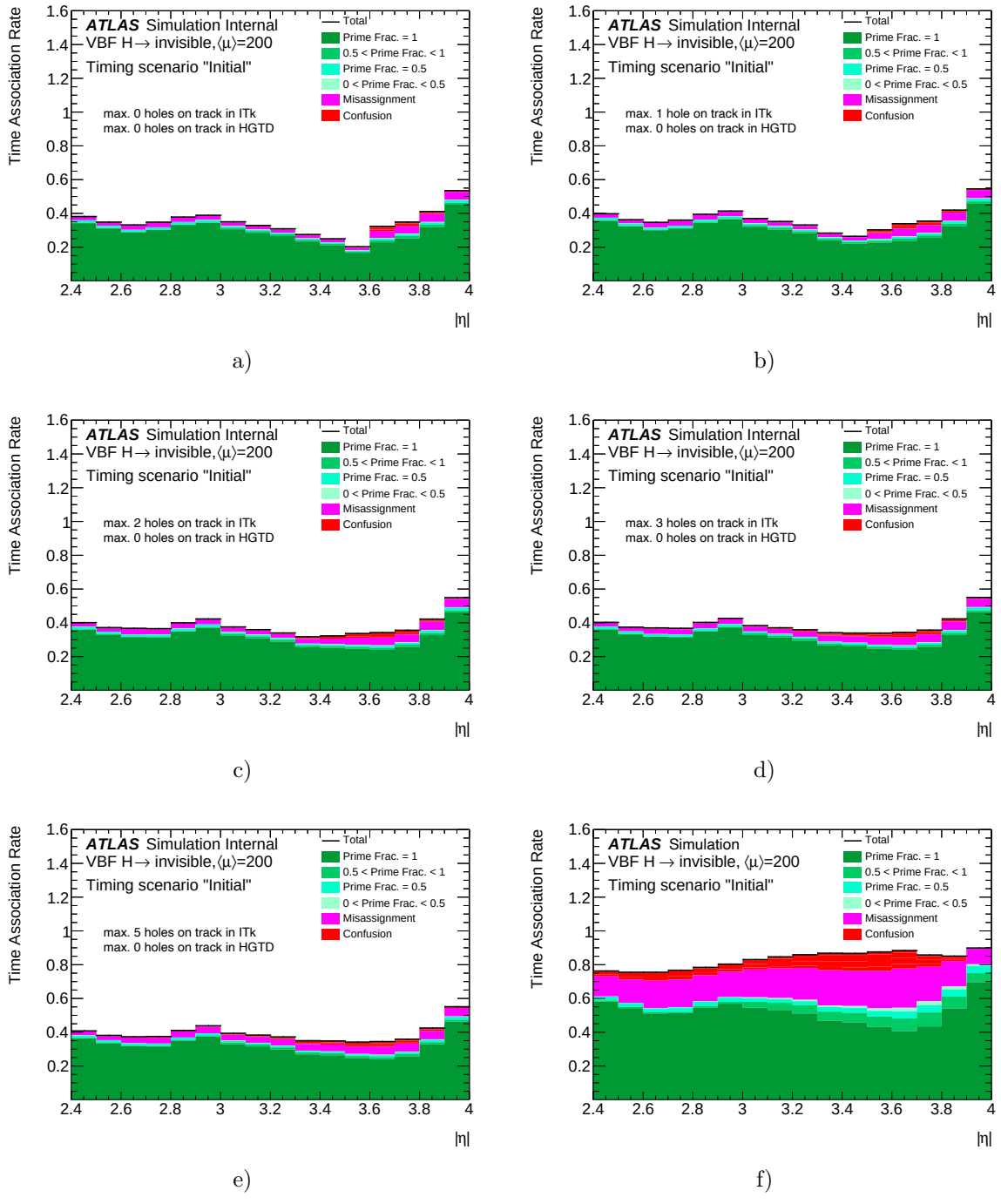


Figure C.1: *The HGTD Track-time association rates after implementing the holes on track cleaning at 0σ tolerance level. In figures (a-e), the number of maximum allowed holes on track in HGTD is set to 0 and the number of allowed holes in ITk varies from 0 (a) to 5 (e). Figure (f) shows the performance without any cut.*

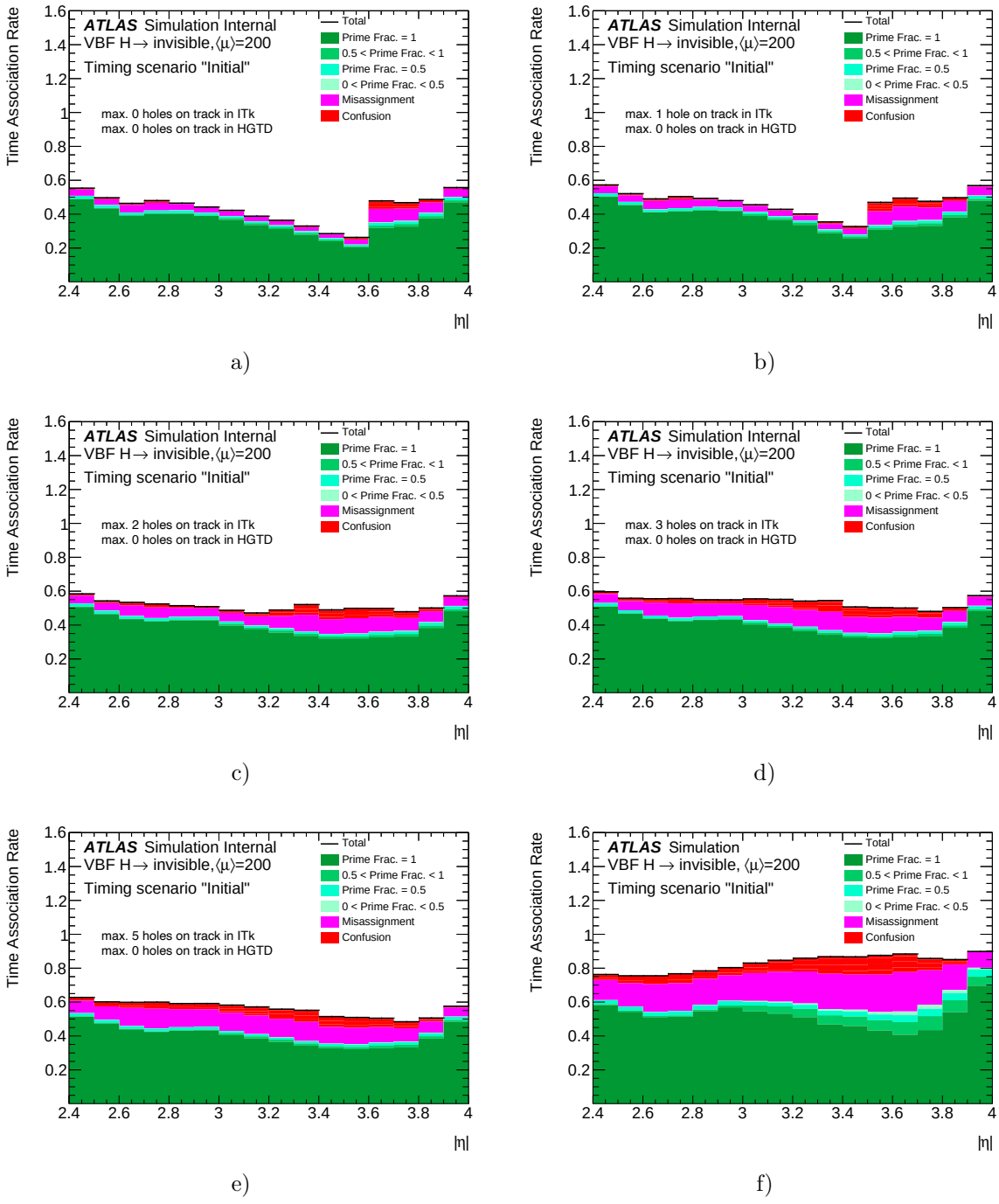


Figure C.2: *The HGTD Track-time association rates after implementing the holes on track cleaning at 9σ tolerance level. In figures (a-e), the number of maximum allowed holes on track in HGTD is set to 0 and the number of allowed holes in ITk varies from 0 (a) to 5 (e). Figure (f) shows the performance without any cut.*

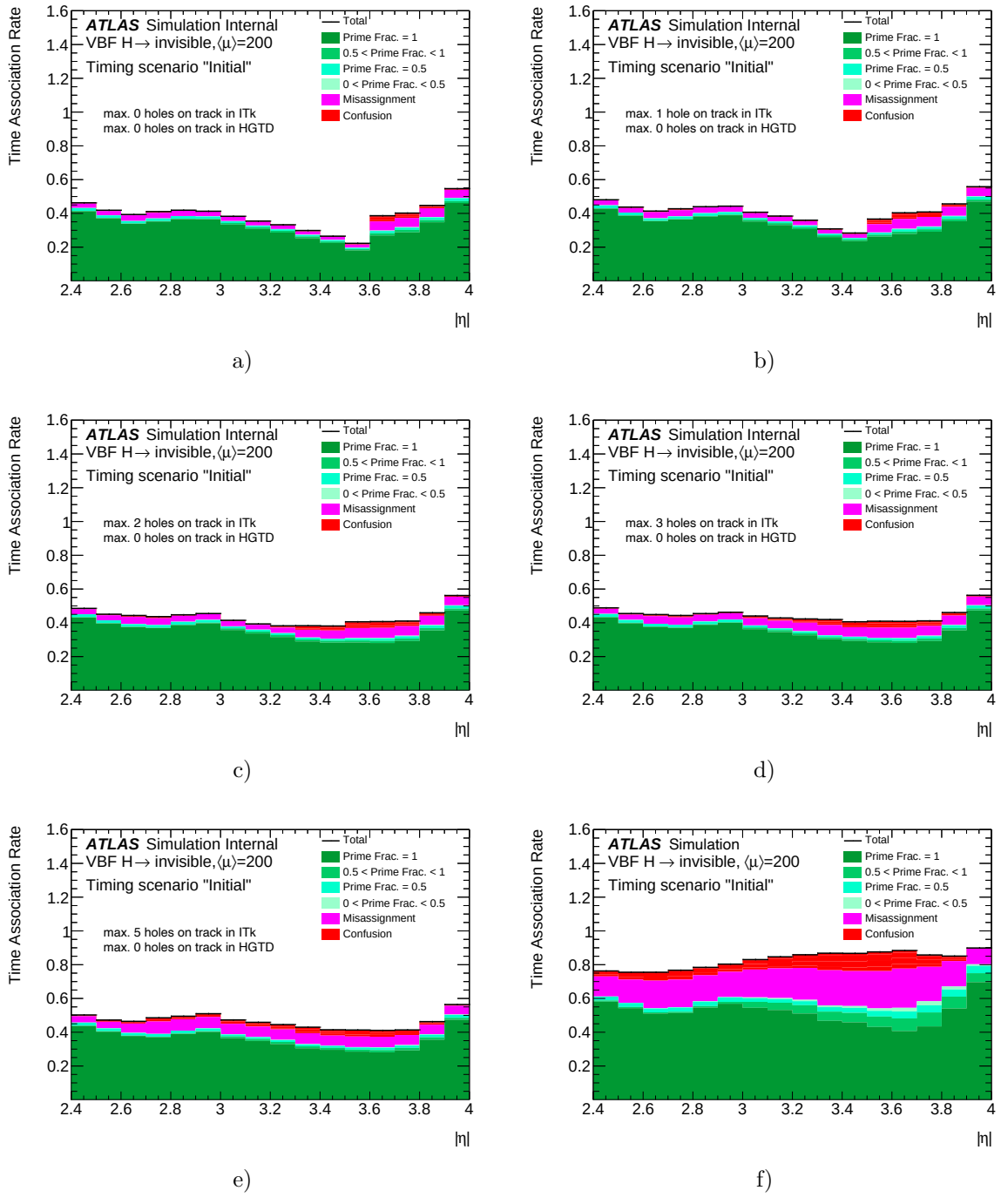


Figure C.3: *The HGTD Track-time association rates after implementing the holes on track cleaning at 3σ tolerance level. In figures (a-e), the number of maximum allowed holes on track in HGTD is set to 0 and the number of allowed holes in ITk varies from 0 (a) to 5 (e). Figure (f) shows the performance without any cut.*

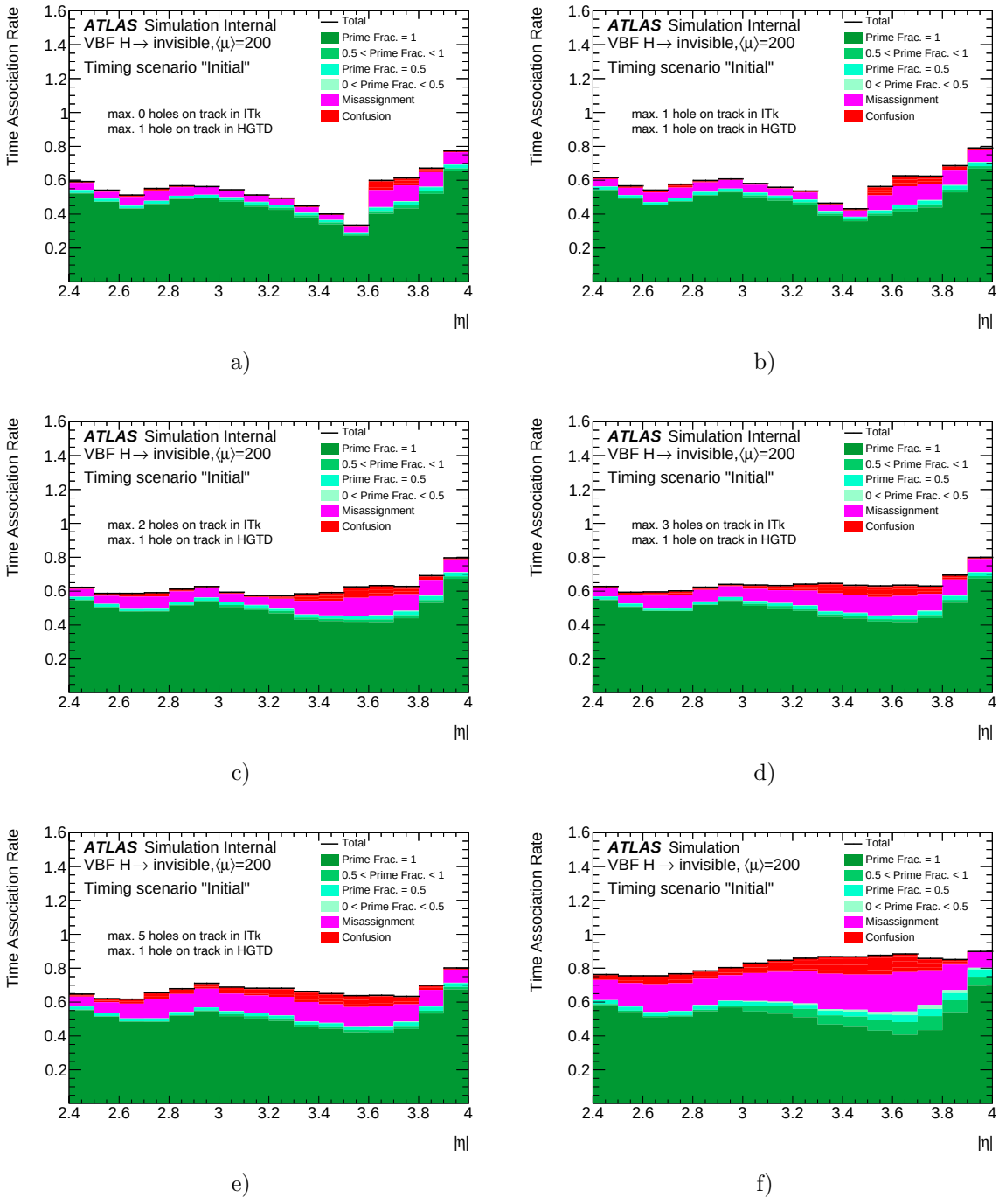


Figure C.4: *The HGTD Track-time association rates after implementing the holes on track cleaning at 3σ tolerance level. In figures (a-e), the number of maximum allowed holes on track in HGTD is set to 1 and the number of allowed holes in ITk varies from 0 (a) to 5 (e). Figure (f) shows the performance without any cut.*

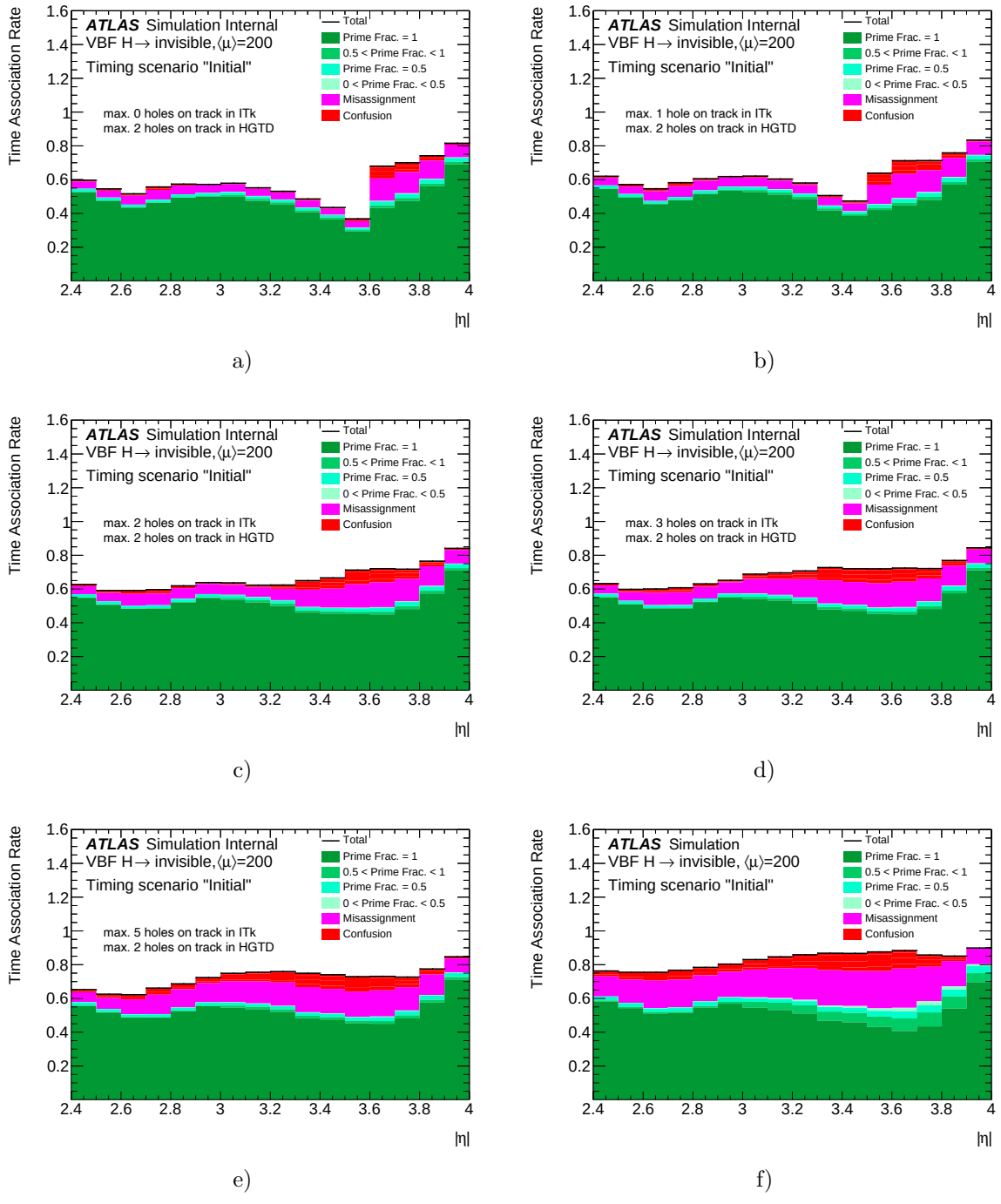


Figure C.5: *The HGTD Track-time association rates after implementing the holes on track cleaning at 3σ tolerance level. In figures (a-e), the number of maximum allowed holes on track in HGTD is set to 2 and the number of allowed holes in ITk varies from 0 (a) to 5 (e). Figure (f) shows the performance without any cut.*

Bibliography

[1] LHC Design Report Vol.1: The LHC Main Ring. Technical Report CERN-2004-003, CERN, Geneva, 2004. https://cds.cern.ch/record/782076/files/CERN-2004-003-V1-ft.pdf.

[2] CERN. Facts and figures about the lhc, 2023. https://home.cern/resources/faqs/facts-and-figures-about-lhc.

[3] The ATLAS Collaboration. *A 25-Year Insider Story of the LHC Experiment.* World Scientific Publishing Co. Pte. Ltd., 2019.

[4] Andrea Dainese et al. Report on the Physics at the HL-LHC, and Perspectives for the HE-LHC. pages 9–20, 2019. https://cds.cern.ch/record/2703572.

[5] M. Herrero. The Standard model. *NATO Sci. Ser. C*, 534:1–59, 1999.

[6] P. G. Ferreira and G. D. Starkman. Einstein's theory of gravity and the problem of missing mass. *Science*, 326(5954):812–815, Nov 2009.

[7] Wikipedia contributors. Standard model — Wikipedia, the free encyclopedia, 2010. https://en.wikipedia.org/wiki/Standard_Model, [Online; accessed 14-September-2020].

[8] Florian Scheck. *Electroweak and Strong Interactions.* Springer, 2012.

[9] CERN. Hunting the heavyweights with ua1 and ua2, 2023. https://public-archive.web.cern.ch/en/research/UA1_UA2-en.html.

[10] D. Buskulic et al. Performance of the ALEPH detector at LEP. *Nucl. Instrum. Meth. A*, 360:481–506, 1995.

[11] Steve (CERN) Brüning, Oliver (CERN) ; Myers. *Challenges and goals for accelerators in the XXI century.* Hackensack, NJ : World Scientific, 2016.

[12] CERN. Accelerating: Radiofrequency cavities, 2023. https://home.web.cern.ch/science/engineering/accelerating-radiofrequency-cavities.

[13] CERN. Pulling together: Superconducting electromagnets, 2023. https://home.cern/science/engineering/pulling-together-superconducting-electromagnets.

[14] ATLAS Experiment. Public atlas luminosity results for run-3 of the lhc, 2023. https://twiki.cern.ch/twiki/bin/view/AtlasPublic/LuminosityPublicResultsRun3.

[15] Luminosity determination in pp collisions at $\sqrt{s} = 13$ TeV using the ATLAS detector at the LHC. 12 2022.

[16] R.L. Workmanet al.(Particle Data Group). Review of Particle Physics. Prog. Theor. Exp. Phys.2022, 083C01, 2022. https://pdg.lbl.gov/2022/reviews/contents_sports.html.

[17] Craig Wiglesworth. Overview of recent results from atlas. ATL-PHYS-PROC-2020-004, 2021. https://doi.org/10.48550/arXiv.2001.05353.

[18] ATLAS Experiment. Summary plots from the atlas standard model physics group, 2023. https://atlas.web.cern.ch/Atlas/GROUPS/PHYSICS/CombinedSummaryPlots/SM/index.html#ATLAS_b_SMSummary_FiducialXsect.

[19] The ATLAS Collaboration. Compilation plots of run 2 heavy ions results for quark matter 2019. ATL-PHYS-PUB-2020-003, 2020. https://cds.cern.ch/record/2710577/files/ATL-PHYS-PUB-2020-003.pdf.

[20] ATLAS Collaboration. Technical Design Report: A High-Granularity Timing Detector for the ATLAS Phase-II Upgrade. Technical Report CERN-LHCC-2020-007; ATLAS-TDR-031, CERN, 2020. https://cds.cern.ch/record/2719855.

[21] M. Cepeda et al. Higgs Physics at the HL-LHC and HE-LHC. 2019. https://cds.cern.ch/record/2650162/files/fermilab-pub-19-074-ppd-t.pdf.

[22] ATLAS Experiment. The atlas detector, 2023. https://atlas.cern/Discover/Detector.

[23] ATLAS inner detector: Technical design report. Vol. 1. 4 1997.

[24] ATLAS inner detector: Technical design report. Vol. 2. 4 1997.

[25] G. Aad et al. ATLAS pixel detector electronics and sensors. *JINST*, 3:P07007, 2008.

[26] ATLAS Experiment. The atlas caloremeters, 2023. https://atlas.cern/Discover/Detector/Calorimeter.

[27] C.W. Fabjan and F. Gianotti. Calorimetry for particle physics. *Rev. Mod. Phys.*, 75:1243–1286, 2003.

[28] P.Krieger. The atlas liquid argon calorimeter: construction, integration, commissioning and performance from selected particle beam test results. In *2005 IEEE Nuclear Science Symposium and Medical Imaging Conference (2013 NSS/MIC)*. IEEE, oct 2005. https://doi.org/10.1109/NSSMIC.2005.1596428.

[29] ATLAS Experiment. Muon spectrometer, 2023. https://atlas.cern/Discover/Detector/Muon-Spectrometer.

[30] ATLAS Experiment. Magnet system, 2023. https://atlas.cern/Discover/Detector/Magnet-System.

[31] G. Aad et al. The ATLAS Experiment at the CERN Large Hadron Collider. *JINST*, 3:S08003, 2008.

[32] ATLAS Collaboration. Technical Design Report for the Phase-II Upgrade of the ATLAS Trigger and Data Acquisition System. Technical Report CERN-LHCC-2017-020 ; ATLAS-TDR-029, CERN, 2017. http://cds.cern.ch/record/2285584.

[33] Leggett C. et al. AthenaMT: upgrading the ATLAS software framework for the many-core world with multi-threading. 2017.

[34] Athena 24.0.X. Upgrade, analysis, derivations. DOI 10.5281/zenodo.2641997.

[35] G. Barrand et al. GAUDI - A software architecture and framework for building HEP data processing applications. *In: Comput. Phys. Commun. 140 (2001)*, 00254-5, 2001. DOI 10.1016/S0010-4655(01).

[36] Osgi patterns, 2023. https://enroute.osgi.org/FAQ/400-patterns.html.

[37] E. Moyse and F. Åkesson. The ATLAS Event Data Model. CHEP (Mumbai), 2006. https://indico.cern.ch/event/408139/contributions/979862/.

[38] G. Aad et al. The ATLAS Simulation Infrastructure. *Eur. Phys. J.*, C70:823–874, 2010.

[39] S. Agostinelli et al. GEANT4: A Simulation toolkit. *Nucl. Instrum. Meth.*, A506:250–303, 2003.

[40] Ali Abbas. The kernel samepage merging process, 2016. https://web.archive.org/web/20160808174912/http://alouche.net/blog/2011/07/18/the-kernel-samepage-merging-process/.

[41] Paul Gessinger-Befurt. Development and improvement of track reconstruction software and search for disappearing tracks with the ATLAS experiment. 5 2021.

[42] CERN. Teaching established software new tricks, 2023. https://atlas.cern/updates/briefing/renovating-athena.

[43] CERN. High-luminosity large hadron collider (hl-lhc): Technical design report. Technical Report CERN-2020-010, CERN, 2020. https://e-publishing.cern.ch/index.php/CYRM/issue/view/127/111.

[44] ATLAS Collaboration. Technical Design Report for the ATLAS Inner Tracker Pixel Detector. Technical Report CERN-LHCC-2017-021, CERN, Geneva, July 2018. https://cds.cern.ch/record/2285585.

[45] ATLAS Collaboration. Technical Design Report for the Phase-II Upgrade of the ATLAS TDAQ System. Technical Report CERN-LHCC-2017-020 ; ATLAS-TDR-029, CERN, 2017. https://cds.cern.ch/record/2285584.

[46] ATLAS Collaboration. Technical Design Report for the ATLAS Inner Tracker Strip Detector. Technical Report CERN-LHCC-2017-005 ; ATLAS-TDR-025, CERN, 2017. https://cds.cern.ch/record/2257755.

[47] ATLAS Collaboration. Technical Design Report for the Phase-II Upgrade of the ATLAS Tile Calorimeter. Technical Report CERN-LHCC-2017-019 ; ATLAS-TDR-028, CERN, 2017. https://cds.cern.ch/record/2285583.

[48] ATLAS Collaboration. Technical Design Report for the Phase-II Upgrade of the ATLAS Muon Spectrometer. Technical Report CERN-LHCC-2017-017 ; ATLAS-TDR-026, CERN, 2017. https://cds.cern.ch/record/2285580.

[49] The ATLAS collaboration. Expected tracking and related performance with the updated ATLAS Inner Tracker layout at the High-Luminosity LHC. Technical Report ATL-PHYS-PUB-2021-024, CERN, 2021. https://cds.cern.ch/record/2776651/files/ATL-PHYS-PUB-2021-024.pdf.

[50] ATLAS Collaboration. Electron and photon reconstruction and performance in ATLAS using a dynamical, topological cell clustering-based approach. ATL-PHYS-PUB-2017-022, 2017. https://cds.cern.ch/record/2298955.

[51] Alexander Leopold. Dark Matter Searches in Association with a Higgs Boson using $\sqrt{s} = 13$ TeV ATLAS Data and Performance Evaluation of the High-Granularity Timing Detector. 12 2020.

[52] The ATLAS Collaboration. Luminosity determination in p p collisions at s$_{\sqrt{}}$=13 TeV using the ATLAS detector at the LHC. ATLAS-CONF-2019-021, 2019. https://cds.cern.ch/record/2677054/files/ATLAS-CONF-2019-021.pdf.

[53] A. Sidoti, editor. *Minimum Bias Trigger Scintillators in ATLAS Run II*, volume 10.1088/1748-0221/9/10/C10020 of *ATL-DAQ-PROC-2014-010*, 2014.

[54] RD50 collaboration. https://rd50.web.cern.ch/rd50.

[55] Agapopoulou et al. A prototype ASIC for the ATLAS High Granularity Timing Detector. *In preparation.*

[56] L Amaral et al. The versatile link, a common project for super-lhc. *Journal of Instrumentation*, 4(12):P12003, 2009.

[57] ATLAS Collaboration. Technical Specification for HGTD modules and detector units. Technical report, CERN, 2021. EDMS 2632083, https://cds.cern.ch/record/2719855.

[58] G. Lutz. *Semiconductor Radiation Detectors*. Springer-Verlag Berlin Heidelberg, 2007.

[59] S. N. Ahmed. *Physics and Engineering of Radiation Detection*. Elsevier, 2014.

[60] Reem H. Taibah. Upgrade of the ATLAS tracking detector in preparation for the High-Luminosity phase of the LHC : Planar pixel module characterisation and calibration for the current and future ATLAS inner tracker. 09 2021.

[61] Alfredo Ferrari, Paola R Sala, Alberto Fasso, and Johannes Ranft. FLUKA: A multi-particle transport code. Technical report, 2005.

[62] H. F.-W. Sadrozinski et al. Ultra-fast silicon detectors (ufsd). *Elsevier*, 831, 2016. https://doi.org/10.1016/j.nima.2016.03.093.

[63] F. Foerster. Novel silicon detector technologies for the HL-LHC ATLAS upgrade. Presented 28 July 2020. https://cds.cern.ch/record/2730681.

[64] Gregor Kramberger. LGADs for timing detectors at HL-LHC. *CERN Detector Seminar*, 2021. https://indico.cern.ch/event/1088953/.

[65] Agapopoulou et al. Performance of a front-end prototype ASIC for the ATLAS High Granularity Timing Detector. *JINST*. https://arxiv.org/pdf/2306.08949.pdf.

[66] Chiara Grieco. Low Gain Avalanche Detectors for the ATLAS High Granularity Timing Detector. 07 2022.

[67] HGTD Collaboration. The public plots of the HGTD collaboration, 2023. https://twiki.cern.ch/twiki/bin/view/AtlasPublic/HGTDPublicPlots.

[68] ARALDITE 2011, 2023. https://www.huntsman.com/products/araldite2000/araldite-2011.

[69] PEEK characteristics, 2023. https://www.ensingerplastics.com/en/thermoplastic-materials/peek-plastic.

[70] ATLAS HGTD Module Group. Technical specifications for the hgtd modules and detector units. (AT2-G-ES-0011), 2022. https://edms.cern.ch/document/2632083.

[71] General tolerances . https://www.iso.org/obp/ui/#iso:std:iso:2768:-1:ed-1:v1:en.

[72] FESTO, 2023. https://www.festo.com/fr/fr/c/produits-id_pim1/.

[73] Poly Dispensing Systems, 2023. https://polydispensing.com/en/product-details/volumetric-dispenser-precifluid/.

[74] Accura 25, 2023. https://www.3dsystems.com/materials/accura-25-sla.

[75] Carbon fiber T300, 2023. https://www.rockwestcomposites.com/media/wysiwyg/T300DataSheet_1.pdf.

[76] Polyimide Heaters , 2023. https://farnam-custom.com/custom/polyimide-heaters?gad=1&gclid=CjwKCAjwhJukBhBPEiwAniIcNfKNMvp9EAp4qA3gN59Jsn1lAamyBMAN-PqlAAPsJoZRXonuvHCtVxoC
BwE.

[77] PT100 resistance temperature detector , 2023. https://peaksensors.co.uk/what-is/pt100-sensor/#:~:text=Pt%20refers%20to%20that%20the,uses%20resistance%20to%20measure%20temperature.

[78] Lydia Beresford on behalf of the demonstrator team. Heater demonstrator overview, 2022. https://indico.cern.ch/event/1127322/#154-heater-demonstrator-result.

[79] Stefan Guindon. High Granularity Timing Detector. CAT General Meeting. 2020. https://indico.cern.ch/event/918627/contributions/3860813/attachments/2049613/3435119/CAT_General_HGTD.pdf.

[80] TESA-Hite, 2023. https://tesatechnology.com/en-gb/products/mesureurs-verticaux/mesureurs-verticaux-1d/tesa-hite_p47093.htm.

[81] Afonso Ferreira. Cooling plate Graphite + thermal grease tests. 2022. https://indico.cern.ch/event/1127940/contributions/4869159/attachments/2440958/4181703/HGTD-Graphite_Grease-Plate-Test.pdf.

[82] C. Allaire et al. Beam test measurements of Low Gain Avalanche Detector single pads and arrays for the ATLAS High Granularity Timing Detector. *JINST*, 13:P06017, 2018.

[83] C. Agapoupoulou et al. Performance in beam tests of irradiated Low Gain Avalanche Detectors for the ATLAS High Granularity Timing Detector. *JINST*, 17:P09026, 2022.

[84] J.Behr et al. Performance of the EUDET-type beam telescopes. *EPJ Techniques and Instrumentation*, 3:835–844, 2016. DOI 10.1140/epjti/s40485-016-0033-2.

[85] I. Rubinskiy Koetz. User Manual: ATLAS FE-I4A Pixel Module as a Trigger Plane for the Beam Telescope.

[86] Galloway Z. et al. Properties of HPK UFSD after neutron irradiation up to 6×10^{15} n_{eq}/cm^2. *Nucl. Instr. Meth. A*, (940):19–29, 2019.

[87] NIM Powered Crates, 2018. https://www.caen.it/families/nim-powered-crates/.

[88] D. Cussans. *Description of the JRA1 Trigger Logic Unit (TLU), v0.2c*. https://www.eudet.org/e26/e28/e42441/e57298/EUDET-MEMO-2009-04.pdf.

[89] M. Dyndal et al. Mini-MALTA: Radiation hard pixel designs for small-electrode monolithic CMOS sensors for the high luminosity LHC. *JINST*, 15(02):P02005, 2020.

[90] Rademakers F Brun R. ROOT: an object oriented data analysis framework. *Nuclear instruments and Methods*, (389), 1997.

[91] Wikipedia contributors. Constant fraction discriminator — Wikipedia, the free encyclopedia, 2021. https://en.wikipedia.org/wiki/Constant_fraction_discriminator.

[92] S. Bharthuar et al. Study of interpad-gap of hpk 3.1 production lgads with transient current technique. *Nuclear Inst. and Methods in Physics Research, A*, 979(164494), 2021.

[93] Moritz Kiehn. Proteus beam telescope reconstruction (v1.4.0). *Adv. Cryog. Eng. A*, Zenodo, 2009.

[94] J. Myrheim and L. Bugge. A fast Runge-Kutta method for fitting tracks in a magnetic field. *In: Nucl. Instrum. Meth.*, (160.1), 1979. DOI:10.1016/0029-554X(79)90163-0.

[95] R. Fruhwirth. Application of Kalman filtering to track and vertex fitting. *Nucl. Instrum. Meth. A*, 262:444–450, 1987.

[96] ATLAS. Production of the reconstruction for HGTD TDR samples. https://prodtask-dev.cern.ch/prodtask/inputlist_with_request/27587/.

[97] Paolo Nason. A New method for combining NLO QCD with shower Monte Carlo algorithms. *JHEP*, 11:040, 2004.

[98] Simone Alioli, Paolo Nason, Carlo Oleari, and Emanuele Re. NLO Higgs boson production via gluon fusion matched with shower in POWHEG. *JHEP*, 04:002, 2009.

[99] Stefano Frixione, Paolo Nason, and Carlo Oleari. Matching NLO QCD computations with Parton Shower simulations: the POWHEG method. *JHEP*, 11:070, 2007.

[100] Torbjörn Sjöstrand, Stefan Ask, Jesper R. Christiansen, Richard Corke, Nishita Desai, Philip Ilten, Stephen Mrenna, Stefan Prestel, Christine O. Rasmussen, and Peter Z. Skands. An introduction to PYTHIA 8.2. *Comput. Phys. Commun.*, 191:159–177, 2015.

[101] ATLAS Collaboration. Measurement of the Z/γ^* boson transverse momentum distribution in pp collisions at $\sqrt{s} = 7$ TeV with the ATLAS detector. *JHEP*, 09:145, 2014.

[102] Hung-Liang Lai, Marco Guzzi, Joey Huston, Zhao Li, Pavel M. Nadolsky, Jon Pumplin, and C. P. Yuan. New parton distributions for collider physics. *Phys. Rev.*, D82:074024, 2010.

[103] Simone Alioli, Paolo Nason, Carlo Oleari, and Emanuele Re. A general framework for implementing NLO calculations in shower Monte Carlo programs: the POWHEG BOX. *JHEP*, 06:043, 2010.

[104] The ATLAS Collaboration. Summary of ATLAS Pythia 8 tunes. 2012. ATL-PHYS-PUB-2012-003.

[105] Cern gitlab, 2023. https://gitlab.cern.ch.

[106] Github, 2023. https://github.com.

[107] C. Arnault. Configuration Management Tool, 2023. http://www.cmtsite.net.

[108] Subversion, 2023. https://subversion.apache.org.

[109] Git, 2023. https://git-scm.com.

[110] CMake, 2023. https://cmake.org.

[111] Xiaocong Ai et al. A Common Tracking Software Project. 2022. https://doi.org/10.1007/s41781-021-00078-8.

[112] P.V.S. Rao. *Computer System Architecture (Section 19.1, The x86 family of processors)*. 2009.

[113] Learn the architecture - Introducing the ARM architecture. https://developer.arm.com/documentation/102404/0201/?lang=en.

[114] Jacob B et al. Guennebaud G. Eigen v3, 2010. http://eigen.tuxfamily.org.

[115] Boost, 2023. https://www.boost.org.

[116] The ATLAS Collaboration. The fast atlas track simulation (fatras). ATL-SOFTPUB-2008-001, 2008. https://cds.cern.ch/record/1091969.

[117] Petric M. et al. Detector simulations with dd4hep. *J Phys Conf Ser.*, 2017. https://doi.org/10.1088/1742-6596/898/4/042015.

[118] Boudreau J Tsulaia V. The geomodel toolkit for detector description. *CHEP*, 2004. https://indico.cern.ch/event/0/contributions/1294152/.

[119] ATLAS Collaboration. Development of ATLAS primary vertex reconstruction for LHC Run 3. *Technical report, ATL-PHYS-PUB-2019-015*, 2019.

[120] X. Ai et al. A GPU-Based Kalman Filter for Track Fitting. *Comput Softw Big Sci 5*, 2021. https://doi.org/10.1007/s41781-021-00065-z.

[121] H. Spieler. *Semiconductor Detector Systems*. Oxford University Press, 2005.

[122] Michael Moll. The NIEL project. Towards a more complex NIEL concept for radiation damage modelling and prediction, 2020. https://indico.cern.ch/event/979793/contributions/4127788/attachments/2156198/3636946/NIEL%20project_201204v1.pdf.

[123] I. Pintilie E. Fretwurst, G. Lindstrom and J. Stahl. Radiation damage in silicon detectors caused by hadronic and electromagnetic irradiation. *arXiv preprint physics/0211118*, (DESY 02-199), 2002. https://arxiv.org/pdf/physics/0211118.pdf.